Statistical Electronics

- Noise Processes in Integrated Communication Systems -

Thesis by

Donhee Ham

In Partial Fulfillment of the Requirements

for the Degree of

Doctor of Philosophy

California Institute of Technology

Pasadena, California

2002

(Submitted May 31, 2002)

Acknowledgements

First of all, I would like to express my sincere gratitude to my advisor, Prof. Ali Hajimiri. Through his many roles as an advisor, a mentor, and a friend, he has had a tremendous influence on both my professional and personal development. I am very grateful for his support and encouragement throughout my Ph.D. work and also for always making sure that I did not fall. My greatest intellectual debt is also to him. Without his deep insight and sharp mind, this research and thesis could not have been possible. He always believed in me so much and bore with my slow learning-curve with almost inhuman patience when I started studying circuit engineering.

I am deeply indebted to my former advisor, Prof. Barry Barish, for his support throughout my Caltech life. During the transitional period from the Physics to the Electrical Engineering department, Barry sincerely encouraged me to find and pursue the right career path for me. He helped me a great deal even during the EE years on several occasions with extreme generosity.

I am very grateful to Prof. P. P. Vaidyanathan, who took much care of my settlement in the EE department and has given me continuous words of encouragement. I would also like to thank him for serving on my oral committee, reading this thesis, and giving me invaluable comments on this work.

I first became ensnared by the charms of noise problems in the course *Application of Classical Physics*, which Prof. Michael Cross taught in my first year at Caltech. In *Statistical Physics* he taught, I became equipped with a coherent framework with which I could tackle noise problems in circuits systematically. I owe many thanks to him for sharing his knowledge with me, reading this thesis, and serving on my orals committee. His in-depth insight helped me a great deal in advancing a key step forward in my study of fluctuations in nonlinear circuits.

I am also fortunate to have received technical wisdom from Professors Dave Rutledge and Yu-Chong Tai. They read this thesis, served on my orals committee, and offered insightful suggestions on this work. I am especially indebted to Dave for his continuous support on many occasions throughout the EE years. I also extend thanks to Professor Shuki Bruck for his time and dedication to serve on my oral committee.

My work and life at Caltech have tremendously benefited from intellectual and personal interactions with Chris White and Behnam Analui, my friends, colleagues, and officemates. Countless discussions with them on the subject of noise made conspicuous contributions to this work. With their warm personalities and big hearts, they have offered me such an enjoyable working environment and have been always supportive through the final stretch. I would also like to thank them for

their tireless patience in listening to my endless arguments about our beloved composer Beethoven and his music, the "ultimately sublime noise." I am especially indebted to Chris, for reading all my paper manuscripts, this thesis and my research proposal and for giving me valuable comments on the material.

Very special thanks goes to my colleagues and friends in the Caltech High-Speed Integrated Circuits Group, especially to Ichiro Aoki, Hui Wu, Hossein Hashemi, and Abbas Komijani. This research and thesis could not have been possible without the collaboration, encouragement, and aid of them. They have also deeply enriched my graduate school years with their friendship. I am specially indebted to Ichiro Aoki for his valuable lessons on microwave circuits.

I am also very grateful to other various colleagues in the past and present for their friendship and support: many thanks to Dai Lu, Lawrence Cheung, Carol Sosnowski, Heather Jackson, Yujin Chung, Prof. Bumman Kim, Dr. John Davis, Dr. Taavi Hirvonen, and Paula Vo. I also thank Linda Dosza for her administrative help, and Naveed Near-Ansari, Lisa Bogue and Larry Wallace for their CAD support.

I would like to acknowledge the IBM Corporation for their financial support for my fourth year through IBM Research Fellowship and for generously fabricating distributed amplifier chips for free. They also gave me the opportunity to work as a summer intern at T. J. Watson Research Center where I had in-depth exposure to various problems in integrated circuit design. I am especially indebted to Dr. Mehmet Soyuer, Dr. Dan Friedman, and Dr. Mark Ritter, my mentors during the T. J. Watson period. Also I wish to thank Dr. Jungwook Yang for his insightful lessons on circuits and CAD. Dr. Jean-Olivier Plouchart, Dr. Modest Oprysko, Herschel Ainspan, and Noah Zamdmer also deserve my thanks. Conexant Systems fabricated oscillator and mixer chips for free and I would particularly like to acknowledge Bijan Bhattacharyya, Frank In'tveld, and Rahul Magoon for their consistent help and support. Partial funding for this work came from Lee Center for Advanced Networking and from the National Science of Foundation.

Outside of school life, I have many people to thank for their continued support and friendship. Paul Kim, Hyotcherl Ihee, Kashif Alvi, Hern Paik, Yi Tang, Soma Mukerjee, Soumya Mohanty, Chris Liu, Jun-R Huh, Bumki Min, Nathan Good, Pratip Bhattacharyya, and countless others have richened my graduate school years. I am deeply obliged to Young-Chul Ra, Cheol-Woong Lee, Min-Chul Lee and Gloria Choi for their huge mental support, which has been a great source of strength for me.

But it was my parents who provided the most encouragement and I dedicate this thesis to them with my deepest gratitude. Without their inspiration and love, I could never have achieved this goal in my life. Lastly, I am grateful for my two sisters, who were always so loving and cheerful.

Abstract

This thesis presents a comprehensive investigation of noise and thermodynamics in electronic circuits and systems. This study of "statistical electronics" spans two disciplines, statistical thermodynamics and electronic circuit engineering, and leads to a general picture that bridges electronics and statistical thermodynamics.

Our work on statistical electronics has both scientific and engineering implications. Scientifically, this work is an extensive study of statistical thermodynamics in the context of electrical circuits, which has made several significant contributions to the understanding of noise processes in electrical circuits. The technological importance is a demonstration of how the fundamental physical considerations evolve to practical high-performance novel circuit design. The power of our fundamental approach is demonstrated through several practical circuit examples.

First, our investigation of fluctuations in nonlinear electrical circuits provides deep insight into the nonlinear fluctuation phenomena. Especially, the study of fluctuations in nonlinear active devices constitutes an important sector in this investigation, verifying the physical soundness of the contemporary active device noise modeling and leading to clear understanding of fluctuation-dissipation relations in nonlinear devices.

Second, we apply statistical electronics to noise problems involved in frequency conversion, an essential function in modern RF and microwave receivers. This study leads to two novel observations of noise figure degradation due to cyclostationary noise and conversion gain enhancement, both dependent on the size of energy storing elements. This novel behavior is experimentally verified with a direct measurement of integrated switching mixers. The results provide new insight into cyclostationary noise processes in frequency conversion and optimum design for switching mixers.

Third, application of statistical electronics to noise in frequency generation by self-sustained oscillators leads to a new theory of oscillator noise. This study demonstrates the direct correspondence between the phase noise and the Einstein relation, revealing the underlying physics of oscillator noise. Our approach clarifies the fluctuation-dissipation relation in oscillator noise generation, establishing a link between currently available fluctuation-based and dissipation-based phase noise models and leading to a clear definition of loaded quality factor of an oscillator. The novel concepts of virtual damping and linewidth compression put resonators and oscillators in a unified framework, providing immediate design optimization insight. The power of this theoretical development is demonstrated through experimental measurements of various integrated oscillators.

Our work on statistical electronics combining circuit engineering and physical science has also

resulted in other useful engineering methods, such as graphical optimization, noise simulations for computer-aided design (CAD), and time-varying filter theory.

Contents

Acknowledgements iii

Abstract v

1 Introduction 1

1.1 Motivation 1

1.2 Organization 3

2 RF Signal Detection Issues 5

2.1 A Generic RF Signal Detector 5

2.2 Noise in RF Detection 8

2.2.1 Signal-Path Noise 8

2.2.2 Frequency-Reference Noise 9

2.2.3 Noise in Time-Varying Systems 10

3 Thermal Fluctuation Fundamentals 13

3.1 Brownian Motion 13

3.1.1 Equilibrium Property 14

3.1.2 Langevin Equation 16

3.1.3 Fluctuation-Dissipation Theorem 22

3.1.4 Fokker-Planck Equation 23

3.2 Brownian Motion in Electrical Circuits 29

3.2.1 Johnson-Nyquist Noise 29

3.2.2 Fluctuation-Dissipation Theorem Revisited 31

3.2.3 Probability Distribution of Voltage 32

3.2.4 More on the k_BT/C-Noise 34

3.3 Forced Brownian Motion 40

3.3.1 Mechanical Case 40

3.3.2 Electrical Case 42

3.3.3 Probability Distribution of Displacement 43

3.4 Summary 45

4 Fluctuations and Thermodynamics in Nonlinear Electrical Circuits **48**

4.1 Motivation . . . 48

4.2 Problem Formulation . . . 56

4.3 Fluctuations in Linear *RC*-Circuits, Revisited . . . 57

4.3.1 Energetics . . . 58

4.3.2 Entropy Evolution . . . 60

4.4 Fluctuations in *RC*-Circuits with Nonlinear Resistors . . . 62

4.4.1 Steady-State Properties . . . 63

4.4.2 Energetics . . . 66

4.4.3 Entropy Evolution . . . 70

4.5 Fluctuations in *RC*-Circuits with Nonlinear Capacitors . . . 71

4.6 Summary . . . 74

5 Noise in Time-Varying Driven Circuits **75**

5.1 Introduction . . . 75

5.2 Cyclostationary Noise Fundamentals . . . 79

5.3 LTI Low-Pass Filtering of Cyclostationary Noise . . . 85

5.4 Switching Mixer Example . . . 89

5.4.1 Operational Principle . . . 89

5.4.2 State Equation . . . 91

5.5 Time-Varying Filtering Theory - I : Deterministic Dynamics . . . 94

5.6 Time-Varying Filtering Theory - II : Stochastic Dynamics . . . 99

5.7 Simulation and Design Implication . . . 104

5.7.1 Conversion Gain Simulation . . . 104

5.7.2 Noise Simulation . . . 105

5.8 Experimental Verification . . . 109

5.8.1 Measurement Setup . . . 109

5.8.2 Measurement Results . . . 110

5.9 Summary . . . 112

6 Noise in Time-Varying Autonomous Circuits **113**

6.1 Introduction . . . 113

6.2 Self-Sustained Oscillator Fundamentals . . . 115

6.2.1 Self-Sustained Oscillation . . . 115

6.2.2 Examples . . . 118

6.2.3 State-Space and Limit Cycle . . . 120

6.2.4 Approximation for Resonator-Based Oscillators . . . 122

6.3 Phase Noise Fundamentals 124
6.3.1 Phase Diffusion 124
6.3.2 Phase Noise 128
6.3.3 Leeson Model and Hajimiri-Lee Model 131
6.4 Virtual Damping 134
6.5 Physical Derivation of Virtual Damping Rate 138
6.5.1 Time-Invariant Case 140
6.5.2 Time-Varying Case 141
6.6 Mathematical Derivation of Virtual Damping Rate 143
6.7 Principles of Oscillator Noise Optimization 146
6.7.1 Behavior of Noise-to-Carrier Ratio, NCR 148
6.7.2 Behavior of Virtual Damping Rate, D 153
6.8 Design Example 155
6.8.1 *LC VCO Topology, Design Constraints and Phase Noise* 156
6.8.2 *LC* VCO optimization via graphical methods 163
6.8.3 Simulation 168
6.8.4 Experimental Results 172

7 Conclusion **176**

8 Appendices **177**
8.1 Appendix 1 177
8.2 Appendix 2 178

Bibliography **179**

List of Figures

2.1 A generic RF signal receiver. 5

2.2 Frequency downconversion using a mixer and a local oscillator. 6

2.3 Performance measure in RF signal detection - dynamic range and selectivity. 7

2.4 Image and wanted signals. 7

2.5 A cascaded system. 9

2.6 Adverse effects of frequency-reference noise on the selectivity of radio receivers (a) A situation where a desired signal comes from a distant base-station and an unwanted signal comes from a nearby base-station. (b) Frequency downconversion with a noiseless local oscillator. (c) Frequency downconversion with a noisy local oscillator. 11

3.1 An archetypical model of Brownian motion. 14

3.2 Equilibrium steady-state and nonequilibrium steady-state. 17

3.3 Illustration of the Einstein relation (a) Two Brownian particles with different masses ($m_1 < m_2$) suspended in the same type of fluid ($\gamma_1 = \gamma_2$). The mean-squared velocities are different, *i.e.*, $\langle v_1^2 \rangle > \langle v_2^2 \rangle$. The diffusion constant of the lighter particle is larger than that of the heavier particle: $D_1 > D_2$. (b) Two Brownian particles with the same mass ($m_1 = m_2$) immersed in the different fluids with different friction constants ($\gamma_1 > \gamma_2$). The mean-squared velocities are the same, *i.e.*, $\langle v_1^2 \rangle = \langle v_2^2 \rangle$, as they are determined from the equipartition theorem and have no dependence on the friction constant. However, the diffusion constants are different: the Brownian particle in the less viscous medium diffuses faster than the one in the more viscous medium, *i.e.*, $D_1 > D_2$. 21

3.4 Probability in-flux from y_1 to y_2 and out-flux from y_2 to y_1. 23

3.5 Evolution of $P(v,t)$ starting from the initial condition of $P(v, t = 0) = \delta(v)$. $t_1 < t_2$. For $t \to \infty$, $P(v,t)$ converges to the Boltzmann distribution. 27

3.6 Evolution of $P(x,t)$ starting from the initial condition of $P(x, t = 0) = \delta(x)$. $t_1 < t_2 < t_3$. For $t \to \infty$, $P(x,t)$ approaches zero for any given x and the probability distribution becomes more and more thinly distributed over x. 28

3.7 Johnson-Nyquist thermal noise in an ohmic resistor. (a) Thevenin equivalent noise model. $\overline{v_n^2/\Delta f} = 2k_BTR$. (b) Norton equivalent noise model. $\overline{i_n^2/\Delta f} = 2k_BT/R$. (c) An electrical analogue to the mechanical Brownian motion. 30

3.8 The probability distribution of the voltage across the capacitor in the *RC*-circuit in thermal equilibrium. The distribution is that of Boltzmann and the standard deviation of the distribution is $\sqrt{k_BT/C}$, which is obtained from the equipartition theorem. 33

3.9 Various LRC circuits. In any circuits, $\langle v^2 \rangle = k_B T/C$. 35

3.10 Contour integration. 37

3.11 Forced Brownian motion. (a) A Brownian particle with mass m and charge q subject to an electric field E or an electric force $F = qE$. (b) A Brownian particle with mass m subject to a gravitational field g or a gravitational force $F = mg$. (c) An electrical analogue of the forced Brownian motion. The RC-circuit is driven by a current source. 41

3.12 Evolution of $P(v,t)$ for the velocity in the forced Brownian motion with an initial condition of $P(v, t = 0) = \delta(v)$. $t_1 < t_2$. $P(v,t)$ ultimately converges to the Boltzmann distribution whose mean is the terminal velocity v_0. 41

3.13 $P(v,t)$ ultimately converges to the Boltzmann distribution whose mean is the terminal velocity v_0. 43

3.14 (a) Evolution of $P(x,t)$ for the forced Brownian motion. (b) Steady-state distribution $P_0(x)$ in the presence of the boundary at $x = x_0$. 44

4.1 A general nonlinear RC-circuit consisting of a nonlinear resistor and a nonlinear capacitor. The circuit is coupled to an ideal current source generating a constant bias current of I_0. 49

4.2 Nonlinear resistor and its conductance $G(v)$. 50

4.3 Nonlinear charge $q(v)$ and nonlinear capacitor $C(v)$ versus voltage v across the capacitor. 51

4.4 (a) A MOS transistor as a nonlinear resistor and its widely adopted channel thermal noise model. The fitting parameter γ in the noise PSD depends on the bias voltages and behaves differently between the short and long channel transistors. (b) A MOS transistor in parallel with an external capacitor is coupled to an ideal current source. (c) a small-signal model for the circuit in (b). (d) The capacitor in the circuit can store mean fluctuation energy much larger than $k_B T/2$. 53

4.5 A linear RC-circuit. 57

4.6 Energetics in the linear RC-circuit. In the steady-state, the dissipation of the fluctuation energy in the resistor and the heat flux from the thermal bath to the circuit via fluctuation cancel each other out. 60

4.7 (a) A nonlinear RC-circuit with a nonlinear resistor and a linear capacitor. (b) An example of such nonlinear circuit: A MOS transistor in parallel with a linear capacitor. For a fixed gate-source voltage, the MOS transistor acts as a nonlinear resistor. 62

4.8 Analogy using the tank with a hole. 68

4.9 A nonlinear capacitor in parallel with an ohmic resistor. The circuit is coupled with a current source generating bias current I_0. 71

4.10 Mean thermal energy stored in a nonlinear capacitor, depending upon the nonlinearity. 73

5.1 Mixer as a time-varying driven circuit. 75

5.2 Generic time-varying driven circuits. 76

5.3 (a) Simple passive mixer; (b) Active mixer. 77

5.4 Noise translation and folding. 78
5.5 MOS sample-and-hold and cyclostationary noise. 80
5.6 Signal processing in conventional measurement systems. 82
5.7 Measurement of a cyclostationary noise. 83
5.8 Noise flow in a generic mixer noise measurement setup. 84
5.9 RC low-pass filtering of cyclostationary voltage noise $n_p(t) = n(t)p(t)$. The fundamental frequency of the noise modulating function, $p(t)$, is f_0. We assume $\omega_\tau \ll 2\pi f_0$. 86
5.10 Cyclostationary noise and its filtering. 88
5.11 *MOS switching mixer.* 89
5.12 Equivalent RC-model of the switching mixer including noise sources. 90
5.13 $g_T(t)$ and $m(t)$ in (a) hard-switching (b) soft-switching modes. 92
5.14 (a) The circuit corresponding to the deterministic dynamics (5.40) of the switching mixer. This circuit is no more than the Thévenin equivalent circuit of the mixer for $G_{source} = \infty$ and $R_{IF} = \infty$ in Fig. 5.12. (b) The circuit corresponding to the stochastic dynamics (5.41) of the switching mixer. 93
5.15 Conversion gain contribution from the f_{IF} and non-f_{IF} components of $m(t)v_{rf}(t)$. The solid curve represents the total conversion gain while the broken curve represents the conversion gain contribution from the f_{IF} component of $m(t)v_{rf}(t)$. 95
5.16 Sampling and recovering of the f_{IF} component of $m(t)v_{rf}(t)$ for small IF capacitance C. 96
5.17 An example of a pattern unit generation and repetition (beating) in sampling of a non-f_{IF} component of $m(t)v_{rf}(t)$. In this simplified example, f_{LO}=3Hz, f_{RF}=4Hz, and the non-f_{IF} component of $m(t)v_{rf}(t)$ at $f_{LO} + f_{RF}$ = 7Hz is considered. The sampling rate is $2f_{LO}$ =6Hz. 97
5.18 Contributions of f_{IF} and non-f_{IF} components of $m(t)v_{rf}(t)$ to the f_{IF} component at the mixer output $v_s(t)$. 98
5.19 Explanation of the time-invariant $\langle v_n^2 \rangle = k_B T/C$ in the context of the equivalent circuit of switching mixer for noise, redrawn from Fig. 5.14(b). 101
5.20 $R_{v_n}(\tau;t)$ versus τ for two different measurement times $t = t_1$ and $t = t_2$ for large enough $C \gg g_{T,0}/(2\omega_{LO})$. 102
5.21 $R_{v_n}(\tau;t)$ versus τ for four different measurement times $t = t_1, t_2, t_3$ and t_4 for small enough $C \ll g_{T,0}/(2\omega_{LO})$. 103
5.22 Simulated A_{conv} versus C for the two different switching modes. 105
5.23 Simulated $S_{v_n}(f_{IF};t)$ versus t during a period of LO for various capacitor values in the hard-switching mode. 106
5.24 Simulated $S_{v_n}(f_{IF};t)$ versus t during a period of LO for various capacitor values in the soft-switching mode. 106
5.25 Simulated $\overline{S_{v_n}(f_{IF};t)}$ versus C. 107
5.26 Simulated A_{conv}, $\overline{S_{v_n}(f_{IF};t)}$ and NF versus IF capacitance C. 108

5.27 Die photo of the mixer chip. 109
5.28 Mixer measurement setup. 110
5.29 Measured voltage conversion gain versus IF capacitance for different switching modes. 111
5.30 Measured noise figure versus IF capacitance C for different switching modes. 111
5.31 Simulated and measured noise figure versus IF capacitance C in the hard-switching mode. 112

6.1 Oscillator output in frequency- and time-domain for (a) noiseless oscillators and (b) noisy oscillators. The "X" marks in the time-domain signify the ideal zero crossings. 114
6.2 A generic model for a self-sustained LC oscillator. 116
6.3 LC cross-coupled oscillators with (a) bipolar transistors and (b) MOS transistors. In the figures, R explicitly represents the parasitic tank loss. 119
6.4 $v - w$ state-space and limit cycle. 121
6.5 A typical waveform for LC-type oscillators when the nonlinearity is weakly coupled, or $Q \gg 1$. . . 123
6.6 An ensemble of N identical oscillators. 125
6.7 (a) Oscillation points from the ensemble in the state-space. (b) Time evolution of $P(\phi, t)$. (c) Time evolution of $P(\theta, t)$. (d) Output signals from the ensemble at different times. 127
6.8 Time evolution of $P(\phi, t)$ in the presence of boundary condition. 128
6.9 Power spectral density of the oscillator output for different diffusion constants: $D_1 < D_2 < D_3$. . . 130
6.10 Power spectral density at the offset frequency, $\Delta\omega$. 131
6.11 LC oscillator as an energy conversion engine. The *energy transfer efficiency* of the active device can be defined as $(P_{total} - P_{active})/P_{total}$. 133
6.12 Ensemble average of $v(t)$ and virtual damping. 135
6.13 Measurement setup for the virtual damping using a digital oscilloscope. 135
6.14 Measured $\langle v(t) \rangle_{512}$ versus t for a 5 MHz ring oscillator. 136
6.15 Resonator versus oscillator. The X's on the t-axis represent the ideal zero-crossings. 137
6.16 Damping in resonators and virtual damping in self-sustained oscillators. 138
6.17 Brownian particle and LC tank with losses. 139
6.18 Oscillation trajectory in state-space and phase diffusion. 139
6.19 Geometric derivation of phase noise Langevin equation. 143
6.20 Details of linewidth compression in oscillators. 147
6.21 E_{tank} versus L curves obtained from (2) for two different tank energies $E_{tank,2} > E_{tank,1}$. With an increasing inductance, the tank amplitude grows along the solid parts of the curves until it reaches V_{limit} (inductance-limited regime). Once the tank amplitude reaches V_{limit}, it stops growing with the further increase of inductance (voltage-limited regime). The parts of curves with broken lines are unrealizable. 149

6.22 L/R_L^2, r_0 and NCR versus L for a given I_{bias}: (a) L/R_L^2 increasing with an increasing inductance L (b) L/R_L^2 decreasing with an increasing inductance L. 152
6.23 Simulated maximum inductor quality factor Q_L and minimum effective parallel conductance g_L versus the inductance L. 155
6.24 $L^2 g_L^2$ versus the inductance L. 156
6.25 VCO core schematic. 157
6.26 Equivalent oscillator model. 158
6.27 Symmetric spiral inductor model. 158
6.28 LC tank and MOSCAP varactor. 158
6.29 $L^2 g_L^2 / I_{bias}$ versus the bias current I_{bias}. 163
6.30 Design constraints for $I_{bias} = 4$ mA. 165
6.31 Effect of changes in the minimum small-signal loop gain. 166
6.32 Design constraints with $L = L_{opt}$. (a) L-reduction limited by the tank amplitude constraint (b) L-reduction limited by the start-up constraint without waste of power (c) L-reduction limited by the start-up constraint with waste of power. 167
6.33 Process variations and resultant constraint change. 169
6.34 Nonsymmetric spiral inductor model. 169
6.35 Impulse sensitivity function (ISF). 170
6.36 Noise modulating function (NMF). 171
6.37 Effective ISF. 171
6.38 Chip photograph. 172
6.39 Frequency tuning. 173
6.40 Measured phase noise versus f_{off} at 1.91GHz. 173
6.41 PFN for various oscillators. 175
6.42 PFTN for various oscillators. 175

List of Tables

3.1 C versus $\sigma = \sqrt{k_B T/C}$ at $T = 300$K. 34

3.2 Numerical calculation results for the integration in (3.89) for various values of α and β. 39

3.3 Various types of random processes. This table also shows the conversion from a given Langevin equation to the corresponding Fokker-Planck Equation. The noise source $\zeta(t)$ is assumed to be white Gaussian whose mean is zero and $\langle \zeta(t)\zeta(t') \rangle = \Gamma\delta(t - t')$. a is a constant. 46

4.1 Probability distribution and mean fluctuation energy in linear and nonlinear Brownian systems in their steady-state. y is the fluctuating quantity, $P_0(y)$ is the steady-state probability distribution, and $E(y - y_0)$ is the fluctuation energy. 49

6.1 Measured D, phase noise calculated from the measured D, and phase noise measured using a spectrum analyzer. The offset frequency is 1MHz and the center frequency of the oscillator is 5MHz. . 136

Chapter 1 Introduction

1.1 Motivation

Radio engineers were among the early investigators of noise. "Noise" derived its name from the hiss constantly heard from radio speakers. Efforts to explain the physical origin of noise soon revealed that the seemingly chaotic phenomenon is actually governed by fundamental physical laws and is predictable on statistical bases. The classic paper by Nyquist calculated the thermal noise generated by a resistor using an elegant thermodynamic argument [1]. Noise quickly became one of the central topics in RF and microwave engineering and since then the importance has only increased.

Especially during the last decades, we have witnessed an enormous growth in interest in noise and emphasis on low-noise design in different disciplines of science and engineering. Higher sensitivity detectors are needed to probe the physical world more and more accurately. An extreme example is the *Laser Interferometer Gravitational-Wave Observatory* (LIGO) [2] to detect astrophysical gravitational waves. Direct detection of gravitational waves requires an unprecedented sensitivity to measure sub-atomic scale dimension change using 4-kilometer giant interferometers and hence noise plays a key role in successful operation of the observatory [3]. Other state-of-the-art signal detectors ranging from radio astronomy telescopes to microwave/optical spectrometers to RF/microwave measurement systems unavoidably suffer from various noise issues. In communications engineering, recent emphasis on low-noise design reflects the fast development of wireless technology and the phenomenal growth of the wireless communication market. According to Shannon's theorem [4], the demand for higher information capacity in communication systems makes noise one of the critical design bottlenecks.

Modern RF and microwave receivers implement three key functions: *amplification*, *frequency conversion*, and *frequency synthesis*. While noise processes involved in amplifiers are well understood due to the linear time-invariant (LTI) nature of the circuits, noise processes in frequency conversion and frequency synthesis are quite complicated because they involve nonlinear time-varying circuits such as mixers and oscillators. These circuits exhibit strong nonlinearity, rich dynamics, and time-variance, which jointly entangle the noise evolution. For this reason, noise problems in mixers and oscillators remain an active field of research.

The mainstream research efforts to cope with the noise problems in oscillators and mixers in contemporary receiver design lies in construction of a more comprehensive, and unavoidably more complex, noise models for oscillators and mixers, by absorbing more of the second-order details. This

direction of study undoubtedly has helped scientists and engineers understand the noise processes better and predict noise more accurately. Construction of such inclusive noise models is of special importance in implementing noise simulation tools for computer-aided design (CAD).

However, such contemporary noise modeling efforts are phenomenology-based and lack physical understanding. Most of the currently available noise models do not reflect the intimate link between noise and statistical thermodynamics. This tends to block insight into the design optimization of a mixer or oscillator, especially when the noise models contain many cross-related design parameters. A big-picture physical behavior of noise is hard to see in complex noise formulae without a firm grasp of the underlying physics of the noise process and designers often have to resort to local optimizations with minor details or brute-force design methods relying on computer-aided design (CAD) tools. This lack of a global picture of the noise behavior not rarely leads to misconceived design guidelines.

This thesis is an outgrowth of the attempt to solve noise problems in oscillators and mixers based on fundamental physics while an ultimate research goal is to benefit practical low-noise design. The distinguishing feature of our approach is to place a strong emphasis on statistical thermodynamics governing noise processes in the time-varying systems, and hence our approach deviates from the conventional design practice. The power of this more fundamental approach is demonstrated experimentally, confirming the practical advantages of emphasizing fundamental physics in low-noise design. In this thesis, a special attention is paid to electrical operation of oscillators and mixers, and our theoretical framework is demonstrated through integrated circuits. However, our treatment of noise processes in the time-varying systems is general and the concepts and methods developed in our work can be applied to various different types of operations and implementations of time-varying systems, *e.g.*, lasers (optical oscillators).

The study has significant scientific and technological implications. Scientifically, our work is an extensive study of statistical thermodynamics which has led to deeper understanding of thermal fluctuations in electronic circuits. This study is an important demonstration of how fundamental physical considerations can evolve to practical low-noise circuit design. The circuit engineering combined with physical concepts has also resulted in useful engineering methods, such as graphical optimization, noise simulations for CAD, and time-varying filter theory.

This thesis presents the foundation of "*statistical electronics*" with emphasis on fluctuations and thermodynamics in nonlinear electrical circuits (Chapter 4), noise in mixers (Chapter 5), and noise in oscillators (Chapter 6).

1.2 Organization

In Chapter 2, we review the basic issues in modern radio-frequency (RF) signal detection with special attention to the negative effects of noise on the signal detection performance, using a generic RF signal detector. We will introduce two major performance measures of high-frequency signal detection, that is, dynamic range and selectivity, and discuss how the signal-path noise and the frequency-reference noise present in the RF signal detector affect these two figures of merit. Difficulties in dealing with noise processes in frequency downconversion and reference-frequency generation for RF signal detection are discussed.

Chapter 3 is tutorial on thermal fluctuation theory. This material is often lacking from the standard electrical engineering curriculum. The physics and mathematics from this chapter is frequently used in later chapters. Using Brownian motion and thermal noise in resistors as examples, we will discuss key physical concepts of thermal fluctuations, such as equipartition theorem, Einstein relation, and fluctuation-dissipation theorem. This chapter also introduces the mathematical foundations for analyzing such fluctuation phenomena, *i.e.*, the mathematical theory of random processes. We will present two powerful mathematical tools for the analysis of random processes: Langevin equation and Fokker-Planck equation. The solution of the Langevin equation will be used to describe the evolution of the statistical averages such as mean, variance, etc., of a fluctuating quantity. The solution of the Fokker-Planck equation will be used to describe the time evolution of the probability distribution of a fluctuating quantity. The mathematics used in this chapter is not complicated and the prerequisites are basic probability theory and elementary calculus.

Chapter 4 presents one of the main results of this thesis, *i.e.*, fluctuations and thermodynamics in nonlinear electrical systems. First, we investigate thermal fluctuations in electrical circuits involving nonlinear resistors such as active devices. We clarify so-far-confusing issues in this subject, verifying physical soundness of the contemporary noise models for nonlinear resistors and leading to a palpable understanding of nonlinear fluctuation-dissipation balance in a practical circuits context. This investigation is facilitated through a close examination of the energetics in the nonlinear electrical systems. Additionally, our study will illuminate how the nonlinear resistors change the energy equipartition property in electrical circuits. Second, we investigate how nonlinear energy storing elements such as nonlinear capacitors modify the energy equipartition property.

In Chapter 5, we present another primary result of this work, that is, noise in time-varying driven circuits (mixers). By utilizing the concepts and methods in thermal fluctuation theory introduced in Chapter 3, we lead to a new observation of a noise phenomenon involved in the frequency downconversion: noise figure degradation due to cyclostationary noise, dependent on the size of energy storing elements. Additionally, this chapter establishes a time-varying filter theory, leading to another new observation in the frequency donwconversion: conversion gain enhancement with

an increasing size of energy storing elements. These novel behaviors are experimentally verified through a direct measurement of integrated switching mixers. The results provide new insights into cyclostationary noise processes in the frequency downconversion and the optimum design of mixers.

Chapter 6 presents one of the most important contributions of our work on statistical electronics: noise in time-varying autonomous circuits (self-sustained oscillators). The fundamental investigation of fluctuation phenomena in oscillators in this chapter exemplifies the power of statistical electronics, leading to a new theory of oscillator phase noise. Demonstration of a direct correspondence between the oscillator phase noise and Einstein relation reveals the underlying physics of oscillator noise, filling in the gap between the fundamental physics of noise and the existing phase noise theories. Novel concepts of virtual damping and linewidth compression allow us to view oscillators and resonators in a unified framework, leading to a general oscillator design optimization strategy. Additionally, we develop an intuitive graphical method to execute the oscillator design optimization strategy.

Chapter 2 RF Signal Detection Issues

In this chapter, we review the primary issues in radio-frequency (RF) signal detection with special emphasis on the negative effects of noise on the signal detection performance, using a generic RF signal receiver shown in Figure 2.1. Typical examples of RF receivers widely used in engineering and science are communication radio receivers, astronomical radio telescopes, and RF/microwave measurement systems such as spectrum analyzers, to name a few. For a more comprehensive review of RF detectors, readers are referred to [5] - [10].

2.1 A Generic RF Signal Detector

Amplification, frequency donwconversion and *reference-frequency generation* are three essential functions utilized in almost any modern RF signal detectors. These functions are used to amplify the RF signal and translate it to a lower intermediate frequency (IF). The three functions are all executed in the *front-end* of the RF receiver, which is located inside the box in Fig. 2.1. In this RF front-end, the amplification is performed by the low-noise amplifier (LNA), while the mixer and local oscillator are used for frequency conversion and frequency generation.

The mixer is essentially an analog multiplier which multiplies the amplified RF signal at the output of the LNA, $a(t)\cos[\omega_{RF}t+\phi(t)]$, by the reference signal generated from the LO, $v_0\cos(\omega_{LO}t)$. Here, $a(t)$ and $\phi(t)$ correspond to amplitude and angle modulations, respectively, which contain low-bandwidth information. Also, ω_{LO} and ω_{RF} are the LO and RF frequencies. The multiplication of the LO and RF signals results in a low-frequency component at $|\omega_{LO}-\omega_{RF}|$ and a high-frequency component at $\omega_{LO}+\omega_{RF}$. The low-frequency component corresponds to the downconverted IF

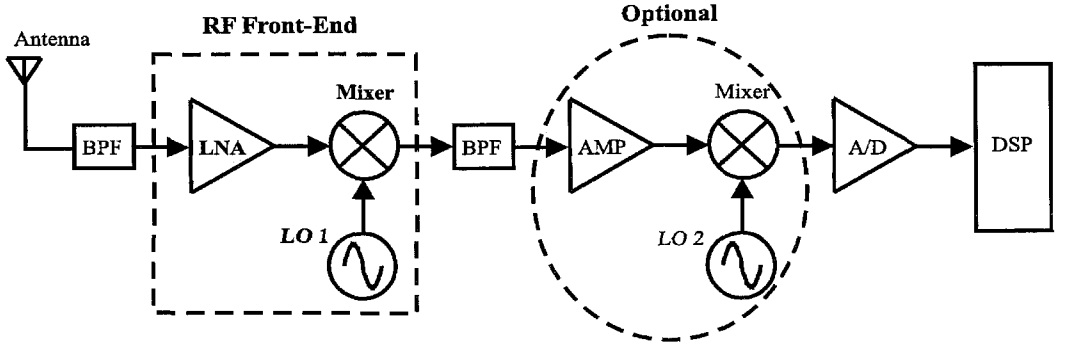

Figure 2.1: A generic RF signal receiver.

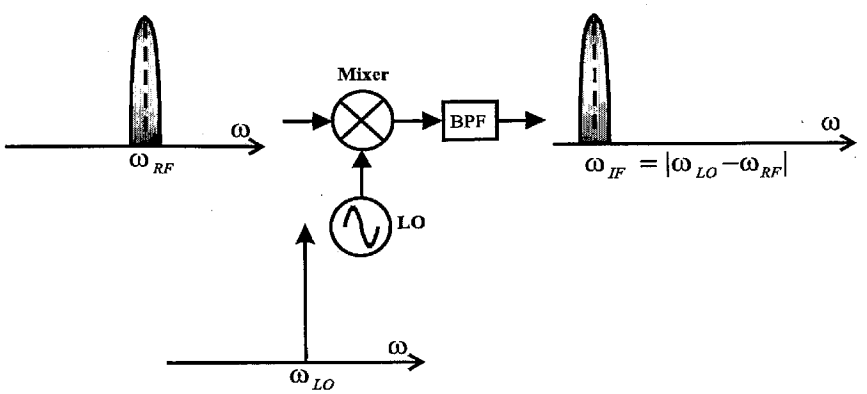

Figure 2.2: Frequency downconversion using a mixer and a local oscillator.

signal with the IF frequency of $\omega_{IF} \equiv |\omega_{RF} - \omega_{LO}|$, while the higher-frequency component is filtered out at the mixer output. The frequency-domain view of this frequency downconversion is illustrated in Fig. 2.2. If the RF and LO frequencies are equal, we call the receiving scheme *homodyning*, where the IF frequency is zero. In the homodyning, the second frequency downconversion block shown inside the circle in Fig. 2.1 is not needed. On the other hand, if the RF and LO frequencies are different, the receiving scheme is called *heterodyning*, in which the second frequency downconversion block can be opted for depending upon the design issues.

Signal handling in the RF front-end is one of the most challenging signal processing steps in the whole receiver. This difficulty is mainly due to high frequency and weak signal in the front-end, which jointly present stringent design constraints. For instance, noise in the front-end circuits affects the receiver performance much more severely than noise in the rest of the receiver due to the weak signal in the front-end, as will be more fully discussed shortly.

The *dynamic range* and *selectivity* is a traditional measure of the RF receiver performance. As shown on the left-hand side of Fig. 2.3, the dynamic range is defined as the difference between the minimum and the maximum signal levels that can be detected without considerable loss of information. On the other hand, the selectivity pertains to the receiver's capability to select a desired signal while rejecting unwanted interferers from the neighboring channels (right-hand side of Fig. 2.3).

The dynamic range and the selectivity are affected by many different design parameters as shown in the diagram in the middle of Fig. 2.3 [8]. For instance, gain and linearity of the receiver are two major design parameters that determine the maximum detectable signal level of the dynamic range. If the incoming RF signal is large enough to drive the receiver into a nonlinear regime after signal amplification, the information carried by the signal will be distorted, increasing the bit-error-rate (BER). Hence gain and linearity of the receiver determine the upper bound of the dynamic range.

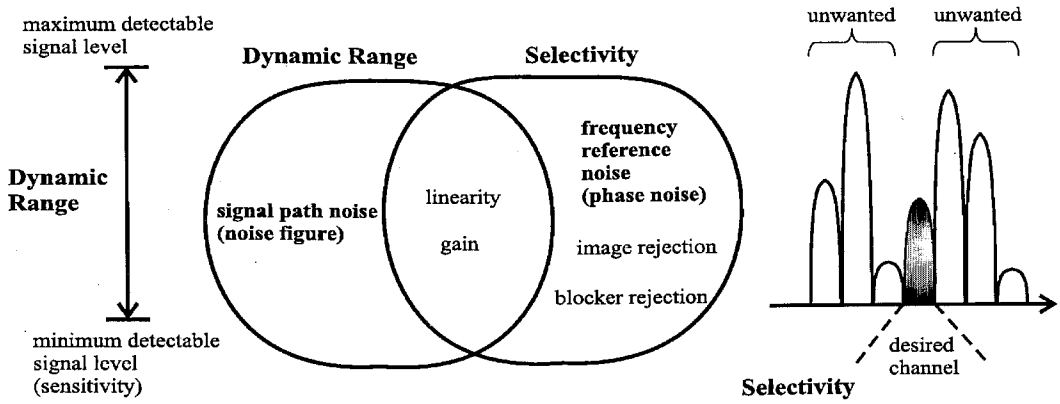

Figure 2.3: Performance measure in RF signal detection - dynamic range and selectivity.

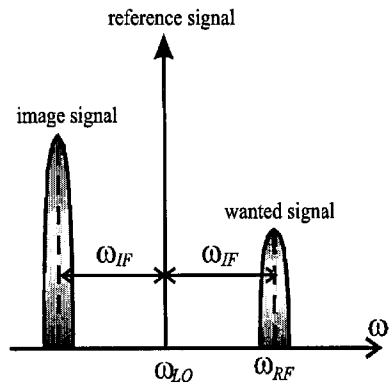

Figure 2.4: Image and wanted signals.

The selectivity of the receiver is affected by linearity, gain, image/blocker rejection ratios, frequency reference noise, etc. (Fig. 2.3) [8]. For example, the nonlinearity of the receiver often generates spurious in-band signals by intermodulating out-of-band signals and hence degrades the selectivity of the receiver. For another example, let us consider the image rejection problem [8]. In heterodyning, the bands symmetrically located above and below the LO frequency are downconverted to the same IF frequency. Hence, as shown in Fig. 2.4, if an unwanted signal *accidentally* happens to mirror the desired RF signal about the LO frequency, the unwanted signal will be downconverted to the same IF band, seriously affecting the selectivity performance of the receiver. This unwanted signal is called the image signal. There are several receiver architectures to suppress the image effect [8], [11], [12], but the problem of image rejection still presents difficult challenges to RF designers.

Although the effects of the various design parameters on the RF signal detection deserve more discussion, we direct readers to [5] - [9] for the subject and in the following section, we will primarily

focus on noise and its effects on the RF signal detection.

2.2 Noise in RF Detection

The fundamental importance of noise in RF signal detection can be well appreciated with the help of Shannon's theorem [4]:

$$C = B \cdot \log_2(1 + \frac{S}{N}) \tag{2.1}$$

which relates the capacity, C, of a given communication channel with bandwidth, B, signal intensity, S, and noise power, N. As can be seen, for given bandwidth and signal intensity, a smaller noise power will result in a larger information capacity, hence leading to a better receiver performance. Furthermore, Shannon's theorem suggests that the noise in the RF receiver is a key performance parameter not only in the stand-alone receiver but also in the whole RF communication system. For instance, as a parameter in a communication link budget, a lower receiver noise allows smaller antennas or lower transmitter power for the same system performance. In the context of the modern wireless cellular communication engineering, reduction of the noise in the wireless RF receivers can lead to more sparse distribution of the base-stations, hence cutting down the construction cost for the cellular network infrastructure.

In more concrete terms, there are two types of noise in the RF receiver, that is, *signal-path noise* and *frequency-reference noise*. As shown in the diagram in the middle of Fig. 2.3, the signal-path noise affects the dynamic range of the RF receiver while the frequency-reference noise degrades the selectivity of the receiver. In the following two subsections, we will elaborate on the harmful effects of noise on the receiver performance.

2.2.1 Signal-Path Noise

In the dynamic range, while the maximum detectable signal level is determined by the linearity and the gain of the receiver as mentioned earlier, the minimum detectable signal level is set by the signal-path noise, *i.e.*, the amount of noise that is added when a signal goes through the receiver chain in Fig. 2.1. This lower limit of the dynamic range is often called the *sensitivity*. Conventionally, the signal-path noise in the receiver is quantified using a figure of merit called *noise figure* (NF). The noise figure of any two-port system is defined as the ratio of the signal-to-noise ratio (SNR) at the input to the SNR at the output and hence represents a quantitative measure of the SNR degradation [8], [13]:

$$NF = \frac{\mathrm{SNR}_{in}}{\mathrm{SNR}_{out}} \tag{2.2}$$

In a system where multiple functional blocks are cascaded as schematically shown in Fig. 2.5, the overall noise figure NF_{total} of the cascaded system can be expressed in terms of gain and noise figure

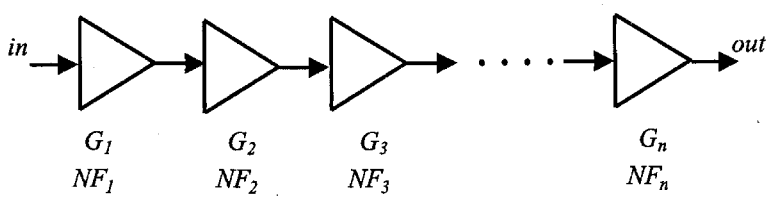

Figure 2.5: A cascaded system.

of each building block using the Friis equation [13]. Let us assume that the i-th block ($1 \leq i \leq n$) has an available power gain of G_i and a noise figure of NF_i. For the sake of brevity, we assume that all input impedances, output impedances and source impedance are the same, with respect to which all the noise figures, NF_1, NF_2, ..., NF_n and NF_{total}, are calculated. Then the Friis equation for the overall noise figure NF_{total} can be written as follows [13]:

$$NF_{total} = NF_1 + \frac{NF_2 - 1}{G_1} + \frac{NF_3 - 1}{G_1 G_2} + \cdots + \frac{NF_n - 1}{G_1 G_2 \cdots G_{n-1}} \tag{2.3}$$

Therefore, if the gain of the first stage, G_1, is sufficiently large and the gains of the subsequent stages (G_2, G_3, ..., G_n) are not too small, the noise figure of the first stage dominates in the overall noise figure while the noise figures of the subsequent blocks are suppressed progressively by the gain of second to n-th stage. This is intuitively understandable since once the first-stage amplifies a weak signal, the following stages only have to deal with fairly large signals which are more immune to the noise present in the stages. Accordingly, in the generic RF receiver of Fig. 2.1, the overall noise figure of the receiver is dominated by the noise figure of the front-end as far as the gain of the front-end is sufficiently large. Therefore, it is important to firmly understand and effectively predict noise of the RF front-end to be able to design low-noise receivers.

2.2.2 Frequency-Reference Noise

In the previous subsection, we discussed signal-path noise characterized by noise figure and its effect on the lower limit of the dynamic range (sensitivity) of RF receivers. Now we will discuss how *frequency-reference noise* affects the performance of the RF receivers.

As mentioned earlier, reference-frequency generation by local oscillators is an essential function in any modern RF receiver. Due to the noise present in the oscillator, the power spectrum of the oscillator output signal has linewidth broadening around the oscillation frequency as shown on the left of Fig. 2.6(c). This linewidth broadening is normally referred to as *phase noise* and a quantitative definition of phase noise will be presented in Chapter 6. This phase noise is synonymous with the frequency-reference noise.

The phase noise of local oscillators degrades the selectivity in the RF signal detection, as indicated

by the diagram in the middle of Fig. 2.3. To appreciate this effect in the context of modern wireless communication engineering, let us consider a feasible situation where a desired RF signal is already significantly attenuated at a mobile unit after traveling from a distant base-station while a nearby base-station is transmitting a strong interferer signal through the neighboring channel as shown in Fig. 2.6(a). If a local oscillator in use were noiseless and hence had a delta-function-like output spectrum in the frequency domain as shown in Fig. 2.6(b), the strong undesired signal would not interfere with the weak desired signal after the frequency downconversion as shown in the same figure. Unfortunately, this is not a realistic case as any oscillators have phase noise or linewidth broadening in their output power spectrum. The left-hand side of Fig. 2.6(c) depicts the output power spectrum of a noisy oscillator along with the desired yet weak RF signal in the presence of the strong, unwanted interferer signal in a neighboring channel. In this realistic case, after the frequency downconversion, the "phase noise skirts" of the unwanted IF signal interfere with the desired IF signal to a significant degree as shown on the right-hand side of Fig. 2.6(c), hence downgrading the receiver selectivity.

The local oscillator noise is an important parameter not only in evaluating the performance of a stand-alone receiver but also in assessing the capacity of the whole wireless communication system. In the context of cellular communication engineering, for instance, a lower phase noise simply allows a larger number of channels and hence more cell phone users in a given cell at a given time.

Summarizing, the signal-path noise quantified by noise figure degenerates the sensitivity and the local oscillator noise characterized by the phase noise degrades the selectivity in the RF signal detection. We have noted that noise in the RF front-end shown in Fig. 2.1 is especially critical in improving the noise performance of the whole receiver.

2.2.3 Noise in Time-Varying Systems

As mentioned previously, the RF front-end executes three key functions for RF signal detection, *i.e.*, amplification, frequency downconversion, and frequency generation. The noise process in amplification by the LNA is a very well understood topic due to the linear time-invariant (LTI) nature of the amplifier [14] - [17]. In contrast, noise processes in local oscillators and mixers are a difficult challenge for circuit designers and theorists. This difficulty in dealing with noise in mixers and oscillators mainly arises from their time-variance, nonlinearity, and resultant rich dynamics, which all together complicate the noise processes.

There has been considerable research endeavors to address the noise issues in oscillators and mixers in many different disciplines of science and engineering. These research efforts have largely focused on accurate noise modeling of the time-varying circuits, by taking more of the second-order effects and minor details into account. These studies undoubtedly have helped circuit designers predict noise in oscillators and mixers more accurately. However, most of the studies assume phenomenological and/or mathematical standpoints, but with little attention to the fundamental phys-

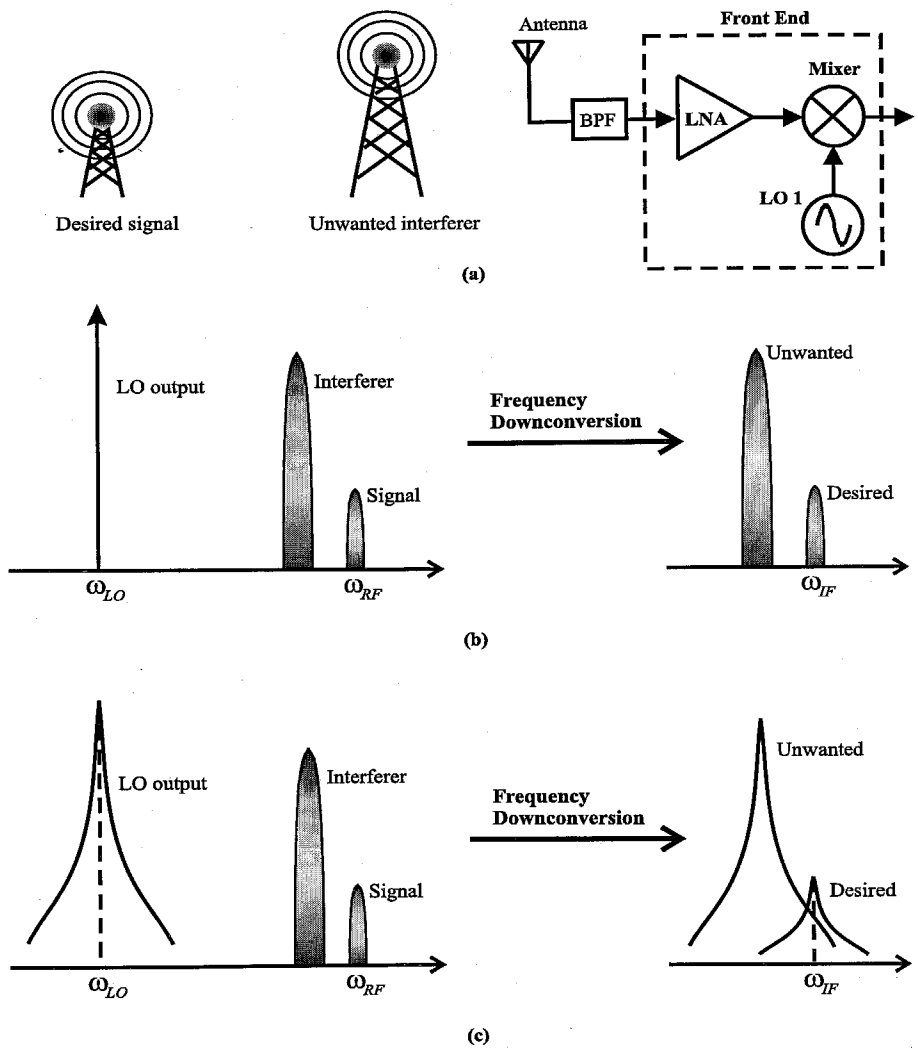

Figure 2.6: Adverse effects of frequency-reference noise on the selectivity of radio receivers (a) A situation where a desired signal comes from a distant base-station and an unwanted signal comes from a nearby base-station. (b) Frequency downconversion with a noiseless local oscillator. (c) Frequency downconversion with a noisy local oscillator.

ical aspects of the noise processes. Since noise is a physical process intimately linked with statistical thermodynamics, a thorough intuitive understanding of the physical processes can greatly facilitate design optimization of the circuits, providing insights into a global physical behavior of noise in the complex RF design environment. Often, the complicated noise models with little comprehension of the underlying physics merely block designers' insight into design optimization, leading to design misconceptions. Working with noise models lacking a physical basis, many designers often have to resort to partial optimization with minor details or brute-force simulations solely relying on computer-aided design (CAD) tools.

Two important themes of this thesis are noise in mixers and oscillators, which are presented in Chapters 5 and 6, respectively. The distinguishing feature of our approach from conventional low-noise design practice is to place a strong emphasis on statistical thermodynamics governing noise processes in the time-varying systems. The fundamental physical considerations evolve to insightful and practical design theories, whose power is demonstrated in the implementation of various integrated circuits.

Before diving into the topic of noise in oscillators and mixers, we will first review basic physical concepts and mathematical methods to understand and describe thermal fluctuations in physical systems in the following chapter. In Chapter 4, we will present one of the main results of this work besides noise in oscillators and mixers, *i.e.*, fluctuations and thermodynamics in nonlinear electrical circuits.

Chapter 3 Thermal Fluctuation Fundamentals

In this chapter, we review central concepts and methods in the theory of thermal fluctuation. The physical examples used in this chapter are Brownian motion and its analogue in the electrical circuits. Even though we will singly focus on fluctuations in electrical circuits in the main body of this thesis, the Brownian motion is presented in this chapter since it brings clear physical insights into the fluctuation phenomena appealing to our everyday experiences and provides an excellent analogy with the fluctuations in electrical circuits. Additionally, the theory of thermal fluctuation was initially developed to explain Brownian motion, and hence the review of the Brownian motion will put the thermal fluctuation theory in historical perspective. The concepts and methods introduced in this chapter will be essential in understanding the rest of this thesis, frequently appearing throughout this thesis and playing a crucial role in our development of statistical electronics. While more comprehensive reviews on the Brownian motion can be found in classic literature, such as [18] - [25], this chapter serves as a sufficient review for understanding the rest of this thesis.

3.1 Brownian Motion

The theory of thermal fluctuation originally grew out of efforts to explain Brownian motion. This incessant, random movement of pollen particles suspended in liquid was first discovered in 1827 by a British botanist Robert Brown. As a botanist, Robert Brown was inclined to explain the observation by endowing the pollen grains with a vital force. Later, this biologically inspired idea was dispelled by Brown himself, who observed that tiny particles of inorganic substances were also subjected to the same erratic motion. As a consequence, theory of Brownian motion drifted from biology to physics where the first major theoretical foundation on the dynamic phenomenon was layed at the turn of the 20th century by Einstein and Smoluchowski in their seminal articles [26], [27], [28][1]. The theoretical breakthrough by Einstein and Smoluchowski was further advanced by another set of pioneering studies on Brownian motion by Langevin [29], Fokker [30], and Planck [31], who provided further deep physical insights and powerful mathematical tools. Since the major advances in theory of Brownian motion in the early 20th century, Brownian motion has been at the heart of the field of stochastic processes and thermal fluctuations. The field has flourished, producing a huge repository of methods to study a wide range of dynamic systems subject to the influence of noise [18] - [25].

This section serves as an introduction to this theory of thermal fluctuation, where the analysis vehicle is an archetypical case of one-dimensional Brownian motion shown in Fig. 3.1. In this figure,

[1]The article in [27] is an English translation of the original [26].

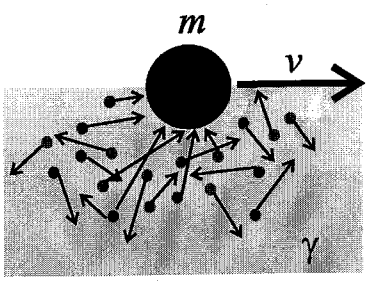

Figure 3.1: An archetypical model of Brownian motion.

the Brownian particle of mass m suspended in a fluid experiences two types of forces both originating from the same surrounding fluid: a frictional force F_f that dissipates the kinetic energy of the particle via interaction with the thermal bath kept at absolute temperature T and a random force $\zeta(t)$ that pushes the particle in an erratic fashion. For a small enough velocity of the Brownian particle, v, the frictional force F_f can be expressed as $F_f = -m\gamma v$, where γ is a friction constant. As will be discussed later in this chapter, the fact that the frictional force and the random force originate from the same source will lead to an intimate relationship between fluctuation and dissipation. Fluctuating quantities that are of interest to us in the Brownian motion are the velocity, $v(t)$, and the displacement, $x(t)$, of the Brownian particle.

There are two general methods of calculating the time-evolution of fluctuations in velocity and displacement in the Brownian motion. The first method, based on the so-called *Fokker-Planck equation*, focuses on time-evolution of the probability distributions[2] of the fluctuating quantities. The second method, based on the so-called *Langevin equation*, focuses on time-evolution of the statistical averages (mean, variance, autocorrelation, etc.) of the fluctuating quantities. We will discuss these two methods separately in Subsections 3.1.2 and 3.1.4 along with relevant key concepts in Brownian motion. Subsection 3.1.3 will discuss one of the most important concepts in Brownian motion, the *fluctuation-dissipation theorem*. However, before directly jumping into the theory of thermal fluctuation, we will first discuss the equilibrium property of the Brownian system in the following subsection.

3.1.1 Equilibrium Property

No matter what the initial condition is, the Brownian system of Fig. 3.1 will eventually reach thermal equilibrium after a sufficiently long time if there is no external pumping of energy into the system. The probability distribution of the energy E of the (classical) Brownian particle in thermal

[2]or, probability densities. We will use these two names interchangeably in this thesis.

equilibrium is given by the *Boltzmann distribution* according to statistical physics [32]:

$$P_0(E) \propto \exp\left[-\frac{E}{k_B T}\right] \tag{3.1}$$

where k_B is the Boltzmann constant and T is the absolute temperature. If the energy E of the Brownian particle is a function of a certain fluctuating quantity y, that is, if $E = E(y)$, the equilibrium probability distribution of y is also given by the same Boltzmann distribution:

$$P_0(y) \propto \exp\left[-\frac{E(y)}{k_B T}\right] \tag{3.2}$$

The mean fluctuation energy of the Brownian particle can then be evaluated as in the following[3]:

$$\langle E(y)\rangle = \int_{-\infty}^{\infty} E(y) \exp\left[-\frac{E(y)}{k_B T}\right] dy \Big/ \int_{-\infty}^{\infty} \exp\left[-\frac{E(y)}{k_B T}\right] dy \tag{3.3}$$

where the denominator is no more than a normalization factor.

If the energy $E(y)$ assumes a *quadratic* form of y, *i.e.*, $E(y) = Ay^2/2$ with a certain constant A, we can easily prove that the above equation (3.3) results in

$$\langle E(y)\rangle = \frac{k_B T}{2} \tag{3.4}$$

or

$$\langle y^2\rangle = \frac{k_B T}{A} \tag{3.5}$$

This is the famous *equipartition theorem* in statistical physics [32]. More generally put, the theorem states that any independent degree of freedom in a system in thermal equilibrium kept at absolute temperature T has a mean thermal energy of $k_B T/2$. Here, one of the conditions to be an independent degree of freedom is of course to have a quadratic-form energy expression. Many systems in nature have quadratic-form energy expressions. For instance, the kinetic energy of the Brownian particle is given by $E(v) = mv^2/2$ (v:velocity) and the energy stored in a capacitor, C, is given by $E(v) = Cv^2/2$ (v:voltage).

In our example of the Brownian motion in Fig. 3.1, the equilibrium probability distribution of the velocity of the Brownian particle is given by the following Boltzmann distribution, according to (3.2):

$$P_0(v) \propto \exp\left[-\frac{mv^2}{2k_B T}\right] \tag{3.6}$$

Also, the mean energy of the Brownian particle in thermal equilibrium is $k_B T/2$ according to the

[3]Throughout this thesis, $\langle x\rangle$ represents an ensemble average for a random process x, while $\overline{x}$ represents a time average.

equipartition theorem:

$$\langle E(v)\rangle = \langle \frac{mv^2}{2} \rangle = \frac{k_B T}{2} \tag{3.7}$$

This results in the famous mean-squared velocity formula:

$$\langle v^2 \rangle = \frac{k_B T}{m} \tag{3.8}$$

As can be reasoned from our foregoing argument, Boltzmann distribution is a more general equilibrium property than the equipartition theorem. A fluctuating quantity associated with energy (*e.g.*, velocity in the Brownian motion) *always* has a Boltzmann distribution in thermal equilibrium while the equipartition theorem ensues only when the energy is a quadratic form of the fluctuating quantity.

As an additional yet important note, we need to distinguish thermal equilibrium from steady-state. If a time-dependent probability distribution $P(y,t)$ of a certain fluctuating quantity, y, reaches a time-independent probability distribution, $P_0(y)$, after a long run, the probability distribution of y is said to have reached its steady-state. Thermal equilibrium requires more physical conditions than only having a time-independent probability distribution. In thermal equilibrium, the net exchange of heat between the Brownian particle and the thermal bath should be zero, to maximize the total entropy of the whole system [32]. Henceforth, thermal equilibrium states constitute a subset of the set of steady-states as shown in Fig. 3.2 and hence we encounter the notion of "nonequilibrium steady-state".

A pertinent example of such nonequilibrium steady state is water contained in a tank, whose top surface temperature and bottom surface temperature are kept different. After sufficiently long time, the system reaches a steady-state while it never reaches thermal equilibrium due to the constant heat flow. This distinction between the thermal equilibrium and the steady-state will be crucial in understanding fluctuations and thermodynamics in electrical circuits, as will be seen later. When one solves either the Langevin or the Fokker-Planck equation in the following subsections, the steady-state solutions of the equations should agree with the equilibrium properties presented in this subsection, *if* the system of concern reaches equilibrium in the steady-state.

3.1.2 Langevin Equation

The Langevin's approach [18], [19], [29] is to directly solve the equation of motion for the Brownian particle, which in the case of Fig. 3.1 is given by

$$m\dot{v} = -m\gamma v + \zeta(t) \tag{3.9}$$

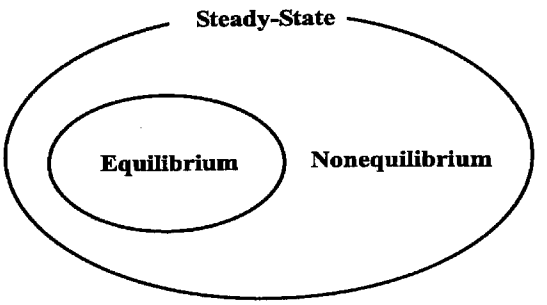

Figure 3.2: Equilibrium steady-state and nonequilibrium steady-state.

where the dot in the equation signifies time-derivative. By dividing the above equation by m, we obtain

$$\dot{v} = -\gamma v + \frac{1}{m} \cdot \zeta(t) \tag{3.10}$$

Due to the stochastic driving force, $\zeta(t)$, the Langevin equation (3.10) is an example of *stochastic differential equations* (SDE) [33].

The random force, $\zeta(t)$, is assumed to be Gaussian due to the central limit theorem while its mean is zero thanks to the randomness of the collisions by molecules in the surrounding fluid. The random force, $\zeta(t)$, at two different times, is assumed to be uncorrelated while this assumption is based on the fact that the resolution of our observation time is too coarse to resolve the relatively small correlation time of the random force. These statistical properties can be mathematically described as

$$\begin{aligned} \langle \zeta(t) \rangle &= 0 \\ \langle \zeta(t_1)\zeta(t_2) \rangle &= \Gamma \delta(t_1 - t_2) \end{aligned} \tag{3.11}$$

where $\delta(t_1 - t_2)$ is the Dirac delta function. The intensity of noise, Γ, can be determined from the equilibrium property of the Brownian system as can be seen later.

No correlation of the random force, $\zeta(t)$, at two different times as shown in (3.11) implies that $\zeta(t)$ is white noise in the frequency domain [33]. This can be easily seen by using the Wiener-Khintchin theorem [33], stating that the power spectral density of a stationary random process is a Fourier transform of its autocorrelation, *i.e.*,

$$\begin{aligned} S_\zeta(f) &= \int_{-\infty}^{\infty} e^{-2j\pi f\tau} \langle \zeta(t)\zeta(t+\tau) \rangle d\tau \\ &= \Gamma \int_{-\infty}^{\infty} e^{-2j\pi f\tau} \delta(\tau) d\tau \\ &= \Gamma \end{aligned} \tag{3.12}$$

As clearly seen, the power spectral density of the random force, $\zeta(t)$, is independent of the frequency, and hence $\zeta(t)$ is white noise. The power spectral density in (3.12) is the double-side band (DSB) representation, while its single-side band (SSB) representation which is perhaps more familiar to electrical engineers is given by

$$\frac{\overline{\zeta^2}}{\Delta f} \equiv 2S_\zeta(f) = 2\Gamma \tag{3.13}$$

While solving the stochastic differential equation (3.10) for $v(t)$ itself is meaningless since $v(t)$ is stochastic, we can still solve it for statistical averages of $v(t)$, such as mean, variance, and autocorrelation. Methods of calculating statistical averages of fluctuating quantities from the Langevin equation constitute *stochastic calculus* [33]. In the followings, we will show how the mean and autocorrelation of $v(t)$ are obtained from the Langevin equation, (3.10).

Mean Velocity

A differential equation for the mean velocity, $\langle v(t)\rangle$, is obtained by taking an ensemble average of (3.10):

$$\frac{d}{dt}\langle v(t)\rangle = -\gamma\langle v(t)\rangle + \frac{1}{m}\cdot\langle\zeta(t)\rangle = -\gamma\langle v(t)\rangle \tag{3.14}$$

where we have used $\langle\zeta(t)\rangle = 0$ in (3.11). The solution of (3.14) is easily shown to be $\langle v(t)\rangle \propto e^{-\gamma t}$. Hence, after the initial transient dies away, the mean velocity $\langle v(t)\rangle$ converges to zero, *i.e.*,

$$\langle v(t)\rangle = 0 \tag{3.15}$$

Velocity Autocorrelation

The calculation of the autocorrelation of the velocity, $\langle v(t_1)v(t_2)\rangle$, is more involved than the mean velocity calculation. The calculation routine to obtain $\langle v(t_1)v(t_2)\rangle$ from (3.10) consists of two steps.

In the first step, we derive the cross-correlation of $v(t)$ and $\zeta(t)$, *i.e.*, $\langle v(t_2)\zeta(t_1)\rangle$, from (3.10). This cross-correlation will be used in the second step. The differential equation for this cross-correlation can be obtained by multiplying (3.10) at time t_2 by $\zeta(t_1)$ and taking an ensemble average, *i.e.*,

$$\frac{\partial}{\partial t_2}\langle v(t_2)\zeta(t_1)\rangle + \gamma\langle v(t_2)\zeta(t_1)\rangle = \frac{1}{m}\cdot\langle\zeta(t_1)\zeta(t_2)\rangle = \frac{\Gamma}{m}\delta(t_1 - t_2) \tag{3.16}$$

where we have used $\langle\zeta(t_1)\zeta(t_2)\rangle = \Gamma\delta(t_1 - t_2)$ in (3.11). The solution of the equation above after the initial transient decays is given by

$$\langle v(t_2)\zeta(t_1)\rangle = \frac{\Gamma}{m}e^{-\gamma(t_2-t_1)}u(t_2 - t_1) \tag{3.17}$$

where $u(t)$ is the unit-step function.

In the second step, we derive the autocorrelation of the velocity, $\langle v(t_1)v(t_2)\rangle$, utilizing the result of the previous step, (3.17). The differential equation for $\langle v(t_1)v(t_2)\rangle$ can be obtained by multiplying (3.10) at time t_1 by $v(t_2)$ and taking an ensemble average:

$$\frac{\partial}{\partial t_1}\langle v(t_1)v(t_2)\rangle + \gamma\langle v(t_1)v(t_2)\rangle = \frac{1}{m}\cdot\langle v(t_2)\zeta(t_1)\rangle = \frac{\Gamma}{m^2}e^{-\gamma(t_2-t_1)}u(t_2-t_1) \tag{3.18}$$

where we have used (3.17). This is a deterministic differential equation whose solution is

$$\langle v(t_1)v(t_2)\rangle = \frac{\Gamma}{2\gamma m^2}\left[e^{-\gamma|t_1-t_2|} - e^{-\gamma(t_1+t_2)}\right] \tag{3.19}$$

Let us define two new variables $t \equiv t_1$ (absolute measurement time) and $\tau \equiv t_2 - t_1$ (measurement time difference). Then, the second exponential term in (3.19) is merely an initial transient which dies away after large enough time (large t) and hence we can rewrite the autocorrelation of the velocity, $v(t)$, in (3.19) as

$$R_{v,v}(\tau) \equiv \langle v(t)v(t+\tau)\rangle = \frac{\Gamma}{2\gamma m^2}e^{-\gamma|\tau|} \tag{3.20}$$

after the initial transient removal. Note that the autocorrelation of $v(t)$ only depends upon the measurement time difference, $\tau = t_1 - t_2$, indicating that $v(t)$ is a *stationary* random process.

As an additional note, the technique introduced here to obtain the autocorrelation from the Langevin equation will be frequently used in this thesis. Especially in the study of noise in mixers in Chapter 5, this technique will play a key role.

Noise Intensity

Now the noise intensity, Γ, can be determined using (3.20) together with the equilibrium properties of the Brownian system discussed in Subsection 3.1.1. When the thermal equilibrium between the Brownian particle and the surrounding fluid is obtained after a sufficiently long time, the Brownian particle has a mean energy of $k_BT/2$ due to the equipartition theorem, which is equivalent to $\langle v^2(t)\rangle = k_BT/m$. Comparing this to (3.20) for $t_1 = t_2$, we can determine the noise intensity Γ:

$$\Gamma = 2\gamma m k_B T \tag{3.21}$$

which is proportional to the particle mass, friction coefficient, and absolute temperature. Using the equilibrium properties such as equipartition theorem to determine noise intensity is a powerful technique that has been widely employed to study various systems under the influence of thermal fluctuations. As will be discussed later in Section 3.2, the Johnson-Nyquist thermal noise of resistors can be easily obtained using this technique.

Power Spectral Density

The velocity autocorrelation, $R_{v,v}(\tau) = \langle v(t_1)v(t_2)\rangle$, $(\tau \equiv t_1 - t_2)$ also allows us to evaluate the power spectral density of the velocity, $S_v(f)$. Using the Wiener-Khintchen theorem [33] together with (3.20) and (3.21), the power spectral density of the velocity is given by:

$$\begin{aligned} S_v(f) &= \int_{-\infty}^{\infty} e^{j2\pi f\tau} R_{v,v}(\tau) d\tau \\ &= \frac{k_B T}{m} \cdot \frac{2\gamma}{\gamma^2 + 4\pi^2 f^2} \end{aligned} \tag{3.22}$$

which is a Lorentzian distribution. The mean-squared velocity of the Brownian particle can be calculated by integrating $S_v(f)$ with respect to f from $-\infty$ to ∞, *i.e.*,

$$\langle v^2 \rangle = \int_{-\infty}^{\infty} S_v(f) df = \frac{k_B T}{m} \tag{3.23}$$

which is consistent with the equipartition theorem.

Mean-Square Displacement

So far we have discussed the statistical properties of the velocity, $v(t)$, of the Brownian particle. We now study the statistical properties of the displacement, $x(t)$, of the Brownian particle. From our everyday experience (*e.g.*, an ink droplet in water), we can guess that an ensemble of Brownian particle will diffuse in the surrounding fluid and hence the mean-squared displacement, $\langle x^2(t)\rangle$, will grow with time. Now we will quantify this diffusion process starting from the Langevin equation (3.10).

Multiplying (3.10) by $x(t)$, we obtain

$$x\frac{dv}{dt} = \frac{d}{dt}(xv) - v^2 = -\gamma xv + \frac{1}{m} \cdot x\zeta(t) \tag{3.24}$$

Taking an ensemble average of the above equation and using the equipartition theorem, *i.e.*, $\langle v^2 \rangle = k_B T/m$, and also noting the negligible correlation between the displacement, $x(t)$, and the random force, $\zeta(t)$[4], we obtain

$$\frac{d}{dt}\langle xv \rangle = \frac{k_B T}{m} - \gamma \langle xv \rangle \tag{3.25}$$

The solution of (3.25) is given by

$$\langle xv \rangle = Ae^{-\gamma t} + \frac{k_B T}{m\gamma} \tag{3.26}$$

where A is a certain constant which can be determined from the initial condition. Noting that $xv = (1/2) \cdot (d/dt)x^2$ and neglecting the first term corresponding to the initial transient in the above

[4]Namely, the statistical properties of the force is independent of the actual physical displacements.

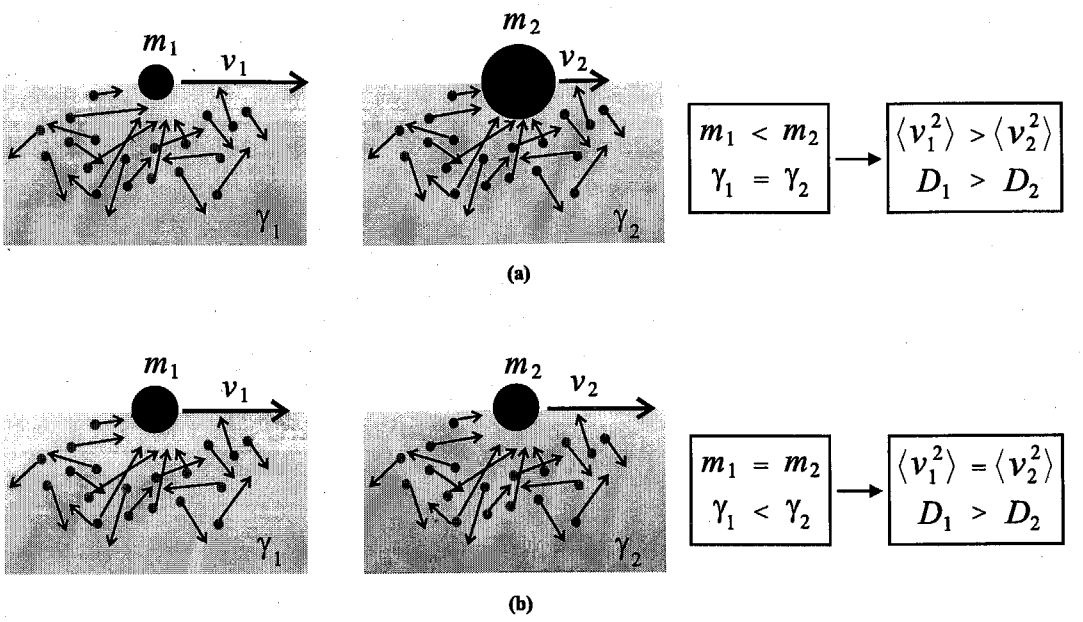

Figure 3.3: Illustration of the Einstein relation (a) Two Brownian particles with different masses ($m_1 < m_2$) suspended in the same type of fluid ($\gamma_1 = \gamma_2$). The mean-squared velocities are different, *i.e.*, $\langle v_1^2 \rangle > \langle v_2^2 \rangle$. The diffusion constant of the lighter particle is larger than that of the heavier particle: $D_1 > D_2$. (b) Two Brownian particles with the same mass ($m_1 = m_2$) immersed in the different fluids with different friction constants ($\gamma_1 > \gamma_2$). The mean-squared velocities are the same, *i.e.*, $\langle v_1^2 \rangle = \langle v_2^2 \rangle$, as they are determined from the equipartition theorem and have no dependence on the friction constant. However, the diffusion constants are different: the Brownian particle in the less viscous medium diffuses faster than the one in the more viscous medium, *i.e.*, $D_1 > D_2$.

equation, we advance to

$$\langle x^2(t) \rangle = 2Dt \tag{3.27}$$

where the *diffusion constant*, D, is given by

$$D = \underbrace{\frac{k_B T}{m}}_{\text{sensitivity}} \times \underbrace{\frac{1}{\gamma}}_{\text{friction}} \tag{3.28}$$

This formula for the diffusion constant was first derived by Einstein and is called *Einstein relation* [26], [27]. Equation (3.27) demonstrates that the Brownian particle does exhibit *diffusion* with the diffusion constant of D, agreeing with our everday acquaintance.

The Einstein relation (3.28) illuminates the Brownian movement by identifying two key physical elements governing the diffusion process: the *sensitivity* of the Brownian particle undergoing the diffusion and the *friction* (energy loss) of the environment in which the diffusion process occurs.

First, the $k_B T/m$ factor in (3.28) represents the *sensitivity* of the Brownian particle to the perturbations originating from the thermal fluctuations. A lighter Brownian particle is more sensitive to perturbations, and therefore has a larger diffusion rate than a heavier Brownian particle when immersed in the same fluid (the same friction constant) as shown in Fig. 3.3(a). This sensitivity

factor is independent of the friction constant of the liquid and is obtained using the equipartition theorem for the velocity, *i.e.*, $\langle v^2 \rangle = k_B T/m$.

Second, the $1/\gamma$ factor in (3.28) represents the *friction* (energy loss) element in the diffusion process. This friction factor indicates that when two identical Brownian particles (same mass) are suspended in liquids with different friction constants, the Brownian particle suspended in a medium with more friction will exhibit a slower diffusion as shown in Fig. 3.3(b). The friction constant, γ, was defined through the relation $\dot{v} = -\gamma v$ in (3.10) in the absence of the noise term.

This Einstein relation will play a key role in our study of phase noise in oscillators in Chapter 6.

3.1.3 Fluctuation-Dissipation Theorem

The Brownian particle exchanges energy with the thermal bath via fluctuation and dissipation. Fluctuation tends to increase the energy of the particle while dissipation is an energy flow from the particle to the thermal bath. In thermal equilibrium, these two flows of energy cancel each other and the mean energy of the particle remains constant at the value of $k_B T/2$ which is determined by energy equipartition. This delicate balance between fluctuation and dissipation constitutes an important theorem in statistical physics, which is called *fluctuation-dissipation theorem* [32], [34], [35], [36], [37], [38].

We have already hinted this intimate link between fluctuation and dissipation in establishing the Langevin equations (3.9) by mentioning that the frictional force, $-m\gamma v$, and the random force, $\zeta(t)$, arise from the same surrounding fluid. The frictional force retarding the motion of the Brownian particle is indeed determined by the average of the vast number of rapidly varying individual forces exerted by the molecules in the surrounding medium. At the same time, exactly because the average frictional force is due to a large number of individual molecular motions, the frictional, dissipative force should be essentially linked to the random force, $\zeta(t)$, which arises from the thermal fluctuations of the molecules.

Through the Einstein relation, (3.28), Einstein first demonstrated analytically and physically this essential and fundamental connection between the average force (friction or dissipation) and the fluctuation. As can be seen in (3.28), the diffusion constant, D, due to the thermal fluctuation is directly linked to the friction constant, γ, which is responsible for the dissipation.

There have been subsequently a considerable number of developments and ramifications of Einstein's discovery of this vital relationship, such as Nyquist's theorem [1] to explain Johnson's observation [39] of thermal noise in resistors, and the further theoretical development in which the official name, "fluctuation-dissipation theorem", was coined by Callen and Welton [34] - [38]. We shall revisit the fluctuation-dissipation theorem in the context of the Johnson-Nyquist thermal noise of resistors in Section 3.2. Summarizing, thermal fluctuation and dissipation always go hand in hand, arising from the same surrounding fluid where the Brownian motion occurs: *whenever there*

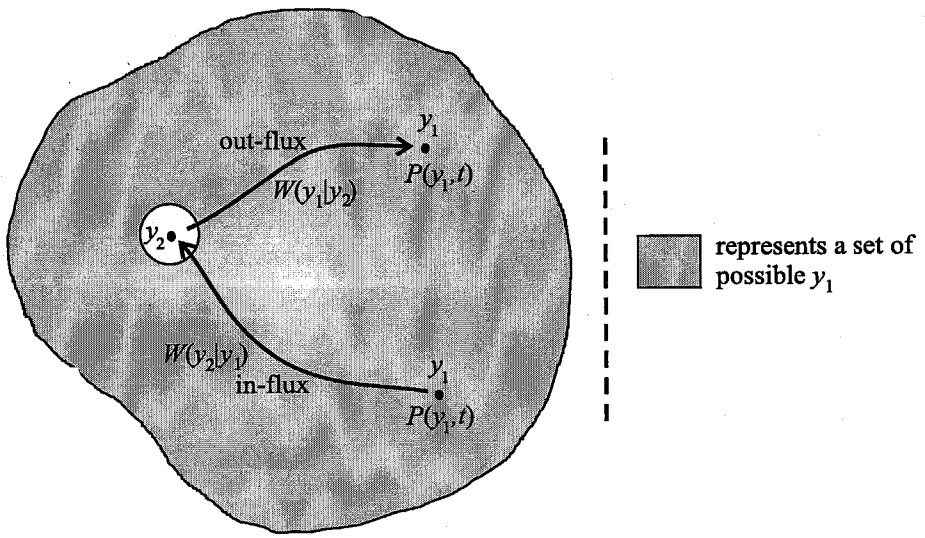

Figure 3.4: Probability in-flux from y_1 to y_2 and out-flux from y_2 to y_1.

is thermal fluctuation, there exists associated dissipation and vice versa.

So far, we have considered the fluctuation-dissipation theorem in the linear case where the frictional force is proportional to the velocity, or friction constant is a constant. In the nonlinear case, where the friction constant depends upon the velocity, the problem becomes much more involved. However, even in the nonlinear case, the fluctuation-dissipation relation must remain valid in the physical sense that the thermal fluctuation and dissipation should always balance each other for energy conservation. However, the simple mathematical fluctuation-dissipation relations such as (3.28) are not valid any more in the nonlinear case [40]. The fluctuation-dissipation relation in the nonlinear friction is still an active field of research and we will also address this issue in the context of nonlinear resistors (transistors) in Chapter 4.

3.1.4 Fokker-Planck Equation

In Subsection 3.1.2, we discussed how the statistical averages, such as $\langle v(t)\rangle$, $\langle v(t_1)v(t_2)\rangle$ and $\langle x^2(t)\rangle$, evolve with time in the Brownian motion using the Langevin equation. In this subsection, we will focus on the time-evolution of the probability distribution of the velocity, $P(v,t)$, and the probability distribution of the displacement, $P(x,t)$, in the Brownian motion. The partial differential equations describing the time-evolution of such probability distributions are called *Fokker-Planck equations* (FPE) [24], [25], [30], [31]. The solution of the Fokker-Planck equation shows how an ensemble of Brownian particles that begins out of statistical nonequilibrium is brought into equilibrium steady-state (or in certain cases, nonequilibrium steady-state as seen later in this Chapter) through contact with a heat bath.

Derivation of Fokker-Planck Equation

Here we will show how the Fokker-Planck equation is derived using a generic fluctuating quantity, y, and its probability distribution, $P(y,t)$. In the case of Brownian motion, y can be the velocity or the displacement. We define $W(y_2|y_1)$ as a transition probability per unit time from y_1 to y_2. At a given time t, the net increase of the probability at y_2 per unit time, $(\partial/\partial t)P(y_2,t)$, is given by the probability increase at y_2 per unit time due to the transition from y_1 to y_2, $\int_{-\infty}^{\infty} W(y_2|y_1)P(y_1,t)dy_1$, minus the probability decrease at y_2 per unit time due to the transition from y_2 to y_1, $\int_{-\infty}^{\infty} W(y_1|y_2)P(y_2,t)dy_1$, where y_1 runs all over the possible space[5] as shown in Fig. 3.4. Therefore, we can establish the following integro-differential equation governing the probability distribution:

$$\frac{\partial P(y_2,t)}{\partial t} = \int_{-\infty}^{\infty} \left[W(y_2|y_1)P(y_1,t) - W(y_1|y_2)P(y_2,t)\right] dy_1 \tag{3.29}$$

This type of probability evolution equation based on the transition probability has many different versions of essentially the same nature, which have obtained different names such as Smoluchowski equation, Chapman-Kolmogorov equation, and master equation, depending on their specific forms [19]. In this thesis, we will simply call this type of equation *master equation*. If we define $\epsilon \equiv y_1 - y_2$, $y \equiv y_2$, and $W(y;\epsilon) \equiv W(y_1|y_2)$, $W(y_2|y_1)$ is equal to $W(y+\epsilon;-\epsilon)$ and (3.29) can be rewritten as

$$\frac{\partial P(y,t)}{\partial t} = \int_{-\infty}^{\infty} \left[W(y+\epsilon;-\epsilon)P(y+\epsilon,t) - W(y;\epsilon)P(y,t)\right] d\epsilon \tag{3.30}$$

The master equation such as (3.29) or (3.30) is one of the more general equations describing many random processes[6] in nature. In the master equation, physics governing the random process comes into play through the transition probability, $W(y_1|y_2)$, as will be seen shortly.

The Fokker-Planck equation we will derive now is obtained as an approximation of the master equation (3.30). With an *a priori* assumption that fluctuations are very small ($\epsilon \ll 1$), we take the Taylor expansion of the first term in the integrand of the right-hand side up to the second order of ϵ to obtain

$$\frac{\partial P(y,t)}{\partial t} \approx -\frac{\partial}{\partial y}\left[\int_{-\infty}^{\infty} \epsilon W(y;\epsilon)d\epsilon\right] P(y,t) + \frac{1}{2}\frac{\partial^2}{\partial y^2}\left[\int_{-\infty}^{\infty} \epsilon^2 W(y;\epsilon)d\epsilon\right] P(y,t) \tag{3.31}$$

By defining the *n-th jump moment*, $A_n(y)$, as

$$A_n(y) \equiv \int_{-\infty}^{\infty} \epsilon^n W(y;\epsilon)d\epsilon \tag{3.32}$$

[5] In the one-dimensional case, y_1 runs from $-\infty$ to ∞.

[6] More accurately, Markov processes.

we can rewrite (3.31) as

$$\frac{\partial P(y,t)}{\partial t} = -\frac{\partial}{\partial y}\{A_1(y)P(y,t)\} + \frac{1}{2}\frac{\partial^2}{\partial y^2}\{A_2(y)P(y,t)\} \tag{3.33}$$

which is *a general form of the Fokker-Planck equation.*

The derivation of the Fokker-Planck equation (3.33) so far is of purely mathematical nature based on probability transition. Now, physics governing the fluctuation comes on the scene through the aptly named *jump moments* defined in (3.32): $\epsilon = y_1 - y_2 = \Delta y$ represents a jump from y_2 to y_1 and $A_n(y)$ in (3.32) is simply the n-th moment of ϵ per unit time. The first and the second jump moments, $A_1(y)$ and $A_2(y)$, in the Fokker-Planck equation (3.33), are determined by the specific physical properties of the system under consideration. According to (3.32), $A_1(y)$ is the average of the jump $\epsilon = \Delta y$ per unit time for a given y, *i.e.*,

$$A_1(y) = \frac{\langle \Delta y \rangle_y}{\Delta t} \tag{3.34}$$

where the subscript y signifies that y is a fixed value from which the jump $\epsilon = \Delta y$ occurs. Similarly, $A_2(y)$ can be re-expressed as

$$A_2(y) = \frac{\langle (\Delta y)^2 \rangle_y}{\Delta t} \tag{3.35}$$

These jump moments are extremely important as the physics governing the random process comes into play through these jump moments. We will shortly calculate these moments more specifically using Brownian motion as an example.

The Fokker-Planck equation (3.33) can be rewritten in the form of *continuity equation*

$$\frac{\partial P(y,t)}{\partial t} = \frac{\partial J(y,t)}{\partial y} \tag{3.36}$$

where the probability in-flux, $J(y,t)$, is defined as

$$J(y,t) = -A_1(y)P(y,t) + \frac{1}{2}\frac{\partial}{\partial y}\{A_2(y)P(y,t)\} \tag{3.37}$$

The continuity equation implies that the probability density increase per unit time at given y and at a given time t is equal to the effective probability flux into y per unit time. This is analogous to the familiar situation where the electric current density flow (J) changes the charge density (ρ) in space for charge conservation, which in a one-dimensional case, is described by the following continuity equation:

$$\frac{\partial \rho(x,t)}{\partial t} = \frac{\partial J(x,t)}{\partial x} \tag{3.38}$$

where J signifies the in-flow current density[7].

Fokker-Planck Equation for Velocity in Brownian Motion

Now we will consider the probability density of the velocity, $P(v,t)$, in the Brownian motion and its evolution with time. First of all, we should determine the velocity jump moments, $A_1(v)$ and $A_2(v)$. According to (3.34), the first jump moment is $A_1(v) = \langle \Delta v \rangle_v / \Delta t$ and we can easily see from (3.10) that this quantity is equal to $-\gamma v$, that is,

$$A_1(v) = -\gamma v \tag{3.39}$$

The second jump moment in (3.35) for the velocity is given by $A_2(v) = \langle (\Delta v)^2 \rangle_v / \Delta t$. Since this quantity is always positive, the second jump moment can be expressed as $A_2(v) = c_0 + c_2 v^2 + \cdots$ where $c_0 > 0$, c_2, ... are expansion coefficients. The first order term $c_1 v$ should vanish in the expansion (*i.e.*, $c_1 = 0$) as we must have $A_2(v) = A_2(-v)$. Now assuming small fluctuations just as we did in the derivation of the Fokker-Planck equation, we neglect the second- or higher-order terms in the expansion of $A_2(v)$, leading to:

$$A_2(v) \approx c_0 \tag{3.40}$$

The coefficient c_0 will be obtained shortly using the equilibrium property of the Brownian system.

Now plugging (3.39) and (3.40) into (3.33), we obtain the following Fokker-Planck equation for the velocity of the Brownian particle:

$$\frac{\partial P(v,t)}{\partial t} = \frac{\partial}{\partial v}\left[\gamma v P(v,t) + \frac{c_0}{2}\frac{\partial P(v,t)}{\partial v}\right] \tag{3.41}$$

When the Brownian system reaches equilibrium, the time-dependent term in the left-hand side vanishes and hence we have

$$\gamma v P_0(v) + \frac{c_0}{2}\frac{d}{dv}P_0(v) = 0 \tag{3.42}$$

where $P_0(v)$ signifies the steady-state solution of the Fokker-Planck equation, that is, $P_0(v) = \lim_{t\to\infty} P(v,t)$. Now by resorting to the equilibrium property, we can determine the unknown constant c_0. By multiplying (3.42) by v and integrating it over v and using the equipartition theorem $\langle v^2 \rangle = k_B T/m$, we obtain

$$\gamma \cdot \frac{k_B T}{m} + \frac{c_0}{2}\int_{-\infty}^{\infty} v\frac{d}{dv}P_0(v)dv = \gamma \cdot \frac{k_B T}{m} - \frac{c_0}{2}\int_{-\infty}^{\infty} P_0 dv = \gamma \cdot \frac{k_B T}{m} - \frac{c_0}{2} = 0 \tag{3.43}$$

where the second equation was obtained via integration by parts while $vP_0(v)|_{v=\infty} = vP_0(v)|_{v=-\infty} = 0$ as the distribution, $P_0(v)$, is sharp and narrow around its mean and decays fast to zero as v departs

[7]Perhaps a more familiar form in a three-dimensional case using the out-flow current density is $\nabla \cdot J + \frac{\partial \rho}{\partial t} = 0$.

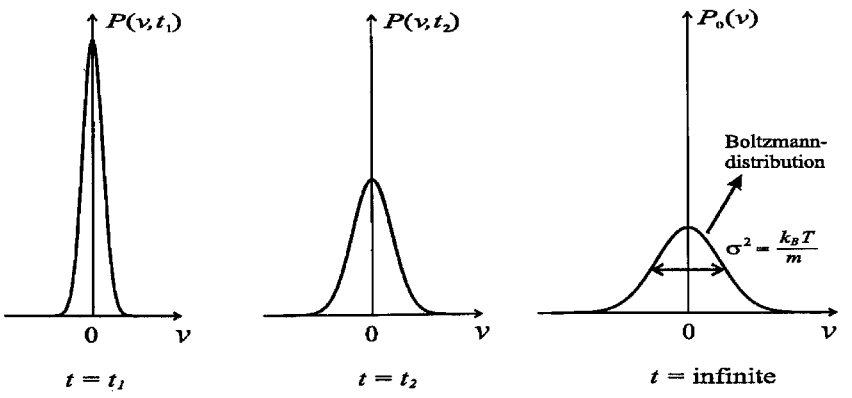

Figure 3.5: Evolution of $P(v,t)$ starting from the initial condition of $P(v,t=0)=\delta(v)$. $t_1 < t_2$. For $t \to \infty$, $P(v,t)$ converges to the Boltzmann distribution.

away from the mean. Therefore, $c_0 = 2\gamma k_B T/m$, and the Fokker-Planck equation (3.41) becomes

$$\frac{\partial P(v,t)}{\partial t} = \frac{\partial}{\partial v}\left[\gamma v P(v,t) + \frac{\gamma k_B T}{m}\frac{\partial P(v,t)}{\partial v}\right] \tag{3.44}$$

Now the steady-state solution of (3.44), *i.e.*, the solution of (3.42) with $c_0 = 2\gamma k_B T/m$ becomes

$$P_0(v) \propto \exp\left[-\frac{mv^2}{2k_B T}\right] \tag{3.45}$$

which is the *Boltzmann distribution*, agreeing with the statistical physics discussed in Subsection 3.1.1. The proportional constant is determined by the probability normalization condition $\int_{-\infty}^{\infty} P_0(v)dv = 1$.

The time-dependent solution of (3.44) with an initial condition of $P(v,t=0)=\delta(v)$ can be shown to be

$$P(v,t) = \left[\frac{2\pi k_B T}{m}(1-e^{-2\gamma t})\right]^{-1/2} \exp\left[-\frac{m}{2k_B T}\frac{v^2}{1-e^{-2\gamma t}}\right] \tag{3.46}$$

which converges to the Boltzmann distribution after a sufficiently long time. The evolution of $P(v,t)$ in (3.46) is depicted in Fig. 3.5.

Fokker-Planck Equation for Displacement in Brownian Motion

In a fashion similar to the velocity case, we can establish a Fokker-Planck equation for the displacement probability distribution, $P(x,t)$, in the Brownian motion. Intuitively, the first displacement jump moment is given by $A_1(x) = \langle \Delta x \rangle_x / \Delta t = 0$ as the average change in the displacment, Δx, is zero regardless of x. The second displacement jump moment is given by $A_2(x) = \langle (\Delta x)^2 \rangle_x / \Delta t = 2D$

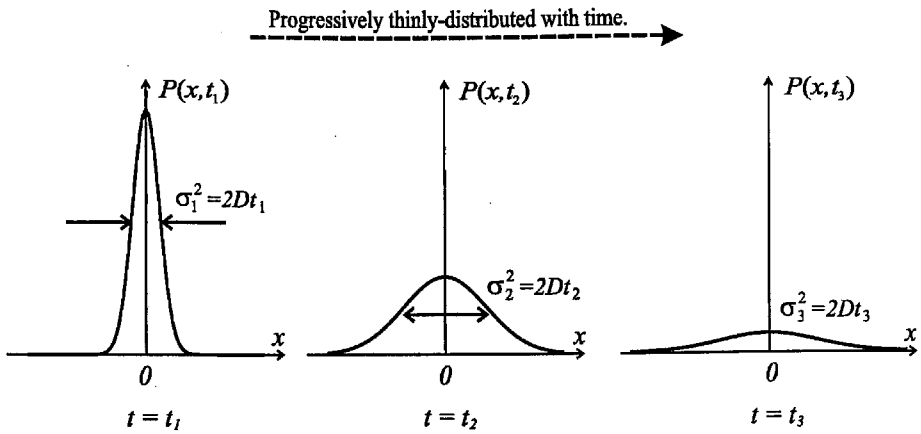

Figure 3.6: Evolution of $P(x,t)$ starting from the initial condition of $P(x,t=0)=\delta(x)$. $t_1 < t_2 < t_3$. For $t \to \infty$, $P(x,t)$ approaches zero for any given x and the probability distribution becomes more and more thinly distributed over x.

according to (3.27). Now, the Fokker-Planck equation (3.33) for the displacement can be written as

$$\frac{\partial P(x,t)}{\partial t} = D\frac{\partial^2}{\partial x^2}P(x,t) \tag{3.47}$$

which is the well-known *diffusion equation.*

The solution of the diffusion equation with an initial condition of $P(x,t=0)=\delta(x)$ in the absence of any boundaries becomes

$$P(x,t) = \frac{1}{\sqrt{4\pi Dt}}\exp\left[-\frac{x^2}{4Dt}\right] \tag{3.48}$$

This is a Gaussian distribution whose mean, $\langle x\rangle$, is zero and whose variance, $\sigma_x = \sqrt{\langle x^2(t)\rangle}$, is equal to $\sqrt{2Dt}$, or

$$\langle x^2(t)\rangle = 2Dt \tag{3.49}$$

which perfectly agrees with (3.27) obtained using the Langevin equation. The time-evolution of $P(x,t)$ described by (3.48) is illustrated in Fig. 3.6.

Wiener and Ornstein-Uhlenbeck Process

As seen in (3.48), the probability distribution of the displacement of the Brownian particle does not reach steady-state. As time goes by, the probability density at any given x approaches zero while the standard deviation of the distribution approaches infinity, proportionally increasing with $\sqrt{t}$. This is the key signature of any diffusion processes. The diffusion process was rigorously studied by Nobert Wiener and the diffusion process is often referred to as *Wiener process* in the theory of random process [33]. As can be seen from (3.47), the Fokker-Planck equation describing the Wiener process

does not involve the first jump moment (*e.g.*, $A_1(x) = 0$ in (3.47)). Since the statistical averages in the Wiener process vary with time, as seen in (3.49), the Wiener process is a nonstationary process.

On the other hand, the velocity of the Brownian particle is ultimately a stationary process as the probability distribution of the velocity eventually reaches the steady-state distribution, which corresponds to the Boltzman distribution. These types of random process are called *Ornstein-Uhlenbeck processes* [41] (reprinted in [18]). Equation (3.44) is a typical form of the Fokker-Planck equation that describes the Ornstein-Uhlenbeck process. Interestingly, the Ornstein-Uhlenbeck process is the only process which is stationary, Gaussian, and Markovian at the same time [42] (reprinted in [18]).

Here, we should make an important comment on the small-fluctuation approximations we have used to derive the Fokker-Planck equation, and their different effects on the two processes. For the Ornstein-Uhlenbeck process which ultimately attains the steady-state distribution, the small-fluctuation assumption and the resultant approximation in the Fokker-Planck equation will result in a sharply distributed steady-state probability distribution around the mean. This is because even in the steady-state, the fluctuations should be still small. However, in the Wiener-process which does not achieve the steady-state distribution, the small-fluctuation can accumulate and the probability density can be broadened without limit as we saw earlier in the diffusion process.

3.2 Brownian Motion in Electrical Circuits

3.2.1 Johnson-Nyquist Noise

In his pioneering paper dated in 1928 [39], Johnson first reported an experimental observation that an electric linear (ohmic) resistor, R, generates white noise of thermal origin. His measurement demonstrated that the single-side-band (SSB) power spectral density (PSD) of the equivalent thermal voltage noise in Fig. 3.7(a) is given by

$$\frac{\overline{v_n^2}}{\Delta f} = 4k_BTR \tag{3.50}$$

which is equivalent to the following autocorrelation expression:

$$\langle v_n(t_1)v_n(t_2)\rangle = 2k_BTR \cdot \delta(t_1 - t_2) \tag{3.51}$$

Figure 3.7(b) depicts the Norton equivalent current noise model for the resistor where the SSB PSD of the current noise is given by:

$$\frac{\overline{i_n^2}}{\Delta f} = \frac{4k_BT}{R} \tag{3.52}$$

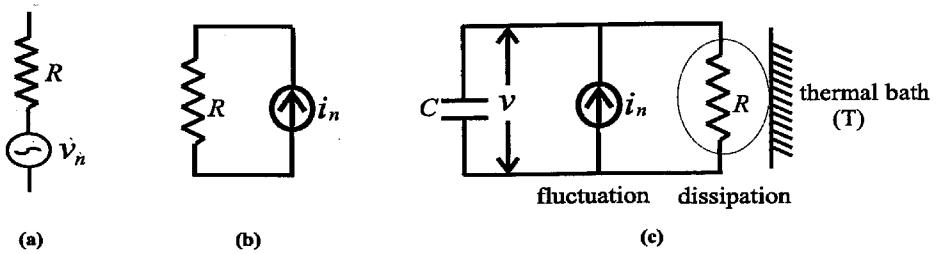

Figure 3.7: Johnson-Nyquist thermal noise in an ohmic resistor. (a) Thevenin equivalent noise model. $\overline{v_n^2/\Delta f} = 2k_BTR$. (b) Norton equivalent noise model. $\overline{i_n^2/\Delta f} = 2k_BT/R$. (c) An electrical analogue to the mechanical Brownian motion.

or, equivalently,

$$\langle i_n(t_1)i_n(t_2)\rangle = \frac{2k_BT}{R}\cdot\delta(t_1-t_2) \tag{3.53}$$

The credit for acquiring deep physical insight into the thermal noise in resistors goes to Nyquist, who theoretically verified the Johnson's observation based upon an elegant thermodynamic argument [1]. The basic principle Nyquist used was that of thermal equilibrium, and hence essentially the same as that used by Einstein and Langevin. To illustrate the principle used by Nyquist, let us consider an RC-circuit shown in Fig. 3.7(c), which is an electrical analogue of the mechanical Brownian system discussed in the previous section. In this analogy, the capacitor functioning as an energy storing element corresponds to the inertia of the Brownian particle while the dissipative resistor corresponds to the surrounding fluid. The thermal fluctuations of electrons tend to increase the energy of the capacitor. However, excess energy stored in the capacitor is dissipated through the resistor, flowing into the thermal bath kept at temperature T. This subtle balance between fluctuation and dissipation ultimately drives the system towards equilibrium, in which the capacitor stores the mean energy of $k_BT/2$ according to the equipartition theorem.

Now we will show how the Johnson noise can be derived from the equilibrium property (equipartition theorem). Nyquist's derivation in his paper is a bit different from our derivation here but the concepts of both methods are essentially the same. The Langevin equation governing the voltage across the capacitor, $v(t)$, in Fig. 3.7(c) is given by

$$\dot{v} = -\frac{1}{RC}v + \frac{i_n(t)}{C} \tag{3.54}$$

which is obtained using Kirchoff's current and voltage law (KCL, KVL). The white Gaussian current noise, $i_n(t)$, has an intensity of Λ, which will prove to be $2k_BT/R$ shortly using the equilibrium property:

$$\langle i_n(t_1)i_n(t_2)\rangle = \Lambda\delta(t_1-t_2) \tag{3.55}$$

From the Langevin equation (3.54) we can obtain the autocorrelation of $v(t)$ using the method

introduced in Subsection 3.1.2:

$$\langle v(t_1)v(t_2)\rangle = \frac{R\Lambda}{2C}\exp\left[\frac{-|t_1-t_2|}{RC}\right] \tag{3.56}$$

where we have already discarded the initial transient term. Since the energy stored in the capacitor C is $E_C = Cv^2/2$, the mean fluctuation energy of the capacitor becomes

$$\langle E_C\rangle = \frac{1}{2}C\langle v^2\rangle = \frac{R\Lambda}{4} \tag{3.57}$$

where we have used (3.56). Since $\langle E_C\rangle$ must be equal to $k_BT/2$ according to the equipartition theorem, we arrive at

$$\Lambda = \frac{2k_BT}{R} \tag{3.58}$$

corresponding to

$$\frac{\overline{i_n^2}}{\Delta f} = \frac{4k_BT}{R} \tag{3.59}$$

which is the Johnson noise.

3.2.2 Fluctuation-Dissipation Theorem Revisited

The thermal equilibrium of the RC-circuit in Fig. 3.7(c) is achieved via the balance between fluctuation and dissipation, as mentioned previously, and hence we reencounter the fluctuation-dissipation theorem in the context of electrical circuits: As can be seen in (3.50), the fluctuation intensity has a direct dependence upon the dissipation element R, that is, the dissipation R and its corresponding thermal fluctuation $4k_BTR$ always go hand in hand. Wherever there is dissipation, there is thermal fluctuation and *vice versa*.

If dissipation did not accompany thermal fluctuations in a given system, the system cannot develop the balance between fluctuation and dissipation and will exhibit a nonphysical behavior. For example, if the dissipation element R were taken out in Fig. 3.7(c) leaving only the thermal fluctuation, the capacitor works as an ideal integrator of the thermal fluctuation, $i_n(t)$, as can be seen in (3.54) with $R = \infty$:

$$v(t) = \frac{1}{C}\int_0^t i_n(t')dt' \tag{3.60}$$

Hence the autocorrelation function of $v(t)$ in this unrealistic case becomes

$$\begin{aligned}\langle v(t_1)v(t_2)\rangle &= \frac{1}{C^2}\int_0^{t_1}dt'\int_0^{t_2}dt''\langle i_n(t')i_n(t'')\rangle \\ &= \frac{2k_BT}{RC^2}\int_0^{t_1}dt'\int_0^{t_2}dt''\delta(t'-t'') \\ &= \frac{2k_BT}{RC^2}\min\{t_1,t_2\}\end{aligned} \tag{3.61}$$

where $\min\{t_1, t_2\}$ signifies the minimum value between t_1 and t_2. Therefore, for $t \equiv t_1 = t_2$, the mean-squared voltage grows with time indefinitely

$$\langle v^2(t) \rangle = \frac{2k_B T}{RC^2} \cdot t \tag{3.62}$$

or equivalently, the mean fluctuation energy of the capacitor grows with time without bound

$$\langle E_C \rangle = \frac{1}{2} C \langle v^2 \rangle = \frac{k_B T}{RC} \cdot t \tag{3.63}$$

In other words, the voltage across the capacitor assumes the Wiener or diffusion process, which is physically prohibited as the energy of the capacitor cannot grow indefinitely in the absence of external energy sources due to the law of energy conservation. This clearly shows that the unrealistic imbalance between thermal fluctuation and dissipation gives rise to physically impossible situations. Hence, in circuit noise modeling, care should be taken of to accompany any thermal noise source by its corresponding dissipation. This important notion of fluctuation-dissipation balance will be encountered several times in this thesis, and will play specially substantial roles in the treatment of oscillator phase noise presented in Chapter 6. The fluctuation-dissipation balance in the presence of nonlinearity investigated in Chapter 4 will be a key to fundamental understanding of thermal fluctuations of nonlinear resistors such as transistors.

3.2.3 Probability Distribution of Voltage

In this subsection, we will study the probability distribution of the voltage across the capacitor in Fig. 3.7(c). To this end, we have to calculate the first and second voltage jump moments, $A_1(v)$ and $A_2(v)$ in the Fokker-Planck equation, (3.33).

The first jump moment $A_1(v)$ in (3.34) can be easily obtained by resorting to the Langevin equation, (3.54):

$$A_1(v) = \frac{\langle \Delta v \rangle_v}{\Delta t} = -\frac{v}{RC} \tag{3.64}$$

The second jump moment $A_2(v)$ in (3.35) will be approximated as an unknown positive constant, c_0, where the justification for this approximation can be found in the explanation above (3.40):

$$A_2(v) = \frac{\langle (\Delta v)^2 \rangle_v}{\Delta t} \approx c_0 \tag{3.65}$$

The constant c_0 will be determined using the equilibrium property.

Plugging (3.64) and (3.65) in (3.33), we obtain the Fokker-Planck equation for the probability

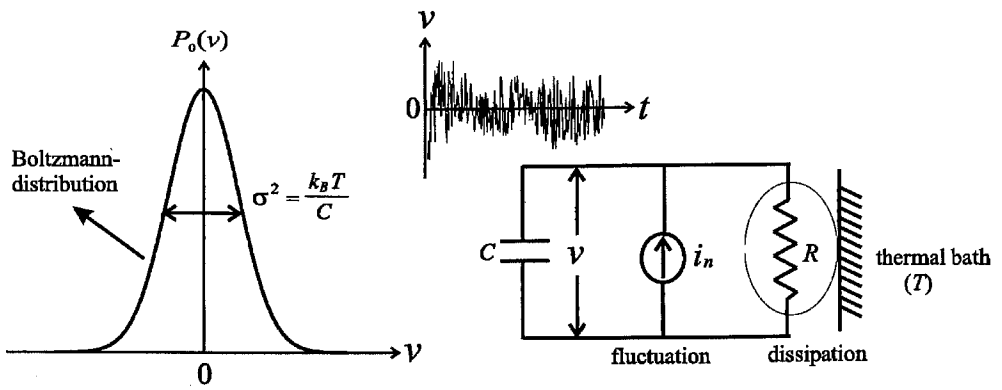

Figure 3.8: The probability distribution of the voltage across the capacitor in the RC-circuit in thermal equilibrium. The distribution is that of Boltzmann and the standard deviation of the distribution is $\sqrt{k_B T/C}$, which is obtained from the equipartition theorem.

distribution of the voltage, $P(v,t)$:

$$\frac{\partial P(v,t)}{\partial t} = \frac{\partial}{\partial v}\left[\frac{v}{RC}P(v,t) + \frac{c_0}{2}\frac{\partial}{\partial v}P(v,t)\right] \tag{3.66}$$

When the system eventually reaches equilibrium, the left-hand side of (3.66) becomes zero as the equilibrium probability distribution is independent of time and hence we have

$$\frac{v}{RC}P_0(v) + \frac{c_0}{2}\frac{d}{dv}P_0(v) = 0 \tag{3.67}$$

where $P_0(v) \equiv \lim_{t\to\infty} P(v,t)$ is the equilibrium probability distribution. By multiplying (3.67) by v and integrating it over v and using $\langle v^2\rangle = k_B T/C$ (equipartition theorem), we obtain

$$\frac{1}{RC}\cdot\frac{k_B T}{C} + \frac{c_0}{2}\int_{-\infty}^{\infty} v\frac{d}{dv}P_0(v)dv = \frac{1}{RC}\cdot\frac{k_B T}{C} - \frac{c_0}{2} = 0 \tag{3.68}$$

where the second equation was obtained via integration by parts while $vP_0(v)|_{v=\pm\infty} = 0$ due to the fast decay of $P_0(v)$ for large $|v|$. Therefore, $c_0 = 2k_B T/(RC^2)$ and the Fokker-Planck equation is now completely determined:

$$\frac{\partial P(v,t)}{\partial t} = \frac{\partial}{\partial v}\left[\frac{v}{RC}P(v,t) + \frac{k_B T}{RC^2}\frac{\partial}{\partial v}P(v,t)\right] \tag{3.69}$$

The solution of the Fokker-Planck equation (3.69) for the initial condition of $P(v,t=0) = \delta(v)$ is given by

$$P(v,t) = \left[\frac{2\pi k_B T}{C}(1-e^{-2t/(RC)})\right]^{-1/2}\cdot\exp\left[-\frac{C}{2k_B T}\frac{v^2}{1-e^{-2t/(RC)}}\right] \tag{3.70}$$

C (F)	σ (V)
10f	$\sim 600\ \mu$
100f	$\sim 200\ \mu$
1p	$\sim 60\ \mu$
10p	$\sim 20\ \mu$
100p	$\sim 6\ \mu$

Table 3.1: C versus $\sigma = \sqrt{k_B T/C}$ at $T = 300$K.

For $t = \infty$ when the system reaches equilibrium, the corresponding probability distribution $P_0(v)$ becomes the Boltzmann distribution

$$P_0(v) = \left[\frac{2\pi k_B T}{C}\right]^{-1/2} \cdot \exp\left[-\frac{Cv^2}{2k_B T}\right] \tag{3.71}$$

which is depicted in Fig. 3.8. The standard deviation of the Boltzmann distribution, $\sigma_v = \sqrt{\langle v^2 \rangle}$, which indicates the width of the distribution in Fig. 3.8 is given by $\sqrt{k_B T/C}$ thanks to the equipartition theorem. The distribution width σ for typical values of capacitors is shown in Table 3.1 for the temperature of 300 K. As can be seen from the table, the voltage fluctuation in the capacitor is very small for typical values of the capacitor.

3.2.4 More on the $k_B T/C$-Noise

In Subsection 3.2.1, we have derived the Johnson-Nyquist noise based on *a priori* knowledge of the equipartition theorem in the simple RC-circuit of Fig. 3.7(c). In this subsection, we will start with *a priori* knowledge of the Johnson-Nyquist noise to verify the equipartition theorem or equivalently, the $k_B T/C$-variance of the probability distribution of the voltage across the capacitor (the so-called $k_B T/C$-noise) in more complex arrangements of R, C, and L. The examples of LRC-networks that will be used for this verification are shown in Fig. 3.9, where the current sources represent the Johnson-Nyquist noise generated by the ohmic resistors in the circuits. This reverse derivation serves a purpose of examining the consistency between the Johnson's $4k_B TR$-noise and the equipartition theorem in various linear networks of passive elements.

First-Order RC-Circuit with Multiple Resistors

Here, we will derive the $k_B T/C$-noise in the first-order RC-circuit with multiple resistors shown in Fig. 3.9(a). Using the KCL at both nodes of the capacitor at an angular frequency ω, we obtain

$$\frac{v_\perp}{R_1} + (j\omega C + \frac{1}{R_3})v = i_{n,1} - i_{n,3} \tag{3.72}$$

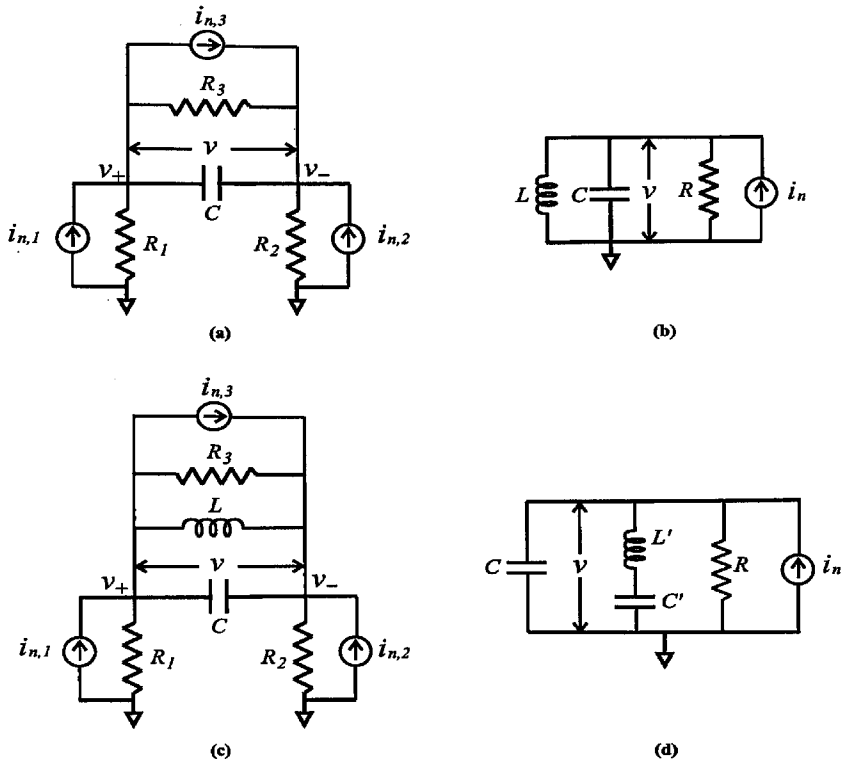

Figure 3.9: Various LRC circuits. In any circuits, $\langle v^2 \rangle = k_B T/C$.

$$\frac{v_-}{R_2} - (j\omega C + \frac{1}{R_3})v \quad = \quad i_{n,2} + i_{n,3} \tag{3.73}$$

where $v = v_+ - v_-$. After a simple manipulation of the simultaneous equations, we obtain

$$v = \frac{R_1 i_{n,1} - R_2 i_{n,2} - (R_1 + R_2) i_{n,3}}{j\omega C(R_1 + R_2) + (R_1 + R_2 + R_3)/R_3} \tag{3.74}$$

Using (3.52) and (3.74) and also assuming uncorrelation among $i_{n,1}$, $i_{n,2}$ and $i_{n,3}$ as they are from different resistors, we obtain the power spectral density for the differential voltage v:

$$\frac{\overline{v^2}}{\Delta f} = 4k_B T \cdot \frac{r}{1 + \omega^2 C^2 r^2} \tag{3.75}$$

where a new parameter $r \equiv (R_1 + R_2) \cdot R_3/(R_1 + R_2 + R_3)$ was introduced for simplicity. Now, the mean-squared voltage $\langle v^2 \rangle$ is obtained through integration of the power spectral density in (3.75) over the whole frequency range from 0 to ∞:

$$\begin{aligned} \langle v^2 \rangle &= \int_0^\infty \frac{d\omega}{2\pi} \frac{\overline{v^2}}{\Delta f} \\ &= 4k_B T \int_0^\infty \frac{d\omega}{2\pi} \frac{r}{1 + \omega^2 C^2 r^2} \end{aligned}$$

$$= \frac{k_B T}{C} \tag{3.76}$$

which verifies the equipartition theorem in the first-order circuit.

Simple Second-Order LC-Resonator

Now we will derive the $k_B T/C$-noise in the simple second-order LC-resonator depicted in Fig. 3.9(b). The ohmic resistor in parallel with the LC-tank can be viewed as either an explicit external resistor or the internal loss of the resonator. Since the resonator is a linear time-invariant (LTI) system, we can easily relate the power spectral density of the voltage across the tank to the power spectral density of the Johnson current noise:

$$\begin{aligned} \frac{\overline{v^2}}{\Delta f} &= \left| j\omega L \| \frac{1}{j\omega C} \| R \right|^2 \times \frac{\overline{i_n^2}}{\Delta f} \\ &= 4k_B T R \cdot \frac{\omega_\tau^2 \omega^2}{(\omega^2 - \omega_0^2)^2 + \omega_\tau^2 \omega^2} \end{aligned} \tag{3.77}$$

where $\omega_\tau \equiv (RC)^{-1}$ and $\omega_0^2 \equiv (LC)^{-1}$. Then, the mean-squared voltage can be obtained by integrating the power spectral density of the voltage over the whole frequency range:

$$\begin{aligned} \langle v^2 \rangle &= \int_0^\infty \frac{d\omega}{2\pi} \frac{\overline{v^2}}{\Delta f} \\ &= \frac{2k_B T}{\pi R C^2} \cdot \int_0^\infty d\omega \frac{\omega^2}{(\omega^2 - \omega_0^2)^2 + \omega_\tau^2 \omega^2} \\ &= \frac{2k_B T}{C} \cdot \frac{\alpha}{\pi} \cdot \int_0^\infty dx \frac{x^2}{x^4 + (\alpha^2 - 2)x^2 + 1} \end{aligned} \tag{3.78}$$

where $x \equiv \omega/\omega_0$ and $\alpha \equiv \omega_\tau/\omega_0$. The 4 poles of the integrand $f(z)$

$$f(z) \equiv \frac{z^2}{z^4 + (\alpha^2 - 2)z^2 + 1} \tag{3.79}$$

constitute the four corners of a rectangle in the complex z-plain as shown in Fig. 3.10, *i.e.*, $z_1 = a + bi$, $z_1^* = a - bi$, $z_2 = -a - bi$, and $z_2^* = -a - bi$ for $a > 0$ and $b > 0$. The residues r_1 and r_2 for the poles z_1 and z_2 of the integrand $f(z)$ are then given by

$$\begin{aligned} r_1 &= \lim_{z \to z_1} (z - z_1) f(z) = \frac{a + i\alpha/2}{4ia\alpha} \\ r_2 &= \lim_{z \to z_2} (z - z_2) f(z) = \frac{a - i\alpha/2}{4ia\alpha} \end{aligned} \tag{3.80}$$

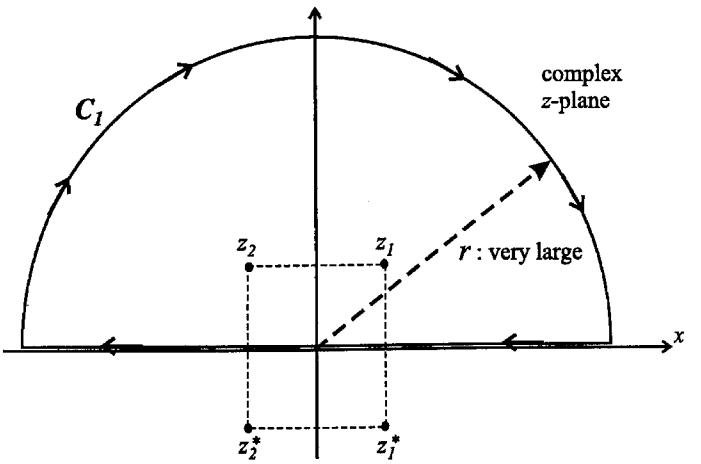

Figure 3.10: Contour integration.

Then the contour integration of $f(z)$ along the contour C_1 in Fig. 3.10 with an infinite radius leads to

$$\oint_{C_1} f(z)dz = 2\int_0^\infty f(x)dx = 2\pi i(r_1 + r_2) = \frac{\pi}{\alpha} \tag{3.81}$$

and therefore, the integration (3.78) results in the k_BT/C noise,

$$\langle v^2 \rangle = \frac{k_BT}{C} \tag{3.82}$$

which confirms the validity of the equipartition theorem in the LC-resonator. This notion of the k_BT/C-dependence of the tank voltage noise will be extremely important later on in the treatment of phase noise of LC-oscillators.

Second-Order LC-Resonator with Multiple Resistors

Now we consider a bit more complicated LC-resonator shown in Fig. 3.9(c) which contains multiple resistors and hence multiple noise sources. Using KCL at both nodes of the capacitor, we obtain

$$\frac{v_+}{R_1} + (j\omega C + \frac{1}{j\omega L} + \frac{1}{R_3})v = i_{n,1} - i_{n,3} \tag{3.83}$$

$$\frac{v_-}{R_2} - (j\omega C + \frac{1}{j\omega L} + \frac{1}{R_3})v = i_{n,2} + i_{n,3} \tag{3.84}$$

where $v = v_+ - v_-$. A simple manipulation of the simultaneous equations leads to

$$v = \frac{R_1 i_{n,1} - R_2 i_{n,2} - (R_1 + R_2) i_{n,3}}{(j\omega C + 1/(j\omega L)) \cdot (R_1 + R_2) + (R_1 + R_2 + R_3)/R_3} \tag{3.85}$$

and henceforth, the power spectral density of v is given by

$$\frac{\overline{v^2}}{\Delta f} = 4k_BT \cdot \frac{L^2\omega_0^2}{r} \cdot \frac{x^2}{x^4 + ((L\omega_0/r)^2 - 2)x^2 + 1} \tag{3.86}$$

where $\omega_0^2 = (LC)^{-1}$, $r \equiv (R_1 + R_2) \cdot R_3/(R_1 + R_2 + R_3)$ and $x \equiv \omega/\omega_0$. In the derivation, we have assumed that the noise sources are uncorrelated among each other as they originate from different resistors. By utilizing the contour integral result of (3.81), we obtain

$$\begin{aligned} \langle v^2 \rangle &= \int_0^\infty \frac{d\omega}{2\pi} \frac{\overline{v^2}}{\Delta f} = \int_0^\infty \omega_0 \frac{dx}{2\pi} \frac{\overline{v^2}}{\Delta f} \\ &= \frac{\omega_0}{2\pi} \cdot 4k_BT \cdot \frac{L^2\omega_0^2}{r} \int_0^\infty dx \frac{x^2}{x^4 + ((L\omega_0/r)^2 - 2)x^2 + 1} \\ &= \frac{k_BT}{C} \end{aligned} \tag{3.87}$$

which again results in the k_BT/C-noise, demonstrating the equipartition theorem.

Simple Third-Order LC-Resonator

The resonator shown in Fig. 3.9(d) is a third-order system, which makes the calculation of the mean-squared voltage across the capacitor nontrivial. The power spectral density of the voltage across the capacitor is given by

$$\begin{aligned} \frac{\overline{v^2}}{\Delta f} &= \left| \frac{1}{j\omega C} \| (j\omega L' + \frac{1}{j\omega C'}) \| R \right|^2 \times \frac{\overline{i_n^2}}{\Delta f} \\ &= 4k_BTR \cdot \frac{(1-x^2)^2}{(1-x^2)^2 + \alpha x^2\{(1-x^2) + \beta\}^2} \end{aligned} \tag{3.88}$$

where $\omega_0^2 \equiv 1/(L'C')$, $x \equiv \omega/\omega_0$, $\alpha = \omega_0 RC$, and $\beta \equiv C'/C$. The mean-squared voltage is then given by

$$\begin{aligned} \langle v^2 \rangle &= \int_0^\infty \frac{d\omega}{2\pi} \frac{\overline{v^2}}{\Delta f} \\ &= \frac{k_BT}{C} \cdot \frac{\alpha}{\pi} \cdot \int_0^\infty dx \frac{(1-x^2)^2}{(1-x^2)^2 + \alpha^2 x^2\{(1-x^2) + \beta\}^2} \end{aligned} \tag{3.89}$$

As can be seen, the integrand $g(\alpha;\beta;x)$ in the above integral

$$g(\alpha;\beta;x) \equiv \frac{(1-x^2)^2}{(1-x^2)^2 + \alpha^2 x^2\{(1-x^2) + \beta\}^2} \tag{3.90}$$

is a function of x with two independent parameters α and β. If the mean-squared voltage in (3.89) is to be k_BT/C, the integration in the equation should result in π/α, regardless of the value of β. While this seems unlikely due to the explicit dependence of the integrand on β, numerical integrations verify

	$\alpha = 0.1$ ($\pi/\alpha \approx 31.42$)	$\alpha = 1$ ($\pi/\alpha \approx 3.142$)	$\alpha = 5$ ($\pi/\alpha \approx 0.6283$)	$\alpha = 10$ ($\pi/\alpha \approx 0.3142$)	$\alpha = 100$ ($\pi/\alpha \approx 0.03142$)
$\beta = 0.1$	31.4224	3.1361	0.6280	0.3132	0.03132
$\beta = 1$	31.3978	3.1362	0.6281	0.3139	0.03131
$\beta = 10$	31.3959	3.1362	0.6281	0.3140	0.03130
$\beta = 100$	31.4109	3.1362	0.6281	0.3144	0.03130

Table 3.2: Numerical calculation results for the integration in (3.89) for various values of α and β.

that the integration in (3.89) is indeed π/α as shown in Table 3.2. Therefore, $\langle v^2 \rangle$ again becomes $k_B T/C$, once again confirming the equipartition theorem.

Validity of the $k_B T/C$-Noise

In this subsection, we have demonstrated through examples that a capacitor C in linear LRC-networks in which resistors generate the Johnson noise always stores a mean-squared voltage of $k_B T/C$ in equilibrium. This $k_B T/C$-noise is a direct result of the equipartition theorem. This notion of energy equipartition can be extremely powerful in circuit noise calculation as seen in the third-order LC resonator example in Fig. 3.9(d). While the noise calculation routine using the typical LTI theory becomes progressively complex with an increasing order of the system, resorting to the energy equipartition makes the noise calculation one liner.

However, in many practical circuit arrangements and operations, the conditions with which the equipartition theorem is established are violated, leading to non-$k_B T/C$-noise. As discussed in Subsection 3.1.1, there are two conditions that validate the equipartition theorem. First, the probability distribution of the voltage across the capacitor should be the Boltzmann distribution. Second, the energy in the capacitor should assume a quadratic form with respect to the voltage across it, *i.e.*, $E_C = Cv^2/2$. For the equipartition theorem to hold good, both of these conditions should be satisfied. A few example cases where these conditions are violated:

- when nonlinear capacitors such as MOSCAPs, varactor diodes, etc. are energy storing elements. The energy stored in the nonlinear capacitor does not have the quadratic form in general, as the capacitance varies with the voltage across the capacitor. However, in most practical cases, fluctuations are small and we can approximate the nonlinear capacitor as a linear capacitor. Within the accuracy of this approximation, the energy stored in the nonlinear capacitor has the quadratic form and hence the equipartition theorem holds good as far as the probability distribution of the voltage across the capacitor is Boltzmann. We will discuss this in full details in Section 4.5 in the next chapter.

- when a system involving a nonlinear resistor is in *nonequilibrium steady-state*. As will be demonstrated in the next chapter, the probability distribution of the voltage across the capac-

itor in the presence of nonlinear resistors is not Boltzmann in the nonequilibrium steady-state. In such cases, the equipartition theorem is not valid in general.

3.3 Forced Brownian Motion

Section 3.1 focused on the Brownian motion in the absence of any external force. Similarly in Section 3.2, we have discussed the thermal fluctuations in circuits in the absence of any external bias current. However, in the real physical world, the Brownian motion is often subject to an external force and hence this *forced Brownian motion* has a considerable practical importance. In this section, we will study such forced Brownian motions, in both mechanical and electrical cases.

3.3.1 Mechanical Case

Let us consider a Brownian particle subject to a constant force F as illustrated in Fig. 3.11(a) or (b). In Fig. 3.11(a), the Brownian particle with mass m and charge q is subject to an electric field, E, or an electric force, $F = qE$. In Fig. 3.11(b), the Brownian particle with mass m is subject to a gravitational field, g, or a gravitational force, $F = mg$. In either case, the Langevin equation describing the Brownian motion is given by

$$\dot{v} = -\gamma v + \frac{1}{m} \cdot \zeta(t) + \frac{1}{m} \cdot F \tag{3.91}$$

After a sufficiently long time, the mean velocity of the Brownian particle will reach a steady-state value or the so-called *terminal velocity* as the external force, F, ultimately becomes equal to the frictional force, $m\gamma v$. Therefore, if we denote this terminal velocity as v_0, we have

$$v_0 \equiv \lim_{t\to\infty} \langle v(t) \rangle = \frac{F}{m\gamma} \tag{3.92}$$

With the help of (3.92), the Langevin equation (3.91) can be rewritten as

$$\frac{d}{dt}(v - v_0) = -\gamma(v - v_0) + \frac{1}{m} \cdot \zeta(t) \tag{3.93}$$

Comparing the Langevin equation above to the Langevin equation (3.10) in the case of no external force, the only change that has been made is replacement of v with $v - v_0$. Henceforth, the Fokker-Planck equation in this case can be obtained by replacing v with $v - v_0$ in (3.44):

$$\frac{\partial P(v,t)}{\partial t} + \gamma v_0 \frac{\partial}{\partial v} P(v,t) = \frac{\partial}{\partial v}\left[\gamma v P(v,t) + \frac{\gamma k_B T}{m} \frac{\partial P(v,t)}{\partial v}\right] \tag{3.94}$$

where we have used $P(v - v_0, t) = P(v,t)$ and $\partial/\partial(v - v_0) = \partial/\partial v$. The steady-state probability

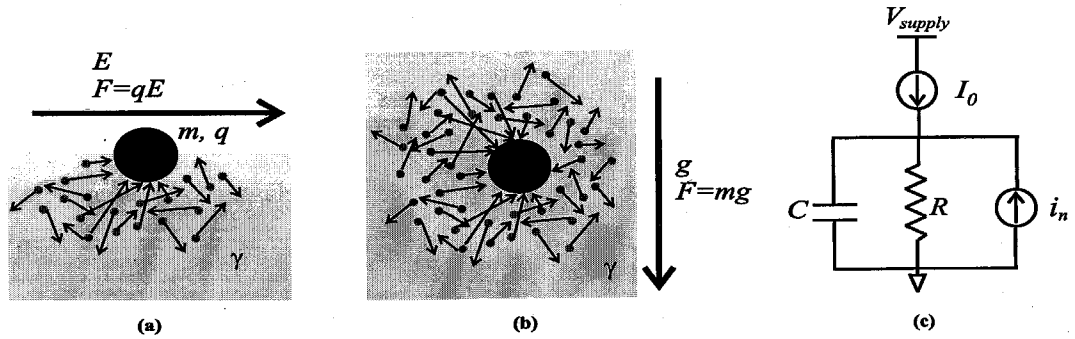

Figure 3.11: Forced Brownian motion. (a) A Brownian particle with mass m and charge q subject to an electric field E or an electric force $F = qE$. (b) A Brownian particle with mass m subject to a gravitational field g or a gravitational force $F = mg$. (c) An electrical analogue of the forced Brownian motion. The RC-circuit is driven by a current source.

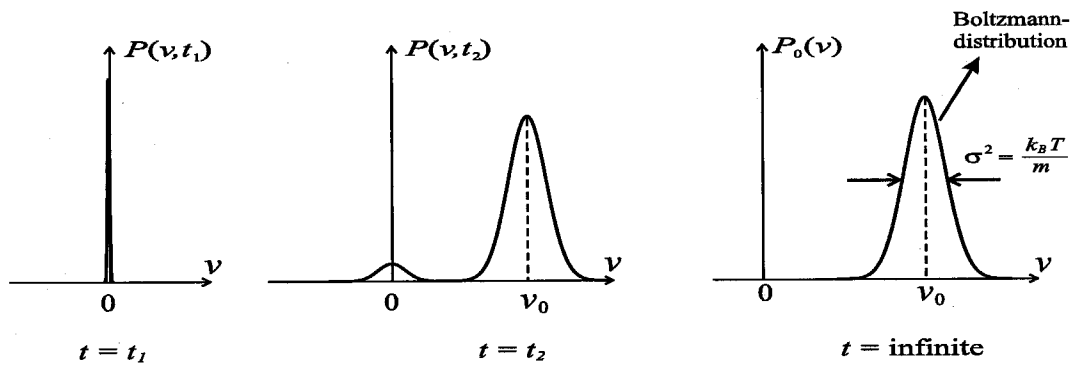

Figure 3.12: Evolution of $P(v,t)$ for the velocity in the forced Brownian motion with an initial condition of $P(v,t=0) = \delta(v)$. $t_1 < t_2$. $P(v,t)$ ultimately converges to the Boltzmann distribution whose mean is the terminal velocity v_0.

distribution of the velocity, $P_0(v)$, will then assume the Boltzmann distribution as in (3.45) while we must replace v with $v - v_0$:

$$P_0(v) = \left[\frac{2\pi k_B T}{m}\right]^{-1/2} \exp\left[-\frac{m}{2k_B T}(v - v_0)^2\right] \tag{3.95}$$

In other words, the steady-state probability distribution of the velocity of the Brownian particle in the presence of the external force is the Boltzmann distribution centered around $v_0 = F/(m\gamma)$ instead of $v_0 = 0$. Fig. 3.12 shows the time-evolution of $P(v,t)$ starting with an initial condition of $P(v,t=0) = \delta(v)$, which eventually leads to the Boltzmann distribution given by (3.95). The equipartition theorem still holds good, as we can easily demonstrate using (3.95) that

$$\langle (v - v_0)^2 \rangle = \frac{k_B T}{m} \tag{3.96}$$

An important thing to note is that when a Brownian particle is subject to an external force with no physical boundary (such as a wall) stopping its drift, the whole system consisting of the Brownian particle, the surrounding medium, and the thermal bath, *never* reaches thermal equilibrium even though $P(v,t)$ reaches its steady-state distribution $P_0(v)$ given by (3.95). In the steady-state, the Brownian particle continuously receives mechanical work, Fv_0, per unit time and converts it all into heat instead of turning it into kinetic energy, hence keeping its velocity at a constant value, v_0. Therefore, even in the steady-state, there is constant heat-flux into the thermal bath and the system is never in thermal equilibrium. This is the notion of *nonequilibrium steady-state*, which was discussed in Subsection 3.1.1.

In light of this observation, the Boltzmann distribution (3.95) and the equipartition theorem (3.96) in the nonequilibrium steady-state look quite peculiar as they are the equilibrium properties as discussed in Subsection 3.1.1. The Boltzmann distribution and the equipartition theorem in this nonequilibrium steady-state are actually a consequence of *linearity* of the system. As the linear Langevin equation (3.91) suggests, the Brownian particle's overall response to the stochastic force, $\zeta(t)$, the damping force, $-m\gamma v$, and the external force, F, will be the superposition of the response to each force thanks to the linearity. Hence, the Boltzmann distribution still appears even in the presence of the external force which keeps the system out of the equilibrium. When nonlinearity is involved, the situation becomes vastly different, which we will extensively investigate in Chapter 4 in an electrical circuits context.

3.3.2 Electrical Case

Figure 3.11(c) illustrates a noisy RC-circuit coupled with a constant bias current, I_0, which is an electrical analogue of the forced Brownian motion of the previous subsection. The Langevin equation describing the dynamics of the voltage across the capacitor is given by

$$\frac{d}{dt}(v - v_0) = -\frac{v - v_0}{RC} + \frac{i_n(t)}{C} \tag{3.97}$$

where v_0 is the bias voltage across the resistor, *i.e.*, $v_0 = I_0 R$, which is analogous to the terminal velocity in the mechanical case. Again, the only difference between the Langevin equation (3.54) in the absence of the bias current and the equation above is the replacement of v with $v - v_0$. Accordingly, the steady-state probability distribution of the voltage across the capacitor will be the Boltzmann distribution like (3.71), but with replacement of v with $v - v_0$:

$$P_0(v) = \left[\frac{2\pi k_B T}{C}\right]^{-1/2} \exp\left[-\frac{C(v - v_0)^2}{2k_B T}\right] \tag{3.98}$$

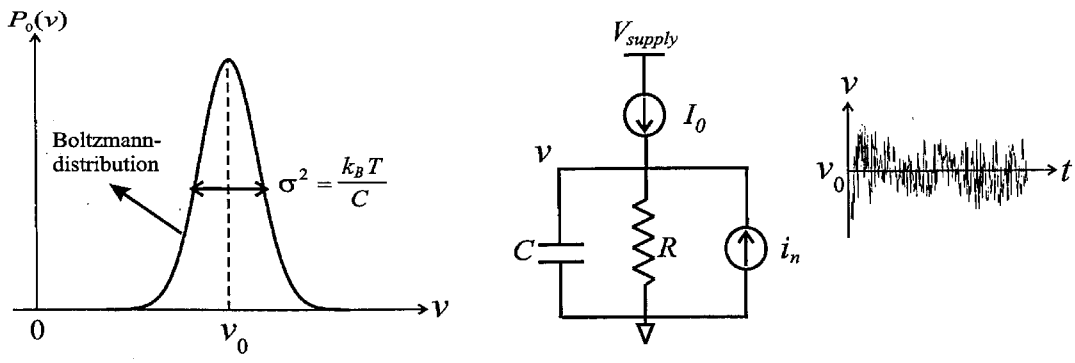

Figure 3.13: $P(v,t)$ ultimately converges to the Boltzmann distribution whose mean is the terminal velocity v_0.

The variance of the probability distribution is then given by

$$\langle (v - v_0)^2 \rangle = \frac{k_B T}{C} \tag{3.99}$$

The steady-state probability density and its variance are both shown in Fig. 3.13. Note that the RC-circuit never reaches thermal equilibrium even in the steady-state yet achieves the Boltzmann distribution (3.98) and the equipartition theorem (3.99) thanks to the linearity of the system as mentioned earlier.

3.3.3 Probability Distribution of Displacement

In this subsection, we will consider the probability distribution of the displacement, $P(x,t)$, in the case of the forced Brownian motion. To obtain the corresponding Fokker-Planck equation, we should evaluate the jump moments, $A_1(x)$ and $A_2(x)$, in (3.34) and (3.35). The first jump moment can be obtained intuitively

$$A_1(x) = \frac{\langle \Delta x \rangle_x}{\Delta t} = v_0 \tag{3.100}$$

as the Brownian particle has the drift velocity of v_0. According to (3.27), the second jump moment is given by

$$A_2(x) = \frac{\langle (\Delta x)^2 \rangle_x}{\Delta t} = 2D = 2 \cdot \frac{k_B T}{m\gamma} \tag{3.101}$$

where we used the Einstein relation (3.28) in the last equation. Therefore, the general form Fokker-Planck equation (3.33) becomes

$$\frac{\partial P(x,t)}{\partial t} = -v_0 \frac{\partial P(x,t)}{\partial x} + D \frac{\partial^2 P(x,t)}{\partial x^2} \tag{3.102}$$

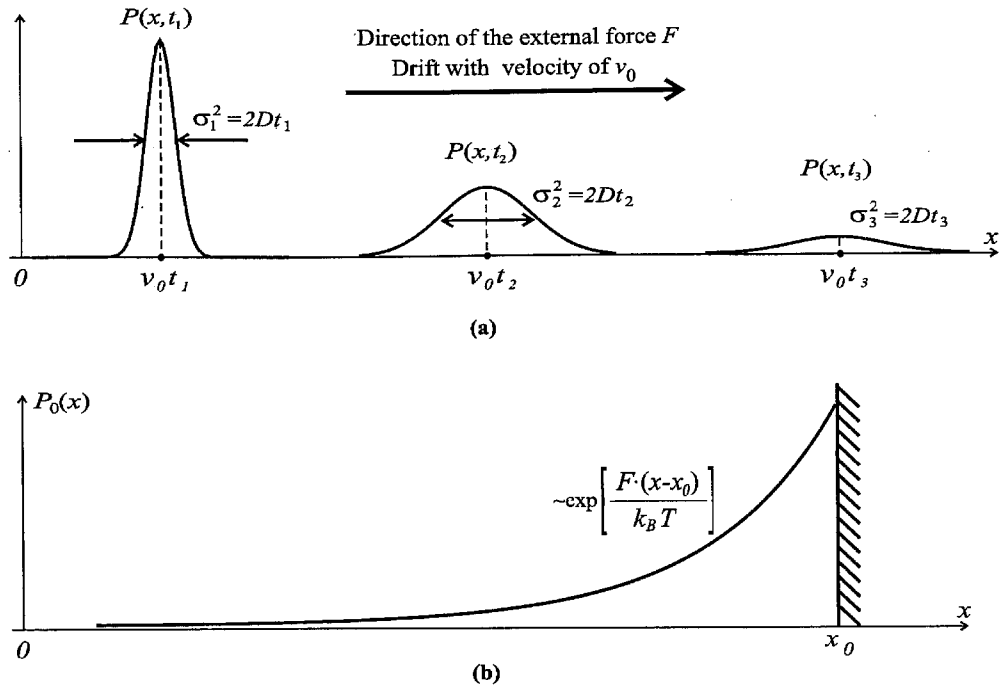

Figure 3.14: (a) Evolution of $P(x,t)$ for the forced Brownian motion. (b) Steady-state distribution $P_0(x)$ in the presence of the boundary at $x = x_0$.

The second term on the right-hand side corresponds to diffusion while the first term on the right-hand side corresponds to drift of the Brownian particle with the terminal velocity of v_0.

The solution of the equation above is given by

$$P(x,t) = \frac{1}{\sqrt{4\pi Dt}} \exp\left[-\frac{(x-v_0 t)^2}{4Dt}\right] \tag{3.103}$$

for the initial condition of $P(x, t=0) = \delta(x)$, which is illustrated in Fig. 3.14(a) for different times $t_1 < t_2 < t_3$. In the figure, the translation of the center of the distribution with time corresponds to the drift of the Brownian particle, while the broadening of the distribution corresponds to diffusion.

In the presence of boundaries (*e.g.* a wall that stops the drift of the Brownian particle), we can obtain a steady-state solution for the drift-diffusion equation (3.102). In case where there is a wall at $x = x_0$ as shown in Fig. 3.14(b), the steady-state solution becomes

$$P_0(x) \propto \exp\left[\frac{v_0}{D} \cdot (x - x_0)\right] = \exp\left[\frac{F(x-x_0)}{k_B T}\right] \tag{3.104}$$

which is no more than the Boltzmann distribution as the potential energy of the Brownian particle is given by $U = F(x_0 - x)$. For instance, if the constant force F is the gravitational force, *i.e.*,

$F = mg$, then (3.104) can be rewritten as

$$P_0(x) \propto \exp\left[\frac{mg(x - x_0)}{k_B T}\right] \tag{3.105}$$

which is the famous Barometric distribution [32].

3.4 Summary

In the foregoing sections, we have reviewed fundamental concepts and mathematical tools to understand and describe thermal fluctuation phenomena, using mechanical and electrical Brownian motions as analysis vehicles. We have seen that the balance between thermal fluctuation and thermal dissipation plays an important role in the energetics of the Brownian motion and in achieving thermal equilibrium. The Einstein relation and Johnson-Nyquist noise are the quantitative representations of the fluctuation-dissipation relation. The Einstein relation which illuminates the diffusion process by identifying its two key elements, sensitivity and friction, will play a critical role in the study of oscillator phase noise in Chapter 6. The Boltzmann probability distribution and energy equipartition are key characteristics in equilibrium. In a linear system, the Boltzmann distribution and energy equipartition are still valid even in nonequilibrium steady-state.

We have introduced Langevin equation and Fokker-Planck equation as powerful mathematical tools to describe fluctuations. The Langevin equation is used to describe the time-evolution of statistical averages of fluctuations. The solutions of the Fokker-Planck equations are time-dependent probability distributions of fluctuating quantities.

In Table 3.3, we have listed various types of random processes and corresponding Langevin equations. In each Langevin equation, the white Gaussian noise $\zeta(t)$ has the following properties:

$$\begin{aligned} \langle \zeta(t) \rangle &= 0 \\ \langle \zeta(t')\zeta(t'') \rangle &= \Gamma \delta(t' - t'') \end{aligned} \tag{3.106}$$

The table shows conversion from a given Langevin equation to a corresponding Fokker-Planck equation by specifying jump moments $A_1(y)$ and $A_2(y)$ for the general form Fokker-Planck equation (3.33), which is rewritten in the following for convenience:

$$\frac{\partial P(y,t)}{\partial t} = -\frac{\partial}{\partial y}\{A_1(y)P(y,t)\} - \frac{1}{2}\frac{\partial^2}{\partial y^2}\{A_2(y)P(y,t)\} \tag{3.107}$$

We will frequently use this conversion from the Langevin equation to the Fokker-Planck equation throughout this work. In the following, we will give examples for each type of random process in Table 3.3.

Type	Langevin Eq.	Jump Moments in (3.33)		Process
		$A_1(y)$	$A_2(y)$	
I	$\dot{y} = -\gamma y + \zeta(t)$	$-\gamma y$	Γ	Ornstein-Uhlenbeck
II	$\dot{y} = -\gamma y + \zeta(t) + a$	$-\gamma y + a$	Γ	Ornstein-Uhlenbeck
III	$\dot{y} = \zeta(t)$	0	Γ	Wiener (Diffusion)
IV	$\dot{y} = \zeta(t) + a$	a	Γ	Wiener (Diffusion)
V	$\dot{y} = C(y) + D(y)\zeta(t)$	$C(y)$	$\Gamma D^2(y)$	N/A

Table 3.3: Various types of random processes. This table also shows the conversion from a given Langevin equation to the corresponding Fokker-Planck Equation. The noise source $\zeta(t)$ is assumed to be white Gaussian whose mean is zero and $\langle \zeta(t)\zeta(t') \rangle = \Gamma\delta(t - t')$. a is a constant.

- Type-I

  The velocity of the linear Brownian motion in Fig. 3.1 and the voltage across the capacitor in the linear RC-circuit in Fig. 3.7(c) fall into this category.

- Type-II

  The velocity of the linear forced Brownian motion in Fig. 3.11(a)/(b) and the voltage across the capacitor in the linear RC-circuit driven by a constant current in Fig. 3.11(c) are categorized here.

- Type-III

  The displacement of the linear Brownian motion in Fig. 3.1 is the type-III random process. As will be seen in Chapter 6, the phase noise of self-sustained oscillators, *i.e.*, $\phi(t)$ in the total oscillator phase $\theta(t) = \omega_0 t + \phi(t)$ (ω_0 : oscillation frequency), also falls into this category.

- Type-IV

  The displacement of the linear forced Brownian motion in Fig. 3.11(a)/(b) is in this category. As will be seen in Chapter 6, the total oscillator phase $\theta(t) = \omega_0 t + \phi(t)$ is also this Type-IV process.

- Type-V

  In the Langevin equation for this type-V random process, the coefficients $C(y)$ and $D(y)$ have general dependence on y. This Langevin equation is used to describe *nonlinear* Brownian motion, which we will study in the next chapter. Once nonlinearity is introduced in random processes, the fluctuation phenomenon becomes much more difficult to understand, and this nonlinear Brownian motion is still a field of active research, including our own research on fluctuations and thermodynamics in nonlinear electrical circuits in Chapter 4.

  The conversion procedure from the Langevin equation to the Fokker-Planck equation in the Type-V nonlinear random process is rather involved while the appropriate treatment can be found in [19], [24], and [25] among many others. Depending upon the physical interpretation of

the nonlinear random process, the Langevin equation can lead to two different forms of Fokker-Planck equations, *i.e.*, Ito's form [43], [44] and Stratonovich's form [45]. Table 3.3 shows the Ito's form and unless otherwise mentioned, we will use this Ito's form for the Fokker-Planck equation. For the reference, the Stratonovich's form of the Fokker-Planck equation for this type-V nonlinear random process is given by

$$\frac{\partial P(y,t)}{\partial t} = -\frac{\partial}{\partial y}\{C(y)P(y,t)\} + \frac{\Gamma}{2}\cdot\frac{\partial}{\partial y}\left[D(y)\frac{\partial}{\partial y}\{D(y)P(y,t)\}\right] \tag{3.108}$$

Chapter 4 Fluctuations and Thermodynamics in Nonlinear Electrical Circuits

This chapter presents one of the main contributions of our work on statistical electronics, that is, fluctuations and thermodynamics in nonlinear electrical circuits.

4.1 Motivation

In the previous chapter, we reviewed the theory of thermal fluctuations in *linear* Brownian systems. The analytical examples were a Brownian particle immersed in liquid with a linear friction and a simple RC-circuit consisting of an ohmic resistor and a linear capacitor. The study of the thermal fluctuation in such linear systems was facilitated via Langevin or Fokker-Planck equations, which we could solve explicitly to describe the time evolution of the statistical averages or the probability distributions of the fluctuating quantities.

Let us recall the steady-state properties of the linear Brownian system discussed in the previous chapter. If there is no external energy pumping into the linear Brownian system via external force or bias current (*unforced Brownian motion*), the system ultimately reaches equilibrium steady-state, where the probability distribution of the fluctuating quantity, y, is given by the Boltzmann distribution:

$$P_0(y) \propto \exp\left[-\frac{E(y)}{k_B T}\right] \tag{4.1}$$

in which $E(y)$ is the energy stored in the associated energy storing element. For a linear energy storing element, the energy $E(y)$ normally takes a quadratic form in y, *i.e.*, $E(y) = Ay^2/2$ with a certain constant A. For instance, the energy of a linear capacitor, C, is given by $E(v) = Cv^2/2$ where v is the voltage across the capacitor. If the energy assumes the quadratic form, the mean fluctuation energy $\langle E(y)\rangle$ in equilibrium is $k_B T/2$, or $\langle y^2\rangle = k_B T/A$, as shown in (3.3) and (3.4), leading to the so-called equipartition theorem.

When energy is pumped into the linear Brownian system from an external source, such as an external force or a bias current (*forced Brownian motion*), the linear system will eventually reach nonequilibrium steady-state. In the previous chapter, using both mechanical Brownian motions and noisy RC-circuits, we have demonstrated that the Boltzmann distribution and the equipartition theorem are valid even in this nonequilibrium steady-state as far as the system is linear. These steady-state properties of the linear Brownian system are summarized in Table 4.1.

Brownian Motion	$y_0 \equiv \langle y \rangle$	Steady-State	Linear System		Nonlinear System	
			$P_0(y)$	$\langle E(y-y_0) \rangle$	$P_0(y)$	$\langle E(y-y_0) \rangle$
Unforced	$y_0 = 0$	Equilibrium	Boltzmann	$k_BT/2$	Boltzmann	$\neq k_BT/2$ in general
Forced	$y_0 \neq 0$	Nonequilibrium	Boltzmann	$k_BT/2$	non-Boltzmann	$\neq k_BT/2$ in general

Table 4.1: Probability distribution and mean fluctuation energy in linear and nonlinear Brownian systems in their steady-state. y is the fluctuating quantity, $P_0(y)$ is the steady-state probability distribution, and $E(y-y_0)$ is the fluctuation energy.

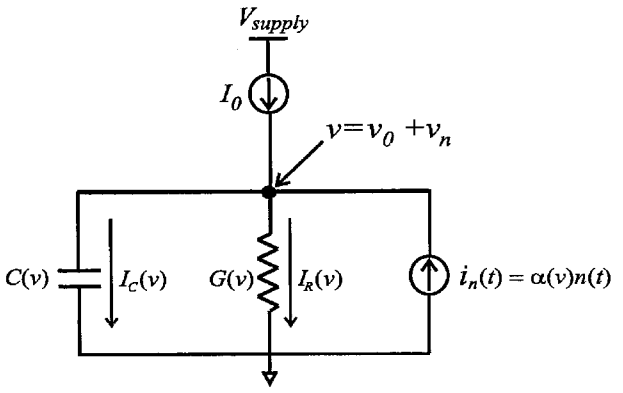

Figure 4.1: A general nonlinear RC-circuit consisting of a nonlinear resistor and a nonlinear capacitor. The circuit is coupled to an ideal current source generating a constant bias current of I_0.

Many circuits encountered in practical circuit design involve nonlinearity of various sorts. In our familiar example of the RC-circuit in Fig. 3.7(c) (unforced brownian system) or Fig. 3.11(c) (forced Brownian system), nonlinearity can be introduced by either replacing the linear capacitor with a nonlinear capacitor or replacing the linear resistor with a nonlinear resistor. Figure 4.1 illustrates a general nonlinear RC-circuit, which consists of a nonlinear resistor and a nonlinear capacitor. The circuit is coupled to an ideal current source generating a bias current of I_0.

The current through the nonlinear resistor, $I_R(v)$, varies nonlinearly with the voltage, v, across it and hence the incremental resistance, $R(v)$, or the incremental conductance, $G(v) = 1/R(v)$, defined as

$$G(v) = \frac{1}{R(v)} \equiv \frac{dI_R}{dv} \tag{4.2}$$

varies with v in general. Active devices are such nonlinear resistors. For instance, in a MOS transistor, the drain current depends nonlinearly upon the drain-source voltage for a given gate-source voltage. Figure 4.2 shows a hypothetical nonlinear current-voltage relation, which resembles the IV-curve of the MOS transistor.

The nonlinear capacitor in Fig. 4.1 accumulates electric charge, $q(v)$, which has a nonlinear dependence on the voltage, v, across the capacitor, as shown on the left-hand side of Fig. 4.3. The

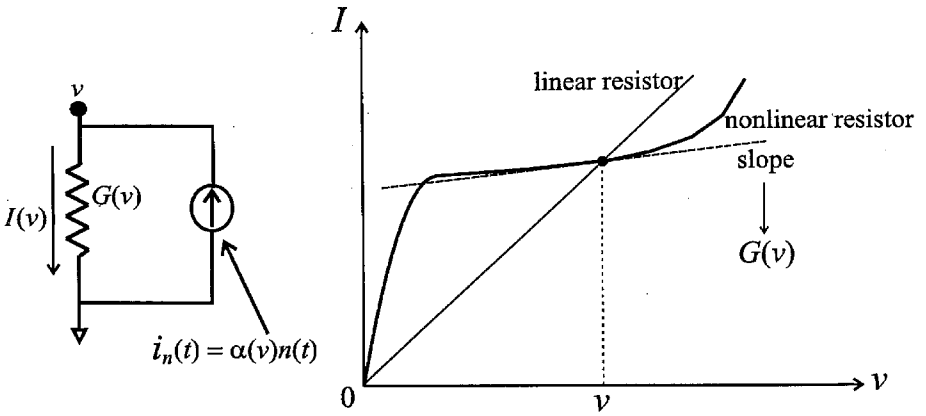

Figure 4.2: Nonlinear resistor and its conductance $G(v)$.

incremental capacitor, $C(v)$, defined as a derivative of the charge with respect to the voltage

$$C(v) = \frac{dq}{dv} \tag{4.3}$$

varies with v, in general. Typical examples of such nonlinear capacitors are capacitance of a reverse-biased junction diodes, MOS capacitors, etc. [46]. The current in the nonlinear capacitance is given by

$$I_C(t) = \frac{dq}{dt} = \frac{dv}{dt} \cdot \frac{dq}{dv} = C(v)\dot{v} \tag{4.4}$$

where we have used (4.3). The energy stored in the nonlinear capacitor is given by

$$E_C(v) = \int_0^q v(q)dq = \int_0^v C(v)vdv \tag{4.5}$$

where we have used (4.3) again. This energy stored in the capacitor corresponds to the shaded area in the q-v curve on the left-hand side of Fig. 4.3. The energy of the nonlinear capacitor does not assume the quadratic form in general, as will be seen later in Section 4.5.

As shown in Fig. 4.1, we assume that the nonlinear resistor generates white thermal current noise[1], $i_n(v;t)$, which is widely modeled as

$$i_n(v;t) = \alpha(v)n(t) \tag{4.6}$$

where $\alpha(v)$ is a deterministic function of the quiescent voltage, v, across the resistor, and is determined by the specific physical construction and property of the nonlinear resistor and $n(t)$ is

[1]Some nonlinear resistors such as MOS transistors generate thermal noise while other nonlinear resistors such as bipolar junction transistors generate noise of non-thermal origin, *e.g.*, shot noise.

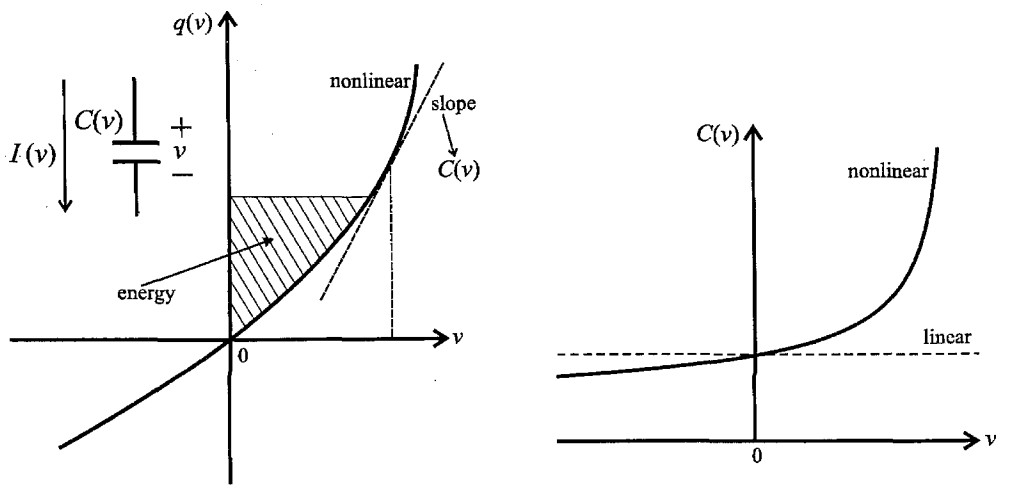

Figure 4.3: Nonlinear charge $q(v)$ and nonlinear capacitor $C(v)$ versus voltage v across the capacitor.

stationary white Gaussian whose mean is zero and double-side band (DSB) PSD is N, that is,

$$\begin{aligned} \langle n(t) \rangle &= 0 \\ \langle n(t')n(t'') \rangle &= N\delta(t'-t'') \quad \text{or} \quad \frac{\overline{n^2}}{\Delta f} = 2N \end{aligned} \tag{4.7}$$

For the linear case of the ohmic resistor, R, $\alpha(v)$ and N are simply

$$\begin{aligned} \alpha(v) &= 1 \\ N &= \frac{2k_B T}{R} \end{aligned} \tag{4.8}$$

The steady-state properties of the nonlinear RC-circuit in Fig. 4.1 are quite different from those of the linear RC-circuit discussed earlier. First, when the nonlinear circuit undergoes unforced Brownian motion in the absence of bias current ($I_0 = 0$), it eventually evolves to equilibrium steady-state, in which probability distributions are Boltzmann. This is because no matter if the Brownian system is linear or nonlinear, equilibrium probability distributions must be Boltzmann demanded by statistical physics [32]. However, the equipartition theorem does not necessarily hold true even in equilibrium if the energy storing element is nonlinear due to the nonquadratic form of the energy expression, as will be seen in Section 4.5.

Second, when the nonlinear RC-circuit of Fig. 4.1 experiences forced Brownian motion coupled with external bias current ($I_0 \neq 0$), it will reach nonequilibrium steady-state. In the nonequilibrium steady-state and in the presence of nonlinearity, the Boltzmann distribution and the equipartition theorem are not valid in general since the conditions under which the two properties hold true are not satisfied any more. The probability distribution and the mean energy cannot be determined unless

physical details of the nonlinear systems are known. The steady-state properties of the nonlinear Brownian system are also summarized in Table 4.1.

Fluctuations in nonlinear systems still remains a difficult subject and constitute an active field of research in many disciplines [19], [40]. The subject becomes particularly hard when the nonlinearity is introduced in the resistors and their corresponding fluctuations (that is, in the presence of the nonlinear resistor), involving several conceptual difficulties of a physical nature. For instance, there is much confusion and many unsettled disputes on the fluctuation-dissipation balance in nonlinear systems [40].

We will exemplify this difficulty in understanding fluctuations in nonlinear systems using a MOS transistor shown in Fig. 4.4(a) as a practical example of the nonlinear resistor: for a fixed gate-source voltage, the drain current varies nonlinearly with the drain-source voltage. The nonlinear resistance, r_{out}, depicted in Fig. 4.4(a) is commonly referred to as the output resistance and is defined as

$$\frac{1}{r_{out}} = \frac{\partial I_D}{\partial v_{ds}} \tag{4.9}$$

This $1/r_{out}$ is a special case of $G(v)$ defined in (4.2). The MOS transistor can operate in three different regimes, *i.e.*, off, pinch-off and triode regimes [46]. In the pinch-off regime, the drain current depends weakly on the drain-source voltage, and hence the output resistance, r_{out}, can be quite large. In the triode-regime, the MOS transistor behaves similarly to the ohmic resistor (but it still exhibits nonlinearity) and the output resistance, r_{out}, is often called channel resistance as it models the energy dissipation in the conductive channel of the MOS transistor.

Fig. 4.4(a) also shows a commonly used model for the channel thermal noise, $i_n(t)$, of the MOS transistor, whose power spectral density is given by [47], [48]

$$\frac{\overline{i_n^2}}{\Delta f} = 4k_B T \gamma g_{d0} \tag{4.10}$$

where g_{d0} is the channel conductance when the voltage difference between drain and source is zero, *i.e.*,

$$g_{d0} \equiv \frac{\partial I_D}{\partial v_{ds}}|_{v_{ds}=0} = \frac{1}{r_{out}}|_{v_{ds}=0} \tag{4.11}$$

and γ is a fitting parameter which varies with the bias conditions [47], [48]. Figure 4.4(a) shows γ versus v_{ds} for a fixed v_{gs} for both mobility-limited and velocity-saturated transistors. These two modes of operation are loosely called long and short channel regimes, respectively. The MOS channel thermal noise shown in (4.10) is *not* Johnson-Nyquist type (3.52) in the sense that the extra factor γ varies with the bias voltages.

This channel thermal noise model of the MOS transistor, (4.10), is a special case of the more general noise model for the nonlinear resistor given by (4.6) and (4.7), where $\alpha(v)$ and N in this

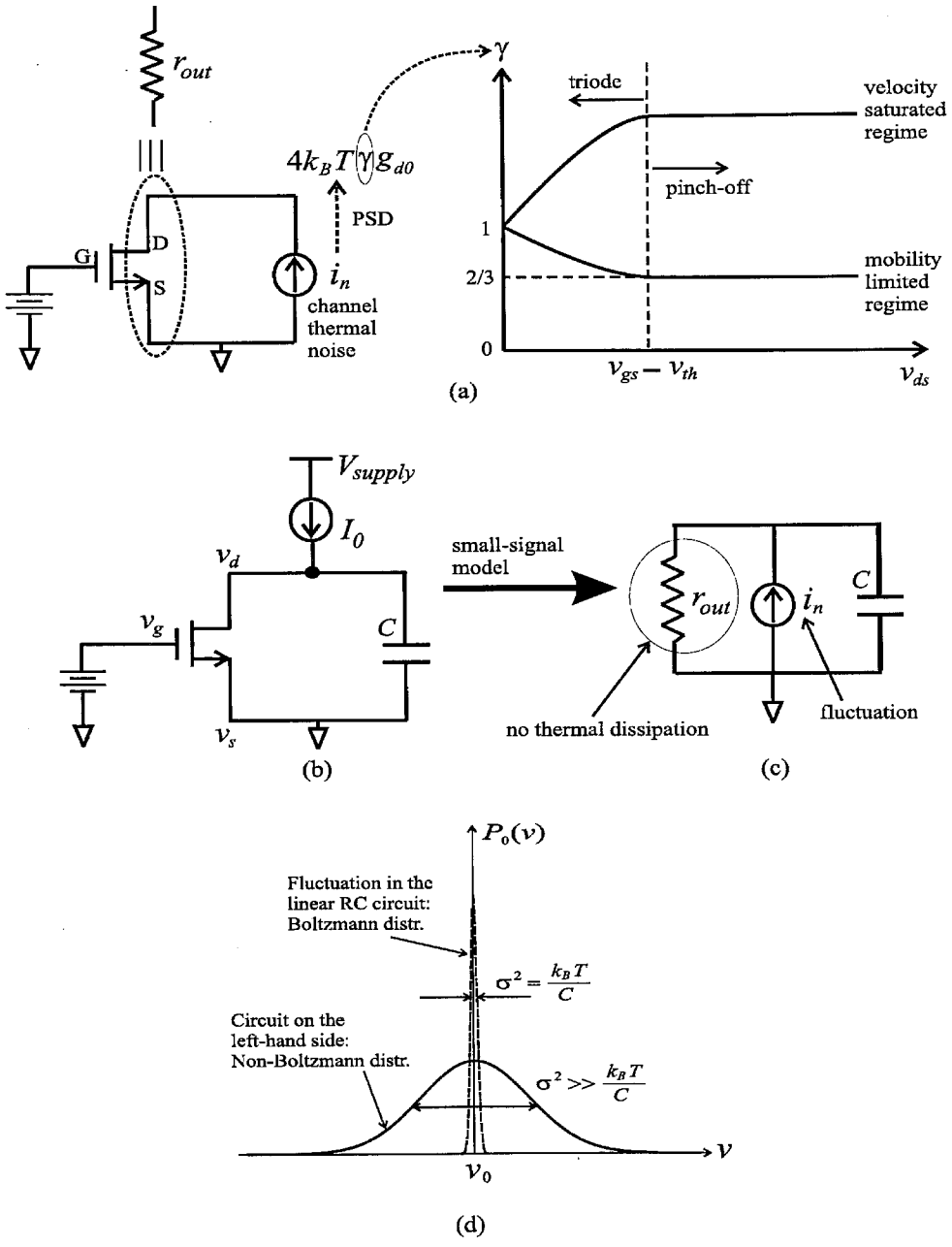

Figure 4.4: (a) A MOS transistor as a nonlinear resistor and its widely adopted channel thermal noise model. The fitting parameter γ in the noise PSD depends on the bias voltages and behaves differently between the short and long channel transistors. (b) A MOS transistor in parallel with an external capacitor is coupled to an ideal current source. (c) a small-signal model for the circuit in (b). (d) The capacitor in the circuit can store mean fluctuation energy much larger than $k_BT/2$.

special case are given by

$$\begin{aligned} \alpha(v) &= \sqrt{\gamma(v)} \\ N &= 2k_B T g_{d0} \end{aligned} \tag{4.12}$$

respectively, where the voltage, v, corresponds to the drain-source voltage for a given gate-source voltage.

Figure 4.4(b) depicts a MOS transistor with a fixed gate-source voltage, which is in parallel with an external capacitor, C, and is coupled to an ideal current source generating bias current of I_0. The equivalent small-signal circuit including the channel thermal noise is shown in Fig. 4.4(c), where, r_{out} is the output resistance of the transistor at the quiescent defined by (4.9). Now, a close look into the small-signal circuit from thermodynamics viewpoints results in several fundamental questions on the noise model for the MOS transistor:

1. Wyatt and Coram [49] recently made an effort to assess the physical validity of the white thermal noise model of nonlinear resistors given by (4.6) and (4.7) (*e.g.*, the MOS channel thermal noise given by (4.10)), based on laws of thermodynamics. Their study led them to a conclusion that the model does *not* meet the basic requirements of thermodynamics. Their analytical procedure that led to this conclusion is as follows.

   First, in the circuit of Fig. 4.4(b) and for $I_0 = 0$, establish a Fokker-Planck equation for the probability distribution of the voltage across the capacitor, by utilizing the channel thermal noise model given by (4.10). Second, the equilibrium probability distribution of the voltage across the capacitor must be Boltzmann demanded by statistical physics. Third, if one plugs the Boltzmann distribution into the Fokker-Planck equation, one can verify that the Boltzmann distribution is *not* the solution of the Fokker-Planck equation, hence leading to the conclusion that the nonlinear resistor noise model is flawed.

   This incompatibility between the Boltzmann distribution and the nonlinear resistor noise model in Wyatt and Coram's study, if true, presents a serious dilemma since the Boltzmann distribution in equilibrium is a fundamental fact of thermodynamics while the channel thermal noise model is firmly established through a direct measurement of the MOS transistor [47], [48].

2. Aside from the above study in the literature, thermodynamically inspired speculation based on the thermal fluctuation theory in Chapter 3 leads us to a fundamental question about the equivalent small-signal model including the channel thermal noise in Fig. 4.4(c).

   If the bias current I_0 in Fig. 4.4(b) is large enough to drive the MOS transistor into the pinch-off regime, the MOS transistor's output resistance, r_{out}, becomes a fictitious resistance in which no "thermal dissipation" occurs [46]. Even though there exist current through and voltage

across the resistor, the power dissipation in the resistor (multiplication of the voltage and the current) do not correspond to the thermal dissipation but it is conservatively used as "work" to change the kinetic energy of the electrons in the ballistic region of the MOS transistor via channel length modulation. This accounts for the fact that r_{out} does not generate any thermal noise [46]. Hence there does *not* exist any thermal dissipative element corresponding to the thermal noise, $i_n(t)$, in the small-signal circuit in Fig. 4.4(c). Then, how does the circuit achieve the balance between thermal fluctuation and thermal dissipation which we discussed in the previous chapter?

Physically speaking, there actually exists a thermal dissipative element in the circuit of Fig. 4.4(b), which is the transistor's channel, where the electrical energy is turned into heat and thus channel thermal noise is generated. However, this energy dissipation does not seem to be reflected in the small-signal model of Fig. 4.4(c) where we practically calculate all the physical noise processes.

3. In the linear RC-circuit of Fig. 3.7(c) or Fig. 3.11(c), we can use the equipartition theorem to derive the k_BT/C-noise in the capacitor, as discussed in the previous chapter. Alternatively, this k_BT/C-noise arises from the fact that the voltage thermal fluctuation, $4k_BTR$, and the resistance, R, originate from exactly the same physical origin. As R increases, the voltage noise intensity, $4k_BTR$, increases while the bandwidth, $1/(RC)$, decreases, hence keeping the mean-squared voltage across the capacitor at k_BT/C regardless of the resistance [50].

   However, in Fig. 4.4(c), r_{out} and i_n originate from completely different physical origins and hence the mean-squared voltage fluctuation across the capacitor in Fig. 4.4(c) can deviate far from k_BT/C. Indeed, a simple calculation leads to:

$$\begin{aligned}\langle(\Delta v)^2\rangle &= \int_{-\infty}^{\infty}\frac{d\omega}{2\pi}\overline{\frac{(\Delta v)^2}{\Delta f}} \\ &= 2k_BT\gamma g_{d0}\int_{-\infty}^{\infty}\frac{d\omega}{2\pi}\frac{r_{out}^2}{1+\omega^2C^2r_{out}^2} \\ &= \frac{k_BT}{C}\cdot\gamma g_{d0}r_{out} \qquad (4.13)\end{aligned}$$

   Here, the $\gamma g_{d0}r_{out}$ factor can be very large if I_0 is large enough to put the transistor in the pinch-off regime. In the long channel transistor, $g_{d0} = g_m$ where g_m is the transistor transconductance and hence $\gamma g_{do}r_{out} \sim g_m r_{out}$ is the intrinsic voltage gain of the MOS transistor in the common source arrangement loaded with an ideal current source as in Fig. 4.4(b). This gain in the long-channel transistor can be typically as large as several thousands and hence the mean-squared voltage fluctuation across the capacitor can be a few orders of magnitude larger than k_BT/C, or equivalently the mean thermal energy of the capacitor can be orders of magnitude

greater than $k_BT/2$. Figure 4.4(d) compares this non-Boltzmann distribution of the voltage across the capacitor to the Boltzmann distribution for the same capacitor. As can be seen, the non-Boltzmann distribution is much fatter and shorter than the Boltzmann distribution. Even though the mean energy does not have to be $k_BT/2$ as the equipartition theorem is not valid in this nonlinear nonequilibrium steady-state case as seen in Table 4.1, still how could the capacitor store such large thermal fluctuation energy?

To the best of our knowledge, these questions on the physical validity of the contemporary noise model for the nonlinear resistors have not been clearly addressed so far, which justifies our investigation of the fluctuations in nonlinear electrical circuits in this chapter. As the nonlinear noise models such as (4.10) are widely used in the electrical circuit design including our work, we need to confirm its physical soundness, negating the conclusions in [49]. Likewise, we need to address the issues on the fluctuation-dissipation balance in nonlinear resistors as well as the large mean thermal energy of the capacitor. A key to answering the last two questions is a study of energy flows in the nonlinear electrical circuits, as will be seen later.

4.2 Problem Formulation

The nonlinear RC-circuit in Fig. 4.1 will be the analysis vehicle in our study of fluctuations in nonlinear circuits in this chapter. The Langevin equation for the voltage, $v(t)$, across the capacitor is obtained using the KCL and KVL:

$$\dot{v} = \frac{I_0 - I_R(v)}{C(v)} + \frac{\alpha(v)}{C(v)} \cdot n(t) \tag{4.14}$$

where this Langevin equation falls into the category of type-V random process in Table 3.3. According to the table, the corresponding Fokker-Planck equation is given by

$$\frac{\partial}{\partial t}P(v,t) = \frac{\partial}{\partial v}\left[\frac{I_R(v) - I_0}{C(v)}P(v,t)\right] + \frac{N}{2}\frac{\partial^2}{\partial v^2}\left[\frac{\alpha^2(v)}{C^2(v)}P(v,t)\right] \tag{4.15}$$

If we define the probability fluxes $J(v,t)$ and $J_0(v,t)$ as

$$J(v,t) = \frac{I_R(v)}{C(v)}P(v,t) + \frac{N}{2}\frac{\partial}{\partial v}\left[\frac{\alpha^2(v)}{C^2(v)}P(v,t)\right] \tag{4.16}$$

$$J_0(v,t) = -\frac{I_0}{C(v)}P(v,t) \tag{4.17}$$

the Fokker-Planck equation (4.15) can be rewritten as a continuity equation:

$$\frac{\partial}{\partial t}P(v,t) = \frac{\partial}{\partial v}\{J_0(v,t) + J(v,t)\} \tag{4.18}$$

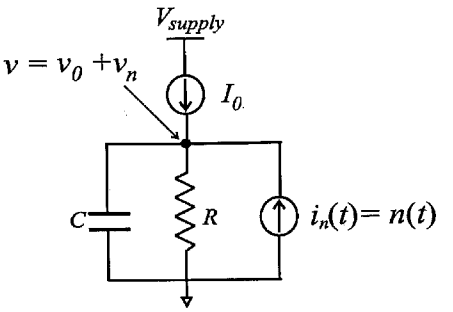

Figure 4.5: A linear RC-circuit.

Once the circuit reaches steady-state, the voltage $v(t)$ can be decomposed into its time-independent mean, $v_0 \equiv \langle v(t) \rangle$, and fluctuation, $v_n(t)$, around the mean voltage, that is,

$$v(t) = v_0 + v_n(t) \tag{4.19}$$

The mean voltage v_0 is determined by the bias condition, *i.e.*,

$$I_0 = I_R(v_0) \tag{4.20}$$

We will consider three different cases in the following sections. In Section 4.3, we study the special case where the resistor and the capacitor in Fig. 4.1 are both linear. Even though we have already discussed this linear circuit in the previous chapter, we will reconsider it in this section with special attention to its energetics. The energetics concepts we develop here prove to be very insightful and will be helpful in understanding nonlinear fluctuations in the following section. In Section 4.4, we consider the case where the resistor is nonlinear and the capacitor is linear in Fig. 4.1. An example of such nonlinear circuit is already presented in Fig. 4.4(b). This section constitutes the most important body of this chapter, and addresses all the questions raised in Section 4.1. Section 4.5 investigates the nonlinear circuit in Fig. 4.1 with a nonlinear capacitor and a linear resistor, mainly focusing on how the nonlinear capacitor modifies the equipartition property.

4.3 Fluctuations in Linear RC-Circuits, Revisited

In this section, we will study the special case where both G and C in Fig. 4.1 are independent of voltage. This linear case is redrawn in Fig. 4.5 for convenience. The ohmic resistor, R, generates Johnson noise, and hence $\alpha(v) = 1$ and $N = 2k_BT/R$ according to (4.8). In this linear case, the

Langevin equation (4.14) and the Fokker-Planck equation (4.15) will simplify to

$$\dot{v} = \frac{v_0 - v}{RC} + \frac{n(t)}{C} \tag{4.21}$$

$$\frac{\partial}{\partial t}P(v,t) = \frac{\partial}{\partial v}\left[\frac{v - v_0}{RC}P(v,t)\right] + \frac{k_B T}{RC^2}\frac{\partial^2}{\partial v^2}P(v,t) \tag{4.22}$$

respectively, where $v_0 = I_0/R$ according to the bias condition (4.20) and $n(t) = i_n(t)$ in (4.6) as $\alpha(v) = 1$. The probability fluxes in (4.16) and (4.17) are also simplified to

$$J(v,t) = \frac{v}{RC}P(v,t) + \frac{k_B T}{RC^2}\frac{\partial}{\partial v}P(v,t) \tag{4.23}$$

$$J_0(v,t) = -\frac{v_0}{RC}P(v,t) \tag{4.24}$$

The Fokker-Planck equation (4.22) will be extremely useful in evaluating energy flows and entropy evolution in the circuit, as can be seen in the following two subsections.

4.3.1 Energetics

This subsection studies energy flows in the linear RC-circuit. The rate of the mean energy increase in the capacitor per unit time is given by

$$\begin{aligned}\frac{d}{dt}\langle E_C(t)\rangle &= \frac{1}{2}C\int_{-\infty}^{\infty} v^2\frac{\partial P}{\partial t}dt \\ &= \frac{1}{2}C\int_{-\infty}^{\infty} v^2\frac{\partial}{\partial v}\{J_0(v,t) + J(v,t)\}dv\end{aligned} \tag{4.25}$$

where we have used the continuity equation in (4.18). Integrating by parts and assuming that the probability density rapidly decays to zero with $v \to \pm\infty$, we obtain

$$\frac{d}{dt}\langle E_C(t)\rangle = -C\int_{-\infty}^{\infty} v\{J_0(v,t) + J(v,t)\}dv \tag{4.26}$$

Using (4.23) and (4.24) here and noting that $\langle v(t)\rangle = v_0$, $\langle v^2(t)\rangle = \langle (v_0 + v_n(t))^2\rangle = v_0^2 + \langle v_n^2(t)\rangle$, we obtain

$$\begin{aligned}\frac{d}{dt}\langle E_C(t)\rangle &= -C\left[-\frac{v_0\langle v\rangle}{RC} + \frac{\langle v^2\rangle}{RC} + \frac{k_B T}{RC^2}\int_{-\infty}^{\infty} v\frac{\partial}{\partial v}P(v,t)dv\right] \\ &= \frac{v_0\langle v\rangle}{R} - \frac{\langle v^2\rangle}{R} + \frac{k_B T}{RC}\int_{-\infty}^{\infty} P(v,t)dv \\ &= -\frac{\langle v_n^2(t)\rangle}{R} - \frac{k_B T}{RC}\end{aligned} \tag{4.27}$$

where we integrated by parts to obtain the second line and used $\int_{-\infty}^{\infty} P(v,t)dv = 1$.

The mean power dissipation in the resistor is given by

$$\begin{aligned} \langle P_R(t)\rangle &= \frac{\langle v^2(t)\rangle}{R} \\ &= \frac{v_0^2}{R} + \frac{\langle v_n^2(t)\rangle}{R} \end{aligned} \tag{4.28}$$

Here the first and the second terms correspond to the dc power dissipation due to I_0 and the dissipation of the fluctuation energy, respectively.

The mean energy input per unit time from the fluctuation and the current source to the circuit is given by

$$\begin{aligned} \frac{d}{dt}\langle E_{in}(t)\rangle &= I_0\langle v(t)\rangle + \langle n(t)v(t)\rangle \\ &= I_0 v_0 + \langle n(t)v_n(t)\rangle \\ &= \frac{v_0^2}{R} + \frac{k_B T}{RC} \end{aligned} \tag{4.29}$$

where $\langle n(t)v_n(t)\rangle = k_B T/(RC)$ was obtained from the Langevin equation (4.21) using the stochastic methods introduced in Subsection 3.1.2.

Now combining (4.27), (4.28), and (4.29), we notice that

$$\frac{d}{dt}\langle E_{in}(t)\rangle = \frac{d}{dt}\langle E_C(t)\rangle + \langle P_R(t)\rangle \tag{4.30}$$

which is the demonstration of the energy conservation, or the first law of thermodynamics. In words, the mean input energy, $\langle E_{in}\rangle$, to the system coming from the thermal bath in the form of fluctuation and the current source will either increase the mean energy of the capacitor, $\langle E_C\rangle$, or result in the mean power dissipation, $\langle P_R(t)\rangle$, in the resistor.

According to the conservation of energy, the *net heat flux*, Q_{net}, per unit time from the RC-circuit to the thermal bath is given by the dc power dissipation due to I_0 in the resistor minus the mean energy increase in the capacitor per unit time, *i.e.*,

$$\begin{aligned} \frac{d}{dt}Q_{net}(t) &= I_0 v_0 - \frac{d}{dt}\langle E_C(t)\rangle \\ &= \underbrace{\frac{v_0^2}{R} + \frac{\langle v_n^2(t)\rangle}{R}}_{\langle P_R(t)\rangle} - \frac{k_B T}{RC} \end{aligned} \tag{4.31}$$

where we have used (4.27). The first and second terms on the right-hand side represent heat dissipation per unit time in the resistor due to I_0 and fluctuations, respectively. These two terms constitute $\langle P_R(t)\rangle$ as can be seen from (4.28), that is, the heat flux from the circuit to the thermal bath through the resistor per unit time. The third term on the right-hand side of (4.31) represents

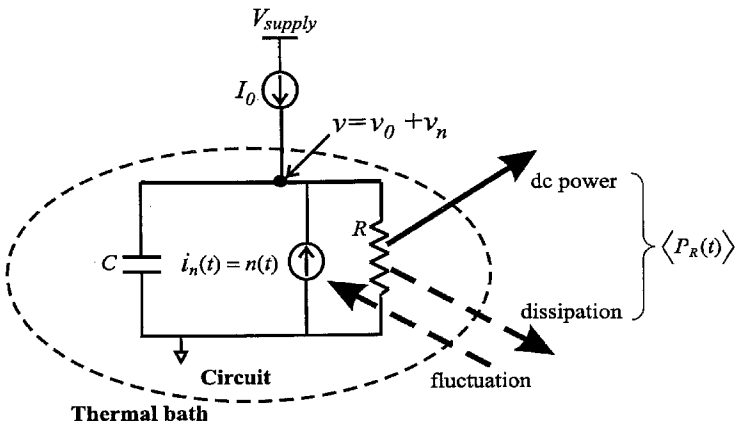

Figure 4.6: Energetics in the linear RC-circuit. In the steady-state, the dissipation of the fluctuation energy in the resistor and the heat flux from the thermal bath to the circuit via fluctuation cancel each other out.

the heat flux from the thermal bath to the circuit in the form of thermal fluctuations per unit time. These heat flows are illustrated in Fig. 4.6.

In the steady-state, the fluctuation in-flux (the third term) and the dissipation out-flux (the second term) must balance each other out and hence we have

$$\langle v_n^2 \rangle = \frac{k_B T}{C} \tag{4.32}$$

which is in complete agreement with the equipartition theorem. The net heat flux from the circuit to the thermal bath per unit time in the steady-state is then $I_0 v_0$. As mentioned earlier, due to this constant net heat flux in the steady-state, the system never achieves thermal equilibrium unless $I_0 = 0$. This notion of nonequilibrium steady-state has been mentioned several times so far, but in rather qualitative fashion. In the following section, we will discuss the entropy evolution in the linear RC-circuit, also quantitatively demonstrating the nonequilibrium steady-state.

4.3.2 Entropy Evolution

This subsection discusses the time-evolution of the entropy in the linear RC-circuit of Fig. 4.5. In the case of $I_0 = 0$, the entropy evolution for the linear circuit has been analytically worked out in [49]. Our calculation in this subsection is the generalization of the work in [49] for an arbitrary bias current, I_0.

The entropy of the RC-circuit can be expressed as

$$S_{RC} = -k_B \int_{-\infty}^{\infty} P(v,t) \ln P(v,t) dv \tag{4.33}$$

where $P(v,t)$ is the probability distribution of the voltage across the capacitor. This is the definition

of entropy in statistical physics [32], [51] and also the same definition is used in information theory [4]. This statistically defined entropy is identical to the thermodynamically defined entropy [32], which will be used to evaluate the entropy increase in the thermal bath, shortly. The instantaneous change of the entropy of the RC-circuit per unit time is

$$\begin{aligned}\frac{d}{dt}S_{RC}(t) &= -k_B\int_{-\infty}^{\infty}\frac{\partial}{\partial t}P(v,t)\ln P(v,t)dv - k_B\frac{\partial}{\partial t}\int_{-\infty}^{\infty}P(v,t)dv \\ &= -k_B\int_{-\infty}^{\infty}\frac{\partial}{\partial v}\{J(v,t)+J_0(v,t)\}\ln P(v,t)dv \\ &= k_B\int_{-\infty}^{\infty}\{J(v,t)+J_0(v,t)\}\frac{1}{P(v,t)}\frac{\partial}{\partial v}P(v,t)dv \\ &= k_B\int_{-\infty}^{\infty}J(v,t)\frac{1}{P(v,t)}\frac{\partial}{\partial v}P(v,t)dv \end{aligned} \tag{4.34}$$

where we have used the continuity equation (4.18) to obtain the second line while we integrated by parts to obtain the third line.

On the other hand, the entropy change in the thermal bath is, by definition in thermodynamics, the net heat flux into the thermal bath from the RC-circuit divided by the temperature of the thermal bath [32]:

$$\frac{d}{dt}S_{bath}(t) \equiv \frac{1}{T}\frac{d}{dt}Q_{net}(t) \tag{4.35}$$

Using (4.31) here, we obtain

$$\begin{aligned}\frac{d}{dt}S_{bath}(t) &= \frac{I_0v_0}{T} - \frac{1}{T}\frac{d}{dt}\langle E_C(t)\rangle \\ &= \frac{C}{T}\int_{-\infty}^{\infty}vJ(v,t)dv \end{aligned} \tag{4.36}$$

where we have used (4.26) to derive the second line.

Since the total entropy, S_{total}, of the whole system consisting of the RC-circuit and the thermal bath is the sum of the entropies of the RC-circuit and the thermal bath, namely,

$$S_{total} = S_{RC} + S_{bath} \tag{4.37}$$

the change in the total entropy per unit time can be calculated using (4.34) and (4.36):

$$\begin{aligned}\frac{d}{dt}S_{total}(t) &= \int_{-\infty}^{\infty}J(\frac{C}{T}v + \frac{k_B}{P}\frac{\partial}{\partial v}P) \\ &= \int_{-\infty}^{\infty}dv\frac{RC^2}{T}\cdot\frac{1}{P}\cdot\left[\frac{v}{RC}P + \frac{k_BT}{RC^2}\frac{\partial}{\partial v}P\right]^2 \geq 0 \end{aligned} \tag{4.38}$$

As the time-derivative of the total entropy is non-negative, the total entropy never decreases

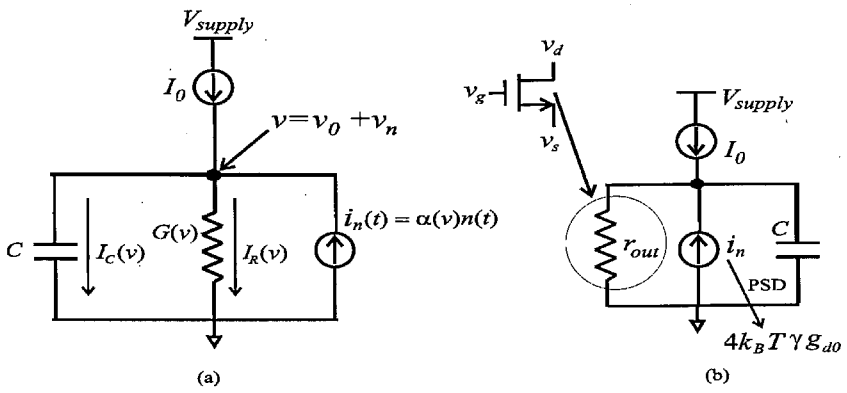

Figure 4.7: (a) A nonlinear RC-circuit with a nonlinear resistor and a linear capacitor. (b) An example of such nonlinear circuit: A MOS transistor in parallel with a linear capacitor. For a fixed gate-source voltage, the MOS transistor acts as a nonlinear resistor.

with time evolution, in agreement with the second-law of thermodynamics. Once a system reaches thermal equilibrium, the total entropy of the system reaches its maximum and stays constant at the maximum value [32]. Hence, the equality in (4.38) is satisfied in equilibrium. This notion can serve as a criterion in determining if a system reached equilibrium or not in its steady-state.

Let us see how this works in the linear RC-circuit. The steady-state solution of the Fokker-Planck equation (4.22) is given by the familiar Boltzmann distribution:

$$P_0(v) \propto \exp\left[-\frac{C(v-v_0)^2}{2k_BT}\right] \tag{4.39}$$

Plugging this steady-state solution into (4.38), one obtains

$$\frac{d}{dt}S_{total} = \frac{I_0 v_0}{T} \qquad \text{[in steady-state]} \tag{4.40}$$

For $I_0 = 0$, $(d/dt)S_{total} = 0$ in steady-state and hence the total entropy does not change any more, implying that the system reached thermal equilibrium in steady-state. For $I_0 > 0$, the total entropy grows without bound even in steady-state according to (4.40) and hence the system never reaches thermal equilibrium. This is a quantitative demonstration of the nonequilibrium steady-state for $I_0 > 0$ (forced Brownian motion).

4.4 Fluctuations in RC-Circuits with Nonlinear Resistors

This section investigates the circuit of Fig. 4.1 with a nonlinear resistor and a linear capacitor, as redrawn in Fig. 4.7(a). This section represents the most important contribution of the work presented in this chapter, and addresses all the questions raised in Section 4.1. An example of

such nonlinear circuit has been already shown in Fig. 4.4(b), which is redrawn in Fig. 4.7(b) for convenience. In this example, a MOS transistor is in parallel with a linear capacitor. For a fixed gate-source voltage, the MOS transistor acts as a nonlinear resistor in which the drain current depends nonlinearly on the drain-source voltage.

The Langevin equation for the voltage, v, across the capacitor in Fig. 4.7(a) is obtained by replacing $C(v)$ with C in (4.14):

$$\dot{v} = \frac{I_0 - I_R(v)}{C} + \frac{\alpha(v)}{C} \cdot n(t) \tag{4.41}$$

Similarly, the Fokker-Planck equation for the probability distribution of v can be obtained from (4.15) to be:

$$\frac{\partial}{\partial t} P(v,t) = \frac{\partial}{\partial v}\left[\frac{I_R(v) - I_0}{C} P(v,t)\right] + \frac{N}{2C^2}\frac{\partial^2}{\partial v^2}\{\alpha^2(v) P(v,t)\} \tag{4.42}$$

The operation bias voltage, v_0, is determined by the bias condition:

$$I_0 = I_R(v_0) \tag{4.43}$$

Now utilizing these equations, we will discuss steady-state properties, energetics, fluctuation-dissipation relations, and entropy evolution in the nonlinear circuit in the following subsections. We will address all the questions raised in Section 4.1 along the way.

4.4.1 Steady-State Properties

The steady-state probability distribution, $P_0(v)$, of v is obtained by solving the Fokker-Planck equation (4.42), while setting its left-hand side to zero and $P(v,t)$ to $P_0(v)$:

$$\frac{2C}{N}\{I_R(v) - I_0\} P_0(v) + \frac{d}{dv}\{\alpha^2(v) P_0(v)\} = 0 \tag{4.44}$$

Equilibrium Steady-State

Let us first discuss the case of $I_0 = 0$, where the system attains the equilibrium steady-state. In this case, the solution of (4.44) for $I_0 = 0$ should be the Boltzmann distribution, as required by statistical physics. However, in [49], Wyatt and Coram showed that the Boltzmann distribution cannot satisfy (4.44) for $I_0 = 0$ and hence the widely accepted noise modeling for the nonlinear resistor (4.6) (*e.g.* MOS transistor's channel thermal noise) used in constructing the Fokker-Planck equation (4.42) is flawed. Indeed, we can explicitly obtain the solution of (4.44) for $I_0 = 0$, which does not follow Boltzmann distribution:

$$P_0(v) \propto \frac{1}{\alpha^2(v)} \cdot \exp\left[-\int \frac{2C I_R(v)}{N\alpha^2(v)} dv\right] \neq \exp\left[-\frac{Cv^2}{2k_B T}\right] \tag{4.45}$$

This consideration seems to present a serious dilemma as emphasized in [49]. On one hand, we must have the Boltzmann distribution as the equilibrium probability density. On the other hand, we have experimentally verified noise models for nonlinear resistors such as MOS transistors' channel thermal noise, which can be modeled as (4.6). And these two facts are seemingly incompatible! This dilemma was raised as the first question in Section 4.1.

However, this paradox can be resolved by closely examining the underlying assumptions of the nonlinear resistor noise model, $i(v;t) = \alpha(v)n(t)$, in (4.6). If fluctuation, $n(t)$, is large, the voltage, v, in $\alpha(v)$ fluctuates by a significant amount due to the large fluctuation, and hence determining $\alpha(v)$ becomes a meaningless task as $\alpha(v)$ itself is a random process. However, in all the practical noise measurements which led to the nonlinear resistor noise model [47], [48], $\alpha(v)$ is always assumed as a fixed value where the dc bias voltage across the nonlinear resistor, v_0, is used as v (in the case of $I_0 = 0$, $v_0 = 0$). This is because the fluctuations are already assumed to be very small: Mathematically speaking, if the fluctuations are small, we have

$$\begin{aligned} \alpha(v) \cdot n(t) &\approx \alpha(v_0) \cdot n(t) + \alpha'(v_0)\Delta v \cdot n(t) \\ &\approx \alpha(v_0) \cdot n(t) \end{aligned} \tag{4.46}$$

where Δv is the fluctuation of the voltage v due to $n(t)$ around the quiescent v_0. In the above calculation, we neglected $\Delta v \cdot n(t)$ as both Δv and $n(t)$ are very small, hence leading to $\alpha(v) \approx \alpha(v_0)$.

Since the nonlinear resistor noise model in (4.6) was derived with this *a priori* assumption that fluctuations are very small, solving (4.44) with the "unapproximated" $\alpha(v)$ and $I_R(v)$, which take into account their dependence upon v all across the possible range of v, only causes approximation inconsistency, leading to a wrong result. The work in [49] led to the dilemma for this reason. In order to stay consistent, before solving (4.44), we should take approximations for $\alpha(v)$ and $I_R(v)$ using Taylor expansion, assuming small fluctuations.

Now we will solve (4.44) using this small-fluctuation approximation. For small fluctuations, we can take the following approximation for $I_R(v)$ in (4.44) (for $I_0 = 0$, $v_0 = 0$ and $v = v_0 - v_n = v_n \ll 1$):

$$I_R(v) \approx G(0) \cdot v + \cdots \tag{4.47}$$

where $G(v)$ is defined in (4.2). Also, we replace $\alpha^2(v)$ with $\alpha^2(0)$ in (4.44) according to (4.46). Then, the differential equation (4.44) for $I_0 = 0$ is approximated as

$$\frac{2C}{N} \cdot \frac{G(0)}{\alpha^2(0)} \cdot vP_0(v) + \frac{d}{dv}P_0(v) = 0 \tag{4.48}$$

whose solution is

$$P_0(v) \propto \exp\left[-\frac{2k_BTG(0)}{N\alpha^2(0)} \cdot \frac{Cv^2}{2k_BT}\right] \tag{4.49}$$

In Fig. 4.7(b) in which the MOS transistor in the triode-regime ($I_0 = 0$) is the nonlinear resistor, $\gamma(v = 0) = \alpha^2(v = 0) = 1$ [47], [48], $G(0) = g_{d0}$ according to (4.2) and (4.11), and $N = 2k_BTg_{d0}$ as shown in (4.12) and hence (4.49) is no more than a Boltzmann distribution, now in complete agreement with the equilibrium statistical physics.

More generally, (4.49) should be Boltzmann distribution demanded by statistical physics and therefore, the following criterion to assess physical validity of the nonlinear resistor's thermal noise model (4.6) is established:

$$\frac{2k_BTG(0)}{N\alpha^2(0)} = 1 \tag{4.50}$$

Then, for $I_0 = v_0 = 0$, the PSD of the thermal noise (4.6) for a nonlinear resistor is given by

$$\frac{\overline{i_n^2}}{\Delta f}|_{I_0=v_0=0} = 2N\alpha^2(0) = 4k_BTG(0) \tag{4.51}$$

where we have used (4.7) and (4.50). This equation (4.51) means that any given nonlinear resistor must behave like an ohmic resistor producing the Nyquist noise for $I_0 = v_0 = 0$ as far as the resistor generates thermal noise.

Nonequilibrium Steady-State

In the presence of the bias current in the nonlinear circuit of Fig. 4.7(a), *i.e.*, for $I_0 \neq 0$, the system will attain nonequilibrium steady-state in the long run and hence the steady-state probability distribution of v is not Boltzmann in general, as shown in Table 4.1. Again using the small-fluctuation approximation, we obtain

$$I_R(v) \approx I_0 + G(v_0) \cdot (v - v_0) + \cdots \tag{4.52}$$

$$\frac{\partial}{\partial v}\{\alpha^2(v)P_0(v)\} \approx \alpha^2(v_0)\frac{\partial}{\partial v}P_0(v) \tag{4.53}$$

which simplify (4.44) to

$$\frac{2C}{N} \cdot \frac{G(v_0)}{\alpha^2(v_0)} \cdot (v - v_0)P_0(v) + \frac{d}{dv}P_0(v) = 0 \tag{4.54}$$

The solution of this equation is

$$P_0(v) \propto \exp\left[-\frac{2k_BTG(v_0)}{N\alpha^2(v_0)} \cdot \frac{C(v - v_0)^2}{2k_BT}\right] \tag{4.55}$$

As pointed out earlier, this is not the Boltzmann distribution or, $2k_BTG(v_0) \neq N\alpha^2(v_0)$ in general. This distribution results in the following mean-squared voltage fluctuation across the capacitor:

$$\langle (v - v_0)^2 \rangle = \frac{k_BT}{C} \cdot \frac{N\alpha^2(v_0)}{2k_BTG(v_0)} \tag{4.56}$$

For example, in Fig. 4.7(b) using the MOS transistor as a nonlinear resistor, $N\alpha^2(v_0) = 2k_BT\gamma g_{d0}$ and $G(v_0) = 1/r_{out}$ by definition, simplifying (4.56) to

$$\langle (v - v_0)^2 \rangle = \frac{k_BT}{C} \cdot \gamma g_{d0} r_{out} \tag{4.57}$$

which is in complete agreement with (4.13) obtained using a small-signal model. As already mentioned in Section 4.1, this variance can be orders of magnitude larger than k_BT/C in the pinch-off regime as shown in Fig. 4.4(d). How could the capacitor in parallel with the nonlinear resistor store mean thermal energy so much larger than $k_BT/2$? This is the third question raised in Section 4.1. Additionally, another question in the context of the MOS transistor circuit in Fig. 4.7(b) is how the circuit balances fluctuation and dissipation as r_{out} physically does not correspond to thermal dissipation as discussed in Section 4.1. Then where is the thermal dissipative element corresponding to the channel thermal noise? This is the second question raised in Section 4.1.

Now, we will address these questions, by closely investigating the energetics of the system.

4.4.2 Energetics

We will again hire the small-fluctuation approximation in dealing with the Fokker-Planck equation (4.42). By using the approximations (4.52) and (4.53) in (4.42), we obtain

$$\frac{\partial}{\partial t}P(v,t) = \frac{\partial}{\partial v}\left[\frac{G(v_0)\cdot(v - v_0)}{C}P(v,t)\right] + \frac{N}{2C^2}\alpha^2(v_0)\frac{\partial^2}{\partial v^2}P(v,t) \tag{4.58}$$

The probability fluxes $J(v,t)$ and $J_0(v,t)$ in (4.16) and (4.17) are then also simplified to

$$J(v,t) = \frac{G(v_0)\cdot v}{C}P(v,t) + \frac{N}{2C^2}\alpha^2(v_0)\frac{\partial}{\partial v}P(v,t) \tag{4.59}$$

$$J_0(v,t) = -\frac{G(v_0)\cdot v_0}{C}P(v,t) \tag{4.60}$$

Now, using the same technique used in Subsection 4.3.1, one can show from (4.58) that the mean energy increase in the capacitor per unit time is given by

$$\frac{d}{dt}\langle E_C(t)\rangle = -G(v_0)\cdot\langle v_n^2\rangle + \frac{N}{2C}\alpha^2(v_0) \tag{4.61}$$

Similarly, using the same technique hired in Subsection 4.3.1, one can show that the mean power

dissipation in the nonlinear resistor is given by

$$\langle P_R(t)\rangle = \langle I(v)\cdot v\rangle = I_0 v_0 + G(v_0)\cdot\langle v_n^2\rangle \tag{4.62}$$

Here, the first and the second terms correspond to the dc power dissipation due to I_0 and the effective thermal dissipation of the fluctuation energy, respectively. Even though $G(v_0)$ is a fictitious conductance in which no physical thermal dissipation occurs in general (*e.g.*, in the MOS transistor, $1/G(v_0) = r_{out}$.) as mentioned earlier, it basically controls the number of electrons flowing into the *nonlinear resistor in which real thermal dissipation occurs* (*e.g.*, in the MOS transistor, the thermal dissipation occurs in the conductive channel) and hence $G(v_0)$ in *any* nonlinear resistor *effectively* represents the thermal dissipation inside the nonlinear resistor, and hence *mathematically* serves as a thermal dissipative element. If $G(v_0)$ is smaller, the number of fluctuating electrons flowing into the nonlinear resistor becomes smaller, reducing the effective thermal dissipation as the second term of (4.62) clearly suggests. This observation will play a key role in addressing the fluctuation-dissipation issue in the nonlinear circuit as will be seen shortly.

The mean energy input per unit time from the thermal bath (in the form of fluctuations) and the bias current to the circuit is given by

$$\frac{d}{dt}\langle E_{in}(t)\rangle = \langle (I_0 + i_n(t))v\rangle = I_0 v_0 + \frac{N}{2C}\alpha^2(v_0) \tag{4.63}$$

Combining (4.61), (4.62), and (4.63) leads to the conservation of energy (first law of thermodynamics):

$$\frac{d}{dt}E_{in}(t) = P_R(t) + \frac{d}{dt}E_C(t) \tag{4.64}$$

As discussed in Subsection 4.3.1, the net heat flux, Q_{net}, per unit time from the circuit to the thermal bath is calculated by subtracting the mean capacitor energy increase per unit time from the dc power dissipation due to I_0 in the resistor:

$$\begin{aligned}\frac{d}{dt}Q_{net} &= I_0 v_0 - \frac{d}{dt}E_C(t)\\ &= \underbrace{I_0 v_0 + G(v_0)\cdot\langle v_n^2\rangle}_{\langle P_R(t)\rangle} - \frac{N}{2C}\alpha^2(v_0)\end{aligned} \tag{4.65}$$

where we have used (4.61). As can be seen, the net heat flux from the circuit to the thermal bath is the heat flux from the circuit to the thermal bath through the resistor (the first and second terms constituting $\langle P_R(t)\rangle$) minus the heat flux from the thermal bath to the circuit via thermal fluctuations (the third term). As mentioned earlier, the second term corresponds to the effective thermal dissipation of the fluctuation energy in the incremental conductance $G(v_0)$. It is important

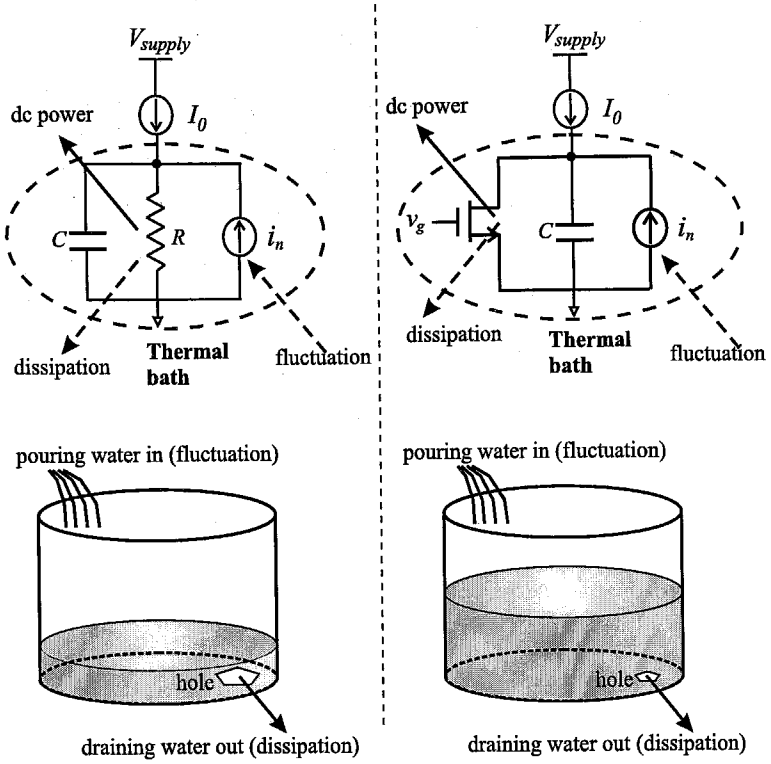

Figure 4.8: Analogy using the tank with a hole.

to emphasize once again that even if $G(v_0)$ *per se* is not a physical thermal dissipative element in general, it effectively serves as a thermal dissipative element for the fluctuation energy as it controls the number of fluctuating electrons flowing into the real thermal dissipative part of the nonlinear resistor.

Previously, we raised a question on how the fluctuation-dissipation balance is achieved in the circuit of Fig. 4.7(a) with a specific example of the MOS transistor circuit of Fig. 4.7(b). The question seemed hard to answer as we thought that $G(v)$ (or $1/r_{out}$ for the MOS transistor) was a fictitious conductance in which no thermal dissipation occurs. But as observed in this subsection, the conductance $G(v)$ is *effectively* a thermal dissipative element for the fluctuation energy and this is exactly how the fluctuation-dissipation balance is achieved in this nonlinear case. In the steady-state, the net heat flux per unit time from the circuit to the thermal bath is $I_0 v_0$ in (4.65) due to the fluctuation-dissipation balance, which sets the second and third terms in (4.65) equal. This fluctuation-dissipation balance leads to the following steady-state mean-squared voltage fluctuation across the capacitor:

$$\langle v_n^2 \rangle = \frac{N}{2C} \cdot \frac{\alpha^2(v_0)}{G(v_0)} \tag{4.66}$$

which is in complete agreement with (4.56).

As already discussed a few times before, (4.66) in the case of the MOS transistor circuit of Fig.

4.7(b) becomes

$$\langle v_n^2 \rangle = \frac{k_B T}{C} \cdot \gamma g_{d0} r_{out} \tag{4.67}$$

which can be much larger than the equipartition value, $k_B T/C$. Now we will provide a physical explanation on how the capacitor can store much larger thermal energy than $k_B T/2$.

The mean-squared voltage, $\langle v_n^2 \rangle$, in (4.66) was obtained using the principle of the fluctuation-dissipation balance, or by setting the second and third terms equal to each other in (4.65). Hence, for the given amount of fluctuation energy in-flux from the thermal bath to the circuit, $\langle v_n^2 \rangle$ is essentially determined by the conductance $G(v_0)$ as can be seen in (4.65). For a given fluctuation energy, if $G(v_0)$ is smaller, $\langle v_n^2 \rangle$ should be larger in order to keep the dissipation $G(v_0) \cdot \langle v_n^2 \rangle$ the same as the fluctuation energy. Hence, if $G(v_0)$ is very small which is the typical case for transistor operations, $\langle v_n^2 \rangle$ becomes very large. Therefore, the very large thermal energy stored in the capacitor in (4.67) is actually the result of the very fluctuation-dissipation balance.

In more physical terms, $G(v_0)$ controls the number of electrons flowing into the nonlinear resistor where the real thermal dissipation occurs. For a given amount of fluctuation energy in-flux, if $G(v_0)$ is small, the capacitor will have to accumulate a larger number of electrons (hence larger $\langle v_n^2 \rangle$) until the number of electrons escaping from the capacitor (via dissipation) becomes equal to the number of electrons getting stored in the capacitor (via fluctuation). An insightful analogy of this concept using a water tank with a hole is illustrated in Fig. 4.8. Water is being poured in the tank at a constant rate. The tank has a hole at the bottom which drains water in the tank while the drain rate is proportional to the height of water as well as the size of the hole. Now, when the hole becomes smaller, the tank will have to store more water until the rates for water in and out become equal. In this analogy, the tank corresponds to the capacitor, water in and out corresponds to fluctuation and dissipation, and the size of the hole corresponds to the conductance, $G(v_0)$. The height of water corresponds to $\langle v_n^2 \rangle$ of the capacitor.

In this subsection, by carefully investigating the energetics of the nonlinear circuit, we were able to address the second and third questions raised in Section 4.1. The nonlinear conductance $G(v_0)$ *effectively* serves as a thermal dissipative element for fluctuations even when it does not physically correspond to thermal dissipation in general, and the exact balance between thermal fluctuation and its effective thermal dissipation through $G(v)$ was the key to understanding the fluctuations in the circuit with the nonlinear resistor. A nonlinear resistor with smaller $G(v)$ (*e.g.*, transistors) increases the mean thermal energy stored in the capacitor to a significant degree from $k_B T/2$ due to the fluctuation-dissipation balance.

4.4.3 Entropy Evolution

This subsection considers the entropy evolution of the nonlinear circuit in Fig. 4.7(a). The calculation technique is essentially the same as in Subsection 4.3.2. The entropy of the nonlinear-circuit can be expressed as [32], [51]

$$S_{circuit} = -k_B \int_{-\infty}^{\infty} P(v,t) \ln P(v,t) dv \tag{4.68}$$

Using the same technique in Subsection 4.3.2, the change of the entropy of the circuit per unit time can be shown to be

$$\frac{d}{dt} S_{circuit}(t) = k_B \int_{-\infty}^{\infty} J(v,t) \frac{1}{P(v,t)} \frac{\partial}{\partial v} P(v,t) dv \tag{4.69}$$

On the other hand, the change of the entropy in the thermal bath is, by definition, the net heat flux into the thermal bath from the circuit divided by the temperature of the thermal bath [32]:

$$\frac{d}{dt} S_{bath}(t) \equiv \frac{1}{T} \frac{d}{dt} Q_{net}(t) \tag{4.70}$$

Using (4.65) in the above equation, we obtain

$$\begin{aligned} \frac{d}{dt} S_{bath}(t) &= \frac{I_0 v_0}{T} - \frac{1}{T} \frac{d}{dt} E_C(t) \\ &= \frac{C}{T} \int_{-\infty}^{\infty} v J(v,t) dv \end{aligned} \tag{4.71}$$

Since the total entropy, S_{total}, of the whole system consisting of the circuit and the thermal bath is the sum of $S_{circuit}$ and S_{bath}, using (4.69) and (4.71), we obtain

$$\begin{aligned} \frac{d}{dt} S_{total}(t) &= \int_{-\infty}^{\infty} J\left(\frac{C}{T} v + \frac{k_B}{P} \frac{\partial}{\partial v} P\right) \\ &= \int_{-\infty}^{\infty} dv \frac{N\alpha^2(v_0)}{2C^2} \cdot \frac{k_B}{P} \cdot \left[\frac{C}{k_B T} vP + \frac{\partial}{\partial v} P\right] \cdot \left[\frac{2CG(v_0)}{N\alpha^2(v_0)} vP + \frac{\partial}{\partial v} P\right] \end{aligned} \tag{4.72}$$

Now if one plugs the steady-state probability density (4.55) into the equation above, one obtains

$$\frac{d}{dt} S_{total} = \frac{I_0 v_0}{T} \qquad \text{[in steady-state]} \tag{4.73}$$

For $I_0 = 0$, the entropy of the whole system does not change with time in the steady-state, implying that the system is in thermal equilibrium. For $I_0 \neq 0$, the system is never in thermal equilibrium in the steady-state as the total entropy indefinitely increases. Again, this is the notion of nonequilibrium steady-state expressed quantitatively.

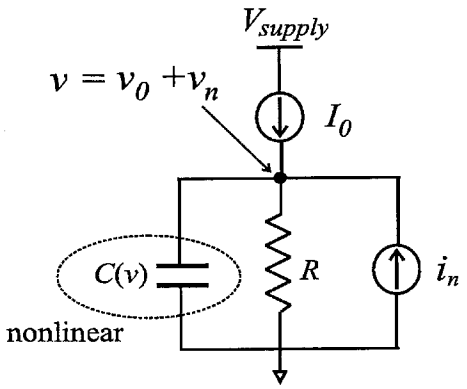

Figure 4.9: A nonlinear capacitor in parallel with an ohmic resistor. The circuit is coupled with a current source generating bias current I_0.

4.5 Fluctuations in RC-Circuits with Nonlinear Capacitors

In this section, we will consider the circuit of Fig. 4.1 with a nonlinear capacitor and a linear resistor, which is redrawn in Fig. 4.9. The energetics and entropy evolution of the system can be studied similarly to the previous sections. However, in this section, we will focus on how the nonlinearity in the capacitor affects the energy equipartition property.

The Fokker-Planck equation for the probability density of the voltage, v, across the capacitor in Fig. 4.9 is obtained from (4.15) by replacing $I_R(v) = v/R$, $I_0 = v_0/R$, $N = 2k_BT/R$ and $\alpha^2(v) = 1$:

$$\frac{\partial}{\partial t}P(v,t) = \frac{\partial}{\partial v}\left[\frac{v - v_0}{RC(v)}P(v,t)\right] - \frac{k_BT}{R}\frac{\partial^2}{\partial v^2}\left[\frac{1}{C^2(v)}P(v,t)\right] \tag{4.74}$$

Again using the small-fluctuation approximation and hence assuming that the steady-state distribution, $P_0(v)$, is a very narrow distribution in the above equation, we obtain the following differential equation for $P_0(v)$:

$$\frac{C(v)}{k_BT}(v - v_0)P_0(v) - \frac{d}{dv}P_0(v) = 0 \tag{4.75}$$

whose solution is no more than the Boltzmann distribution:

$$P_0(v) \propto \exp\left[-\frac{1}{k_BT}\int C(v)(v - v_0)dv\right] = \exp\left[-\frac{E_C(v - v_0)}{k_BT}\right] \tag{4.76}$$

where we have used (4.5). Now, we will consider the case of $I_0 = 0$ for simplicity and will evaluate the mean energy stored in the nonlinear capacitor for different types of nonlinear capacitors.

First, let us consider the case where the nonlinear capacitor has the following voltage-dependence

$$C(v) = av^{2n} \tag{4.77}$$

where $n = 1, 2, 3, \cdots$. The charge stored in the capacitor then has the following voltage-dependence:

$$Q(v) = \frac{a}{2n+1} v^{2n+1} \tag{4.78}$$

while the energy stored in the capacitor is given by

$$E_C(v) = \frac{a}{2n+2} v^{2n+2} \tag{4.79}$$

where we have used (4.5). Then, the mean energy stored in the capacitor can be calculated using the Boltzmann distribution (4.76) as in the following

$$\langle E_C \rangle = \int_{-\infty}^{\infty} E_C(v) \exp\left[\frac{-E_C(v)}{k_B T}\right] dv \Big/ \int_{-\infty}^{\infty} \exp\left[\frac{-E_C(v)}{k_B T}\right] dv \tag{4.80}$$

where the denominator is only the normalization factor. Now the numerator of (4.80) is given by

$$\begin{aligned}
[\text{numerator}] &= \int_{-\infty}^{\infty} \frac{a}{2n+2} v^{2n+2} \cdot \exp\left[-\frac{a}{(2n+2)k_B T} v^{2n+2}\right] dv \\
&= k_B T \left(\frac{2n+2}{a} k_B T\right)^{\frac{1}{2n+2}} \int_{-\infty}^{\infty} x^{2n+2} e^{-x^{2n+2}} dx \\
&= -k_B T \left(\frac{2n+2}{a} k_B T\right)^{\frac{1}{2n+2}} \cdot \frac{\partial}{\partial \lambda} \int_{-\infty}^{\infty} e^{-\lambda x^{2n+2}} dx \,|_{\lambda=1} \\
&= -k_B T \left(\frac{2n+2}{a} k_B T\right)^{\frac{1}{2n+2}} \cdot \frac{\partial}{\partial \lambda} \lambda^{-1/(2n+2)}|_{\lambda=1} \int_{-\infty}^{\infty} e^{-y^{2n+2}} dy \\
&= \frac{k_B T}{2n+2} \left(\frac{2n+2}{a} k_B T\right)^{\frac{1}{2n+2}} \int_{-\infty}^{\infty} e^{-y^{2n+2}} dy
\end{aligned} \tag{4.81}$$

where we used the transformation of variable, $x^{2n+2} = a\{(2n+2)k_B T\}^{-1} v^{2n+2}$ in the second equation, and $y^{2n+2} = \lambda x^{2n+2}$ in the fourth equation. Similarly, we can calculate the denominator of (4.80) as in the following

$$\begin{aligned}
[\text{denominator}] &= \int_{-\infty}^{\infty} \exp\left[-\frac{a}{(2n+2)k_B T} v^{2n+2}\right] dv \\
&= \left(\frac{2n+2}{a} k_B T\right)^{\frac{1}{2n+2}} \int_{-\infty}^{\infty} e^{-x^{2n+2}} dx
\end{aligned} \tag{4.82}$$

where we have used the transformation of variable, $x^{2n+2} = a\{(2n+2)k_B T\}^{-1} v^{2n+2}$. Combining (4.80), (4.81) and (4.82), we obtain

$$\langle E_C \rangle = \frac{k_B T}{2n+2} \tag{4.83}$$

For $n = 0$, which corresponds to a linear capacitor, $\langle E_C \rangle = k_B T/2$ in complete agreement with the equipartition theorem. For $n \neq 0$, the mean thermal energy of the capacitor is always less

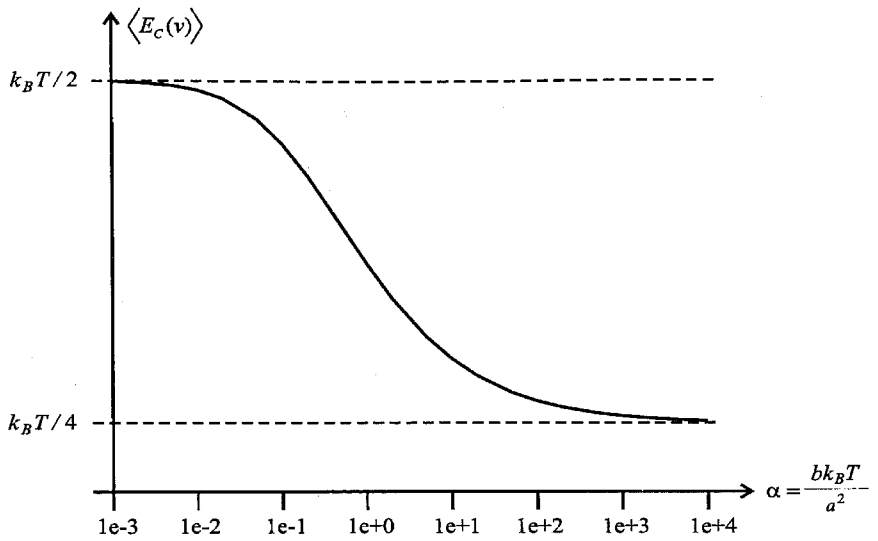

Figure 4.10: Mean thermal energy stored in a nonlinear capacitor, depending upon the nonlinearity.

than the equipartition value, $k_BT/2$. In other words, the nonlinearity in the capacitor reduces its mean thermal energy from the equipartition value of $k_BT/2$. The stronger the nonlinearity in the capacitor, the smaller the mean thermal energy stored in the capacitor. This is opposite the case of the nonlinear resistor in parallel with a linear capacitor, where the mean thermal energy of the capacitor was increased through the nonlinearity of the resistor as shown in the previous section.

Now, let us consider a capacitor with more complex nonlinearity. We will use the following example:

$$C(v) = a + bv^2 \tag{4.84}$$

The energy stored in the capacitor is then given by

$$E_C(v) = \frac{1}{2}av^2 + \frac{1}{4}bv^4 \tag{4.85}$$

according to (4.5). Now by using (4.80) and (4.85) and with some manipulation, we obtain

$$\langle E_C \rangle = k_BT \times \frac{\int_{-\infty}^{\infty}(y^2 - \alpha y^4)e^{-(y^2+\alpha y^4)}dy}{\int_{-\infty}^{\infty} e^{-(y^2+\alpha y^4)}dy} \tag{4.86}$$

where $\alpha \equiv (b/a^2) \cdot k_BT$. Here, α is an indicator of the degree of the nonlinearity: If b is larger, α is larger and vice versa. Now, Fig. 4.10 shows $\langle E_C \rangle$ versus α. When α is small and nonlinearity is not large, the mean thermal energy stays at the equipartition value of $k_BT/2$. As the nonlinearity increases with an increasing α, the mean thermal energy approaches $k_BT/4$. However, k_BT is a very small number and hence practically, α is very small and the thermal mean energy *almost always* stays close to $k_BT/2$, unless the constant term in the $C(v)$ expansion vanishes in (4.84).

Summarizing, nonlinearity in a capacitor tends to decrease the mean thermal energy stored in the capacitor from the equipartition value $k_B T/2$. However in most practical cases where the nonlinear capacitance is expanded as in $C(v) \approx C_0 + \cdots$ and $C_0 \neq 0$, this mean thermal energy reduction effect is typically negligible. If $C(v)$ expansion starts with a higher order term as in (4.77) (which is unusual in reality), the reduction effect can be appreciable.

4.6 Summary

This chapter presented one of the main contributions of our work on fluctuations in nonlinear electrical circuits. The subject studied in this chapter is divided into two categories, that is, (1) fluctuations in the presence of nonlinear resistors such as transistors, and (2) fluctuations in the presence of nonlinear energy storing elements such as nonlinear capacitors.

First, in the category (1), we verified the physical validity of the widely used white thermal noise model for nonlinear resistors such as channel thermal noise of MOS transistors. With this verification, we will be able to use the widely accepted white thermal noise model for nonlinear resistors in the following chapters on mixers and oscillators. Conceptual difficulties in understanding the subject of fluctuations in nonlinear resistors were overcome by rigorous investigation of the energetics in the circuit including the nonlinear resistors, leading to a tangible understanding of nonlinear fluctuation-dissipation balance. The study illuminated the underlying mechanism with which the nonlinear resistors dump much more mean thermal fluctuation energy into a linear capacitor than the equipartition value of $k_B T/2$.

Second, in the category (2), we demonstrated that the mean thermal fluctuation energy stored in the nonlinear capacitors in parallel with a linear resistor becomes smaller than $k_B T/2$ but in most of the practical cases, not by a perceptible margin.

Chapter 5 Noise in Time-Varying Driven Circuits

5.1 Introduction

Earlier in Chapters 1 and 2, it was mentioned that the noise evolution involved in the frequency donwconversion in the RF signal detection is quite complicated, resulting in difficulties in low-noise design of mixers which execute the frequency downconversion. Mixers can be classified into a broader circuit category called *time-varying driven circuits*. As shown in Fig. 5.1, mixers are "time-varying" due to the periodic local oscillator (LO) signal and are "driven" by the RF signal. In this chapter, utilizing the fluctuation theory introduced in Chapter 3, we develop general concepts and methods to understand, describe, and predict the noise in such time-varying driven circuits and hence, this chapter constitutes one of the main contributions of our work on statistical electronics [52], [53]. While special focus in this chapter will lie on the mixers in the RF detecting/receiving systems for the sake of concreteness, this theoretical framework is general and can be applied to various other types of time-varying driven systems.

Generic time-varying driven circuits are schematically shown in Fig. 5.2. The essential elements of the time-varying driven circuits are switches, which turn on and off periodically by the cyclic signal generated by the local oscillator. While the cyclic switching is a key function of any time-varying driven circuit, the signal amplification in Fig. 5.2 is not necessarily needed and can be opted for depending upon the design issues under consideration. The difference between the two circuits in Fig. 5.2(a) and (b) is merely the order of the signal amplification and the switching, and hence is of no fundamental importance.

As can be seen from Fig. 5.2, time-varying driven circuits are in general three-terminal systems where one terminal is used to receive the input signal, another terminal provides the periodic LO or clock signal into the system to commute the signal periodically, and the last terminal provides

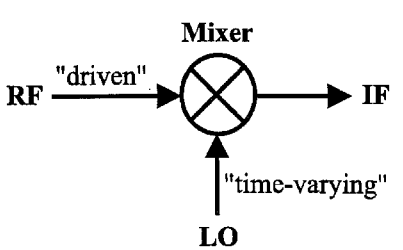

Figure 5.1: Mixer as a time-varying driven circuit.

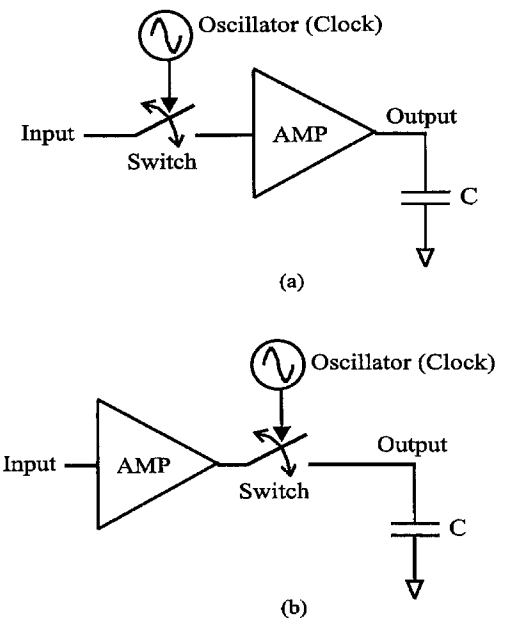

Figure 5.2: Generic time-varying driven circuits.

the output signal. Typically, however, the time-varying driven circuits are treated as if they were two-terminal systems with the input and output terminals while the LO signal is considered as an inherent part of the circuit. The time-varying driven circuits are linear systems when viewed from the input terminals but nonlinear systems when viewed from the LO terminals [8].

Time-varying driven circuits are frequently found in various electrical engineering systems. Specific examples of the time-varying driven circuits are passive and active mixers used in the RF signal detection for frequency downconversion and sample-and-holds (SH) in data conversion systems. For the mixer, the ratio of the fundamental LO frequency to the fundamental frequency of the input (RF) signal is typically close to 1. Among the two functions shown in Fig. 5.2, passive mixers, also known as switching mixers whose simple example is depicted in Fig. 5.3(a), only utilize the switching functions while active mixers, whose example is illustrated in Fig. 5.3(b), incorporate both switchings and signal amplification. For the SH with an oversampling rate, the ratio of the fundamental clock (or LO) frequency to the fundamental frequency of the input signal is much larger than 1.

Noise in the time-varying driven circuits often plays a crucial role in low-noise design of many engineering systems. For instance, as shown in Fig. 2.1, the mixer at the receiver front-end can be a considerable noise contributor. Hence a firm understanding of noise processes in the time-varying driven circuits, as well as accurate and effective prediction of noise is crucial in the design and optimization of many systems encountered in engineering design.

The noise problem in the time-varying driven circuits is very complicated for various reasons.

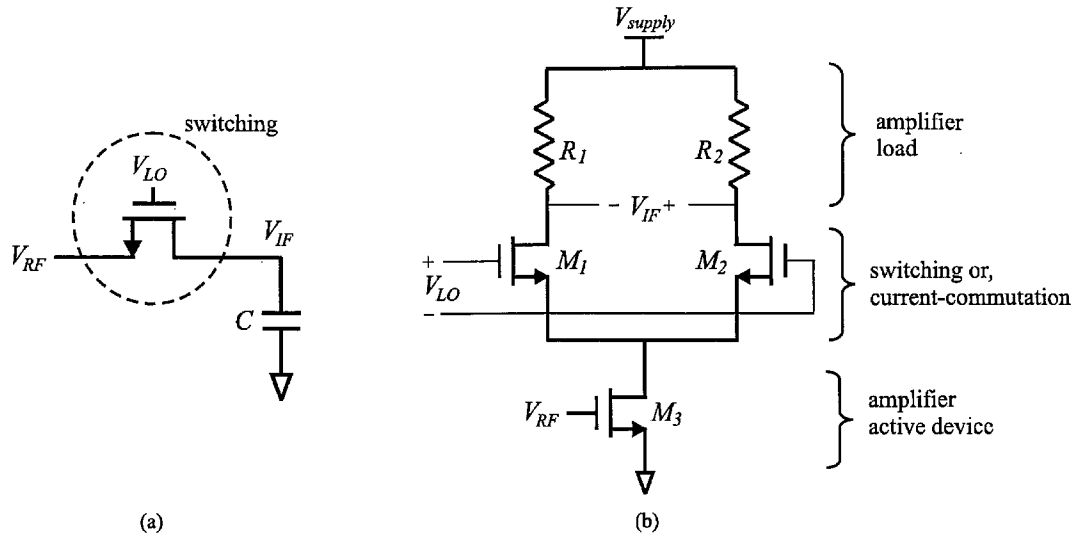

Figure 5.3: (a) Simple passive mixer; (b) Active mixer.

First, in the case of an up- or down-conversion mixer, the noise components at ω_{IF} above and below the integer multiples of ω_{LO} will be downconverted to the IF band and will be folded together there during the frequency downconversion process, as shown in Fig. 5.4. Second, the operating points of the active devices in the time-varying driven circuits periodically change due to the periodic LO drive, which introduces strong time variations in the circuit. Third, due to the same periodic operating point change, the noise generated from the active devices in the circuit is periodically modulated in time, resulting in the so-called *cyclostationary noise*, which makes the noise processes in the circuit even more involved. Finally, energy storing elements such as capacitors present in the time-varying driven circuits tend to "color" white noise.

Recent research efforts towards accurate and effective noise prediction in time-varying driven circuits have led to several simulation-based approaches [54]-[57]. Although these simulation methods constitute essential components of computer-aided design (CAD) tools, they normally involve complex mathematical expressions and hardly provide hands-on intuition to cope with the noise problem in practical design of time-varying driven circuits.

Efforts to understand noise in the time-varying driven circuits on a more intuitive basis have resulted in a few analytical methods [58] - [60], but a clear explanation of the interaction between cyclostationary noise and energy storing elements is still lacking. In [58], cyclostationary noise is considered ignoring the energy storage effects while [59] calculating the circuit noise in the presence of capacitors, but neglecting the cyclostationary noise. The work in [60] brings insight into the physical mechanism for $1/f$ and white noise process in active mixers but it also does not cover the interaction between cyclostationarity and energy storing elements. As will be seen in this chapter,

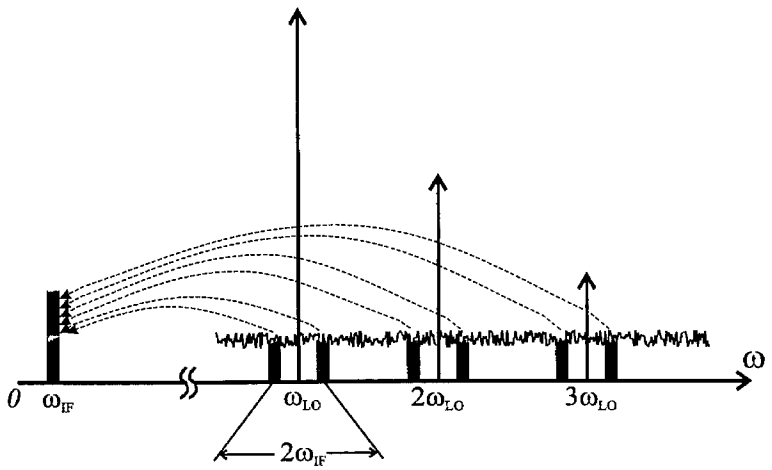

Figure 5.4: Noise translation and folding.

in reality, however, manifestation of cyclostationary noise is significantly affected by energy storing elements, as shown later, and hence the existing approaches provide rather limited design insights.

In this chapter, we present extensive theoretical and experimental study of noise in time-varying driven circuits in the presence of energy storing elements. This investigation utilizes certain methods and concepts of the physical fluctuation theory introduced in Chapter 3 as key analysis tools. Especially the Langevin equation proves to be extremely useful in handling the noise problems in the time-varying driven circuits. Our theoretical framework is general and can be applied to various types of time-varying driven circuits. In this chapter, however, we will study noise in time-varying driven circuits using switching mixers as a specific analysis vehicle. This concrete switching mixer example will put our general theory on noise in time-varying driven circuits in a practical perspective, demonstrating how the fundamental approach can benefit practical circuit design.

Our study will demonstrate that switching mixers in the presence of energy storage components act essentially as *time-varying filters* in which the bandwidth is a periodic function of time. Establishment of *the theory of time-varying filtering* in this chapter in conjunction with the physical fluctuation theory discussed in Chapter 3 leads to an important observation on the switching mixer noise that has remained unknown to this date to our best knowledge: The time-varying filtering of cyclostationary noise in switching mixers results in two different noise generation regimes, *quasi-stationary* and *cyclostationary regime*, depending upon the size of the energy storing elements. Remarkably, in the cyclostationary regime, mixer noise figure is seriously degraded due to the cyclostationarity. Equally importantly, the time-varying filtering theory applied to the deterministic dynamics in switching mixers leads to a so far unknown observation of a conversion gain enhancement for small enough energy storing elements. Both noise figure degradation and conversion gain enhancement in switching mixers are positively verified through a direct measurement of switching

mixers. These two novel results provide an immediate insight into the optimum design of switching mixers.

The organization of this chapter is as follows: Section 5.2 is a review of the cyclostationary noise, which will play an important role in the stochastic dynamics of switching mixers. In Section 5.3, we review the linear time-invariant (LTI) filtering of cyclostationary noise. Section 5.4 introduces a switching mixer as a specific example of the proposed analysis technique and explain its basic operational principles. In Sections 5.5 and 5.6, we investigate the time-varying filtering of signal and cyclostationary noise in switching mixers, respectively, and hence these sections constitute one of the most important sectors of this chapter. In Section 5.7, we present the numerical simulation results. Finally, Section 5.8 verifies the theoretical prediction of Sections 5.5, 5.6 and 5.7 through a direct measurement of integrated switching mixers. The measurements indeed demonstrate the novel behavior of switching mixers, *i.e.*, noise figure degradation due to the cyclostationary noise and conversion gain enhancement.

5.2 Cyclostationary Noise Fundamentals

Cyclostationary noise is a random process whose statistical properties vary cyclically with time [61]. In the time domain, a cyclostationary noise, $n_p(t)$, can be modeled as the product of a stationary random process, $n(t)$, and a deterministic periodic function, $p(t)$, *i.e.*,

$$n_p(t) = n(t)p(t) \tag{5.1}$$

Here, the stationary random process, $n(t)$, can be either white or colored. Due to the periodic modulation by $p(t)$, statistical quantities describing the cyclostationary noise such as mean, variance, and power spectral density (PSD) are also periodic in time in general: a key signature of the cyclostationary noise.

Nature finds many examples of the cyclostationary random process. The temperature of a certain region on Earth is a cyclostationary random process where the periodicity arises from seasons. The radition intensity from a pulsar is another example of the cyclostationary noise where the periodicity is due to the rotation of the pulsar.

In electrical circuits, the cyclostationary noise is observed in time-varying driven circuits such as samplers and mixers and in time-varying autonomous circuits such as oscillators which will be discussed in Chapter 6[1]. Since operating points of active devices in the time-varying circuits change periodically with time, the otherwise stationary noise of the active devices is modulated cyclically, as in (5.1) and exhibits cyclostationarity.

[1]For a general introduction to the cyclostationary noise in electrical circuits, refer to [62]. The work in [63] shows how the cyclostationary noise can be exploited in the design of oscillators.

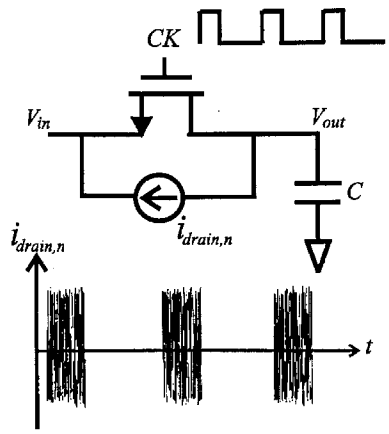

Figure 5.5: MOS sample-and-hold and cyclostationary noise.

For instance, let us consider the MOS sample-and-hold shown in Fig. 5.5. In the channel thermal noise given by (4.10) in the previous chapter [47], both the noise coefficient γ and the channel conductance g_{d0} at $V_{ds} = 0$ are bias-dependent and hence the periodic clock signal which modulates the gate voltage of the MOS transistor will result in the cyclic channel thermal noise PSD:

$$\frac{\overline{i^2_{drain,n}}}{\Delta f} = 4k_B T\gamma(t)g_{d0}(t) \tag{5.2}$$

Fig. 5.5 shows the corresponding hypothetical cyclostationary channel thermal noise in the time domain.

We now calculate the autocorrelation and power spectral density (PSD) of the cyclostationary noise, $n_p(t) = n(t)p(t)$, given in (5.1). If $n(t)$ is white noise, *i.e.*, $\langle n(t_1)n(t_2)\rangle = N\delta(t_1 - t_2)$ or more conventionally put, $\overline{n^2/\Delta f} = 2N$, the autocorrelation function of the cyclostationary noise, $n_p(t)$, is given by

$$\begin{aligned} R_{n_p,n_p}(t_1,t_2) &= \langle n(t_1)n(t_2)\rangle p(t_1)p(t_2) \\ &= N\delta(t_1 - t_2)p^2(t_1) \\ &\equiv R_{n_p,n_p}(\tau;t) \end{aligned} \tag{5.3}$$

where $\tau \equiv t_1 - t_2$ and $t \equiv t_1$. As can be seen, the autocorrelation function is not only a function of the measurement time difference, τ, but also a cyclic function of the absolute measurement time, t.

Evaluating the power spectral density (PSD) of the cyclostationary noise, $n_p(t)$, is a subtle task since in the most rigorous terms, it is not valid to use the Wiener-Khintchen theorem [33] and take the Fourier transform of the autocorrelation in (5.3) in order to obtain the PSD for the cyclostationary random process. This is because the Wiener-Khintchen theorem is originally derived

for the stationary random processes [33].

Putting aside the mathematical definition of PSD for the cyclostationary noise for a while, let us first consider the PSD of $n_p(t)$ which we will get if we "measured" the cyclostationary noise using conventional noise measurement systems such as spectrum analyzers and noise figure meters. Signal processing in the conventional measurement systems is shown in Fig. 5.6. The input signal to the system is truncated over each measurement period T and then filtered by a bandpass filter whose bandwidth is much smaller than the center frequency of the bandpass filter. The output of the band-pass filter is sent to the built-in power meter. This procedure is repeated many times to obtain an estimate of the ensemble average, which then is divided by the truncation time, T. The entire procedure is perfectly captured in the measurement-oriented definition of PSD for an arbitrary random process $x(t)$ [65]:

$$\begin{aligned} S_{x,measured}(f) &\equiv \lim_{T\to\infty} \frac{1}{T}\langle |X_T(f)|^2 \rangle \\ &= \lim_{T\to\infty} \frac{1}{T} \int_0^T \int_0^T dt_1 dt_2 R_{x,x}(t_1,t_2) e^{j2\pi f(t_1-t_2)} \end{aligned} \tag{5.4}$$

where

$$X_T(f) \equiv \int_0^T x(t) e^{j2\pi f t} dt \tag{5.5}$$

Now using $x(t) = n_p(t) = n(t)p(t)$ and the autocorrelation of $n_p(t)$ in (5.3) assuming that $n(t)$ is white noise, we can simplify (5.4) to

$$\begin{aligned} S_{n_p,measured}(f) &= \lim_{T\to\infty} N \cdot \frac{1}{T} \int_0^T p^2(t) \\ &= N \cdot \overline{p^2(t)} \end{aligned} \tag{5.6}$$

where the overline signifies the time-average over a period of the periodic function, $p^2(t)$. In other words, when $n(t)$ is white noise, the measured power spectral density of the cyclostationary noise, $n_p(t) = n(t)p(t)$, is equal to the product of the PSD of $n(t)$ and mean-squared value of the noise modulating function, $p(t)$.

Now, even though the Wiener-Khintchin theorem is valid only for the stationary random processes in the most rigorous sense, we will *define* an *operational PSD* of the cyclostationary noise, $n_p(t)$, as the Fourier transform of the autocorrelation of $n_p(t)$:

$$S_{n_p}(f;t) \equiv \int_{-\infty}^{\infty} e^{j2\pi f\tau} R_{n_p,n_p}(\tau;t) d\tau \tag{5.7}$$

Later we will see how this operational PSD of the cyclostationary noise is related to the measured PSD, $S_{n_p,measured}(f)$. When $n(t)$ in $n_p(t) = n(t)p(t)$ is white noise, by using (5.3) in (5.7), we

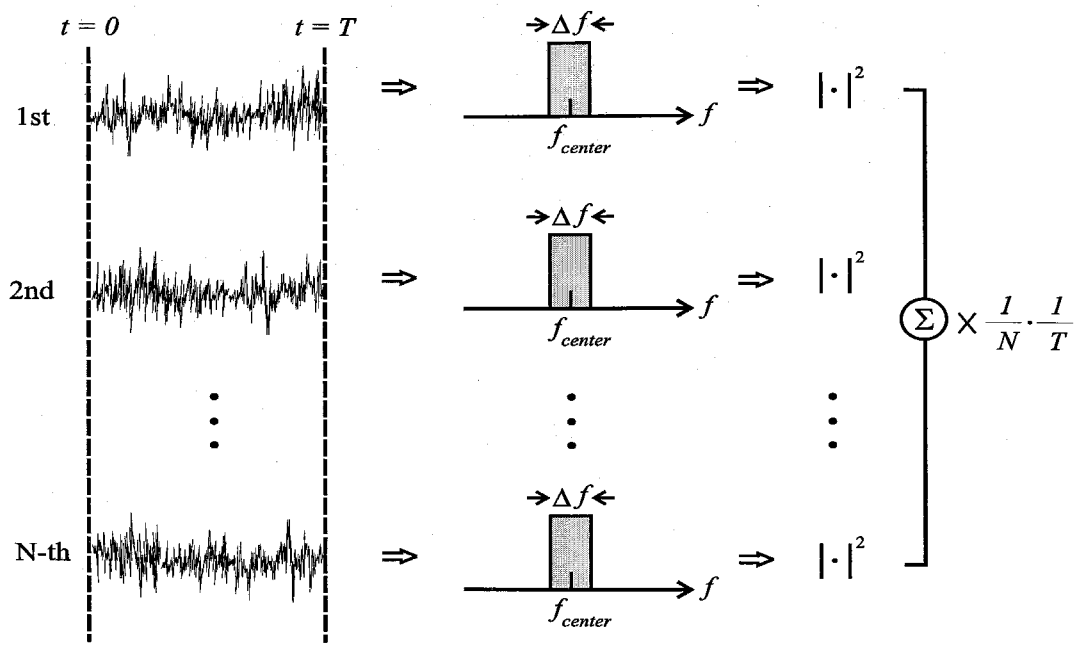

Figure 5.6: Signal processing in conventional measurement systems.

obtain

$$\begin{aligned} S_{n_p}(f;t) &= \int_{-\infty}^{\infty} e^{j2\pi f\tau} R_{n_p}(\tau;t)d\tau \\ &= Np^2(t) \end{aligned} \tag{5.8}$$

As can be seen, the operational PSD of the cyclostationary noise at a given frequency f is a periodic function of time, t. Note that (5.2) is a special case of (5.8). This periodic operational PSD of the cyclostationary noise will be seen repeatedly throughout this chapter. From now on, we will drop the word "operational" and call the PSD of the cyclostationary noise defined in (5.7) simply periodic or cyclic PSD.

Now, comparing the measured PSD in (5.6) with the periodic PSD in (5.8), we note that

$$S_{n_p,measured}(f) = \overline{S_{n_p}(f;t)} \tag{5.9}$$

where the overline signifies the time-average over a period of the periodic function, $p^2(t)$. Equation (5.9) demonstrates that the measurement of a cyclostationary noise whose periodic PSD is $S_{n_p}(f;t)$ results in a stationary noise, whose PSD is given by the time-average of the periodic PSD, that is, $\overline{S_{n_p}(f;t)}$. This observation, which is illustrated in Fig. 5.7, is very important and useful as it links the PSD of the cyclostationary noise that we measure in the lab with the operationally defined periodic

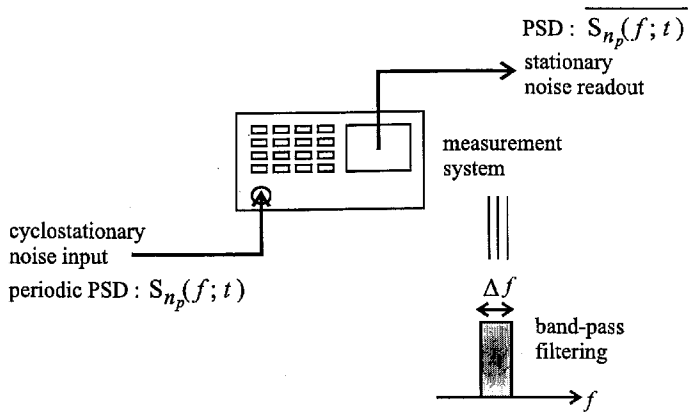

Figure 5.7: Measurement of a cyclostationary noise.

PSD of the cyclostationary noise. As an additional comment, measurement of cyclostationary noise using the conventional measurement systems is essentially equivalent to band-pass filtering of the cyclostationary noise, as we can easily reason from Fig. 5.6.

While the foregoing argument to prove (5.9) was restricted to the case where $n(t)$ is white noise, (5.9) can be shown to be valid in the most general case of colored stationary noise, $n(t)$. Now, we will prove this most general case. The autocorrelation function for the cyclostationary noise, $n_p(t) = n(t)p(t)$, in this most general case is given by

$$R_{n_p,n_p}(t_1,t_2) = R_{n,n}(t_1-t_2)p(t_1)p(t_2) \tag{5.10}$$

According to (5.7), the cyclic PSD of the cyclostationary noise is given by

$$S_{n_p}(f;t) = \int_{-\infty}^{\infty} d\tau e^{j2\pi f\tau} R_{n,n}(\tau)p(t)p(t+\tau) \tag{5.11}$$

where $\tau \equiv t_1 - t_2$ and $t \equiv t_1$. On the other hand, using (5.4), we can obtain the *measured PSD*:

$$\begin{aligned} S_{n_p,measured}(f) &= \lim_{T\to\infty}\frac{1}{T}\int_0^T\int_0^T dt_1dt_2R_{n_p,n_p}(t_1,t_2)e^{j2\pi f(t_1-t_2)} \\ &= \lim_{T\to\infty}\frac{1}{T}\int_0^T\int_0^T dt_1dt_2R_{n,n}(t_1-t_2)e^{j2\pi f(t_1-t_2)}p(t_1)p(t_2) \end{aligned}$$

Through a variable transformation defined as $(t_1,t_2) \to (t,\tau) \equiv (t_1, t_1-t_2)$, the integral above becomes

$$S_{n_p,measured}(f) = \lim_{T\to\infty}\frac{1}{T}\int_0^T dt\int_{-T}^T d\tau R_{n,n}(\tau)e^{j2\pi f\tau}p(t)p(t+\tau) \tag{5.12}$$

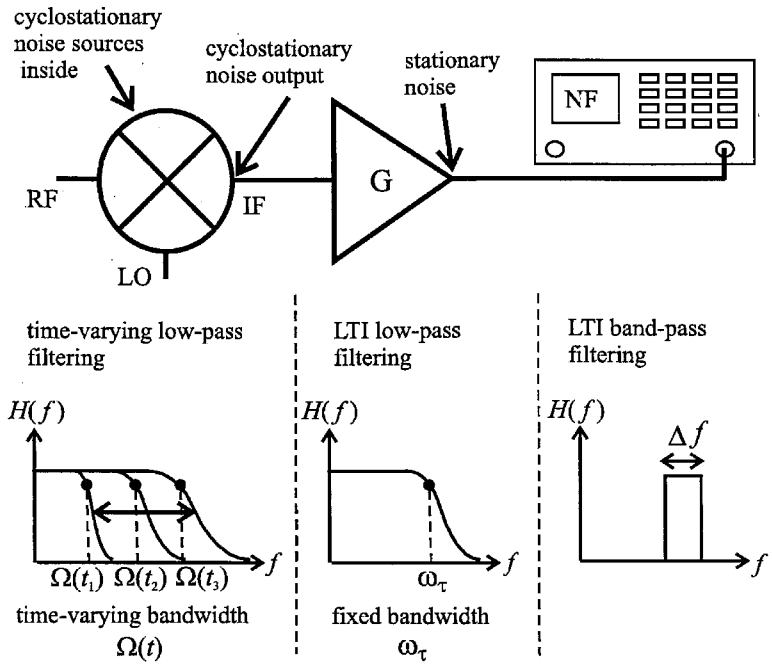

Figure 5.8: Noise flow in a generic mixer noise measurement setup.

By recognizing the identity between the second integral of the equation above and $S_{n_p}(f;t)$ of (5.11) for a sufficiently large T, we can simplify the integral above to

$$S_{n_p,measured}(f) = \lim_{T\to\infty} \frac{1}{T} \int_0^T dt S_{n_p}(f;t) = \overline{S_{n_p}(f;t)} \tag{5.13}$$

which proves (5.9).

Summarizing, in this section, we have reviewed basic properties of the cyclostationary noise and discussed how we can characterize the power spectral density of the cyclostationary noise. The periodic power spectral density of the cyclostationary noise was obtained by taking the Fourier transform of the autocorrelation of the cyclostationary noise. On the other hand, the measured power spectral density of the cyclostationary noise is equal to the time-average of the periodic power spectral density over a period. We have also mentioned that the measurement using the conventional noise measurement systems is essentially equivalent to the band-pass filtering.

In many practical circuit situations, the cyclostationary noise undergoes various types of filterings. To see this, let us take a look at a generic mixer noise measurement setup shown in Fig. 5.8 as an example. Switching components in the mixer driven by the periodic LO signal generate cyclostationary noise inside the mixer. As will be seen later, the mixer then processes this internally generated cyclostationary noise through *time-varying low-pass filtering* whose bandwidth, $\Omega(t)$, is periodically changing, as shown on the left-hand side of Fig. 5.8. The study later will also show that

this time-varying low-pass filtering of the cyclostationary noise again produces yet another cyclostationary noise process at the output IF-port. The IF-port cyclostationary noise will then experience typical linear time-invariant (LTI) low-pass filterings in building blocks such as amplifiers and/or band-pass filterings in band-pass filters or noise measurement systems.

Postponing the investigation of the time-varying filtering of cyclostationary noise in switching mixers to Section 5.6, we study the LTI low-pass filtering of cyclostationary noise in the following section. The LTI band-pass filtering of cyclostationary noise was already studied early in this section in the context of the measurement of the noise.

5.3 LTI Low-Pass Filtering of Cyclostationary Noise

The study of the LTI low-pass filtering of the cyclostationary noise in this section will demonstrate that the LTI low-pass filter output (in the passband) for a cyclostationary noise input, $n_p(t)$, is a stationary noise, whose PSD is the time-average of the periodic PSD of $n_p(t)$, $S_{n_p}(f;t)$, if the bandwidth of the filter is much smaller than the fundamental frequency of $p(t)$ [61]. This study will also serve as a comparison to the time-varying low-pass filtering of cyclostationary noise in mixers discussed in the next section.

Consider an RC low-pass filter as a physical example where the input is cyclostationary voltage noise, $n_p(t) = n(t)p(t)$, as shown in Fig. 5.9. The filter's bandwidth, $\omega_\tau \equiv (RC)^{-1}$, is assumed far smaller than the fundamental frequency, $2\pi f_0$, of the noise modulating function, $p(t)$, *i.e.*, $2\pi f_0 \gg \omega_\tau$. The output voltage across the capacitor is denoted as $v(t)$. For simplicity, $n(t)$ is assumed to be white noise and accordingly, the autocorrelation function and PSD of $n_p(t)$ are given by (5.3) and (5.8), respectively. In the frequency domain, one can easily obtain the power transfer function $|H(\omega)|^2$ of the filter:

$$|H(f)|^2 = \frac{\omega_\tau^2}{(2\pi f)^2 + \omega_\tau^2} \tag{5.14}$$

The corresponding dynamics of $v(t)$ in the time-domain is described by

$$\frac{dv}{dt} + \omega_\tau v = \omega_\tau n_p(t) = \omega_\tau n(t)p(t) \tag{5.15}$$

which is a typical Langevin equation introduced in Chapter 3. While solving (5.15) for $v(t)$ itself is meaningless since $v(t)$ is stochastic, we can still solve it for statistical quantities of $v(t)$ such as mean, variance, and autocorrelation, as discussed in Chapter 3.

In the first step, by multipling (5.15) at time t_2 by $n(t_1)$ and taking an ensemble average, we

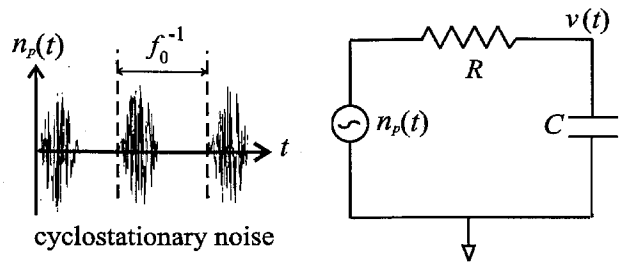

Figure 5.9: *RC* low-pass filtering of cyclostationary voltage noise $n_p(t) = n(t)p(t)$. The fundamental frequency of the noise modulating function, $p(t)$, is f_0. We assume $\omega_\tau \ll 2\pi f_0$.

obtain

$$\frac{\partial}{\partial t_2} R_{n,v}(t_1, t_2) + \omega_\tau R_{n,v}(t_1, t_2) = \omega_\tau N \delta(t_1 - t_2) p(t_2) \tag{5.16}$$

and by using the method of integrating factor [71], the solution of this equation is give by

$$R_{n,v}(t_1, t_2) = N\omega_\tau e^{-\omega_\tau(t_2 - t_1)} p(t_1) u(t_2 - t_1) \tag{5.17}$$

where $u(t)$ is a unit-step function.

In the second step, by multiplying (5.15) at time t_1 by $v(t_2)$ and taking an ensemble average, we obtain

$$\frac{\partial}{\partial t_1} R_{v,v}(t_1, t_2) + \omega_\tau R_{v,v}(t_1, t_2) = \omega_\tau p(t_1) R_{n,v}(t_1, t_2) \tag{5.18}$$

Again, resorting to the integrating factor method and using $R_{n,v}(t_1, t_2)$ obtained just before, the solution of the equation above becomes

$$R_{v,v}(t_1, t_2) = \omega_\tau^2 N e^{-\omega_\tau(t_1 + t_2)} \int_0^{\min(t_1, t_2)} p^2(t') e^{2\omega_\tau t'} dt' \tag{5.19}$$

Using the Fourier series, the periodic function $p(t)$ can be expanded as

$$p(t) = \sum_{n=-\infty}^{\infty} p_n e^{j2\pi n f_0 t} \tag{5.20}$$

and accordingly, $p^2(t)$ can be expressed as

$$p^2(t) = \sum_{n=-\infty}^{\infty} p_n p_{-n} + \sum_{n \neq -m} p_n p_m e^{j2\pi(n+m) f_0 t} \tag{5.21}$$

By substituting (5.21) in (5.19) and leaving out transient terms, the first term of (5.21) results in

$$R_{v,v}(t_1,t_2) = \omega_\tau N\frac{e^{-\omega_\tau|t_1-t_2|}}{2}\sum_{n=-\infty}^{\infty} p_n p_{-n} \quad (5.22)$$

[from the first term of (5.21)]

while the second term of (5.21) leads to

$$\begin{aligned} R_{v,v}(t_1,t_2) &= \omega_\tau N\frac{e^{-\omega_\tau|t_1-t_2|}}{2}\times\sum_{n\neq -m} p_n p_m \frac{e^{j2\pi(n+m)f_0\min(t_1,t_2)}}{1-j(n+m)(2\pi f_0/2\omega_\tau)} \\ &\sim \omega_\tau N\frac{e^{-\omega_\tau|t_1-t_2|}}{2}\cdot O(\frac{\omega_\tau}{2\pi f_0}) \end{aligned} \quad (5.23)$$

[from the second term of (5.21)]

For $2\pi f_0 \gg \omega_\tau$, (5.23) is negligible when compared to (5.22) and $R_v(t_1,t_2)$ can be approximated as

$$R_{v,v}(t_1,t_2) \approx \omega_\tau N\frac{e^{-\omega_\tau|t_1-t_2|}}{2}\overline{p^2(t)} \quad (5.24)$$

where we have used the *Parseval theorem*. As can be seen clearly here, in case of $2\pi f_0 \gg \omega_\tau$, that is, when the fundamental frequency of $p(t)$ of the cyclostationary noise, $n_p(t) = n(t)p(t)$, is much larger than the bandwidth of the low-pass RC filter, the autocorrelation at the output of the filter depends only on the measurement time difference $\tau = t_1 - t_2$. This implies that at the low-pass filter output, the noise, $v(t)$, is approximately stationary as far as the condition, $2\pi f_0 \gg \omega_\tau$, is satisfied.

When $2\pi f_0 \gg \omega_\tau$ holds true and hence $v(t)$ becomes stationary, the power spectral density of $v(t)$ can be obtained by taking the Fourier transform of the autocorrelation:

$$\begin{aligned} S_v(f) &= N\overline{p^2(t)}\cdot\frac{\omega_\tau^2}{(2\pi f)^2+\omega_\tau^2} \\ &= \overline{S_{n_p}(f;t)}\cdot|H(f)|^2 \end{aligned} \quad (5.25)$$

where we have used (5.8) and (5.14). In the passband of the filter where $2\pi f \ll \omega_\tau$, $|H(f)| \approx 1$ and hence we have

$$S_v(f) \approx \overline{S_{n_p}(f;t)} \quad (5.26)$$

Similar to the band-pass filtering case shown with (5.9), the low-pass filtering of a cyclostationary noise whose periodic PSD is $S_{n_p}(f;t)$ results in a stationary noise whose PSD is the time-average of the periodic PSD, *i.e.*, $\overline{S_{n_p}(f;t)}$, as far as the fundamental frequency of the cyclostationarity is much smaller than the bandwidth of the low-pass filter.

The results of this and previous sections demonstrated that once the cyclostationary noise is

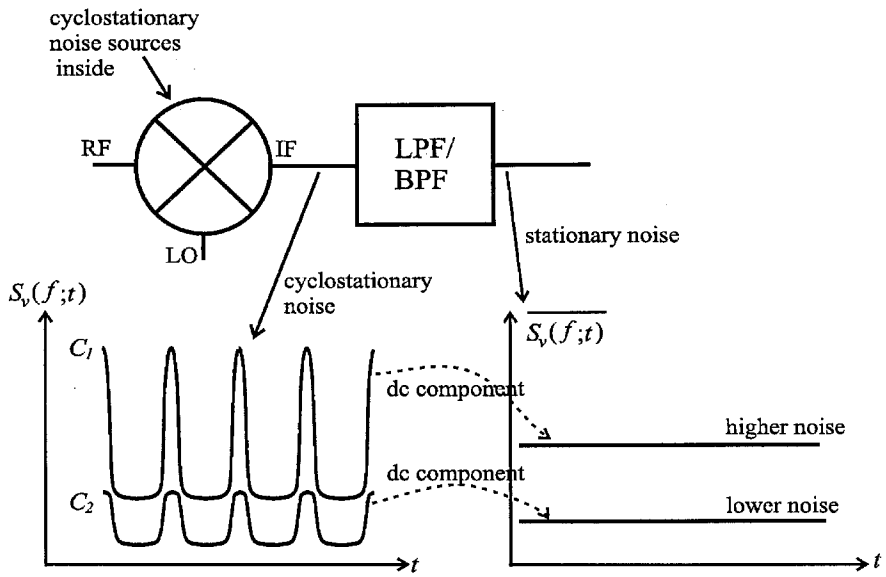

Figure 5.10: Cyclostationary noise and its filtering.

bandpass- or lowpass-filtered with sufficiently small bandwidths, the cyclostationary noise disappears and we will always observe stationary noise at the filter output. As any available contemporary noise measurement systems, such as spectrum analyzers and noise figure meters, essentially employ the bandpass filtering as mentioned earlier, we will *never* be able to observe the cyclostationary noise itself in reality: Whenever we try to measure the cyclostationary noise, it transforms to a stationary noise! Then what is the reason for this emphasis on cyclostationary noise?

To answer this question, we turn to Fig. 5.10 where a mixer is followed by a lowpass or a bandpass filter whose bandwidth is assumed to be much smaller than the fundamental frequency of the cyclostationarity. Now, at the IF-port of the mixer or at the input of the filter, the noise is cyclostationary and has a periodic PSD which is shown at the bottom left of the figure. As will be seen later, depending upon the circuit parameters, the degree of the time-variance of the periodic PSD changes, or alternatively put, the degree of the cyclostationarity varies. Now when this cyclostationary noise passes through the filter following the mixer, according to (5.9) or (5.26), the noise at the filter output becomes stationary and its PSD becomes the time-average of the periodic PSD as shown at the right bottom of Fig. 5.10. However, depending upon the degree of the cyclostationarity, the time-averaged PSD will have different values as shown in Fig. 5.10. Hence, even though we cannot observe the time-varying cyclostationary noise *per se*, we can see the effects of the cyclostationarity.

In the followings, we will investigate how the mixer generates the cyclostationary noise at the IF-port via time-varying filtering and how the degree of the cyclostationarity at the IF-port changes

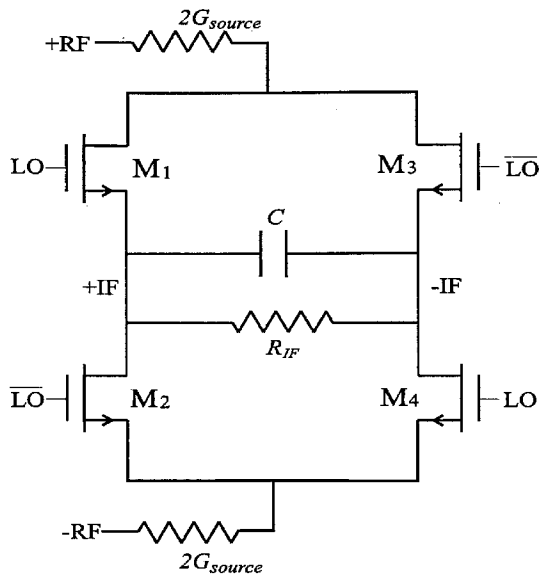

Figure 5.11: MOS switching mixer.

depending upon the circuit parameters, especially the energy storing elements such as capacitors. The main result of this theoretical investigation on the mixer noise will be presented in Sections 5.6 and 5.7 while Section 5.8 positively verifies the theoretical prediction experimentally. The analysis vehicle for the mixer noise study will be a CMOS switching mixer shown in Fig. 5.11, whose operational principles will be discussed in the following Section 5.4. Section 5.5 is dedicated to the investigation of the deterministic dynamics of the switching mixer, which also leads to a new observation of the conversion gain behavior of the circuit.

5.4 Switching Mixer Example

In this section, we will discuss the operational principle and the state equation of the commonly used MOS switching mixer shown in Fig. 5.11, which will be used as an example of the proposed analysis technique in the following sections.

5.4.1 Operational Principle

Figure 5.11 shows a commonly used MOS switching mixer [67], [68], [69]. Transistors M_1 and M_4 are driven by the periodic local oscillator with frequency of f_{LO} and transistors M_2 and M_3 are driven by the opposite phase of the same signal. All transistors operate between off and triode regions. G_{source} is the source conductance (*e.g.*, $1/(50\Omega)$) and the IF-capacitance C is due to the transistor parasitic capacitors and input capacitance of the next stage. Although this IF-capacitor may have

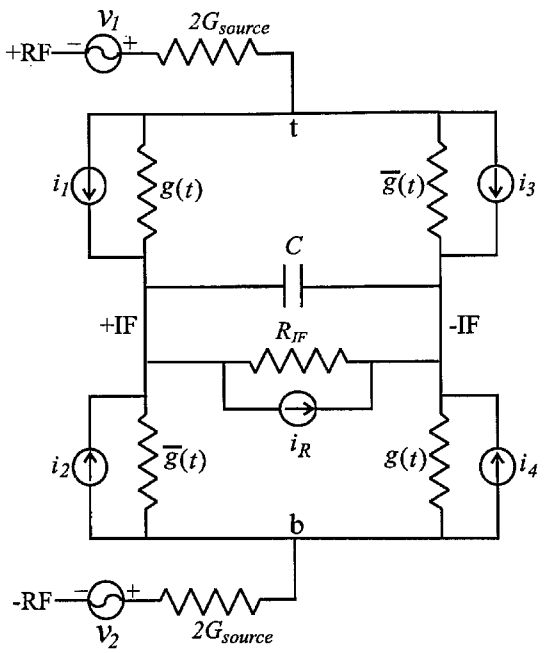

Figure 5.12: Equivalent RC-model of the switching mixer including noise sources.

a weak voltage- and hence time-dependence in general, we will consider it voltage-independent here for the sake of simplicity. The resistor, R_{IF}, represents the input resistance of the next stage and/or bias circuitry (*e.g.*, voltage-divider network).

The mixer can operate in two different switching modes depending upon the biasing scheme, namely, *hard-* and *soft-switching modes* [69]. In hard-switching mode, there is a period when all transistors are off, leaving the IF-port floating. In soft-switching mode, there is no single moment at which all transistors are simultaneously off. The bias criterion to determine the switching mode is given by

$$V_{LO,dc} - V_{RF,dc} - V_{th} \begin{cases} < 0 & \text{(hard-switching)} \\ > 0 & \text{(soft-switching)} \end{cases} \tag{5.27}$$

where V_{th} is the threshold voltage of the MOS transistor and $V_{LO,dc}$, $V_{RF,dc}$, and $V_{IF,dc}$ signify the dc levels of the LO, RF, and IF signals. Note that $V_{RF,dc} = V_{IF,dc}$ from the schematic of Fig. 5.11.

Figure 5.12 shows an equivalent RC model of the mixer including all the noise sources. $g(t)$ and $\overline{g}(t)$, periodic in f_{LO} and in opposite phase, represent channel conductances of MOS transistors. The channel conductance, $g(t)$, in the triode-regime is given by

$$g(t) = \mu_n C_{ox}(W/L)[V_{gs}(t) - V_{ds}(t) - V_{th}] \tag{5.28}$$

and shows dependence on all of the LO, RF, and IF signals. However, in practice, the RF and IF

signals are much smaller than the LO signal and hence we will use the *deep triode approximation* in evaluating $g(t)$, *i.e.*, $V_d(t) \approx V_s(t) \approx V_{RF,dc} = V_{IF,dc}$, throughout our treatment:

$$g(t) \approx \begin{cases} \mu_n C_{ox} \frac{W}{L} [V_g(t) - V_{RF,dc} - V_{th}] & \text{(deep-triode)} \\ 0 & \text{(off)} \end{cases} \tag{5.29}$$

With this approximation, the channel conductance, $g(t)$, only depends on the LO signal. The threshold voltage, V_{th}, in (5.29) can have a weak time-dependence due to the body effect of the MOS transistors, which will be ignored here for brevity.

The noise currents $i_1(t)$ to $i_4(t)$ in Fig. 5.12 represent cyclostationary channel thermal noise of the MOS transistors, whose single-side band (SSB) statistical properties are given by [47]

$$\begin{aligned} \frac{\overline{i_1^2}}{\Delta f} &= \frac{\overline{i_4^2}}{\Delta f} = 4k_B T g(t), \\ \frac{\overline{i_2^2}}{\Delta f} &= \frac{\overline{i_3^2}}{\Delta f} = 4k_B T \overline{g}(t) \end{aligned} \tag{5.30}$$

Here, we have replaced $g_{d0}(t)$ with $g(t)$ since $g(t)$ is calculated for $V_{ds} \approx 0$ in our deep triode approximation. Also we have used unity for the channel thermal noise constant, γ, as we are taking the deep triode approximation [47].

We can safely assume no correlation among $i_1(t)$ to $i_4(t)$ since they are generated by different transistors. $v_1(t)$ and $v_2(t)$ in Fig. 5.12 are voltage noise associated with the source conductance, G_{source}, while $i_R(t)$ is current noise due to the load resistor, R_{IF}.

5.4.2 State Equation

In this section and the following Sections 5.5 and 5.6, we analyze the circuit for $G_{source} = \infty$ and $R_{IF} = \infty$ in Fig. 5.12 in order to gain clear insight. We postpone the general analysis to Section 5.7 where the numerical analysis results are presented. By applying KCL and KVL to the circuit of Fig. 5.12, we obtain the following differential equation for the IF-port voltage $v_{if}(t)$:

$$\frac{dv_{if}}{dt} + \Omega(t) v_{if} = \frac{1}{C}(I_{deter} + I_{sto}) \tag{5.31}$$

[state equation]

where $v_{if}(t) = v_s(t) + v_n(t)$, in which $v_s(t)$ and $v_n(t)$ signify the signal and noise part of the IF-port voltage, respectively. The *time-varying bandwidth*, $\Omega(t)$, the deterministic driving term, I_{deter}, due to the input RF signal, $v_{rf}(t)$, and the stochastic driving term, I_{sto}, due to the transistor channel

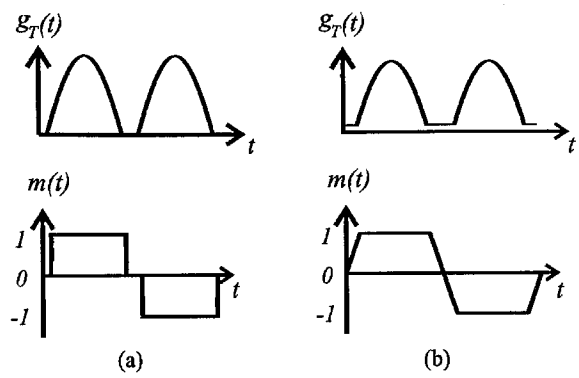

Figure 5.13: $g_T(t)$ and $m(t)$ in (a) hard-switching (b) soft-switching modes.

thermal noise are given by

$$\Omega(t) \equiv \frac{g_T(t)}{C} \tag{5.32}$$

$$I_{deter} \equiv g_T(t)m(t)v_{rf}(t) \tag{5.33}$$

$$I_{sto} \equiv \frac{1}{2}(i_1 - i_2 - i_3 - i_4) \tag{5.34}$$

respectively, where the *effective conductance*, $g_T(t)$, and the *mixing function*, $m(t)$, are defined in terms of $g(t)$ and $\overline{g}(t)$ [69]:

$$g_T(t) \equiv \frac{g(t) + \overline{g}(t)}{2} \tag{5.35}$$

$$m(t) \equiv \frac{g(t) - \overline{g}(t)}{g(t) + \overline{g}(t)} \tag{5.36}$$

The roles these two functions play in the mixer will be explained shortly. Fig. 5.13 shows typical waveforms of $g_T(t)$ over a period of LO for hard- and soft-switching modes [69]. Due to the complementary nature of switches, the fundamental frequency of $g_T(t)$ is $2f_{LO}$. Fig. 5.13 also shows typical $m(t)$ waveforms over a period of LO for the two switching modes [69]. Note that $m(t)$ has a fundamental frequency of f_{LO} and no dc component.

The stochastic driving term, I_{sto}, in (5.34), can be simplified as follows. Assuming no correlation among i_1 to i_4 and using the single-side band (SSB) white noise statistics of (5.30), we can show that

$$\begin{aligned} \overline{\frac{I_{sto}^2}{\Delta f}} &= 4k_BTg_T(t) \\ &= g_T^2(t) \cdot 4k_BT/g_T(t) \end{aligned} \tag{5.37}$$

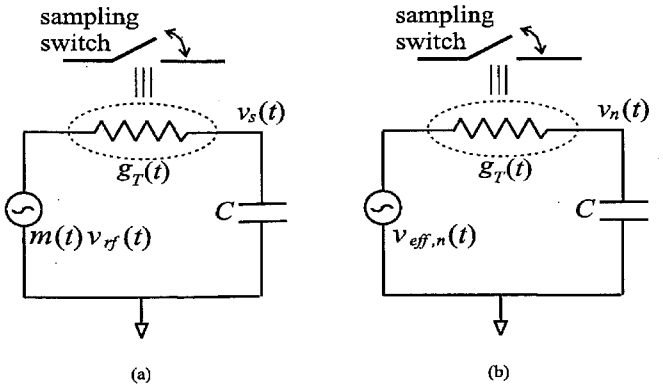

Figure 5.14: (a) The circuit corresponding to the deterministic dynamics (5.40) of the switching mixer. This circuit is no more than the Thévenin equivalent circuit of the mixer for $G_{source} = \infty$ and $R_{IF} = \infty$ in Fig. 5.12. (b) The circuit corresponding to the stochastic dynamics (5.41) of the switching mixer.

This power spectral density corresponds to

$$I_{sto}(t) = g_T(t) v_{eff,n}(t) \tag{5.38}$$

where the *effective cyclostationary voltage noise* $v_{eff,n}(t)$ is characterized as

$$\frac{\overline{v_{eff,n}^2}}{\Delta f} = \frac{4k_B T}{g_T(t)} \tag{5.39}$$

Since $\Omega(t) = g_T(t)/C$ only depends on the already-known LO signal within the accuracy of the deep triode approximation as mentioned earlier, the IF-port voltage $v_{if}(t)$ in (5.31) is a *linear* response to any driving terms on the right-hand side of the equation. Therefore, we can separate (5.31) into deterministic and stochastic parts. In the deterministic part, the signal component $v_s(t)$ of the IF voltage is a response to $I_{deter}(t)$ while in the stochastic part, the noise component $v_n(t)$ of the IF voltage is a response to $I_{sto}(t)$, *i.e.*,

$$\frac{dv_s}{dt} + \Omega(t) v_s(t) = \Omega(t) \cdot m(t) v_{rf}(t) \tag{5.40}$$

[deterministic dynamics]

$$\frac{dv_n}{dt} + \Omega(t) v_n(t) = \Omega(t) \cdot v_{eff,n}(t) \tag{5.41}$$

[stochastic dynamics]

Both (5.40) and (5.41) can be better understood in the light of their corresponding circuits shown in Fig. 5.14(a) and (b), respectively. Note that the circuit in Fig. 5.14(a) is no more than the Thévenin equivalent circuit of the mixer, derived from the RC-model in Fig. 5.12 for $G_{source} = \infty$ and $R_{IF} = \infty$ [69]. The equivalent circuits in Fig. 5.14 suggest that *the switching*

mixer acts as a first-order time-varying filter whose effective conductance and capacitance are $g_T(t)$ and C, respectively, resulting in the time-varying bandwidth of $\Omega(t) = g_T(t)/C$. The time-varying conductance, $g_T(t)$, can be also regarded as the conductance of a sampling switch, as in Fig. 5.14.

In the deterministic dynamics of Fig. 5.14(a), the effective input voltage (Thévenin equivalent input) to the time-varying filter is $m(t)v_{rf}(t)$. In other words, the RF input $v_{rf}(t)$ to the mixer is first multiplied by $m(t)$, hence the name for $m(t)$, *mixing function*. The product is then processed by the time-varying filtering, resulting in the output voltage $v_s(t)$. In the stochastic dynamics of Fig. 5.14(b), the effective input voltage to the time-varying filter is the cyclostationary voltage noise, $v_{eff,n}(t)$, that is, the switching mixer processes the cyclostationary noise $v_{eff,n}(t)$ by the identical time-varying filtering, producing the output $v_n(t)$. Both the time-varying bandwidth, $\Omega(t)$, and the cyclostationary noise, $v_{eff,n}(t)$, originate from the same switching elements in the circuit and hence will maintain a constant phase relation.

The following two sections will separately investigate the deterministic and stochastic dynamics of the switching mixer.

5.5 Time-Varying Filtering Theory - I : Deterministic Dynamics

In this section, we investigate the deterministic dynamics of the switching mixer, specially focusing on the dependence of mixer conversion gain on the IF-port capacitance C in Fig. 5.14(a). We will show that the conversion gain will initially *increase* with C resulting in a peaking in the conversion gain, as conceptually shown with the solid curve in Fig. 5.15. To the best of our knowledge, this conversion gain enhancement with an increasing capacitor in the switching mixer context has remained unknown so far.

Without loss of generality, we assume the RF signal, $v_{rf}(t)$, is a pure sinusoid with the frequency of f_{RF} and unity amplitude:

$$v_{rf}(t) = \cos(2\pi f_{RF} t) \tag{5.42}$$

Defining the IF-frequency as $f_{IF} \equiv |f_{RF} - f_{LO}|$, the key approach to the problem is breaking the Thévenin equivalent input voltage $m(t)v_{rf}(t)$ in Fig. 5.14(a) into f_{IF} and non-f_{IF} components and observing the circuit's response, $v_s(t)$, at the output to the former and latter, separately. Combining (5.42) and the Fourier series expansion of $m(t)$ given by

$$m(t) = \sum_{n=1}^{\infty} m_n \cos(2n\pi f_{LO} t + \phi_n) \tag{5.43}$$

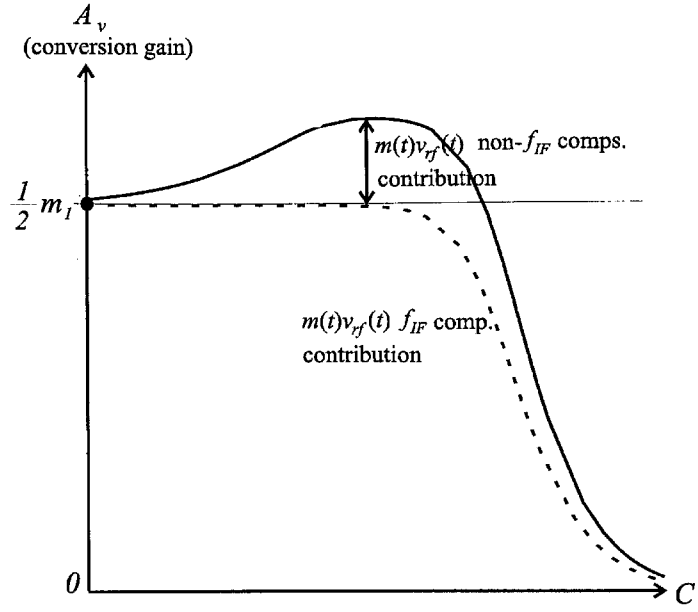

Figure 5.15: Conversion gain contribution from the f_{IF} and non-f_{IF} components of $m(t)v_{rf}(t)$. The solid curve represents the total conversion gain while the broken curve represents the conversion gain contribution from the f_{IF} component of $m(t)v_{rf}(t)$.

we obtain

$$\begin{aligned} m(t)v_{rf}(t) &= \frac{1}{2}m_1 \cos[2\pi f_{IF}t - \phi_1] \\ &\quad + \frac{1}{2}\sum_{n=1}^{\infty} m_n \cos[2\pi(nf_{LO} + f_{RF})t + \phi_n] + \frac{1}{2}\sum_{n=2}^{\infty} m_n \cos[2\pi(nf_{LO} - f_{RF})t + \phi_n] \\ &= \underbrace{\frac{1}{2}m_1 \cos(2\pi f_{IF}t + \phi_1)}_{f_{IF}\text{ component}} + [\text{non-}f_{IF}\text{ comps.}] \end{aligned} \tag{5.44}$$

Since $m_n = 0$ for even n due to the special waveform of $m(t)$ in Fig. 5.13, the non-f_{IF} components of $m(t)v_{rf}(t)$ are at odd integer multiples of f_{LO} plus/minus f_{RF}, *i.e.*, $nf_{LO} + f_{RF}$ for $n = 1, 3, 5, \cdots$ and $nf_{LO} - f_{RF}$ for $n = 3, 5, 7, \cdots$.

For $C = 0$, $v_s(t) = m(t)v_{rf}(t)$ from Fig. 5.14(a) or (5.40). Hence, *for $C = 0$, only the f_{IF} component of $m(t)v_{rf}(t)$ contributes to the conversion gain* where the conversion gain is simply given by

$$A_{conv} = \frac{1}{2}m_1 \quad [\, C = 0\,] \tag{5.45}$$

using (5.44).

For $C \neq 0$, mixer's response $v_s(t)$ to both f_{IF} and non-f_{IF} components of the Thévenin equivalent input $m(t)v_{rf}(t)$ in Fig. 5.14(a) can be better understood by considering the mixer as a sampler.

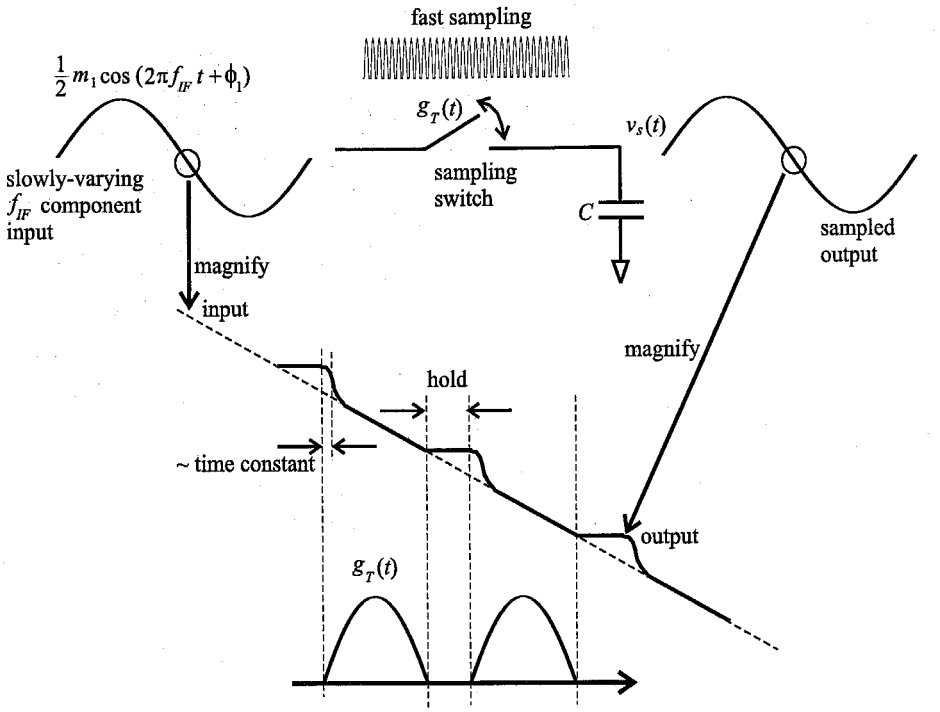

Figure 5.16: Sampling and recovering of the f_{IF} component of $m(t)v_{rf}(t)$ for small IF capacitance C.

The mixer samples the input $m(t)v_{rf}(t)$ with the sampling rate of $2f_{LO}$ (fundamental frequency of $g_T(t)$), resulting in the output $v_s(t)$. We can break down our analysis into f_{IF} and non-f_{IF} components.

The f_{IF} component of $m(t)v_{rf}(t)$ is a slowly varying input to the sampler, when compared to the sampling rate, $2f_{LO}$, as shown in Fig. 5.16. Hence, the sampler almost completely recovers the f_{IF} component of $m(t)v_{rf}(t)$ at its output unless the IF capacitance is too large to follow. Hence the conversion gain is $m_1/2$ for small enough C. As C becomes larger, mixer's response becomes slower and the f_{IF} component of $m(t)v_{rf}(t)$ cannot be fully recovered at the output, leading to a roll-off in conversion gain. This behavior is conceptually depicted with the broken line in Fig. 5.15 consisting of flat and roll-off regions.

The non-f_{IF} frequency components of $m(t)v_{rf}(t)$ in Fig. 5.14(a) will lead to a previously unnoticed conversion gain enhancement. Now we show how the non-f_{IF} components result in the f_{IF} component in the mixer output, $v_s(t)$. When the switch represented by $g_T(t)$ samples *any* given non-f_{IF} component of $m(t)v_{rf}(t)$ with the sampling rate of $2f_{LO}$ for $C \neq 0$ in Fig. 5.14(a), the sampled waveform at the output will be shaped in time due to the *memory effect* of the nonzero capacitor as depicted in Fig. 5.17. Since $g_T(t)$ and the input non-f_{IF} component of $m(t)v_{rf}(t)$ eventually return to the same common phase[2] after a certain period defined as $T_{beat} \equiv 1/f_{beat}$, the

[2]Here, we are restricting our discussion to the integer frequencies and a more general treatment can be found in

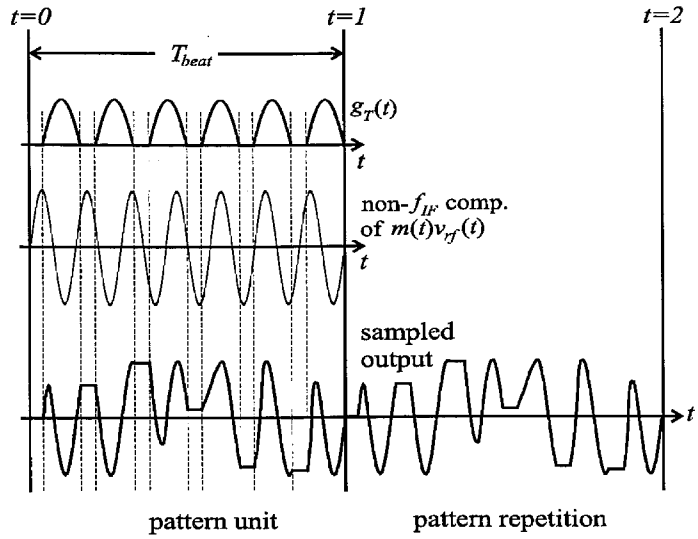

Figure 5.17: An example of a pattern unit generation and repetition (beating) in sampling of a non-f_{IF} component of $m(t)v_{rf}(t)$. In this simplified example, f_{LO}=3Hz, f_{RF}=4Hz, and the non-f_{IF} component of $m(t)v_{rf}(t)$ at $f_{LO}+f_{RF}=7$Hz is considered. The sampling rate is $2f_{LO}$ =6Hz.

sampled (and shaped) output waveform pattern repeats itself with the *beat* frequency of f_{beat} as illustrated in Fig. 5.17.

Now, it can be shown that the IF frequency, f_{IF}, is always an integer multiple of f_{beat} for *any* non-f_{IF} component of $m(t)v_{rf}(t)$. The proof runs as follows.

Let us define two frequencies, f_s and f_{in}, where $f_s \equiv 2f_{LO}$ is the sampling rate and the input frequency f_{in} represents any non-f_{IF} components of $m(t)v_{rf}(t)$, *i.e.*, $f_{in} \equiv nf_{LO} \pm f_{RF}$ ($n = 1, 3, 5, \cdots$ for the plus sign and $n = 3, 5, 7, \cdots$ for the minus sign). We denote the least common multiple (LCM) of f_s and f_{in} as L_f:

$$L_f \equiv LCM(f_s, f_{in}) = k_s f_s = k_{in} f_{in} \tag{5.46}$$

for certain integers k_s and k_{in}. Let us also denote the LCM of k_s and k_{in} as L_k, *i.e.*,

$$L_k \equiv LCM(k_s, k_{in}) \tag{5.47}$$

Since the sampling period is $T_s \equiv f_s^{-1} = k_s/L_f$ and the input signal period is $T_{in} \equiv f_{in}^{-1} = k_{in}/L_f$, the beat period becomes $T_{beat} = L_k/L_f$ or alternatively, the beat frequency is given by

$$f_{beat} \equiv \frac{1}{T_{beat}} = \frac{L_f}{L_k} \tag{5.48}$$

[66].

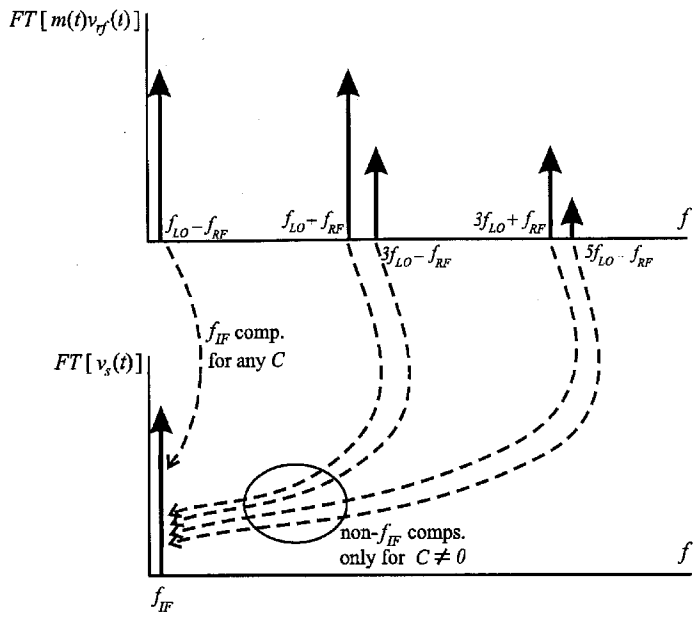

Figure 5.18: Contributions of f_{IF} and non-f_{IF} components of $m(t)v_{rf}(t)$ to the f_{IF} component at the mixer output $v_s(t)$.

Noting $f_{IF} = |(nf_{LO} \mp f_{RF}) - (n \pm 1)f_{LO}| = |f_{in} - n'f_s|$ where $n' \equiv (n \pm 1)/2$ is an integer as n is odd and using (5.46), we obtain

$$f_{IF} = L_f \cdot \left| \frac{k_s - n'k_{in}}{k_{in}k_s} \right| \tag{5.49}$$

Utilizing $k_s k_{in} = G_k L_k$ where G_k is *the greatest common divisor* (GCD) of k_s and k_{in}, which is 1, and using (5.48), we have

$$f_{IF} = \frac{L_f}{L_k} \cdot |k_s - n'k_{in}| = f_{beat} \times [\text{integer}] \tag{5.50}$$

Therefore, any non-f_{IF} component of $m(t)v_{rf}(t)$ does contribute to the mixer conversion gain through one of the harmonics of f_{beat}, which is determined by the integer relation of f_{IF} and f_{beat}.

Let us consider a simple example with $f_{LO} = 3$ Hz, $f_{RF} = 4$ Hz, and $f_{IF} = 1$ Hz. In this example, we consider the $f_{in} = f_{LO} + f_{RF}$ (=7 Hz) component of $m(t)v_{rf}(t)$ as an input to the sampler. The sampling rate is $f_s = 2f_{LO} = 6$ Hz. The corresponding $g_T(t)$ with the 6 Hz sampling rate, input with 7 Hz periodicity and the resulting sampled output waveforms are shown in Fig. 5.17. Since the input and $g_T(t)$ return to the same common phase after one second, the sampled waveform will form a pattern unit during this one second and will repeat it on and on. This *beating* has the frequency of $f_{beat} = 1Hz = f_{IF}$, showing that the non-f_{IF} components of $m(t)v_{rf}(t)$ does generate f_{IF} component at the mixer output, contributing to the conversion gain.

Summarizing (Fig. 5.18), for $C = 0$, the f_{IF} component of the Thévenin equivalent input $m(t)v_{rf}(t)$ is the sole contributor to the conversion gain of $m_1/2$. For $C \neq 0$, the contribution from the f_{IF} component of $m(t)v_{rf}(t)$ to the conversion gain is shown with the broken line in Fig. 5.15 consisting of flat and roll-off regions. Also for $C \neq 0$, the non-f_{IF} components of $m(t)v_{rf}(t)$ result in beating patterns in the mixer output, adding extra amount of f_{IF} response at the output on the top of the response due to the f_{IF} component of $m(t)v_{rf}(t)$ (the broken line in Fig. 5.15). Combining these effects, *the mixer conversion gain increases starting from $m_1/2$ with an increasing C until it ultimately begins decreasing due to the filtering effect for large enough C.* This overall conversion gain versus C behavior is shown with the solid curve in Fig. 5.15. The size of the bump in the curve is then proportional to the harmonic richness of the mixing function $m(t)$ and hence the size of the bump should be larger in the hard-switching than in the soft-switching. *This conversion gain enhancement with an increasing C is a previously unknown phenomenon and can be exploited to achieve an optimum mixer design, as can be seen later.*

5.6 Time-Varying Filtering Theory - II : Stochastic Dynamics

In this subsection, we investigate the stochastic dynamics of the switching mixer, *i.e.*, the time-varying filtering of the cyclostationary noise, in Fig. 5.14(b), or in (5.41), which is rewritten in the following for the sake of convenience:

$$\frac{dv_n}{dt} + \Omega(t)v_n(t) = \Omega(t) \cdot v_{eff,n}(t) \tag{5.51}$$

This is a Langevin equation which has a stochastic driving term on its right-hand side. The method of solving the Langevin equation was already discussed earlier in Chapter 3. We apply the method to derive the autocorrelation function of $v_n(t)$ from (5.51). To begin with, note that (5.39) is equivalent to

$$R_{v_{eff,n},v_{eff,n}}(t_1,t_2) = \frac{2k_BT}{g_T(t_1)}\delta(t_1 - t_2) \tag{5.52}$$

In the first step, by multiplying (5.51) at t_2 by $v_{eff,n}(t_1)$ and taking the expected value utilizing (5.52), we obtain

$$\frac{\partial}{\partial t_2}R_{v_{eff,n},v_n}(t_1,t_2) + \Omega(t_2)R_{v_{eff,n},v_n}(t_1,t_2) = \frac{2k_BT}{C}\delta(t_1 - t_2)$$

Using the integration factor method [71] with $\Phi(t) \equiv \int_0^t \Omega(t')dt'$, the solution of the above equation is shown to be

$$R_{v_{eff,n},v_n}(t_1,t_2) = \frac{2k_BT}{C} e^{[\Phi(t_1)-\Phi(t_2)]} u(t_2 - t_1) \tag{5.53}$$

where $u(t)$ is the unit step function.

In the second step, by multiplying (5.51) at t_1 by $v_n(t_2)$ and taking the expected value, we obtain

$$\frac{\partial}{\partial t_1} R_{v_n,v_n}(t_1,t_2) + \Omega(t_1) R_{v_n,v_n}(t_1,t_2) = \Omega(t_1) \frac{2k_BT}{C} e^{[\Phi(t_1)-\Phi(t_2)]} u(t_2 - t_1) \tag{5.54}$$

where we have used the result in the first step, (5.53). By using the integrating factor technique again, we obtain the following autocorrelation function of v_n:

$$R_{v_n,v_n}(t_1,t_2) = \frac{2k_BT}{C^2} e^{-[\Phi(t_1)-\Phi(t_2)]} \int_0^{min[t_1,t_2]} e^{2\Phi(t)} g_T(t) dt \tag{5.55}$$

By noting $(d/dt)e^{2\Phi(t)} = (2/C)g_T(t)e^{2\Phi(t)}$, we can perform the integral above, leading to

$$R_{v_n,v_n}(t_1,t_2) = \frac{k_BT}{C} e^{-\Lambda(t_1,t_2)} \tag{5.56}$$

where we have ignored the initial transient and the exponent $\Lambda(t_1,t_2)$ is given by

$$\Lambda(t_1,t_2) = \Phi(t_1) - \Phi(t_2) - 2\Phi(\min[t_1,t_2]) \tag{5.57}$$

Using the Fourier series expansion of $g_T(t)$ only with its dc and fundamental frequency components for simplicity[3], *i.e.*,

$$g_T(t) = g_{T,0} + g_{T,1}\cos(2\omega_{LO}t + \theta_1) \tag{5.58}$$

and defining $\tau \equiv t_2 - t_1$ and $t \equiv t_1$, the exponent $\Lambda(t_1,t_2)$ can be expressed as

$$\Lambda(t_1,t_2) = \Lambda(\tau;t) = \frac{g_{T,0}}{C}|\tau + \frac{g_{T,1}}{\omega_{LO}C}\cos[\omega_{LO}\tau + 2\omega_{LO}t + \theta_1]\sin\omega_{LO}|\tau| \tag{5.59}$$

and hence the autocorrelation in (5.56) can be written as

$$R_{v_n,v_n}(\tau;t) = \frac{k_BT}{C} e^{-\Lambda(\tau;t)} \tag{5.60}$$

As can be seen, the autocorrelation $R_{v_n,v_n}(\tau;t)$ depends not only on the measurement time difference $|\tau|$ but also on the absolute measurement time t. This shows that *the time-varying filtering of the cyclostationary noise in switching mixers again produces cyclostationary noise $v_n(t)$ at the mixer's output (IF-port)*. Equation (5.59) suggests that the fundamental frequency of the

[3] $\omega_{LO} = 2\pi f_{LO}$, $\omega_{RF} = 2\pi f_{RF}$, and $\omega_{IF} = 2\pi f_{IF}$

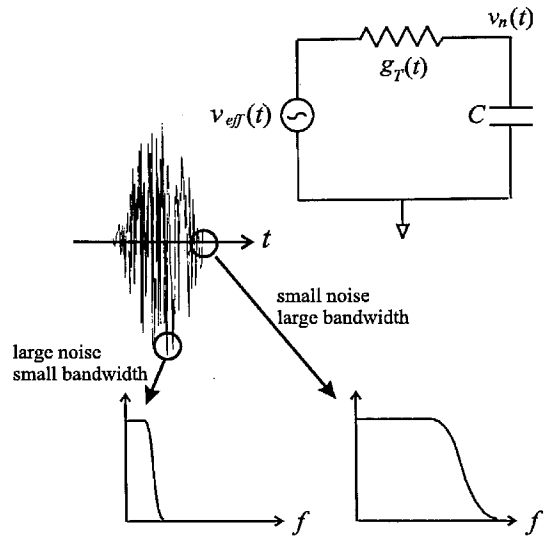

Figure 5.19: Explanation of the time-invariant $\langle v_n^2 \rangle = k_B T/C$ in the context of the equivalent circuit of switching mixer for noise, redrawn from Fig. 5.14(b).

output cyclostationarity is $2f_{LO}$. $R_{v_n,v_n}(\tau;t)$ ultimately decays exponentially with $|\tau|$, implying less correlation with larger $|\tau|$.

For $t_1 = t_2$ or $\tau = 0$, (5.60) reduces to

$$R_{v_n,v_n}(t,t) = \langle v_n^2 \rangle = \frac{k_B T}{C} \tag{5.61}$$

Remarkably, (5.61) shows that the mean-squared voltage noise $\langle v_n^2 \rangle$ is *time-invariant* even in the presence of the cyclostationarity. Furthermore, the mean-squared voltage given above coincides with the value determined from the equipartition theorem, that is, $C\langle v_n^2 \rangle/2 = k_B T/2$, where the equipartition theorem was fully discussed in Chapter 3.

Another way of looking at the time-invariance of $\langle v_n^2 \rangle$ is to note that the instantaneous bandwidth $\Omega(t) \propto g_T(t)$ and input voltage noise intensity $\overline{v_{eff,n}^2/\Delta f} \propto 1/g_T(t)$ in Fig. 5.14(b) (redrawn in Fig. 5.19) vary inversely proportional to each other during the mixer operation: as $g_T(t)$ increases, the bandwidth increases while the input noise intensity decreases and vice versa for decreasing $g_T(t)$. Hence the mean-squared voltage noise at the output stays constant regardless of the measurement time t.

The cyclic power spectral density of v_n at the IF frequency f_{IF} is given by

$$S_{v_n}(f_{IF};t) = \int_{-\infty}^{\infty} e^{-j2\pi f_{IF}\tau} R_{v_n,v_n}(\tau;t)d\tau \tag{5.62}$$

There exist two different regimes of noise generation, depending on the size of the IF capacitor. We can identify the two regimes of noise generation based on the relative size of the dc component

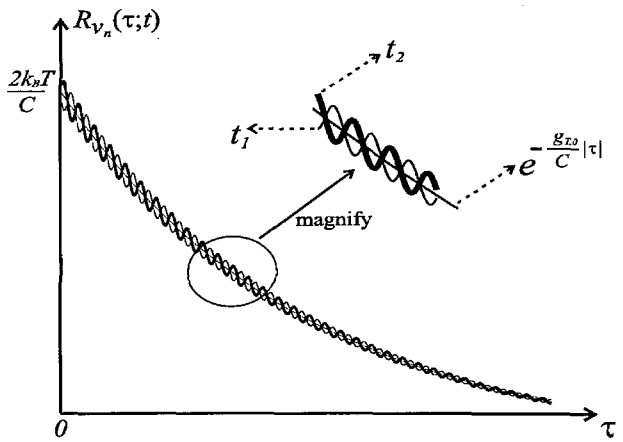

Figure 5.20: $R_{v_n}(\tau;t)$ versus τ for two different measurement times $t = t_1$ and $t = t_2$ for large enough $C \gg g_{T,0}/(2\omega_{LO})$.

of $\Omega(t)$, $\Omega_0 \equiv g_{T,0}/C$, with respect to $2\omega_{LO}$. First, *quasi-stationary regime* is identified with the condition $\Omega_0 \ll 2\omega_{LO}$. For a large enough IF-port capacitance, C, satisfying the condition, $R_{v_n}(\tau;t)$ for a given t assumes a decay $\sim e^{-g_{T,0}/C\cdot|\tau|}$ with rapid, small variations around it due to the trigonometric terms in (5.59) as illustrated in Fig. 5.20. The change of the measurement time t will only introduce the small phase shift of the rapid variations (Fig. 5.20). Therefore, the integral in (5.62) will average out the rapid variations regardless of t, implying a weak manifestation of cyclostationarity. Equation (5.62) then can be approximated as

$$\begin{aligned} S_{v_n}(f_{IF}) &\approx \frac{2k_BT}{C}\int_{-\infty}^{\infty} e^{-j2\pi f_{IF}\tau}e^{-\frac{g_{T,0}}{C}|\tau|}d\tau \\ &= 4k_BT\frac{g_{T,0}}{g_{T,0}^2+4\pi^2f_{IF}^2C^2} \\ &\quad \text{[quasi-stationary approximation]} \end{aligned} \tag{5.63}$$

which could be obtained from Fig. 5.12 by replacing $g(t)$ and $\overline{g}(t)$ with their dc components and hence the name, *quasi-stationary approximation.*

Second, *cyclostationary regime* is identified with the condition $\Omega_0 \gg 2\omega_{LO}$. For a small enough IF-port capacitance C satisfying the condition, $R_{v_n}(\tau;t)$ for a given t decays quickly with $|\tau|$ when compared to the time scale $\sim 1/(2f_{LO})$. By the time $|\tau|$ the autocorrelation decays considerably, it contains only a fraction or a few of $2f_{LO}$ variations due to the trigonometric terms in (5.59) while the size of the variations is appreciable. Accordingly, different measurement time t will result in conspicuously different $R_{v_n}(\tau;t)$ as shown in Fig. 5.21. These variations seriously change the value of power spectral density in (5.62), a clear manifestation of the cyclostationary noise. Additionally, due to the rapid decay of $R_{v_n}(\tau;t)$ with τ when compared to $1/(2f_{LO})$, the effective integration interval of (5.62) is much smaller than $1/f_{IF}$ as $f_{LO} \gg f_{IF}$ in the most practical cases. Therefore,

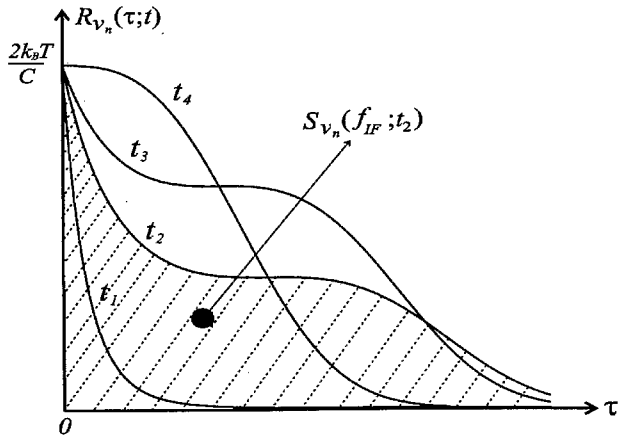

Figure 5.21: $R_{v_n}(\tau;t)$ versus τ for four different measurement times $t = t_1, t_2, t_3$ and t_4 for small enough $C \ll g_{T,0}/(2\omega_{LO})$.

$e^{-j2\pi f_{IF}\tau} \approx 1$ in (5.62) and we have

$$S_{v_n}(f_{IF};t) \approx \int_{-\infty}^{\infty} R_{v_n}(\tau;t)d\tau \quad \text{[cyclostationary regime]} \tag{5.64}$$

in this cyclostationary regime. Henceforth, $S_{v_n}(f_{IF};t)$ for a given time, t, is simply the area under the $R_{v_n}(\tau;t)$ versus τ curve as shown in Fig. 5.21.

In summary, the switching mixer processes the cyclostationary noise generated by the MOS switches through the time-varying filtering, again producing cyclostationary noise at the IF-port. The fundamental frequency of the IF-port cyclostationarity is $2f_{LO}$. There exists two different noise generation regimes depending on the size of the IF-port capacitance C. In the cyclostationary regime, the IF-port cyclostationarity is pronounced and the conventional quasi-stationary approximation can lead to large errors. In the quasi-stationary regime, the manifestation of the cyclostationarity at the IF-port is severely weakened and the quasi-stationary approximation holds good. The border between the two regimes can be defined by $\Omega_0 = 2\omega_{LO}$, which determines the critical capacitance C_{cyclo}:

$$C_{cyclo} \equiv \frac{g_{T,0}}{2\omega_{LO}} \tag{5.65}$$

The cyclostationary regime is identified with $C \ll C_{cyclo}$ while the quasi-stationary regime is identified with $C \gg C_{cyclo}$.

Although not common in practice, let us consider the case where the IF-port capacitance C is very large for the sake of completeness. When C is large enough to satisfy $\Omega_0 \leq \omega_{IF}$, the mixer

filters both IF signal and IF noise. Hence, the critical capacitance, C_{filter}, which determines the onset of the IF signal/noise filtering is given by

$$C_{filter} = \frac{g_{T,0}}{\omega_{IF}} \tag{5.66}$$

We will see these effects more clearly in the following section.

5.7 Simulation and Design Implication

In this section we will use numerical simulations [52] to verify the results of the previous section for the general case where G_{source} and R_{IF} are both finite. The state equation has the same form as in the special case (5.31) while $\Omega(t)$, I_{deter} and I_{sto} are more complicated for this general case [66]. As will be seen shortly, the circuit behavior remains essentially the same as in the special case of the previous section.

The SSB noise figure (NF) of the mixer can be expressed as [92]

$$NF = 1 + \frac{G_{source}}{4k_BT}\frac{\overline{S_{v_n}(f_{IF},t)}}{A_{conv}^2} \tag{5.67}$$

where A_{conv} is its voltage conversion gain and $S_{v_n}(f_{IF},t)$ is the cyclic power spectral density of the IF voltage noise, v_n, while excluding contribution of the noise due to G_{source}. Time-averaged PSD in the numerator is what the noise figure meter measures as demonstrated earlier. Now we will calculate A_{conv}, $S_{v_n}(f_{IF},t)$ and NF by numerically solving (5.31) in the general case.

The following numerical results have been obtained using f_{LO} = 300 MHz, f_{IF} = 10 MHz, f_{RF} = 310 MHz, G_{source} = 0.02 (or, 50Ω source resistance) and $R_{IF} = 10k\Omega$.

5.7.1 Conversion Gain Simulation

The simulated voltage conversion gain, A_{conv}, versus IF-port capacitance, C, is depicted in Fig. 5.22 for hard- and soft-switching modes. As predicted earlier, A_{conv} does increase with increasing C until the trend ultimately reverses at the onset of the f_{IF} component filtering. The critical IF-port capacitance C_{filter} defined by (5.66) in excess of which the IF filtering becomes substantial is shown in the figure for each switching mode. The bump size of the curves is larger in the hard-switching than in the soft-switching as the former has richer harmonic contents, resulting in more contribution from higher order odd integer multiples of f_{LO} plus/minus f_{RF} as predicted earlier in this chapter. An important design implication obtained from the A_{conv} versus C curve is the existence of an optimum capacitance that results in maximum conversion gain. Additionally, we can see that the hard-switching mode yields a higher optimum conversion gain performance than the soft-switching.

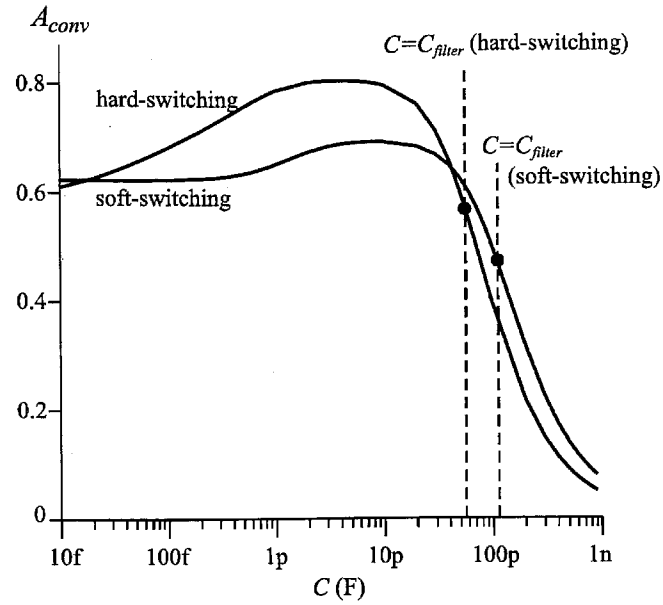

Figure 5.22: Simulated A_{conv} versus C for the two different switching modes.

5.7.2 Noise Simulation

Figures 5.23 and 5.24 show $S_{v_n}(f_{IF};t)$ versus t during a period of LO for different values of C for hard- and soft-switching modes, respectively. As can be seen, $S_{v_n}(f_{IF};t)$ clearly manifests the cyclostationarity with the $2f_{LO}$ periodicity. The instantaneous noise generation at the IF-port is boosted when $g_T(t)$ is small, close to switching and attenuated when $g_T(t)$ is large. As predicted in the previous section, a small IF capacitor results in large variation in the PSD, or stronger cyclostationarity while large IF capacitors average out more of $2f_{LO}$ cyclostationarity and reduce the time-variations of the PSD. Also comparing the numerical values in Figures 5.23 and 5.24, we notice that for a given capacitance, the cyclostationarity is more pronounced in the hard-switching than in the soft-switching.

In Fig. 5.25, the time-averaged PSD $\overline{S_{v_n}(f_{IF};t)}$ versus C is depicted for both hard- and soft-switching modes. The figure also shows the results obtained from the commonly used quasi-stationary approximations of (5.63) with broken lines. As predicted earlier, for large enough capacitances, $\overline{S_{v_n}(f_{IF};t)}$ converges to the stationary approximation. For smaller capacitances, the cyclostationarity is more pronounced and the stationary approximation can result in large errors, especially in the hard-switching. In this cyclostationary noise regime, the reduction rate of $\overline{S_{v_n}(f_{IF};t)}$ with increasing C represents the importance of cyclostationarity and the hard-switching shows a higher level of cyclostationarity. For the soft-switching, the time-variance of the PSD is significantly weaker when compared to the hard-switching mode. The critical capacitance C_{cyclo} defined earlier

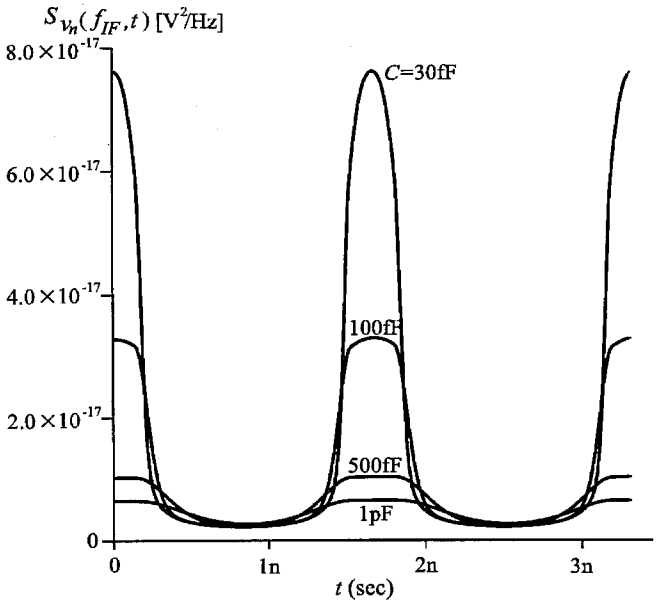

Figure 5.23: Simulated $S_{v_n}(f_{IF};t)$ versus t during a period of LO for various capacitor values in the hard-switching mode.

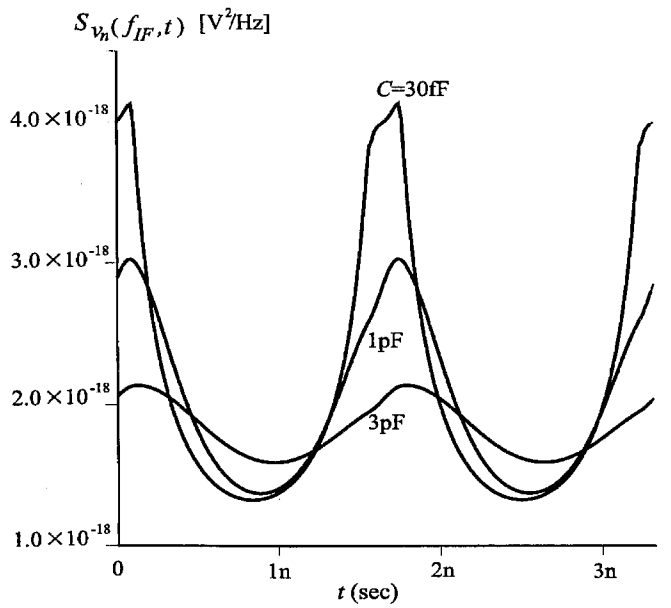

Figure 5.24: Simulated $S_{v_n}(f_{IF};t)$ versus t during a period of LO for various capacitor values in the soft-switching mode.

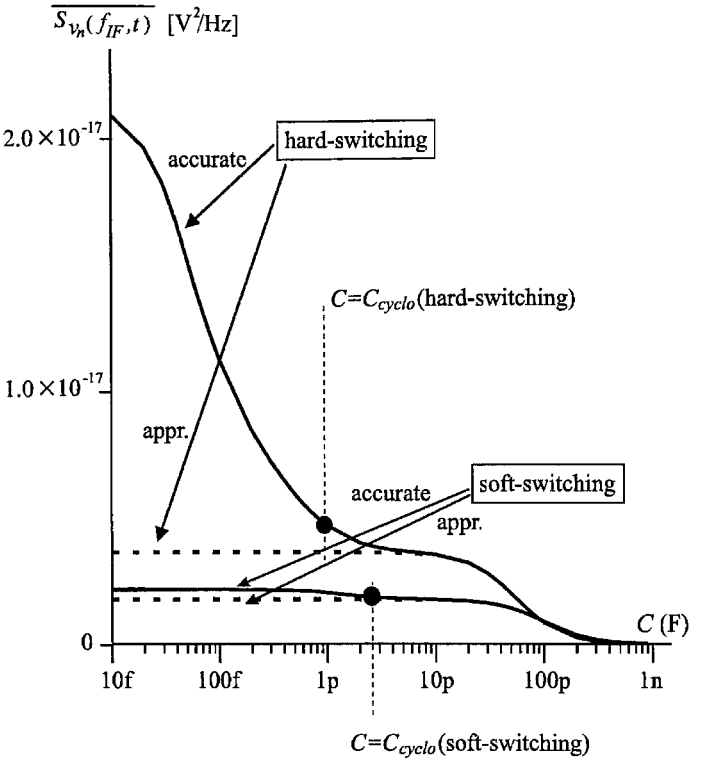

Figure 5.25: Simulated $\overline{S_{v_n}(f_{IF};t)}$ versus C.

in (5.65) appropriately separates the quasi-stationary and cyclostationary regimes.

The upper part of Fig. 5.26 shows the A_{conv} versus C and $\overline{S_{v_n}(f_{IF};t)}$ versus C curves together for the hard-switching mode. The cyclostationary regime ($C < C_{cyclo}$) coincides with the region where the conversion gain increases with C. Once C becomes larger than C_{cyclo}, both the voltage and noise go through the simple first-order filtering process and A^2_{conv} and $\overline{S_{v_n}(f_{IF};t)}$ show the same dependence upon C (plateau and roll-off). Therefore, the noise figure in (5.67) decreases with C roughly until C reaches C_{cyclo} and then remains constant afterwards as the filtering for noise and signal occurs at the same rate as shown in the lower part of Fig. 5.26. The lower part of the figure also compares the noise figure performance for the different switching modes. The best noise performance is achieved by operating the mixer in the soft-switching mode. However, the soft-switching mode has an inferior conversion gain as shown in Fig. 5.22. *For a given switching mode, the maximum conversion gain is achieved while the noise figure stays in the plateau as can be seen from Fig. 5.26. Thus the IF total capacitance should be chosen at the optimum design capacitance* $C_{optimum}$ *that maximizes the conversion gain and minimizes the NF. An IF capacitor in excess of* $C_{optimum}$ *will lower the gain with no effect on the NF.*

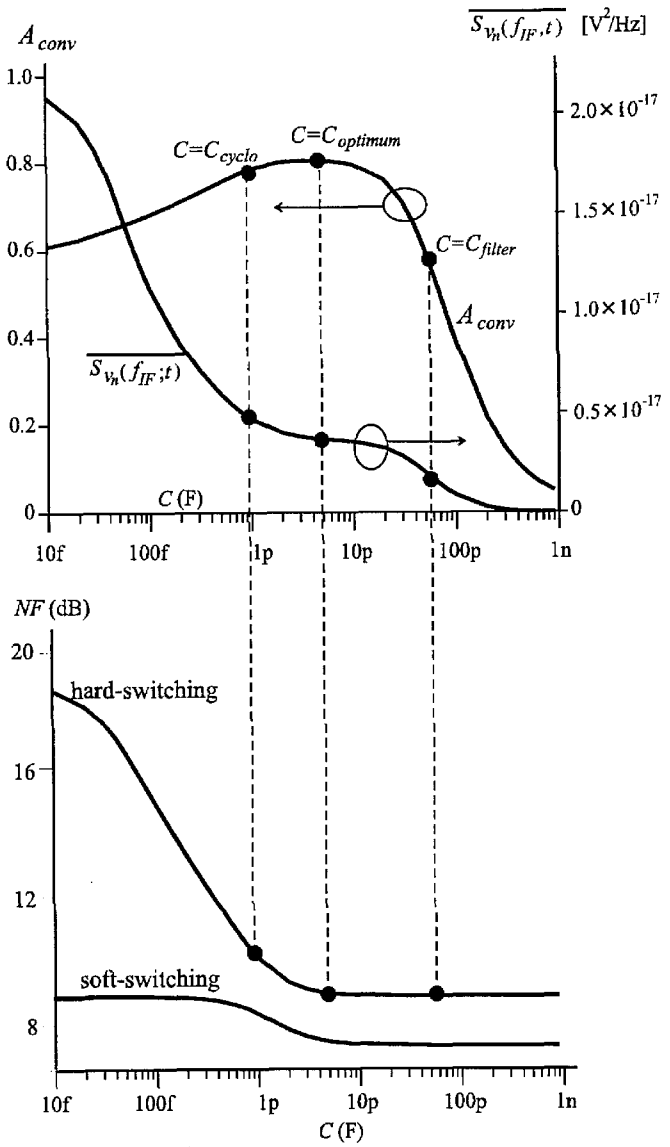

Figure 5.26: Simulated A_{conv}, $\overline{S_{v_n}(f_{IF};t)}$ and NF versus IF capacitance C.

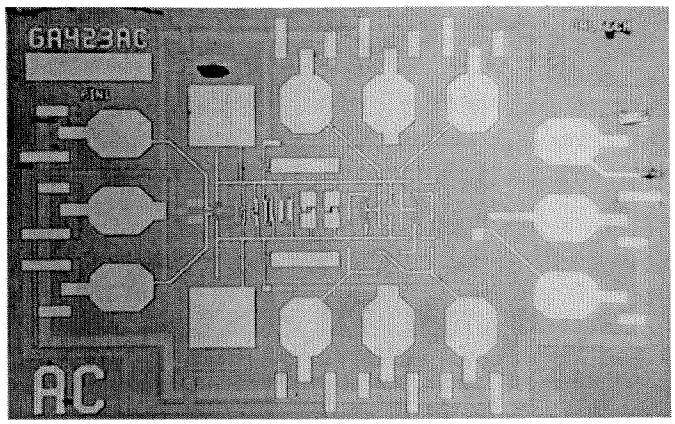

Figure 5.27: Die photo of the mixer chip.

5.8 Experimental Verification

5.8.1 Measurement Setup

Figure 5.27 shows the die photo of the mixer test chip fabricated in a BiCMOS 0.35 μm technology using only MOS transistors. Figure 5.28 shows the gain and noise figure measurement setup using an HP8570A noise figure measurement system and an HP860C diode noise source. The variable capacitor shown in the figure is implemented on chip with a set of multiple capacitors of different values layed-out in parallel across the balanced IF-port. By laser-trimming the capacitors one by one, we can obtain various IF capacitor values. Noise figure and voltage conversion gain were measured for each value of C. The range of the capacitor values used is comparable to or less than $C_{optimum}$ shown in Fig. 5.26 because the most interesting behavior of the mixer is observed when C is in the range of or smaller than $C_{optimum}$ while the behavior is typical when C is much larger than $C_{optimum}$.

The post amplifier following the mixer shown in Fig. 5.28 is a cascade of an on-chip amplifier followed by an off-chip amplifier. The post-amplifier plays the role of isolating the parasitics of the mixer from those of the off-chip interconnects and components, enabling a precise control of the IF-port capacitance. Additionally, as the switching mixer provides gain less than 1, the post amplifier is used to enhance the input noise to the noise figure measurement system, improving the accuracy of the measurement.

The chip has a direct electrical connection (broken lines) between the RF- and IF-ports that by-passes the mixer circuit as shown in Fig. 5.28. This connection was realized in order to de-embed the noise and gain contributions of the post amplifier. The de-embedding process is as follows: First, the by-pass lines are cut via laser-trimming and the noise figure and gain of the whole mixer-amplifier chain is measured at various IF-port capacitances. Second, in a different

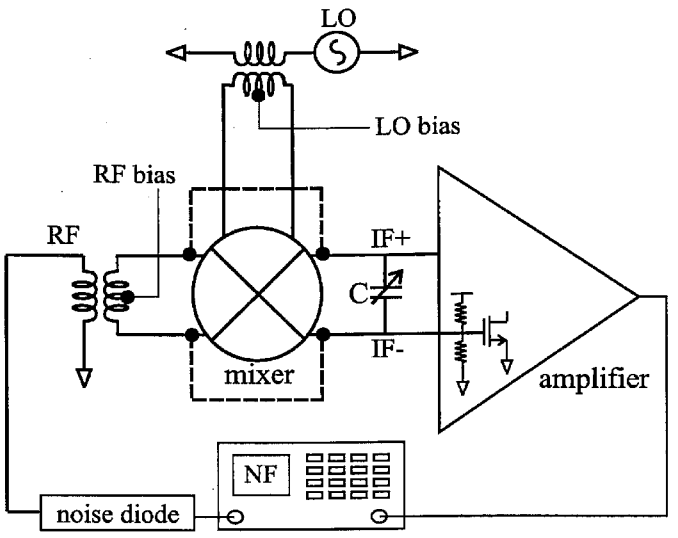

Figure 5.28: Mixer measurement setup.

chip, the RF port is routed directly to the amplifier input (IF-port) while the mixer is isolated from the circuit via laser trimming and the noise figure and gain of the amplifier is measured. Due to the parameter variations of the on- and off-chip components, using two different chips for the de-embedding purpose leads to an inevitable error. Therefore, the second procedure is performed on 7 chips and the statistical data are obtained in the de-embedding process. The input impedance of both the mixer and amplifier are important to take the impedance mismatching effects into account properly. They are characterized using an HP8753D network analyzer. The measurement frequencies are at f_{LO} = 300MHz, f_{IF}=10MHz as in the simulation and SSB noise figure is measured.

5.8.2 Measurement Results

Fig. 5.29 shows the measured A_{conv} versus C curves of the stand-alone mixer for different switching modes. This measurement result agrees with our theoretical predictions of the mixer conversion gain behavior (Compare with Fig. 5.22). The conversion gain enhancement can be clearly seen. The conversion gain grows with an increasing C for a while before it eventually reverses the trend. The size of the bump is larger in the harder-switching mode which has richer harmonic contents.

Fig. 5.30 depicts the measured noise figure versus C curves of the stand-alone mixer for different switching modes. This measurement result agrees well with our theoretical prediction (Compare with Fig. 5.26). First, the noise figure is higher in the hard-switching mode than in the soft-switching mode. Second, the cyclostationary effects are apparent in both switching modes. Third, the cyclostationary effect is more pronounced in the hard-switching than in the soft-switching, showing the rapid increase in the noise figure with the decreasing C ($\mathbf{A_4} \rightarrow \mathbf{A_1}$). In the soft-switching

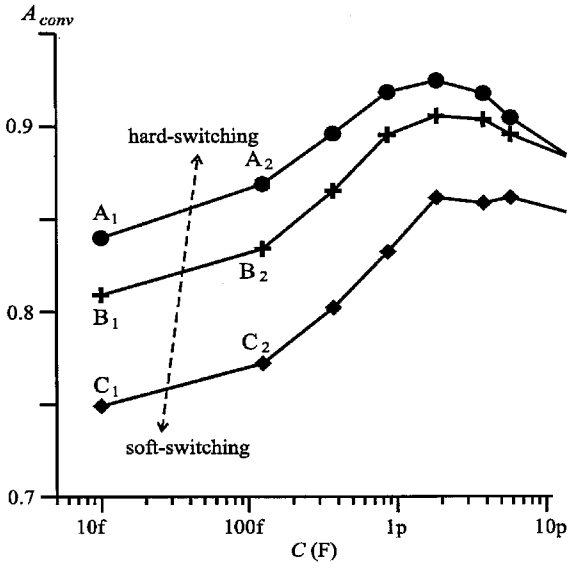

Figure 5.29: Measured voltage conversion gain versus IF capacitance for different switching modes.

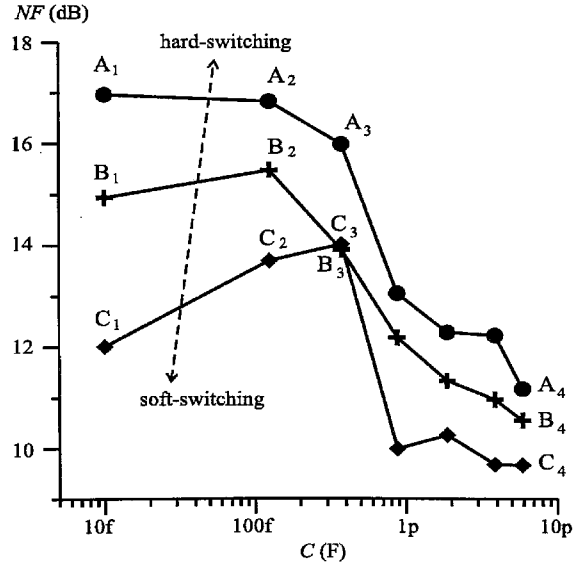

Figure 5.30: Measured noise figure versus IF capacitance C for different switching modes.

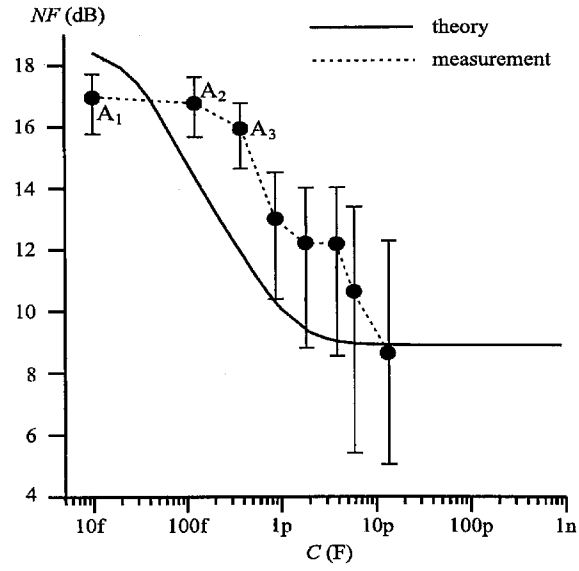

Figure 5.31: Simulated and measured noise figure versus IF capacitance C in the hard-switching mode.

mode, the resulting increase of the noise figure with the decreasing capacitance C ($\mathbf{C_4} \rightarrow \mathbf{C_1}$) is not as strong as in the hard-switching mode.

Fig. 5.31 directly compares the measured noise figure to the simulated noise figure solving (5.31) in the hard-switching mode. The error bar indicates the statistical variance which is obtained from the multiple sets of measurement. The measurement result clearly shows the cyclostationarity and bears the same trend as the theoretical behavior of the noise figure with the decreasing C. For a very small IF capacitance on the order of 100fF or less, the noise figure does not increase as fast as theoretically predicted with the decreasing C as can be seen from $\mathbf{A_2} \rightarrow \mathbf{A_1}$ in Fig. 5.31. This can be explained by the nonzero transistor and interconnect parasitic capacitors on the same order of magnitude. Even though the explicit capacitors are cut in $\mathbf{A_2} \rightarrow \mathbf{A_1}$, the parasitic capacitors are irremovable and their effects become dominant for the small IF capacitor values.

5.9 Summary

This chapter presented extensive study of time-varying filtering in switching mixers for both signal and cyclostationary noise. The study reveals two novel observations of switching mixers: noise figure degradation due to the cyclostationarity and conversion gain enhancement, both for small enough energy storing elements. The theoretical prediction was firmly verified through a direct measurement of CMOS switching mixers. The novel behavior of switching mixers depending on the size of energy storing elements provides immediate design insight into the mixer optimization.

Chapter 6 Noise in Time-Varying Autonomous Circuits

6.1 Introduction

This chapter presents one of the most important contributions of our work on statistical electronics, that is, fluctuations and thermodynamics in *time-varying autonomous circuits* [72], [73].

Differently from the time-varying driven circuits studied in the previous chapter, the time-varying autonomous circuits generate periodic signals autonomously without any input signals. Henceforth, time-varying autonomous systems are actually synonymous with "self-sustained oscillators" or simply put, "oscillators". These time-varying autonomous circuits are frequently used to provide frequency- or timing-references in a variety of systems encountered in science and engineering. For instance, as mentioned earlier in Chapter 2, any modern RF receivers necessitate reference frequencies generated by local oscillators to execute frequency downconversion.

In an ideal case where there is no noise, the oscillator has delta-function-like power spectral density at the fundamental frequency and its integer multiples (harmonics) as shown at the top of Fig. 6.1(a). In the time-domain, the zero-crossings of the noiseless oscillator signal lie at a certain constant plus the integer multiples of half of the oscillation period where the constant corresponds to the first zero-crossing. These zero-crossings of the noiseless oscillator are called *ideal zero-crossings* and they are shown with the "X" marks in Fig. 6.1.

In the presence of noise, the oscillator cannot provide absolutely accurate frequency reference. Noise spreads the oscillation energy around the center frequency and its harmonics, hence making the power spectrum shorter yet fatter when compared to the noiseless case, as shown in Fig. 6.1(b). This linewidth broadening in the oscillator power spectrum corresponds to the errors in the reference frequency, and is called *phase noise*. A quantitative definition of the phase noise will be given in Section 6.3. In the time-domain, the noisy oscillator's zero crossings drift away from the ideal zero crossings as time evolves, and after a sufficiently long time, the zero crossings are completely off from the ideal zero crossings as shown at the bottom of Fig. 6.1(b). This nonideal zero crossings result in errors in timing-reference, which are called *timing jitter*. The adverse effects of this frequency- or timing-reference noise on RF detection was discussed in Chapter 2.

Noise in oscillators has been a subject of active research for over half a century [63], [74] - [77]. The oscillator phase noise has been studied from several different angles, ranging from a mathematical

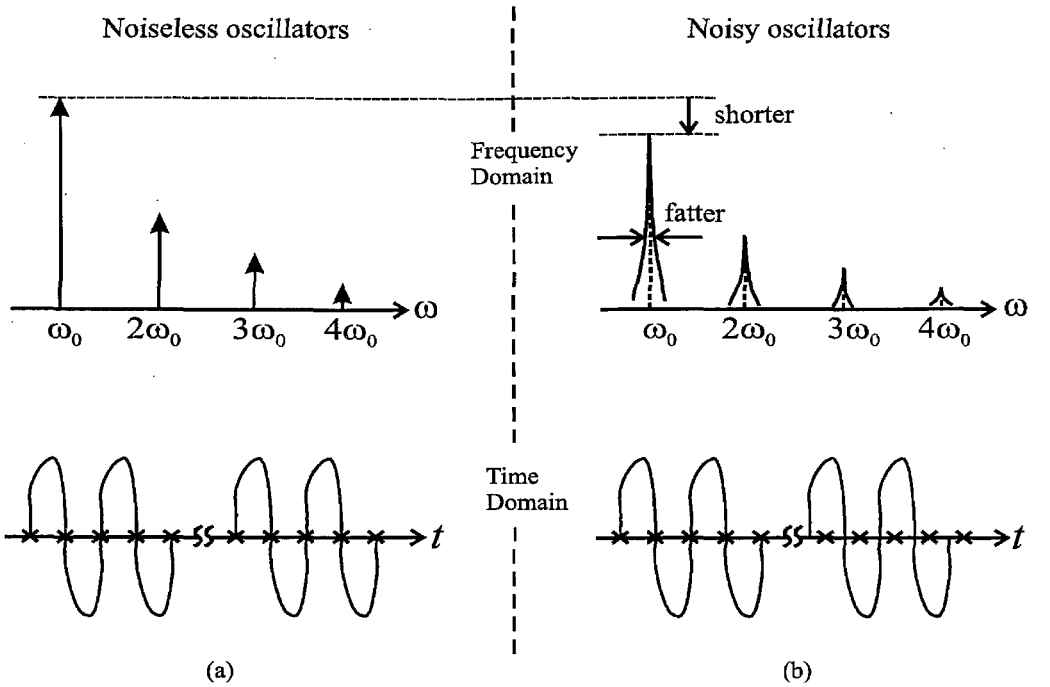

Figure 6.1: Oscillator output in frequency- and time-domain for (a) noiseless oscillators and (b) noisy oscillators. The "X" marks in the time-domain signify the ideal zero crossings.

physics treatment [74] to CAD-oriented, pure-mathematical methods [75], [76] and design-oriented approaches [63], [77], to name a few. The design-oriented approaches have evolved from a familiar linear time-invariant theory [77] to a more accurate time-varying theory [63], adding additional insight into the oscillator design. These theories have helped circuit designers better understand the evolution of noise in oscillators and predict more accurate phase noise, leading to lower noise designs.

However, most of these currently available theories are mainly phenomenology-based, and pay little attention to the connection between oscillator noise and statistical thermodynamics. If combined with fundamental physical understanding, the currently available noise modelings can be much more effective in designing low-noise oscillators. On the other hand, heavy dependence upon the phenomenology with little comprehension of the underlying physics of oscillator noise could block insight into design optimization, leading to design misconceptions. This is even more true as the contemporary oscillator noise models become more complicated with many cross-related design parameters to take into account more details for accurate noise prediction. An example of such design misconceptions is the widely held belief that a larger voltage swing always results in a better phase noise. However, as will be demonstrated later, increasing voltage swing actually *can* degrade phase noise performance.

This chapter presents a new theory of oscillator noise based on fundamental physics, bringing

transparent insight into the oscillator phase noise. Our work consists of four main results. First, by using an ensemble of identical oscillators as a tool, we derive the concept of *virtual damping*, which puts oscillators and resonators in a unified framework. It will be shown that the virtual damping rate is a fundamental measure of phase noise which can be verified experimentally. Second, we demonstrate the direct correspondence between the virtual damping rate and Einstein relation discussed in Chapter 3. Our approach reveals the underlying physics of oscillator phase noise by identifying its two essential elements: *sensitivity* and *friction* (*energy loss*). Also this treatment leads to a physical definition of the loaded quality factor of oscillators, establishing a link between fluctuation-based and dissipation-based phase noise models. Third, the virtual damping concept results in another useful concept, *linewidth compression*, leading to a general oscillator noise optimization principle. Fourth, thermodynamic concepts involved in the oscillator noise processes are clarified, providing more fundamental understanding of the oscillator noise. Our theoretical development is positively verified through virtual damping measurements, low-noise design of oscillators, and direct measurements of the oscillator noise.

Additionally, this work utilizes an insightful graphical design-optimization method for oscillator design. This graphical method facilitates the application of our oscillator noise theory to the practical low-noise design of oscillators. We have demonstrated that identifying the feasible design points using this graphical method is extremely helpful in a complex circuit design environment.

This chapter is organized as follows. Sections 6.2 and 6.3 review the fundamentals of self-sustained oscillators and the oscillator phase noise. In Section 6.4, we develop the concept of virtual damping and demonstrate phase noise as its natural outcome using both theoretical and experimental treatments. In Section 6.5, we derive the virtual damping rate based on physical arguments using the Einstein relation and discuss its physical implications. Section 6.6 mathematically confirms this physical argument by using the Langevin and the Fokker-Planck equations. Section 6.7 develops another useful concept of *linewidth compression*, combining the results of Sections 6.4 and 6.5. From this linewidth compression concept, a general oscillator noise optimization principle is established. In Section 6.8, we present a low-noise design example.

6.2 Self-Sustained Oscillator Fundamentals

Before directly diving into the oscillator noise problem, let us first review the fundamentals of self-sustained oscillation using LC-oscillators as an example.

6.2.1 Self-Sustained Oscillation

A self-sustained LC oscillator model is shown in Fig. 6.2. The resistance, R, is an explicit representation of the parasitic tank loss. The active devices are used to compensate this tank loss by

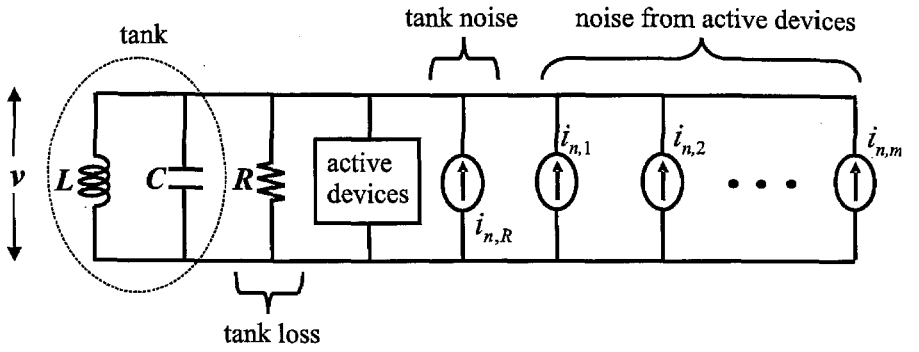

Figure 6.2: A generic model for a self-sustained LC oscillator.

converting dc energy to RF energy and injecting it into the LC tank. The current sources in the model represent equivalent current noise generated from the tank loss and the active devices.

There exist two characteristic frequencies (or equivalently, time constants) involved in the dynamics of the LC oscillator. One is the resonant frequency (oscillation frequency), ω_0, of the oscillator and the other is the inverse of the time-constant, τ, due to the coupling of the resistance, R, to the capacitance, C:

$$\omega_0 = \frac{1}{\sqrt{LC}} \tag{6.1}$$

$$\omega_\tau \equiv \frac{1}{\tau} = \frac{1}{RC} \tag{6.2}$$

These two characteristic frequencies play important roles in understanding the self-sustained oscillation as will be seen shortly.

If the noise in the circuit is ignored, the voltage, $v(t)$, across the LC tank in Fig. 6.2, can be described by the following nonlinear second-order differential equation:

$$\ddot{v} + \omega_0^2 v + \omega_\tau f(v)\dot{v} = 0 \tag{6.3}$$

Here, $f(v)$ is a unitless, voltage-dependent function, and determined by the specific arrangement of the active devices in Fig. 6.2. The first two terms of the above equation represent the frequency selection mechanism utilizing the LC tank. The third term is responsible for the self-sustaining mechanism of the oscillator in which $f(v)$ plays a key role. $f(v)$ becomes negative when $|v|$ approaches zero, leading to "negative damping" or *amplitude boosting*. On the other hand, $f(v)$ becomes positive when $|v|$ becomes large, resulting in the normal damping or, *amplitude limiting*. The amplitude boosting is also responsible for the oscillation start-up and hence the following condition guarantees

the oscillation start-up and its sustenance:

$$f(0) < 0 \tag{6.4}$$

Let us denote the effective parallel conductance due to the active devices as $g_{active}(v)$. In self-sustained oscillators, this effective parallel conductance at $v = 0$ is negative [8]. If the magnitude of $g_{active}(0)$ is larger than the tank loss ($|g_{active}(0)| > 1/R$), the oscillator will start up and will be sustained. Hence, the small-signal loop gain, α, is defined as the ratio of $|g_{active}(0)|$ to $1/R$:

$$\alpha = R \cdot |g_{active}(0)| \tag{6.5}$$

and the start-up condition becomes

$$\alpha > 1 \tag{6.6}$$

Now let us check the consistency between (6.4) and (6.6). Since $f(v) = 1$ in the absence of the active devices, $g_{active}(v)$ is given by

$$g_{active}(v) = \frac{f(v) - 1}{R} \tag{6.7}$$

Combining (6.5) and (6.7), we obtain the following expression for the small-signal loop gain:

$$\alpha = R \cdot \frac{|f(0) - 1|}{R} = 1 - f(0) \tag{6.8}$$

demonstrating the consistency between (6.6) and (6.4).

Self-sustained oscillation can be insightfully understood using an energy argument. The tank energy at resonance, E_{tank}, is given by

$$\begin{aligned} E_{tank} &= \frac{1}{2}Cv^2 + \frac{1}{2}Li^2 \\ &= \frac{1}{2}C(v^2 + \frac{\dot{v}^2}{\omega_0^2}) \\ &= \frac{1}{2}C(v^2 + w^2) \end{aligned} \tag{6.9}$$

where $i = C\dot{v}$ is the current in the LC tank and we have defined a new variable, w, as

$$w \equiv \frac{\dot{v}}{\omega_0} = \frac{i}{\omega_0 C} \tag{6.10}$$

This new variable, w, is essentially the same as the current, i, in the tank, except the scaling factor $1/(\omega_0 C)$. From this point on, we will call this variable, w, *scaled current*. Note that w has the unit

of voltage.

From (6.9), the time-derivative of the tank energy is obtained as

$$\begin{aligned} \frac{dE_{tank}}{dt} &= LC^2\dot{v}(\ddot{v}-\omega_0^2 v) \\ &= -\frac{1}{R\omega_0^2}\dot{v}^2 f(v) \end{aligned} \tag{6.11}$$

where we have used (6.3) to obtain the second line. As can be seen, for $f(v) < 0$, the time-derivative of the tank energy is positive and hence the tank energy increases. This makes sense since $f(v) < 0$ corresponds to the negative damping or energy pumping into the LC tank as mentioned earlier. On the other hand, if $f(v) > 0$, the time-derivative of the tank energy becomes negative, corresponding to the tank energy decrease due to the normal damping. When the oscillator reaches steady-state, these energy loss and gain per one period should be equal and hence

$$\Delta E_{tank} = -\frac{1}{R\omega_0^2}\int_0^{2\pi/\omega_0} \dot{v}^2 f(v)dt = 0 \tag{6.12}$$

where ΔE_{tank} signifies the net energy change in the tank per period. This equation will be used to determine the oscillation amplitude later.

6.2.2 Examples

Van der Pol oscillator

Van der Pol used $f(v) = av^2 - b$ ($a > 0$, $b > 0$) in (6.3) to carry out his classic study on the self-sustained oscillators [78], [79]. For the Van der Pol oscillator, the differential equation (6.3) becomes

$$\ddot{v} + \omega_0^2 v + \gamma\dot{v}(av^2 - b) = 0 \tag{6.13}$$

In this case, $f(0) = -b$ and hence the start-up condition for the Van der Pol oscillator is $b > 0$ according to (6.4). Additionally, the small signal loop gain is given by

$$\alpha = 1 + b \tag{6.14}$$

according to (6.8). In the Van der Pol oscillator, when $|v|$ is small enough, $f(v) = av^2 - b$ becomes negative, resulting in the amplitude boosting. When $|v|$ grows large enough, $f(v) = av^2 - b$ becomes positive, limiting the amplitude. The Van der Pol oscillator is rather a simple model but captures the essence of nonlinear self-sustained oscillation, and hence is widely used to study the generic characteristics of the self-sustained oscillator.

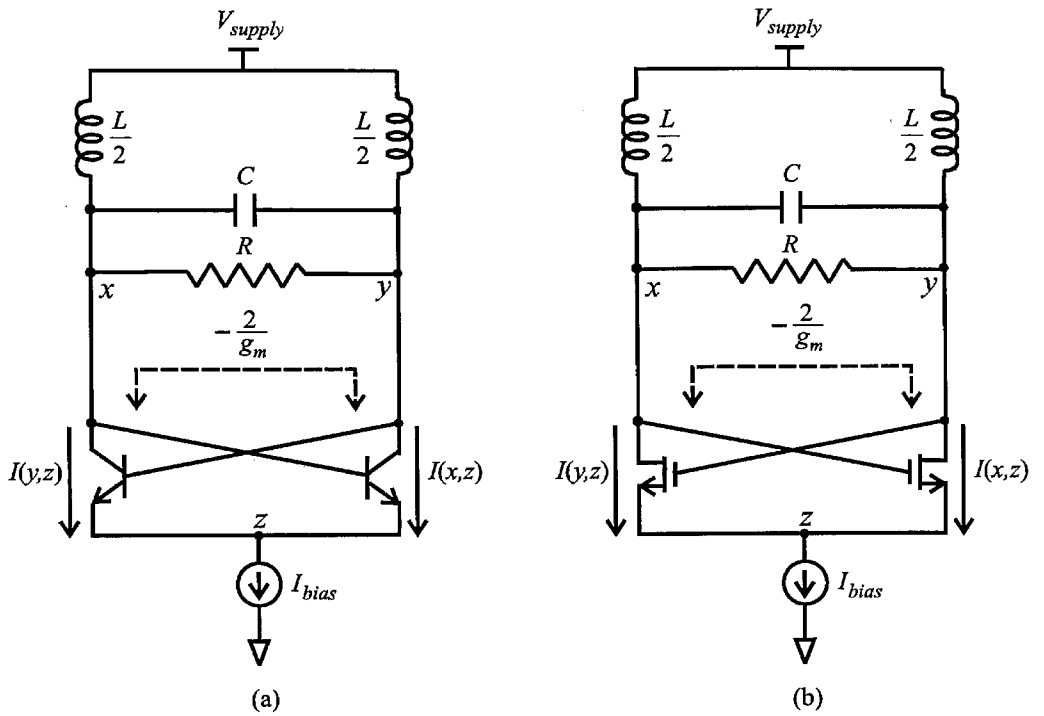

Figure 6.3: LC cross-coupled oscillators with (a) bipolar transistors and (b) MOS transistors. In the figures, R explicitly represents the parasitic tank loss.

Circuit Examples

Practical circuit examples of the self-sustained oscillators are shown in Fig. 6.3(a) and (b), which schematically depict LC oscillators with cross-coupled bipolar transistor pairs and cross-coupled MOS transistor pairs, respectively. The cross-coupled pairs act as a negative resistance when the magnitude of the differential tank voltage, $v = x - y$, is small enough, hence introducing the amplitude boosting mechanism to the circuit. For both of the circuits, the differential equations for the differential tank voltage, $v = x - y$, are given by

$$\ddot{v} + \omega_0^2 v + \omega_\tau \dot{v} + \frac{1}{2C}\frac{d}{dt}[I(y,z) - I(x,z)] = 0 \tag{6.15}$$

where $I(x,z)$ and $I(y,z)$ represent currents flowing through the transistors as shown in Fig. 6.3 and are functions of the voltage difference, $x - z$ and $y - z$, respectively, to the first order. In the oscillator with the bipolar transistors, the base currents are being neglected.

For the oscillator in Fig. 6.3(a), (6.15) becomes

$$\ddot{v} + \omega_0^2 v + \omega_\tau \dot{v} \underbrace{[1 - \frac{Rg_m}{2}\cosh^{-2}(\frac{v}{2V_T})]}_{f(v)} = 0 \tag{6.16}$$

where we have used the exponential relation between the base-emitter voltage and the collector current [46]. In (6.16), g_m is the transconductance of the bipolar transistor when the dc collector current is $I_{bias}/2$ and $V_T = k_B T/e$. Hence, $f(v)$ in (6.3) is given by $f(v) = [1 - (Rg_m/2)\cosh^{-2}(v/2V_T)]$ in this case.

For the oscillator in Fig. 6.3(b), ignoring the triode-regime of MOS transistors, we can reexpress (6.15) as

$$\ddot{v} + \omega_0^2 v + \omega_\tau \dot{v} \underbrace{[1 - \frac{Rg_m}{2} \frac{1 - (v/V_{GS})^2}{\sqrt{1 - (v/V_{GS})^2/2}}]}_{f(v)} = 0 \tag{6.17}$$

where we have used the quadratic relation between the drain current and the gate-source voltage assuming that the MOS transistors are the long channel transistors [46]. Here, g_m is the transconductance of the MOS transistor when the dc drain current is $I_{bias}/2$ and V_{GS} is the gate-source voltage of the MOS transistor when the dc drain current is $I_{bias}/2$.

In both (6.16) and (6.17), the start-up condition (6.4) results in

$$\frac{2}{g_m} < R \tag{6.18}$$

This result can be interpreted from a circuit standpoint. The effective input resistance looking into the cross-coupled pair is shown to be $-2/g_m$ when $v = 0$ as shown in Fig. 6.3. If the oscillator is to start up, the magnitude of this negative resistance should be smaller than the tank loss, hence agreeing with (6.18). Note that in both cases, $f(v)$ becomes positive for a sufficiently large $|v|$, leading to the amplitude limiting.

6.2.3 State-Space and Limit Cycle

It is often convenient to view the dynamics of the LC oscillator in the two-dimensional *state-space* where the two independent variables constituting the state-space are the voltage across the tank, v, and the scaled current in the tank, w, defined by (6.10). Here the use of the scaled current, w, instead of the current, i, is due to the mathematical symmetry between v and w as seen in (6.9) and the resultant convenience but not for any fundamental reasons.

In the course of oscillation, the voltage across and the current in the LC tank periodically change and hence, the dynamics of the oscillator can be mapped onto a solution trajectory in the $v - w$ state-space as shown in Fig. 6.4. If we decompose (6.3) into the following simultaneous differential equations,

$$\begin{aligned} \dot{v} &= \omega_0 w \\ \dot{w} &= -\omega_0 v - \omega_\tau f(v) w \end{aligned} \tag{6.19}$$

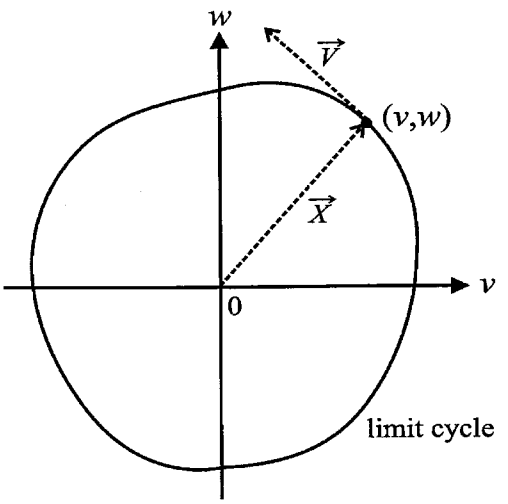

Figure 6.4: $v - w$ state-space and limit cycle.

at any given state-space point $\vec{X} = (v, w)$, the state-space velocity $\vec{V} \equiv (\dot{v}, \dot{w}) = (\omega_0 w, -\omega_0 v - \gamma f(v) w)$ is known from (6.19) and accordingly, we can always find the oscillator trajectory at least in principle in the state-space with a given initial condition. Note that for a purely harmonic oscillator ($\omega_\tau = 0$), (6.19) implies that $\vec{X}$ and $\vec{V}$ are always orthogonal and the solution trajectory for the oscillation becomes a circle centered at the origin. The steady-state solution trajectory representing the oscillation is a closed curve due to the periodicity and is called a *limit cycle* [80]. This limit cycle represents a periodic solution or rather a family of periodic solutions differing only in phase for the differential equation (6.3). All other solution curves ultimately get attracted to the limit cycle after the initial transient fades out. Generally speaking, for any differential equation that has the limit cycle, all solutions of it are ultimately periodic with the same period and amplitude determined by the equation, while only the phase depends on the initial condition [80].

This peculiar property of the self-sustained oscillator directly affects its fluctuation behavior when it is subject to noise. The fluctuations would remain small in the amplitude direction due to the nonlinear oscillator's attribute to return back to the limit cycle. However, fluctuations in the direction along the limit cycle has no tendency to return since the nonlinear oscillator has no fundamental mechanism forcing the changed phase back to the original phase. Consequently, the oscillator phase undergoes "random walk" along the limit cycle in the presence of noise and the probability density of the phase spreads out on the limit cycle, just as the Brownian particle randomly walks in space and the probability density of its displacement diffuses out in space. These fluctuation behaviors of the oscillator will be treated in a quantitative manner later in this chapter.

6.2.4 Approximation for Resonator-Based Oscillators

In general, it is a cumbersome task to analytically solve the nonlinear differential equation (6.3). Fortunately, for resonator-based oscillators such as LC oscillators, we can take a certain approximation to study the oscillator dynamics as far as the unloaded tank quality factor, Q, is sufficiently large [81]. In this subsection, we will study LC oscillator's deterministic dynamics using this approximation.

Earlier in this section, we have mentioned that there are two characteristic frequencies involved in the dynamics of the LC oscillator, which are ω_0 and ω_τ defined in (6.1) and (6.2), respectively. The ratio of these two frequencies is no more than the unloaded tank quality factor, Q [7]:

$$\frac{\omega_0}{\omega_\tau} = RC\omega_0 = Q \tag{6.20}$$

Now in a new time frame $t' \equiv \omega_0 t$ in which the angular frequency becomes 1, (6.3) transforms to

$$\ddot{v} + v + \frac{1}{Q}\dot{v}f(v) = 0 \tag{6.21}$$

where the time-derivative signified with the dots is with respect to the new time, t'. Therefore, if $\omega_0/\omega_\tau = Q \gg 1$ which is typical in LC oscillators, the third nonlinear term is rather weakly coupled to the first two harmonic oscillator terms, resulting in the near-sinusoid steady-state oscillation waveforms.

Typical time evolution of $v(t)$ including the initial transient in this high-Q case is depicted in Fig. 6.5. As will be shown shortly, the amplitude growth in the initial transient occurs with the time constant on the order of ω_τ^{-1}. Since $\omega_0 \gg \omega_\tau$ for $Q \gg 1$, there are many oscillation cycles in the initial transient as shown in Fig. 6.5. Once the oscillation reaches the steady-state, the waveform is near-sinusoid due to the weak coupling of the nonlinearity. Hence in this weak nonlinearity case ($Q \gg 1$), we can use an approximation in which the steady-state solution of (6.3) is regarded as a sinusoid, that is, $v(t) \approx r_0 \cos(\omega_0 t)$, where r_0 is the amplitude of the oscillation, hence the name, *near-sinusoid approximation.*

Let us see how we can determine the oscillation amplitude in this high-Q case using the near-sinusoid approximation. Earlier, we noted that the tank energy loss and gain per period should be equal in the steady-state oscillation, leading to (6.12). In the case of the Van der Pol oscillator, (6.12) becomes

$$\int_0^{2\pi/\omega_0} \dot{v}^2 f(v)dt \;=\; \int_0^{2\pi/\omega_0} \dot{v}^2(av^2 - b)dt = 0 \tag{6.22}$$

By using the near-sinusoid approximation, we plug $v(t) \approx r_0 \cos\omega_0 t$ into the equation above, ob-

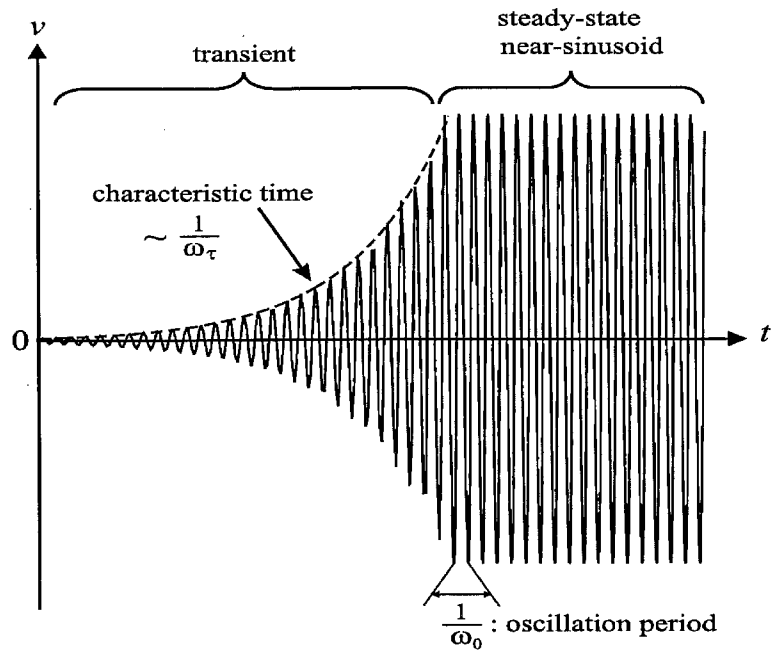

Figure 6.5: A typical waveform for LC-type oscillators when the nonlinearity is weakly coupled, or $Q \gg 1$.

taining

$$r_0 \approx \sqrt{\frac{4b}{a}} \tag{6.23}$$

which is the amplitude of the Van der Pol oscillation in the high-Q case. Earlier, we have noted that b and the small-signal loop gain, α, of the Van der Pol oscillator are related by (6.14) and hence (6.23) implies that a larger small-signal loop gain leads to a larger voltage swing in the Van der Pol oscillator.

In the case of the weak nonlinearity coupling, we can not only calculate the steady-state amplitude, r_0, but also evaluate the time-evolution of the oscillation amplitude in the transient. The technique used to obtain a differential equation for this time-evolution of the oscillation amplitude is so-called "two-timing" method [81], which utilizes the fact that the two characteristic frequencies ω_0 and ω_τ are in different scales for this high-Q case.

In the Van der Pol oscillator, using this two-timing method, we can show that the differential equation for the amplitude evolution is given by

$$\frac{dr}{dt} = \frac{a\omega_\tau r}{8}\left(\frac{4b}{a} - r^2\right) \tag{6.24}$$

where the detailed derivation is given in Appendix 1. In the steady-state, there is no variation in r with time and hence the right-hand side of (6.24) is zero, resulting in the amplitude of $r_0 = \sqrt{4b/a}$, in perfect agreement with (6.23).

The solution of (6.24) is given by

$$r(t) = \frac{1}{\sqrt{A + \frac{b}{\alpha}\omega_\tau t}} \tag{6.25}$$

where the constant A is determined by the initial condition. Using (6.25), we can calculate the start-up time of the oscillation. For example, the time for r to reach $0.9r_0$ starting from $r(0) = 0.1r_0$ is given by

$$\Delta t \approx 6\frac{RC}{b} = 6\frac{\tau}{\alpha - 1} \tag{6.26}$$

where we have used (6.2) and (6.14). As can be seen, the start-up time, Δt, is proportional to the RC-time constant $\tau = RC = 1/\omega_\tau$ of the oscillator as can be intuitively expected. Additionally, the start-up time is inversely proportional to the small-signal loop gain, α, that is, a larger small-signal loop gain results in a smaller start-up time. Also note that the start-up time goes to infinity with $\alpha \to 1$, which implies that there is no oscillation unless $\alpha > 1$. Finally, the start-up time is on the order of $\tau/b = 1/(b\omega_\tau) \sim 1/\omega_\tau$ unless the small-signal loop gain is excessively larger than 1. This time-scale for the start-up in the initial transient was already indicated in Fig. 6.5.

6.3 Phase Noise Fundamentals

This section reviews the fundamentals of oscillator phase noise. As an analysis vehicle, we will use the LC oscillator model shown in Fig. 6.2.

6.3.1 Phase Diffusion

The voltage, $v(t)$, across the LC tank shown in Fig. 6.2 can be expressed as

$$v(t) = r(t)\cos[\omega_0 t + \phi(t)] \tag{6.27}$$

where $r(t)$ represents its amplitude, r_0, plus the fluctuation (amplitude noise) around r_0. $\phi(t)$ represents the fluctuation in the oscillator phase. The total oscillator phase, $\theta(t)$, is defined as

$$\theta(t) \equiv \omega_0 t + \phi(t) \tag{6.28}$$

As discussed in Subsection 6.2.3, the fluctuations remain small in the amplitude direction in the limit cycle of Fig. 6.4 due to the oscillator's tendency to return back to the limit cycle. Henceforth, we will ignore the amplitude noise and replace $r(t)$ with the amplitude r_0. Then (6.27) simplifies to

$$v(t) = r_0\cos[\omega_0 t + \phi(t)] \tag{6.29}$$

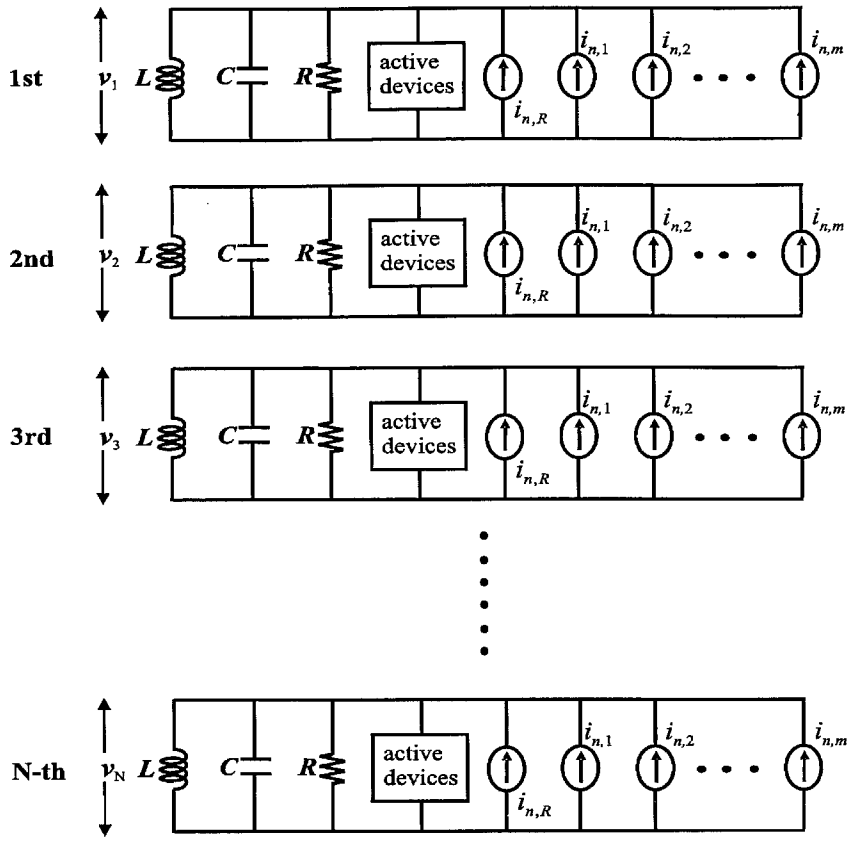

Figure 6.6: An ensemble of N identical oscillators.

The fluctuations in the direction along the limit cycle has no tendency to return since the oscillator has no fundamental mechanism forcing the changed phase back to the original phase. Consequently, the oscillator phase, $\phi(t)$, in (6.29) "randomly walks" along the limit cycle in the presence of noise and hence experiences the diffusion process. To see this *phase diffusion* more clearly, let us consider an ensemble of N identical oscillators shown in Fig. 6.6, which are assumed to be all at the same initial phase at $t = 0$. N is a very large number. In the state-space shown in Fig. 6.7(a), the oscillation points from the ensemble are all on the top of one another initially, rotating on the limit cycle together. However, the rotating oscillation points diffuse along the limit cycle with time, ultimately getting widespread on the limit cycle after a sufficiently long time.

Based on the ensemble of oscillators, we can define the probability distribution of the phase, $P(\phi, t)$, and the probability distribution of the total phase, $P(\theta, t)$, where $\theta(t) = \omega_0 t + \phi(t)$ as defined in (6.28). Figure 6.7(b) shows the time-evolution of $P(\phi, t)$. Since all the oscillators in the ensemble are at the same initial phase (and let's assume that the initial phase is zero without loss of generality), the initial distribution is given by $P(\phi, t = 0) = \delta(\phi)$. As time goes by, the phase undergoes diffusion and the probability distribution of ϕ spreads out. This phase diffusion

is analogous to the diffusion of the Brownian particle in space discussed in Section 3.1, where the time-evolution of the displacement probability density is depicted in Fig. 3.6. If the phase diffusion is due to white noise, the variance of ϕ is given by

$$\langle \phi^2(t) \rangle = 2Dt \tag{6.30}$$

analogous to (3.49). D in the above equation is called *phase diffusion constant* and it depends upon various circuit parameters. As will be seen shortly, the phase diffusion constant is the sole factor that determines the amount of error in the reference frequency (phase noise). If D is very small (*e.g.*, in atomic clock.), the reference-frequency error will be small. If D is relatively large (*e.g.*, in relaxation oscillators.), there will be larger errors in the reference-frequency.

Figure 6.7(b) depicted the phase diffusion in the absence of any boundary conditions, *i.e.*, the phase, ϕ, was assumed to diffuse in the $[-\infty, \infty]$ space. An alternative way of looking at the phase diffusion is to confine the diffusion space to $[-\pi, \pi]$ and impose the boundary conditions:

$$\begin{aligned} P(-\pi, t) &= P(\pi, t) \\ \frac{\partial P(\phi, t)}{\partial \phi}|_{\phi=\pi} &= \frac{\partial P(\phi, t)}{\partial \phi}|_{\phi=-\pi} \end{aligned} \tag{6.31}$$

Figure 6.8 shows the time evolution of $P(\phi, t)$ under these boundary conditions. As can be seen, the phase distribution will ultimately tend to a uniform distribution across the whole range of phase, $[-\pi, \pi]$. With or without the boundary conditions, the rate with which the phase diffuses is always given by the phase diffusion constant, D.

In Fig. 6.8, the uniform phase probability distribution at $t = \infty$ constitutes the most probable (the *maximum entropy*) state. According to the second law of thermodynamics, the entropy of the ensemble of the oscillators will grow and ultimately evolve to this maximum entropy state, which cannot be prevented by any means. The phase diffusion constant D hence is a direct measure of how fast the entropy grows. Even though we cannot stop entropy from growing, we have a control over the *entropy-growth-rate*, or the phase diffusion constant, D, to a certain degree. Minimization of reference frequency errors (minimization of D) is equivalent to minimization of the entropy-growth rate.

The total oscillator phase $\theta(t)$ in (6.28) has both drift and diffusion components in it. $\theta(t)$ drifts with a constant velocity of ω_0 while $\phi(t)$ in the total phase undergoes diffusion. In the time-evolution of the probability density of the total phase, $P(\theta, t)$, shown in Fig. 6.7(c), the center of the distribution moves with the velocity of ω_0 while the distribution around the center spreads out with time. This is analogous to the time-evolution of the probability distribution of the displacement of a forced Brownian particle, which is shown in Fig. 3.14.

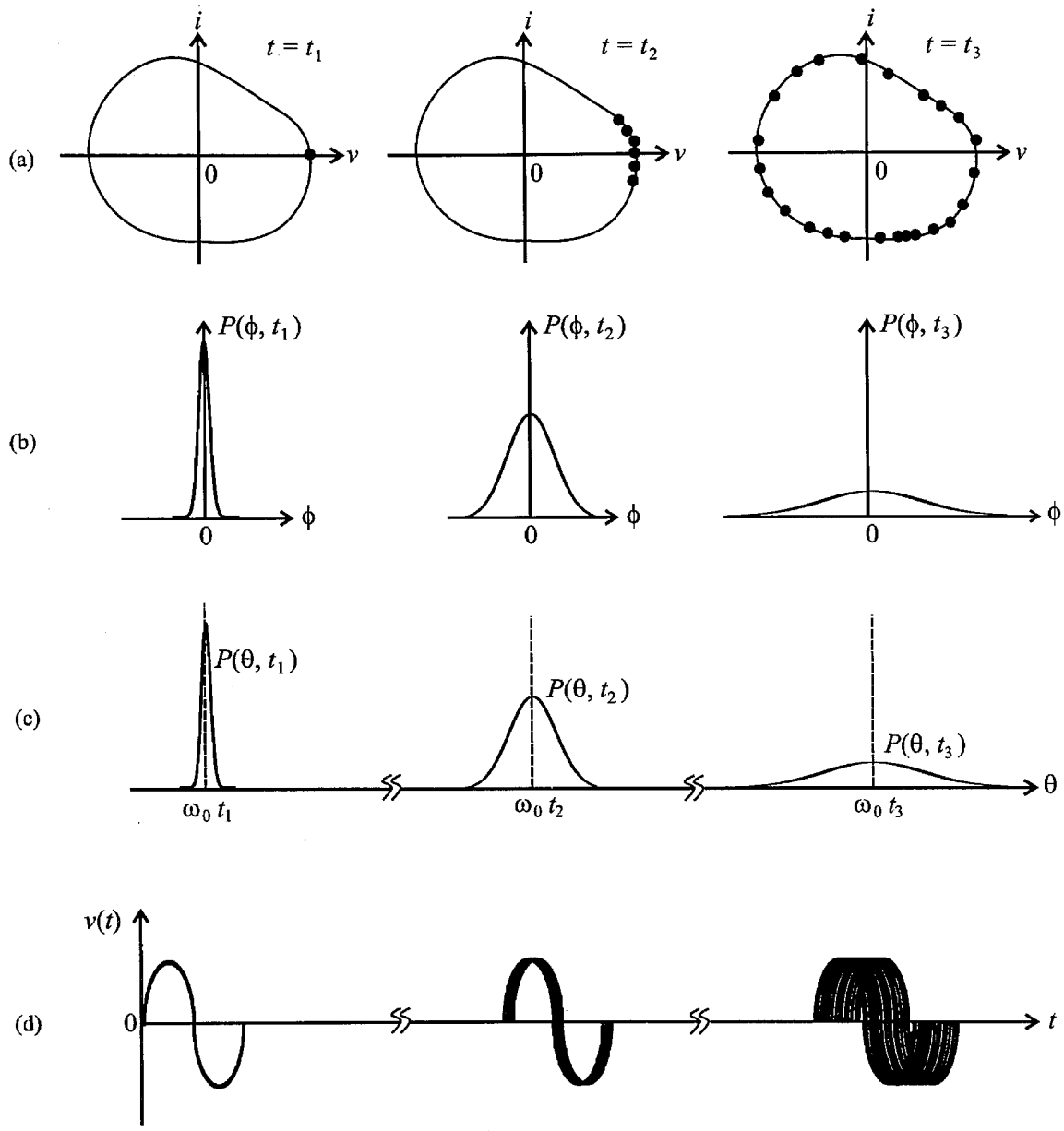

Figure 6.7: (a) Oscillation points from the ensemble in the state-space. (b) Time evolution of $P(\phi, t)$. (c) Time evolution of $P(\theta, t)$. (d) Output signals from the ensemble at different times.

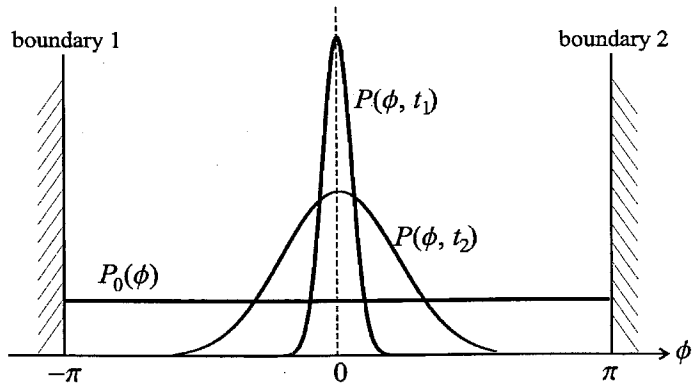

Figure 6.8: Time evolution of $P(\phi, t)$ in the presence of boundary condition.

A time-domain picture of the phase diffusion is shown in Fig. 6.7(d) for the ensemble of oscillators. At the start of oscillation, the oscillator output waveforms are all on the top of each other since the oscillators in the ensemble are at the same initial phase. After a sufficiently long time, however, the output signals from the ensemble become incoherent due to the phase diffusion (a.k.a., jitter accumulation) and eventually go totally "out of sync".

Summarizing, this subsection introduced the concept of *phase diffusion* and defined the phase diffusion constant, D. We have visualized the phase diffusion in state-space and time-domain as well as in terms of the time-evolution of phase probability distributions. Now in the following subsection, we will study how the phase diffusion affects the oscillator power spectrum in the frequency-domain, leading to a definition of the phase noise.

6.3.2 Phase Noise

In this subsection, we evaluate the oscillator power spectrum in the presence of white noise. We have previously mentioned that in the presence of white noise, the oscillator phase undergoes diffusion (Wiener process) and its variance evolves with time according to (6.30). More generally, the autocorrelation of the phase is given by [33], [74]

$$\langle \phi(t_1)\phi(t_2) \rangle = 2D \min\{t_1, t_2\} \tag{6.32}$$

which is a key characteristic of the Wiener process. Note that this equation subsumes (6.30).

To calculate the power spectral density of $v(t)$ in (6.29), let us first evaluate the autocorrelation function for $v(t)$:

$$R_{v,v}(t_1, t_2) \equiv \langle v(t_1)v(t_2) \rangle .$$

$$
\begin{aligned}
&= r_0^2\langle\cos[\omega_0 t_1 + \phi(t_1)]\cdot\cos[\omega_0 t_2 + \phi(t_2)]\rangle \\
&= r_0^2\cos(\omega_0 t_1)\cos(\omega_0 t_2)\langle\cos\phi(t_1)\cos\phi(t_2)\rangle + r_0^2\sin(\omega_0 t_1)\sin(\omega_0 t_2)\langle\sin\phi(t_1)\sin\phi(t_2)\rangle \\
&\quad -r_0^2\cos(\omega_0 t_1)\sin(\omega_0 t_2)\langle\cos\phi(t_1)\sin\phi(t_2)\rangle - r_0^2\sin(\omega_0 t_1)\cos(\omega_0 t_2)\langle\sin\phi(t_1)\cos\phi(t_2)\rangle
\end{aligned} \tag{6.33}
$$

For a Gaussian distribution of $\phi(t)$ at any given time, the statistical averages in the above equation can be calculated as shown in Appendix 2, simplifying (6.33) to

$$
R_{v,v}(t_1,t_2) \tag{6.34}
$$

$$
\begin{aligned}
&= r_0^2\cos[\omega_0(t_1-t_2)]\cdot\exp\left[-\frac{\langle\phi^2(t_1)\rangle + \langle\phi^2(t_2)\rangle - 2\langle\phi(t_1)\phi(t_2)\rangle}{2}\right] \\
&\quad + r_0^2\cos[\omega_0(t_1-t_2)]\cdot\exp\left[-\frac{\langle\phi^2(t_1)\rangle + \langle\phi^2(t_2)\rangle + 2\langle\phi(t_1)\phi(t_2)\rangle}{2}\right]
\end{aligned} \tag{6.35}
$$

Utilizing the special properties of $\phi(t)$ given in (6.32), the above equation can be further simplified to

$$
R_{v,v}(t_1,t_2) = r_0^2\cos[\omega_0(t_1-t_2)]\cdot\left[e^{-D|t_1-t_2|} + e^{-D(t_1+t_2+2\min\{t_1,t_2\})}\right] \tag{6.36}
$$

By defining $\tau = t_2 - t_1$ and noting that the second term in the above equation is an initial transient, we can reexpress (6.36) as

$$
R_{v,v}(\tau) = r_0^2\cos\omega_0\tau\cdot e^{-D|\tau|} \tag{6.37}
$$

The power spectral density of the oscillator output is the Fourier transform of the autocorrelation function (6.37) and can be shown to be the familiar Lorentzian shape [74]

$$
\begin{aligned}
S_v(\omega) &= r_0^2\frac{D}{D^2 + (\omega-\omega_0)^2} \\
&= r_0^2\frac{D}{D^2 + (\Delta\omega)^2} \\
&\equiv S_v(\Delta\omega)
\end{aligned} \tag{6.38}
$$

where $\Delta\omega$ in the second line is defined as $\Delta\omega \equiv \omega - \omega_0$ and is called *offset frequency*. Note that regardless of D, the total oscillation energy is kept at the same value, $r_0^2/2$, as can be easily seen by integrating $S_v(\omega)$ over the whole frequency range:

$$
\langle v^2\rangle = \int_{-\infty}^{\infty} S_v(\omega)\frac{d\omega}{2\pi} = \frac{r_0^2}{2} \tag{6.39}
$$

Figure 6.9 shows $S_v(\omega)$ versus ω for different phase diffusion constants. As D becomes larger,

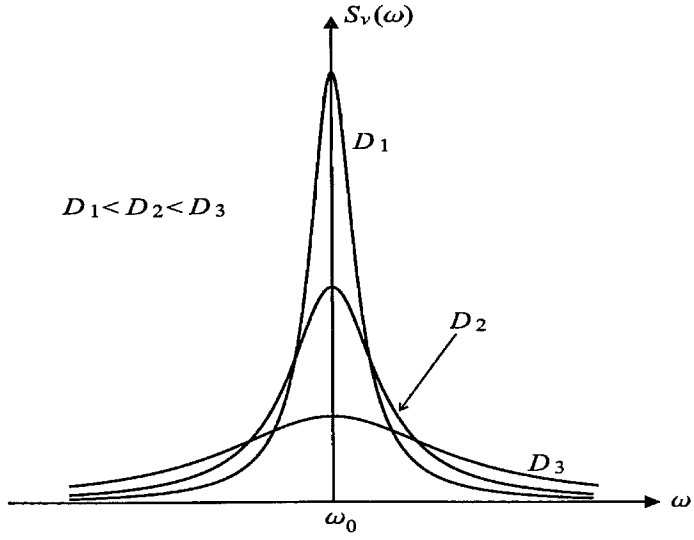

Figure 6.9: Power spectral density of the oscillator output for different diffusion constants: $D_1 < D_2 < D_3$.

the Lorentzian shape becomes shorter yet fatter, distributing the total oscillation energy of $r_0^2/2$ more widely around the center frequency, hence increasing the errors in the reference frequency. This is the frequency domain meaning of the phase diffusion constant, D. This error in the reference frequency is normally called *phase noise* as mentioned earlier. More quantitatively [86], the phase noise of an oscillator at an offset frequency, $\Delta\omega$, is defined as the ratio of the power spectral density at the frequency of[1] $\omega_0 + \Delta\omega$ (shaded area in Fig. 6.10) to the total oscillation energy, $r_0^2/2$:

$$\begin{aligned} \mathcal{L}\{\Delta\omega\} &\equiv \frac{S_v(\Delta\omega)}{r_0^2/2} \\ &= \frac{2D}{(\Delta\omega)^2 + D^2} \end{aligned} \tag{6.40}$$

This phase noise indicates the degree of the energy spreading around the center frequency for a given total energy. We have to emphasize here that *the phase noise solely dependes upon the phase diffusion constant, D*. If the offset frequency is large enough, *i.e.*, for $\Delta\omega \gg D$, (6.40) assumes a familiar f^{-2} behavior [77]:

$$\mathcal{L}\{\Delta\omega\} \approx \frac{2D}{(\Delta\omega)^2} \tag{6.41}$$

It is important to emphasize from (6.41) that a smaller phase diffusion constant D results in a smaller phase noise. In other words, if the phase diffusion occurs more slowly, the spectrum broadening in the frequency domain is smaller.

[1] or alternatively, at $\omega_0 - \Delta\omega$

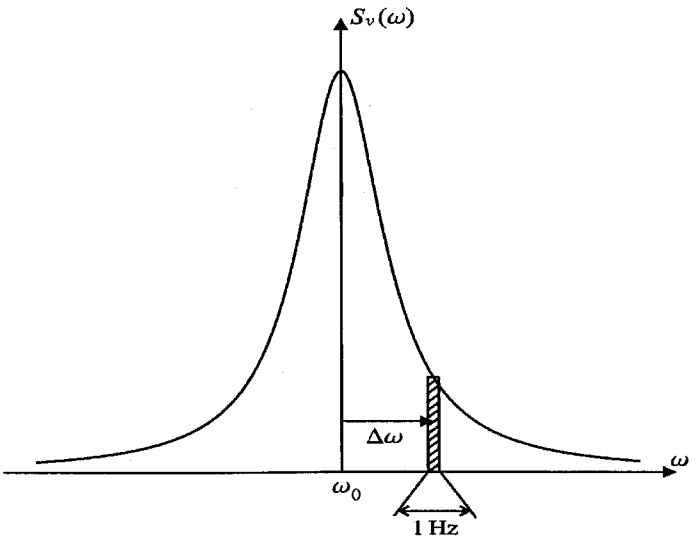

Figure 6.10: Power spectral density at the offset frequency, $\Delta\omega$.

6.3.3 Leeson Model and Hajimiri-Lee Model

In the previous subsections, we have reviewed a generic phase noise model based on phase diffusion. As clearly shown in (6.41), the phase noise optimization is equivalent to minimization of the phase diffusion constant, D. Many efforts have been made to relate the phase diffusion constant, D, with specific circuit parameters. In this subsection, we will discuss two well-known oscillator phase noise models among many others, that is, Leeson model [77] and Hajimiri-Lee model [63].

Leeson Model

The phase noise model proposed in [77] by Leeson is perhaps the most well-known phase noise model for electrical oscillators. The model is based on a linear time-invariant (LTI) approach for the resonator-based oscillators such as LC oscillators. The model predicts the following f^{-2} phase noise behavior:

$$\mathcal{L}\{\Delta\omega\} = \frac{2Fk_BT}{P_s} \cdot \left(\frac{\omega_0}{2Q_{loaded}\Delta\omega}\right)^2 \tag{6.42}$$

where P_s is the average power dissipation in the resistive part of the tank, Q_{loaded} is the effective quality factor of the tank including the loading effects, hence the name, loaded quality factor[2], and F is a fitting parameter determined experimentally. Comparing the generic phase noise model (6.41) and the Leeson model, we can identify the phase diffusion constant in the Leeson model:

$$D = \frac{Fk_BT}{P_s} \cdot \left(\frac{\omega_0}{2Q_{loaded}}\right)^2 \qquad \text{[Diffusion constant in the Leeson model]} \tag{6.43}$$

[2]For the unloaded quality factor, we have used Q

The Leeson model has long been prevailing due to its simple yet intuitive appeal. The model clearly shows the dependence of phase noise on frequencies, power dissipation, and the loaded quality factor. While the Leeson model appropriately predicts the general behavior of the phase noise, there remain several problems with the model. First, the unknown factor, F, is to be empirically determined and hence accurate phase noise prediction is difficult. Second, definition of the loaded quality factor is ambiguous, further adding uncertainty to the phase noise model. Third, while oscillators are time-varying circuits which exhibit time-varying noise processes, the Leeson model is based on the LTI theory.

Hajimiri-Lee Model

To address the problems with the Leeson model, Hajimiri and Lee proposed a time-varying phase noise theory [63], which predicts the following phase noise behavior:

$$\mathcal{L}\{\Delta\omega\} = \frac{1}{2q_{max}^2(\Delta\omega)^2} \sum_n \frac{\overline{i_n^2}}{\Delta f} \cdot \Gamma_{eff,n,rms}^2 \tag{6.44}$$

where q_{max} is the maximum charge swing, i_n represents noise sources in current forms (n is an index counting all the noise sources present in the circuit.), and $\Gamma_{eff,n}$ is the *effective impulse sensitivity function* associated with the n-th noise source, i_n, and takes into account the time-varying effect in the circuit. Comparing this model with (6.41), we can identify the phase diffusion constant in the Hajimiri-Lee model:

$$D = \frac{1}{4q_{max}^2} \sum_n \frac{\overline{i_n^2}}{\Delta f} \cdot \Gamma_{eff,n,rms}^2 \qquad \text{[Diffusion constant in the Hajimiri-Lee model]} \tag{6.45}$$

As can be seen, by taking the time-varying effects into account and using the explicit noise sources in the phase noise expression, the Hajimiri-Lee model removes uncertainties in the Leeson model arising from the empirical factor, F, and the ambiguous loaded quality factor, hence leading to more accurate prediction of phase noise.

Even though the Hajimiri-Lee model looks vastly different from the Leeson model, there is a strong link between these two models, which we will discuss in the following.

Dissipation-Based and Fluctuation-Based Phase Noise Models

The Leeson model does not involve any explicit expressions for the noise sources but is expressed in terms of the loaded tank quality factor. The quality factor, by definition, arises from the dissipation in the circuit, and hence the Leeson model is a *dissipation-based* phase noise model. On the other hand, the Hajimiri-Lee model is expressed in terms of the noise sources present in the oscillator, but does not involve the quality factor. Hence, the Hajimiri-Lee model is a *fluctuation-based* phase noise

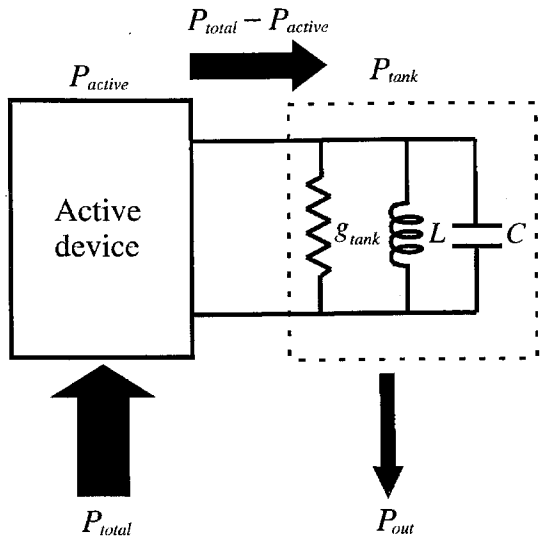

Figure 6.11: *LC* oscillator as an energy conversion engine. The *energy transfer efficiency* of the active device can be defined as $(P_{total} - P_{active})/P_{total}$.

model. How could these two seemingly different models describe the same phase noise phenomenon? In Chapter 3, we have discussed the intimate link between the fluctuation and the dissipation. Whenever there is (thermal) fluctuation, there is dissipation and vice versa: Fluctuation and dissipation always go hand in hand with each other. Due to this intimate link, the fluctuation-based model and the dissipation-based model actually describe the same phenomenon. Our approach presented in the following sections will clearly establish this link between the fluctuation-based and dissipation-based phase noise models.

Fundamental Relation between Loss and Noise

An oscillator can be viewed as an energy conversion engine as shown in Fig. 6.11. In an oscillator, the active device acts as a means to transfer energy from the dc power supply to the resonator and convert it from dc to ac. Every effort should be made to maximize the *energy transfer efficiency* of active devices (See Fig. 6.11), as it will directly increase the tank energy of the resonator for a given power dissipation. The energy loss in the active device is usually a strong function of its voltage and current waveforms and the energy transfer efficiency can be improved by proper timing of the voltage and current as in certain oscillator topologies, such as Colpitts [63].

It has been shown that such efficient operation of active devices is closely linked to the exploitation of cyclostationarity to reduce noise contributions from active devices [63]. This operational perspective can be viewed from a fundamental angle. In *any* physical system, loss components and noise have an intimate connection due to the fluctuation-dissipation relation. The reduced energy loss in the active device by proper timing implies an enhanced screening of resonator from the loss

components in the active devices, which will directly reduce active device's fractional noise contribution to the resonator according to the fluctuation-dissipation theorem. This explains the underlying physics for the active device noise reduction due to cyclostationary effects [63].

6.4 Virtual Damping

In the previous chapter, we reviewed fundamentals of oscillator phase noise and some of the currently available phase noise models. The evolution from the linear time-invariant theory (*e.g.* Leeson model) to the more accurate time-varying theory (Hajimiri model) has helped circuit designers understand the noise processes in oscillators, leading to more accurate phase noise predictions, and lower noise designs. However, these currently available theories assume phenomenological standpoints and a more fundamental, yet intuitive understanding of phase noise is still needed. The rest of this chapter presents our fundamental study of phase noise. We will get started by introducing the powerful concept of *virtual damping* in this section.

Time-domain picture of the phase diffusion was shown in Fig. 6.7(d) using an ensemble of oscillators which have the same initial phase and is redrawn at the top of Fig. 6.12. At the start of oscillation, the oscillators in the ensemble have the same phase and hence the ensemble average, $\langle v(t) \rangle$, is equal to $v(t)$ of any single oscillator in the ensemble. After a sufficiently long time, however, the oscillator signals become incoherent due to the phase diffusion and $\langle v(t) \rangle$ tends to zero with time, as shown at the bottom of Fig. 6.12. We will refer to this damping of the ensemble average as *virtual damping*. Even though the single oscillator output, $v(t)$, *per se* sustains itself, its ensemble average which matters in the measurement of phase noise *virtually damps*. One can logically conceive that *the phase diffusion constant, D, is identical to the virtual damping rate.* A lower phase noise implies a smaller phase diffusion constant or a slower virtual damping rate.

A mathematical verification of the virtual damping is given here. The output voltage $v(t)$ of an oscillator without amplitude fluctuations is given by (6.29), which is rewritten in the following for convenience:

$$v(t) = r_0 \cos[\omega_0 t + \phi(t)] \tag{6.46}$$

As mentioned earlier, in the presence of white noise, the phase noise $\phi(t)$ becomes a Wiener process (diffusion) where $\langle \phi^2(t) \rangle = 2Dt$ with diffusion constant D [74], [84], [85]. For a Gaussian distribution of $\phi(t)$ at any given time, t, we have $\langle \cos\phi \rangle = e^{-\langle \phi^2 \rangle/2}$ and $\langle \sin\phi \rangle = 0$ as seen in Appendix 2 and hence

$$\langle v(t) \rangle = r_0 e^{-\langle \phi^2(t) \rangle/2} \cos(\omega_0 t) = r_0 e^{-Dt} \cos(\omega_0 t) \tag{6.47}$$

which clearly shows the exponential behavior of virtual damping. As can be seen, the virtual damping

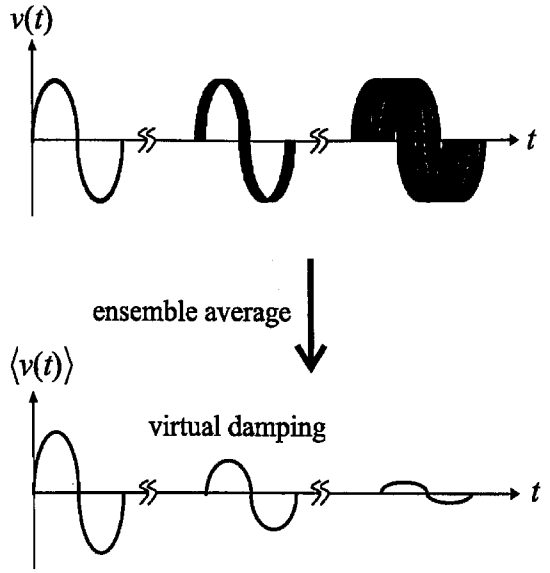

Figure 6.12: Ensemble average of $v(t)$ and virtual damping.

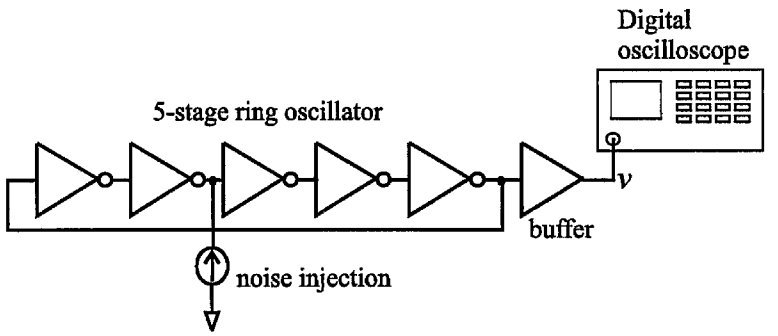

Figure 6.13: Measurement setup for the virtual damping using a digital oscilloscope.

rate is equivalent to the phase diffusion constant, D.

The virtual damping rate, D, and the phase noise of the oscillator are related by (6.41). As a numerical example, a 1 GHz oscillator whose phase noise is -121dBc/Hz at 600 kHz offset has $D \approx 5.645$ Hz or $D/\omega_0 \sim 10^{-9}$ according to (6.41). As can be seen, *typical good oscillators have very slow virtual damping rates when compared to oscillation frequencies.*

We can observe the virtual damping phenomenon experimentally as well. As just discussed, typical oscillators have very slow virtual damping rates making them less suitable for experimental verification. Instead, we use a ring oscillator whose phase noise is degraded by injection of a white noise current whose power spectrum can be controlled externally. This setup is shown in Fig. 6.13. The ring oscillator has a center frequency of 5 MHz. A digital oscilloscope is used to sample the output waveform multiple times and calculate the average over N samples, *i.e.*, $\langle v(t) \rangle_N$. The N output waveforms are triggered at the same phase at $t = 0$. Figure 6.14 shows this average for

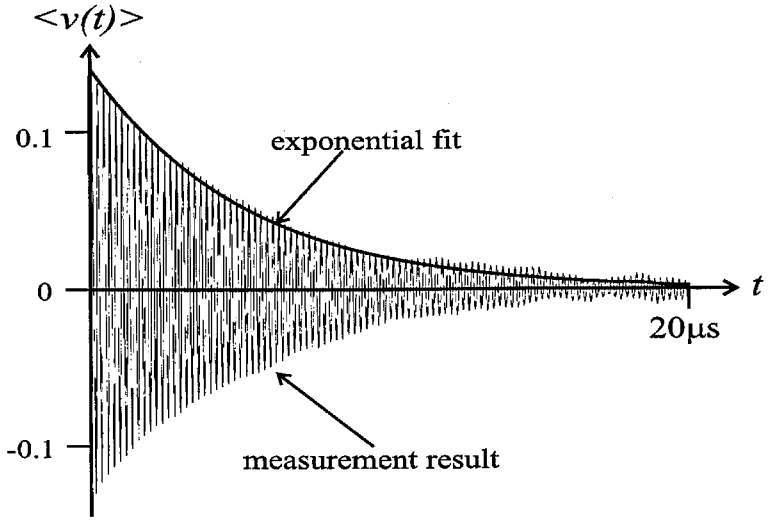

Figure 6.14: Measured $\langle v(t) \rangle_{512}$ versus t for a 5 MIIz ring oscillator.

$\overline{i_n^2}/\Delta f$ (A^2/Hz)	Measured D (sec^{-1})	PN from measured D (dBc/Hz)	PN from spec. analyzer (dBc/IIz)
2.60×10^{-15}	1.02×10^4	-92.9	-93.0
4.84×10^{-15}	1.56×10^4	-91.0	-90.0
9.66×10^{-15}	3.53×10^4	-87.4	-86.5
2.12×10^{-14}	9.30×10^4	-83.3	-81.7
6.04×10^{-14}	1.90×10^5	-80.0	-79.5

Table 6.1: Measured D, phase noise calculated from the measured D, and phase noise measured using a spectrum analyzer. The offset frequency is 1MHz and the center frequency of the oscillator is 5MHz.

$N = 512$ samples as a function of time. As can be seen clearly, the expected value of the output is an exponentially damping sinusoidal even though the single output waveform is a steady-state sinusoidal in complete agreement with the virtual damping concept and equation (6.47).

Using this experiment, the virtual damping rate, D, (reciprocal of the exponential time constant) was measured for different injected noise power levels. D is the inverse of time constant of the best-fit exponential to the resultant time domain waveforms (*e.g.*, Fig. 6.14). The oscillator phase noise was also measured using a spectrum analyzer at 1 MHz offset from the carrier. Equation (6.41) was used to predict the phase noise using the measured virtual damping rate, D. The results are summarized in Table 1 showing close and consistent agreements between the two methods.

The power of this virtual damping concept lies in providing a unified framework in which the resonator and the oscillator are viewed from the same angle. The left-hand side of Fig. 6.15 shows a parallel LC resonator with an effective parallel tank resistance, R, representing energy loss. Due to the loss, the voltage v across the tank shows an exponential damping from a given initial voltage

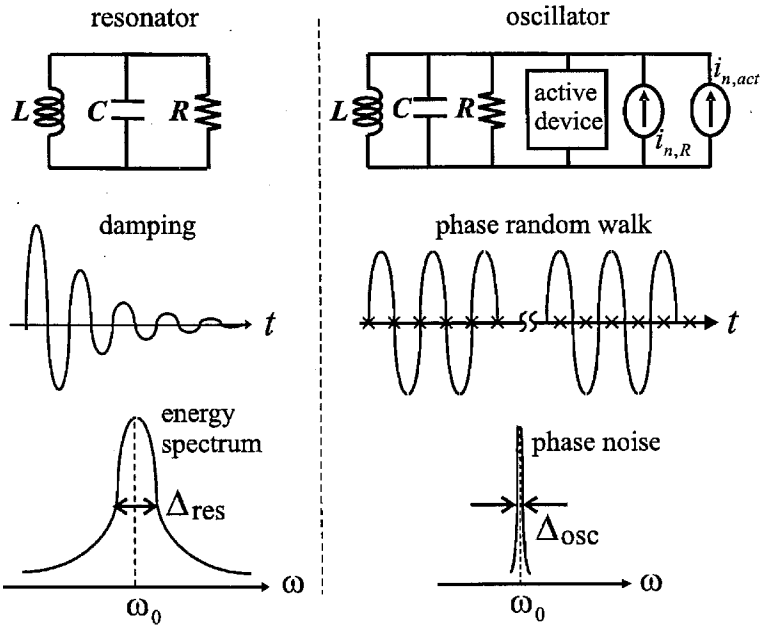

Figure 6.15: Resonator versus oscillator. The X's on the t-axis represent the ideal zero-crossings.

as shown in the figure. This damping corresponds to a Lorentzian line broadening in the energy spectrum. A negative resistance is used to cancel these losses to obtain a self-sustained oscillator, as shown in the right-hand side of Fig. 6.15. The active and passive device noise perturbs the phase of the oscillator, resulting in phase diffusion, which corresponds to a line broadening of oscillator's output power spectral density, or phase noise as discussed earlier. The line broadening of the oscillator is much smaller than that of the resonator yet it still has the Lorentzian shape.

Now, this relatively small spectral line broadening in the oscillator power spectrum can be thought of as the result of the relatively slow exponential virtual damping and this provides an explanation why both resonator's energy spectrum and oscillator's output power spectral density have Lorentzian broadening with different linewidths (Fig. 6.16). Since the virtual damping rate is much slower than the damping in the resonator as discussed earlier, the linewidth of the oscillator output spectrum is much smaller than the linewidth of the resonator's energy spectrum, as shown hypothetically in Fig. 6.16. This is because the damping rate essentially determines the linewidth of the frequency spectrum. In other words, placing a resonator in a positive feedback loop to make a self-sustained oscillator results in the *linewidth compression*. By comparing the damping rate of the resonator (which is $(2RC)^{-1}$) to the virtual damping rate of the oscillator, we can evaluate the ratio of the linewidth of the oscillator power spectrum to that of the resonator energy spectrum:

$$r \equiv \frac{\Delta_{osc}}{\Delta_{res}} = \frac{D}{1/(2RC)} = 2RCD \tag{6.48}$$

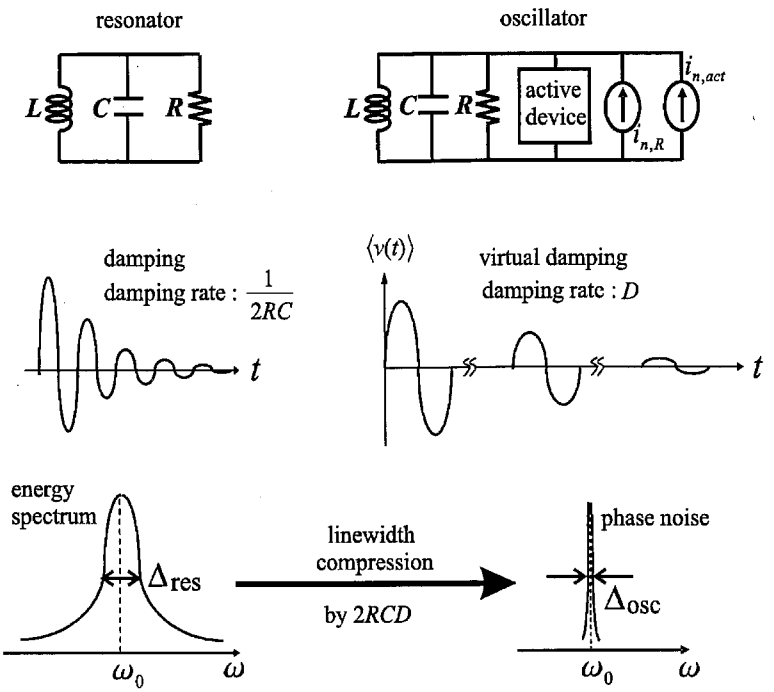

Figure 6.16: Damping in resonators and virtual damping in self-sustained oscillators.

This linewidth ratio will be expressed in terms of circuit parameters after obtaining an explicit expression for D in the following sections. This concept of linewidth compression proves to be powerful, resulting in an immediate design optimization strategy for resonator-based oscillators.

6.5 Physical Derivation of Virtual Damping Rate

In this section, we will determine the virtual damping rate, D, using a fundamental argument based on the theory of Brownian motion and diffusion introduced in Chapter 3. The key to this approach is the notion that the rate of any diffusion process is determined by two elements affecting the process: the *sensitivity* of the physical quantity undergoing the diffusion and the *friction* (energy loss) of the environment in which the diffusion process occurs, as fully discussed in Subsection 3.1.2.

For example, the diffusion constant, D, of a Brownian particle of mass, m, immersed in a liquid at temperature, T, with frictional coefficient of γ in Fig. 6.17 is given by the Einstein relation (3.28), which is written in the following for the sake of convenience:

$$D = \underbrace{\frac{k_B T}{m}}_{\text{sensitivity}} \cdot \underbrace{\frac{1}{\gamma}}_{\text{friction}} \tag{6.49}$$

where γ determines the frictional force of $m\gamma v$ for a Brownian particle with velocity of v. The $k_B T/m$

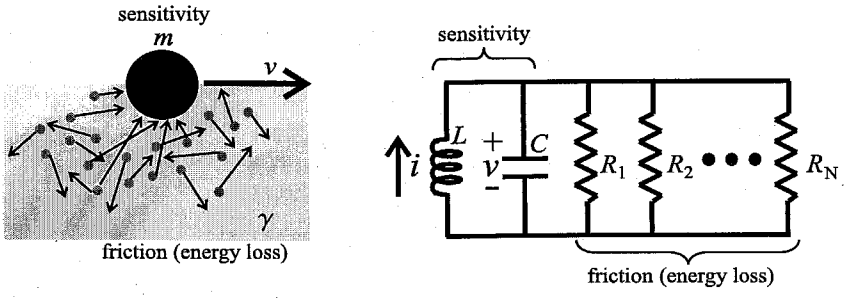

Figure 6.17: Brownian particle and LC tank with losses.

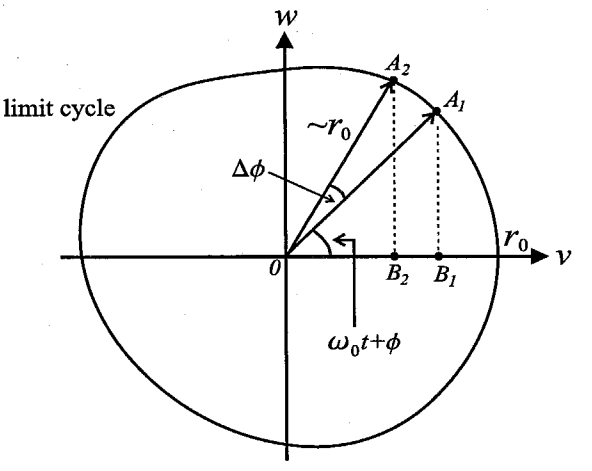

Figure 6.18: Oscillation trajectory in state-space and phase diffusion.

factor represents the *sensitivity* of the Brownian particle to perturbations and becomes smaller with a larger mass (Fig. 3.3(a)). This sensitivity factor is obtained using the equipartition theorem of statistical physics discussed in Chapter 3, which demands that each independent degree of freedom of a system in equilibrium at temperature T has a mean energy of $k_BT/2$, *i.e.*

$$\langle \frac{mv^2}{2} \rangle = \frac{k_BT}{2} \tag{6.50}$$

This sensitivity factor is independent of the friction coefficient of the liquid. Also, if two identical Brownian particles are immersed in liquids with different frictions, the Brownian particle in a medium with more friction will exhibit a slower diffusion (Fig. 3.3(b)), and hence the second factor $1/\gamma$ in (6.49). Summarizing, the diffusion constant can be determined only when both sensitivity and friction (energy loss) elements are known. Now by applying the same concept to the electrical oscillators, we will quantify the phase diffusion, starting with the simpler time-invariant case.

6.5.1 Time-Invariant Case

Fig. 6.18 shows the oscillation trajectory (limit cycle) in the (v, w) state-space for an output signal of the LC oscillator of Fig. 6.2 where w is the scaled current defined in (6.10). A phase random walk by the amount of $\Delta\phi$ corresponds to a random walk of the oscillation trajectory point from $\mathbf{A_1}$ to $\mathbf{A_2}$ or equivalently a voltage random walk from $\mathbf{B_1}$ to $\mathbf{B_2}$. In the following, we will first characterize this voltage diffusion and conversion to the phase diffusion can be easily performed by a multiplicative factor $1/r_0^2$.

Utilizing the *fluctuation-dissipation* relation of statistical physics discussed in Chapter 3, which states the deep-seated connection between a loss (*dissipation*) element and a thermal noise (*fluctuation*) element, any thermal noise source in a circuit can be replaced with a loss. The right-hand side of Fig. 6.17 shows a parallel LC tank with multiple parallel losses in a given oscillator that represent the noise sources. R_1 is always reserved for the effective parallel tank resistance. A MOS transistor in parallel with the LC tank will contribute a loss element $R = 1/(\gamma_{tran} g_{d0})$ as its noise contribution is

$$\frac{\overline{i_n^2}}{\Delta f} = 4k_B T \gamma_{tran} g_{d0} \tag{6.51}$$

where γ_{tran} is the CMOS thermal noise factor and g_{d0} is the channel transconductance at $V_{ds} = 0$ [47]. Note that Fig. 6.17 is *not* an equivalent circuit model for the oscillator but is used to identify the sensitivity and friction parts of the voltage diffusion as in the following.

In the circuit of Fig. 6.17, $\langle v^2 \rangle$ across the capacitor and $\langle i^2 \rangle$ through the inductor can be calculated noting that each of them constitutes a degree of freedom which will have $k_B T/2$ of thermal energy according to equipartition theorem: $\langle v^2 \rangle = k_B T/C$ and $\langle i^2 \rangle = k_B T/L$. This is analogous to the $k_B T/m$ sensitivity factor of the Brownian motion. Just as the sensitivity of the Brownian particle was described in terms of the velocity, v (time-derivative of the displacement, x, that diffuses), as discussed earlier or in Chapter 3, the sensitivity of the voltage diffusion is to be described in terms of its time-derivative, $\dot{v}$, *i.e.*:

$$\langle \dot{v}^2 \rangle = \frac{1}{C^2} \langle i^2 \rangle = \frac{k_B T}{LC^2} = \frac{k_B T}{C} \omega_0^2 \quad \text{[sensitivity factor]} \tag{6.52}$$

The friction (energy loss) associated with the oscillator can be calculated from the LR part of the resonator. Since the current in the circuit satisfies

$$i = -\frac{L}{R_{eq}} \dot{i} \tag{6.53}$$

where

$$R_{eq} \equiv R_1 || R_2 || \cdots || R_N \tag{6.54}$$

in the absence of the capacitor, similar to the equation of motion $\dot{v} = -\gamma v$ for the Brownian motion, we can see the frictional coefficient, γ, of the system is given by

$$\frac{1}{\gamma} = \frac{L}{R_{eq}} \quad \text{[energy loss (friction) factor]} \tag{6.55}$$

Now taking both sensitivity and loss into account and using Einstein relation, the phase diffusion constant D is given by

$$\begin{aligned} D &= \frac{1}{r_0^2} \cdot \langle \dot{v}^2 \rangle \cdot \frac{1}{\gamma} \\ &= \frac{1}{r_0^2} \cdot \frac{k_B T}{C} \cdot \frac{L}{R_{eq}} \\ &= \frac{1}{r_0^2} \cdot \frac{k_B T}{C} \cdot \frac{\omega_0}{Q_{loaded}} \end{aligned} \tag{6.56}$$

where the factor $1/r_0^2$ was introduced to convert the voltage diffusion to the phase diffusion as mentioned earlier and the loaded tank quality factor, Q_{loaded}, is defined as

$$Q_{loaded} \equiv C R_{eq} \omega_0 \tag{6.57}$$

Since $Q_{loaded} = \omega_0 E_{tank}/P_s = \omega_0 C r_0^2/(2P_s)$ where P_s is the power dissipation in the resistive part of the resonator, (6.56) can be rewritten as

$$D = \frac{k_B T}{2P_s} \cdot \left(\frac{\omega_0}{Q_{loaded}} \right)^2 \tag{6.58}$$

Combining this with (6.41) leads to Leeson model (6.42) in the $1/f^2$-region except for the fitting parameter $F/2$.

Summarizing, by evaluating the sensitivity and energy loss (friction) factors of the phase diffusion process, we derived the virtual damping constant and hence, phase noise. The power of this approach lies in the identification of the two essential elements of the oscillator phase noise, which, in conjunction with the linewidth compression concept, will lead to immediate design insights as will be seen in Section 6.7. The largely ignored sensitivity factor $k_B T/C$ in (6.56) will play important role in practical oscillator design optimization [82].

6.5.2 Time-Varying Case

In the foregoing argument, we ignored the time-varying effects in the phase noise evaluation. In actuality, the phase $\phi(t)$ of an oscillator experiences a time-varying diffusion in that the average size of the phase random walk periodically changes in the course of oscillation [63]. The time-varying effects are quantified using the *impulse sensitivity function* $\Gamma(t)$ describing the periodic sensitivity of

the oscillator phase to the perturbation and the *noise modulating function* (NMF) $\alpha(t)$ accounting for the cyclostationary noise generation [63]. This separation of the time-varying effects into the ISF and the NMF agrees perfectly with our earlier view of separating the phase diffusion into the sensitivity and loss (friction) part. The ISF affects the sensitivity part and modulates (6.52) periodically, *i.e.*,

$$\langle \dot{v}^2 \rangle = \frac{k_B T}{C} \cdot \omega_0^2 \cdot \Gamma^2(t) \tag{6.59}$$

On the other hand, the NMF describing the cyclostationary noise is equivalent to periodic circuit loss modulation in the course of oscillation, *i.e.*,

$$\frac{1}{\gamma} = \frac{L}{R_{eq}} \cdot \alpha^2(t) \tag{6.60}$$

Now we will modify our previous derivation of the virtual damping constant D to incorporate the time-varying effects. The time-varying effects modulate the average size of the random walk in the course of oscillation. Since the phase variance $\langle \phi^2(t) \rangle$ in the diffusion process is an accumulation of this time-varying random walk over time, after a long observation time, the details of time-variance in $\langle \phi^2(t) \rangle$ will become negligible, hidden behind the $2Dt$ diffusion where the diffusion constant is now affected by $\Gamma(t)$ and $\alpha(t)$ in an averaged sense, modifying the contribution from the *n-th* noise source R_n in (6.56) to

$$D_n = \frac{1}{r_0^2} \cdot \frac{k_B T}{C} \cdot \frac{\Gamma_{eff,rms,n}^2}{R_n C} \tag{6.61}$$

where $\Gamma_{eff,n}(t) = \Gamma_n(t)\alpha_n(t)$. Now including all the noise sources, we have

$$\begin{aligned} D &= \sum_n D_n \\ &= \frac{1}{r_0^2} \cdot \underbrace{\frac{k_B T}{C}}_{\text{sensitivity}} \cdot \underbrace{\frac{\omega_0}{Q_{loaded}}}_{\text{friction}} \end{aligned} \tag{6.62}$$

where the new definition for the loaded tank quality factor, Q_{loaded}, is

$$Q_{loaded} \equiv \omega_0 C \left[\frac{R_1}{\Gamma_{eff,rms,1}^2} \Big| \cdots \Big| \frac{R_N}{\Gamma_{eff,rms,N}^2} \right] \tag{6.63}$$

As can be seen clearly from (6.62), the phase diffusion constant or the virtual damping rate has the sensitivity element, $k_B T/C$, and the friction (energy loss) element, ω_0/Q_{loaded}. Traditionally, design efforts for the oscillator noise optimization has been focused on the friction (energy loss) element, or the quality factor of the tank while the sensitivity element has been largely ignored. As will be seen in Section 6.7, the sensitivity element will play an equally important role as the quality factor

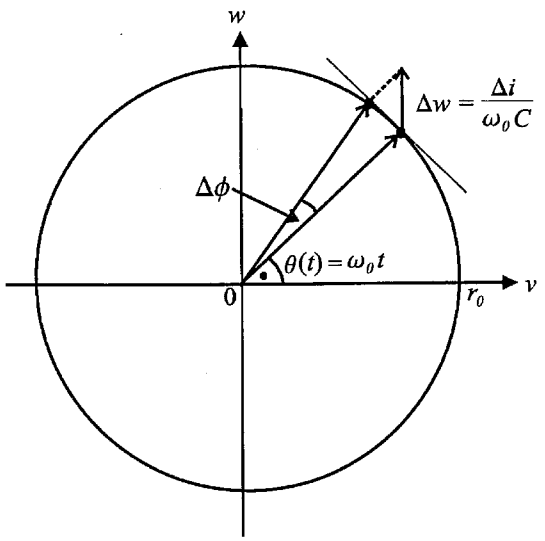

Figure 6.19: Geometric derivation of phase noise Langevin equation.

in the design optimization of the resonator-based oscillator.

Using $q_{max} = r_0 C$ and

$$\frac{\overline{i_n^2}}{\Delta f} = \frac{4k_B T}{R_n} \tag{6.64}$$

D_n in (6.61) can be rewritten as

$$D_n = \frac{\Gamma_{eff,rms,n}^2}{4q_{max}^2} \cdot \frac{\overline{i_n^2}}{\Delta f}. \tag{6.65}$$

and the combination of (6.65), (6.62) with (6.41) lead us to the Hajimiri-Lee model (6.44).

Now a natural question arises: if our physical approach eventually leads to the already existing model [63], why is it so important? As can be seen in Section 6.7, the physical phase diffusion concept entailing the sensitivity and friction (energy loss) in conjunction with the linewidth compression concept will actually lead to an immediate insight into oscillator design optimization and intuitive design methodology.

Before discussing the design implications derived from our physical investigation of oscillator phase noise, we will mathematically re-derive the phase diffusion constant, (6.62), in the following section for the sake of completeness.

6.6 Mathematical Derivation of Virtual Damping Rate

Let us first derive a Langevin equation for the phase, $\phi(t)$, of an ideal sinusoidal output signal of an LC oscillator in the presence of white noise sources. This task can be done geometrically using the

circular limit cycle (for sinusoidal output signal) shown in Fig. 6.19.

The noise current, Δi, injected into the tank during a short time duration, Δt, will result in change in the scaled current

$$\Delta w = \frac{\Delta i}{\omega_0 C} \tag{6.66}$$

where we have used the definition of the scaled current given by (6.10). The contribution of Δw to the phase change, $\Delta\phi$, can be obtained geometrically, as shown in Fig. 6.19:

$$r_0 \Delta\phi = \Delta w \times \cos\omega_0 t = \frac{\Delta i}{\omega_0 C}\cos\omega_0 t \tag{6.67}$$

By dividing both sides of the above equation by Δt and considering the limit $\Delta t \to 0$, we obtain the following Langevin equation:

$$r_0 \dot{\phi} = \frac{1}{\omega_0 C}\dot{i}_n \cos\omega_0 t \tag{6.68}$$

Integrating the right-hand side by parts results in

$$\phi(t) = \underbrace{\frac{1}{r_0\omega_0 C} i_n(t)\cos\omega_0 t}_{\text{White}} + \underbrace{\frac{1}{r_0 C}\int_0^t i_n(t')\sin\omega_0 t' dt'}_{\text{Wiener}} \tag{6.69}$$

Note that the first term is white random process as $i_n(t)$ is assumed to be white noise while the second term is a Wiener process as it is an integration of the white noise [33]. One can easily show that the power spectral densities of the first and the second terms in (6.69) are given by

$$\begin{aligned} S_{\phi,\phi}(\omega) &\approx \frac{N}{2(r_0 C)^2}\cdot\frac{1}{\omega_0^2} \qquad \text{[White process]} \\ S_{\phi,\phi}(\omega) &\approx \frac{2N}{(r_0 C)^2}\cdot\frac{1}{\omega^2} \qquad \text{[Wiener process]} \end{aligned} \tag{6.70}$$

where N is the intensity of the white noise, that is, $\langle i_n(t_1) i_n(t_2)\rangle = N\delta(t_1 - t_2)$. Equation (6.70) reveals that for any ω in the typical offset frequency range, the Wiener process dominates over the white noise in (6.69) by orders of magnitude. The corner frequency at which the white process becomes equal to the Wiener process is $2\omega_0$. Apparently, the white process is of no practical importance. Therefore, we can neglect the first term on the right-hand side of (6.69), reducing the equation to the following differential form:

$$\dot{\phi} = \frac{1}{r_0 C} i_n(t)\sin\omega_0 t \tag{6.71}$$

This is the Langevin equation for the phase, $\phi(t)$. Apart from the time-varying function $\sin\omega_0 t$, the phase $\phi(t)$ is an integration of the white noise, $i_n(t)$, and hence undergoes the Wiener process or

diffusion process as mentioned earlier several times. The phase $\phi(t)$ is of course analogous to the displacement $x(t)$ of the Brownian particle.

The time-varying function, $\sin\omega_0 t$ in (6.71) is the special case of the *impulse sensitivity function* (ISF) for an ideal sinusoidal voltage output, $v(t) = r_0 \cos\omega_0 t$ [63]. In a more general case of a nonsinusoidal oscillator output signal, we can replace $\sin\omega_0 t$ in (6.71) with the general ISF, $\Gamma(t)$, which can be obtained from charge injection simulation [63] in the most general case or from the similar geometric derivation when the effect of amplitude fluctuation is negligible. In general, there is no close form for the ISF function. Additionally, the noise source $i_n(t)$ in oscillator is cyclostationary due to the periodic change of the operating point as fully discussed in Section 5.2, and can be decomposed into

$$i_n(t) = n(t)p(t) \tag{6.72}$$

where $n(t)$ is white noise and $p(t)$ is the periodic noise modulating function as shown in Section 5.2. Then the Langevin equation for $\phi(t)$ in (6.71) is generalized to

$$\begin{aligned} \dot{\phi} &= \frac{1}{r_0 C} n(t)p(t)\Gamma(t) \\ &= \frac{1}{r_0 C} n(t)\Gamma_{eff}(t) \end{aligned} \tag{6.73}$$

where $\Gamma_{eff}(t) \equiv p(t)\Gamma(t)$ is called effective ISF [63].

Now, the phase $\phi(t)$ is the Type-III random process according to Table 3.3, and its corresponding Fokker-Planck equation for the probability distribution of the phase, $P(\phi, t)$, becomes

$$\frac{\partial P}{\partial t} = \frac{N}{2r_0^2 C^2}\Gamma_{eff}^2(t) \cdot \frac{\partial^2 P}{\partial \phi^2} \tag{6.74}$$

according to the same table, where N is the intensity of the white noise, $n(t)$. This is no more than a diffusion equation with a time-varying diffusion constant, $D(t)$:

$$D(t) = \frac{N}{2r_0^2 C^2}\Gamma_{eff}^2(t) \tag{6.75}$$

By plugging

$$P(\phi, t) = \frac{1}{\sqrt{2\pi\sigma^2(t)}} \exp\left[-\frac{\phi^2}{2\sigma^2(t)}\right] \tag{6.76}$$

into (6.74), we obtain the following expression for the variance of the phase, $\sigma^2(t)$:

$$\begin{aligned} \sigma^2(t) &= 2\int_0^t D(t')dt' \\ &= \frac{N}{r_0^2 C^2}(\Gamma_{eff,rms}^2 t + [\text{trigonometric terms}]) \end{aligned} \tag{6.77}$$

where $\Gamma_{eff,rms}$ signifies the root mean square for the effective ISF. In the above equation, as the first term growing with time will be eventually dominating over the second trigonometric terms which are bounded, we can approximate the above equation with

$$\sigma^2(t) \approx \frac{N\Gamma_{eff,rms}^2}{r_0^2 C^2} \cdot t \tag{6.78}$$

By comparing this with $\sigma^2(t) = \langle \phi^2(t) \rangle = 2D_n t$, we eventually obtain the diffusion constant, D_n, for the noise source, i_n:

$$\begin{aligned} D_n &= \frac{N\Gamma_{eff,rms}^2}{2r_0^2 C^2} \\ &= \frac{1}{r_0^2} \cdot \frac{k_B T}{C} \cdot \frac{1}{R_n C} \cdot \Gamma_{eff,rms,n}^2 \end{aligned} \tag{6.79}$$

which is in perfect agreement with (6.61) where we have used (6.64) and $\overline{i_n^2/\Delta f} = 2N$.

As a final comment in this section, we have to emphasize that even though the phase noise SDE (6.73) bears an apparent periodic time-varying effect, the statistical average $\langle \phi^2(t) \rangle = 2D_n t$ does not show such periodic time-varying effects after many cycles, as shown in (6.77) and (6.78). This is why the output signal of the oscillator does not carry any perceptible cyclostationary effects in it. The time-varying nature in (6.73), however, *does affect* the diffusion process in an averaged sense by modifying the diffusion constant D as shown in (6.79) with the rms value of the effective ISF.

6.7 Principles of Oscillator Noise Optimization

In Sections 6.4 and 6.5, we established concepts of virtual damping and linewidth compression and explicitly evaluated the virtual damping constant (phase diffusion constant), D, resorting to a physical argument utilizing Einstein relation. In Section 6.6, we verified the physical argument by mathematically evaluating D using the Fokker-Planck equation. In this section, based upon these previous results, we will establish fundamental principles of oscillator phase noise optimization, leading to an oscillator design optimization strategy.

In Section 6.4, we have argued that the ratio of the linewidth of an oscillator to the linewidth of a resonator which bases the oscillator is given by (6.48), which is rewriting in the following for convenience:

$$r \equiv \frac{\Delta_{osc}}{\Delta_{res}} = 2RCD \tag{6.80}$$

by comparing the damping rate of the resonator to the virtual damping rate of the oscillator. See Fig. 6.16. Using the explicit expression for the virtual damping rate, D, in (6.62), the compression

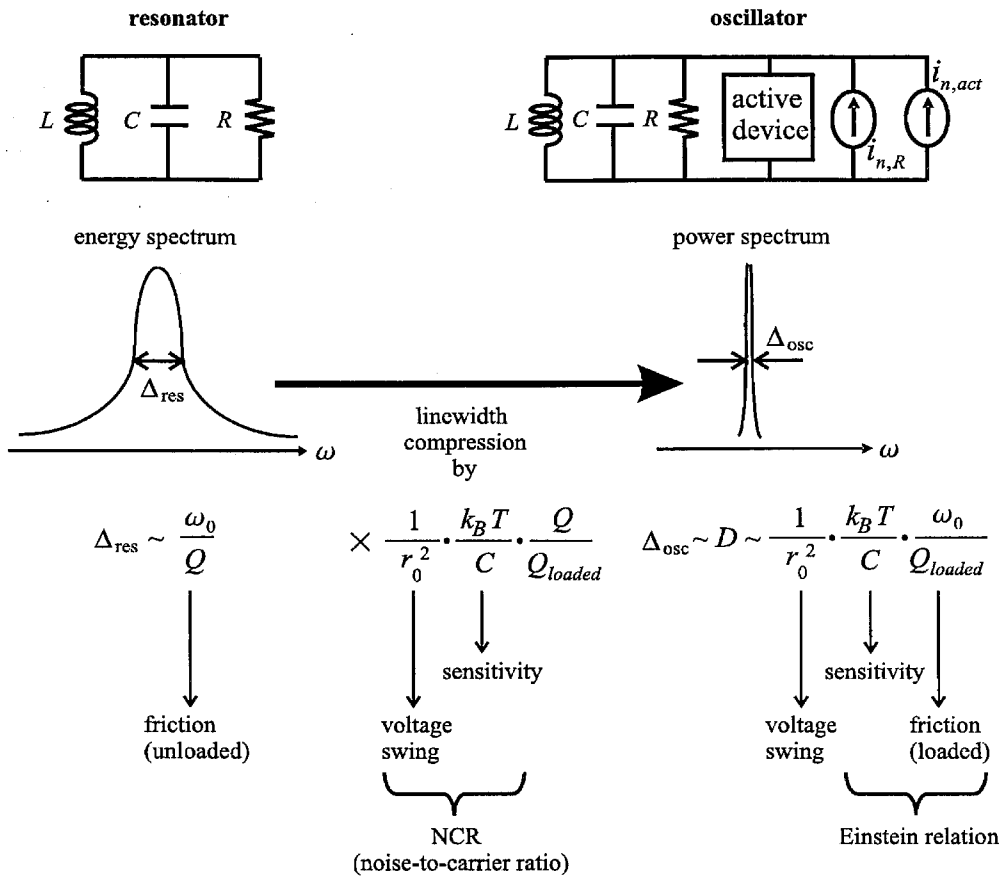

Figure 6.20: Details of linewidth compression in oscillators.

ratio in (6.80) can be expressed as

$$r = 2 \cdot \frac{1}{r_0^2} \cdot \frac{k_B T}{C} \cdot \frac{Q}{Q_{loaded}} \tag{6.81}$$

where we have used $Q = RC\omega_0$ for the unloaded tank quality factor. This ratio r reveals how much linewidth improvement we obtain by placing a given resonator into a feedback loop and making an oscillator. In a typical electrical oscillator at a normal temperature, this ratio is extremely small: for instance, for $C = 1pF$, $r_0 = 1V$, $Q = 10$ and $Q_{loaded} = 5$, $r \approx 1.6 \times 10^{-8}$ and hence shows that the linewidth of a resonator is narrowed by almost 8 orders of magnitude when placed in a positive feedback loop to make an oscillator. In the time-domain picture, this observation is equivalent to the fact that the virtual damping rate of the oscillator is 8 orders of magnitude smaller than the damping rate of the resonator.

In the light of the linewidth compression, the oscillator phase noise is determined by the following steps (Fig. 6.20). First, the unloaded quality factor, Q, of the resonator sets the linewidth of

the resonator. Second, by placing the resonator in the positive feedback loop, the linewidth is compressed by the factor given by (6.81). In this compression process, the resonator Q which is in the denominator of the resonator linewidth expression is cancelled by the Q in the numerator of the compression factor of (6.81). However, the compression factor, r, in (6.81) has a loaded tank quality factor, Q_{loaded}, in its denominator, resulting in Q_{loaded} in the denominator of the linewidth expression for the oscillator. While the effect of the unloaded tank quality factor, Q, *seems* to disappear in the linewidth compression process, the unloaded quality factor, Q, actually affects both the voltage swing, r_0, for a given bias current and the loaded quality factor, Q_{loaded}, and therefore remains a crucial design parameter.

The sensitivity element, k_BT/C, which plays a crucial role in the linewidth compression, should be another important design consideration. This sensitivity element has been largely ignored in contemporary oscillator design community, often leading to misconceived design guidelines. For an example of such design misconceptions, neglecting the sensitivity factor, k_BT/C, can lead to noise optimization guidelines promoting maximization of L as it increases the voltage swing, r_0 [92]. However, increasing L or equivalently decreasing C for a given oscillation frequency also increases the sensitivity factor, k_BT/C. Hence, the hypothesis that increasing L will lead to a better phase noise performance actually does not reflect the physical reality. We will fully discuss this issue shortly.

In this section, we will establish the principles of the oscillator phase noise optimization, focusing on both sensitivity element (capacitance/inductance values) and friction element (loss), leading to essential understanding of the basic trade-offs in an LC oscillator. In Subsection 6.7.1, we will first study the behavior of the *noise-to-carrier ratio* (NCR) defined as[3]

$$NCR \equiv \frac{1}{r_0^2} \cdot \frac{k_BT}{C} = \frac{E_{thermal}}{E_{tank}} \tag{6.82}$$

which constitutes an important part of the linewidth compression ratio, r, as shown in (6.81). Subsection 6.7.2 will investigate the behavior of the phase diffusion constant or the virtual damping rate, D, leading to a phase noise optimization strategy. Although the following argument is limited to the oscillators with parallel LC tanks, a series tank can be analyzed using a dual line of argument.

6.7.1 Behavior of Noise-to-Carrier Ratio, NCR

In order to investigate the behavior of the NCR given in (6.82), we first need to know the behavior of the oscillator voltage amplitude, r_0, depending upon the circuit parameters. Two modes of operation, named *current-* and *voltage-limited regimes*, can be identified for a typical LC oscillator of Fig. 6.2, considering the bias current as the independent variable [104]. In the current-limited regime, the oscillator amplitude, r_0, linearly grows with the bias current according to $r_0 = I_{bias}R$

[3] $E_{tank} = Cr_0^2/2$, $E_{thermal} = k_BT/2$.

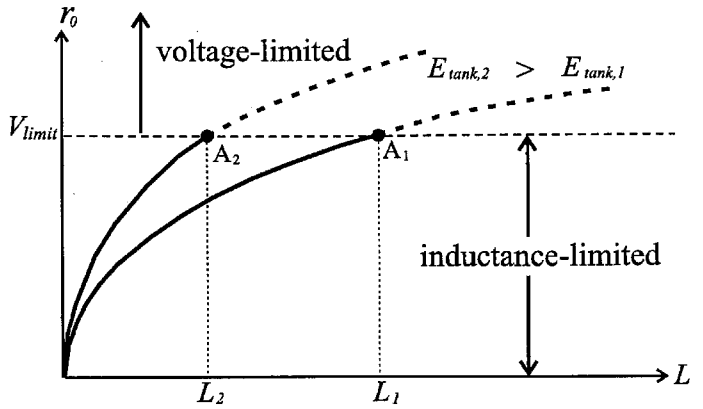

Figure 6.21: E_{tank} versus L curves obtained from (2) for two different tank energies $E_{tank,2} > E_{tank,1}$. With an increasing inductance, the tank amplitude grows along the solid parts of the curves until it reaches V_{limit} (inductance-limited regime). Once the tank amplitude reaches V_{limit}, it stops growing with the further increase of inductance (voltage-limited regime). The parts of curves with broken lines are unrealizable.

until the oscillator enters the voltage-limited regime where R is the tank loss shown in Fig. 6.2. In the voltage-limited regime, the amplitude is limited to V_{limit}, which is determined by the supply voltage and/or a change in the operation mode of active devices (*e.g.*, MOS transistors entering triode region). Thus, r_0 can be expressed as

$$r_0 = \begin{cases} I_{bias}R & (I\text{-limited}) \\ V_{limit} & (V\text{-limited}) \end{cases} \tag{6.83}$$

These two modes of operation can be viewed from a different perspective, by using the tank inductance, L, as the independent variable instead of I_{bias}. Noting that the tank energy, E_{tank}, is defined as $E_{tank} \equiv Cr_0^2/2$, r_0 can be expressed in terms of E_{tank}, *i.e.*,

$$r_0^2 = \frac{2E_{tank}}{C} = 2E_{tank}\omega_0^2 L \tag{6.84}$$

where $\omega_0 = 1/\sqrt{LC}$ is the oscillation frequency. The tank amplitude grows with L for a given E_{tank} and ω_0 as indicated by (6.84) and depicted in Fig. 6.21 for two different tank energies $E_{tank,1} < E_{tank,2}$. While being *the same* as the current-limited regime, we refer to this mode as *inductance-limited regime* when L is the independent variable. Therefore, any equation valid in the current-limited regime must be valid in the inductance-limited regime and *vice versa*. This alternative denomination will facilitate the understanding of various trade-offs in oscillator design. Once the tank amplitude reaches V_{limit}, it stops increasing with further increase of the inductance and the oscillator will enter the voltage-limited regime as before.

Note that many different inductors with the same inductance, L, can be made in any technology. For example, different on-chip spiral inductors with the same L can be designed using different

geometric parameters such as diameter, number of turns, etc. [110]. However, only one of these designs will offer the minimum loss, or the largest equivalent parallel resistance, R_L. Unless otherwise specified, from this point on, whenever we refer to an inductance, L, we assume that this optimization is already performed [110] and hence L corresponds to the inductor with the minimum loss. Note that the minimum loss R_L is a function of L.

The equivalence of the current- and inductance-limited regimes can be used to combine (6.83) and (6.84) to determine the relation between E_{tank} and I_{bias} in the inductance-limited regime. Assuming that the losses due to the on-chip spiral inductors are dominant in the integrated LC oscillators, (*i.e.*, $R \approx R_L$),

$$E_{tank} \propto \frac{I_{bias}^2 R_L^2}{L} \qquad (L\text{-limited}) \tag{6.85}$$

While (6.84) is valid in both inductance- and voltage-limited regimes, it is easier to deal with a constant quantity V_{limit} in the voltage-limited regime and hence we can rewrite (6.84) as

$$r_0^2 = \begin{cases} 2E_{tank}\omega_0^2 L & (L\text{-limited}) \\ V_{limit}^2 & (V\text{-limited}) \end{cases} \tag{6.86}$$

Using (6.86) in (6.82), we can express the NCR of the LC oscillator for a given oscillation frequency as

$$NCR \propto \begin{cases} 1/E_{tank} & (L\text{-limited}) \\ L & (V\text{-limited}) \end{cases} \tag{6.87}$$

Equation (6.87) shows that although r_0 increases with L for a given E_{tank}, as seen in Fig. 6.21, the NCR stays constant in the inductance-limited regime and *does not* depend on the value of the inductor. However, once the oscillator enters the voltage-limited regime, the NCR increases with L. Therefore, choosing an inductance, L, that places the oscillator in the voltage-limited regime results in *waste of inductance* and will only increase the NCR. An important observation is that for a given E_{tank}, a larger tank amplitude obtained by increasing the inductance, L, *does not* result in a better noise performance because the oscillator has a similar response to both the tank energy and the thermal energy. On the other hand, the NCR can indeed be improved by increasing the tank energy as can be seen from (6.87), which will inevitably result in larger power dissipation.

We can draw a mechanical analogy to the LC oscillator to help us understand the dependence of the NCR on the value of the inductor. Consider a mass-spring oscillator in which a mass, m, is fastened to one end of a spring with a spring constant, k, while the other end of the spring is kept stationary. The mass is immersed in water and subject to random bombardment of water molecules. The loss due to the water friction is compensated by a hand which follows the oscillation of the mass and continuously injects compensating energy into the system. The hand is assumed to have

undesirable yet inherent shaking.

The comparison between the differential equations for the velocity of the mass and the voltage across the parallel LC tank reveals the analogy of the mass, m, and the spring constant, k, to the capacitance, C, and the inverse of the inductance, $1/L$, respectively. The mass velocity corresponds to the voltage across the parallel LC tank. The random bombardment of water molecules and the hand shaking correspond to the tank noise and the active device noise, respectively. The hand can only make limited displacements and never allows the mass to exceed its range. This introduces an upper bound for the maximum displacement and hence the maximum velocity of the mass[4], resulting in a *velocity-limited regime* as an analog to the voltage-limited regime.

As expected intuitively, the mass of the oscillator has a similar response to the oscillation energy and the thermal energy. Therefore, a smaller mass results in a larger maximum velocity, a larger velocity noise, and hence a constant noise-to-signal ratio for a given oscillation energy until the oscillation reaches the velocity-limited regime. In the velocity-limited regime, a reduction in mass degrades the noise-to-signal ratio as the velocity noise keeps increasing while the maximum velocity stays constant.

Although (6.87) provides essential insights into the oscillator noise as a function of E_{tank}, the bias current, I_{bias}, is a more practical design parameter for electrical oscillators. To that end, we convert (6.87) into

$$NCR \propto \begin{cases} L/(I_{bias}^2 R_L^2) & (L\text{-limited}) \\ L & (V\text{-limited}) \end{cases} \tag{6.88}$$

by using (6.85).

Two important concepts of *waste of inductance* and *waste of power* in the voltage-limited regime can be seen from (6.88). Increasing L beyond the value that puts the oscillator at the edge of the voltage-limited regime will degrade the NCR in proportion to the excess inductance and hence will result in *waste of inductance*. Similarly, increasing the bias current in excess of the value that places the oscillator at the borderline of the two regimes will not improve the NCR and therefore induces the more commonly appreciated concept of *waste of power*.

Based on (6.88), the optimum NCR for a given bias current is obtained in the inductance-limited regime when L/R_L^2 assumes its minimum value. Note that $L \sim 1/C$ in the expression L/R_L^2 represents the sensitivity of the tank while R_L in the expression represents the friction (energy loss) element and hence NCR depends on both the sensitivity and the friction elements. When L increases or equivalently C decreases for a given oscillation frequency, the sensitivity factor L increases. The friction element, R_L, is also a function of L, and hence the specific behavior of $NCR \propto L/R_L^2$ with the inductance has a strong dependence on the particular implementation of the inductor.

[4] noting that $kx_{max}^2/2 = mv_{max}^2/2$.

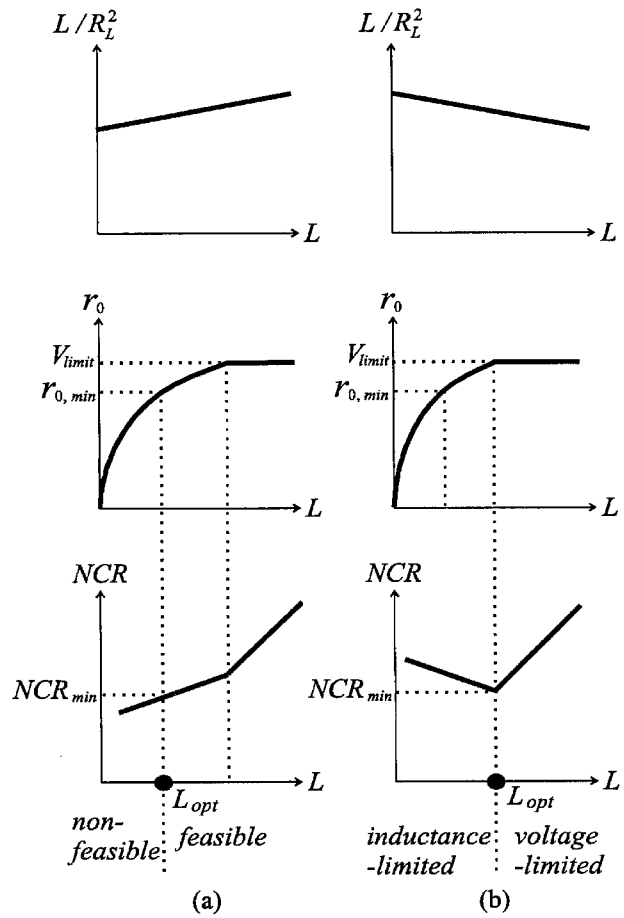

Figure 6.22: L/R_L^2, r_0 and NCR versus L for a given I_{bias}: (a) L/R_L^2 increasing with an increasing inductance L (b) L/R_L^2 decreasing with an increasing inductance L.

Now, we investigate two hypothetical, yet illustrative, cases to show how the optimum inductance for the optimum NCR can be obtained for a given I_{bias}.

- Case 1 : L/R_L^2 increasing with L

First, we consider the case in which L/R_L^2 increases with the inductance. As can be seen from (6.88), a smaller inductance results in a better NCR for a given bias current. However, the inductance cannot be reduced indefinitely since in practice, we always have a minimum tank amplitude constraint $r_0 \geq r_{0,min}$ and/or a start-up condition. The excessive reduction of inductance will eventually violate the minimum tank amplitude or the start-up constraint. Consequently, the optimum inductance for the optimum NCR is determined when the design lies at the verge of the tank amplitude or start-up constraint[5]. Hypothetical curves for L/R_L^2, r_0 and NCR versus L for a fixed bias current in this case are shown in Fig. 6.22(a), where the minimum tank amplitude constraint is the limiting mechanism for this reduction.

- Case 2 : L/R_L^2 decreasing with L

Now we consider the case where L/R_L^2 decreases with increasing inductance. In this case, (6.88) shows that a larger inductance in the inductance-limited regime results in a better NCR for a given bias current. Hence, the optimum inductance for the optimum NCR is the one that places the design at the edge of the inductance-limited regime as seen in hypothetical curves for L/R_L^2, r_0 and NCR versus L for a fixed bias current of Fig. 6.22(b).

Summarizing, the behavior of the NCR is determined by delicate balance between the sensitivity and friction (energy loss) elements in the oscillator in the inductance-limited regime. In the voltage-limited regime, increasing inductance will only increase the NCR. Neglecting the sensitivity in the NCR or the distinction between the voltage- and inductance-limited regimes can wrongly lead to noise optimization guidelines promoting maximization of L [92].

6.7.2 Behavior of Virtual Damping Rate, D

In the previous subsection, the noise-to-carrier ratio (NCR), a main constituent of the linewidth compression ratio given by (6.81), was used to investigate the certain properties of oscillator noise. As shown in (6.62) or in Fig. 6.20, the virtual damping rate (phase diffusion constant), D, has an extra-factor, ω_0/Q_{loaded}, in addition to the NCR:

$$\begin{aligned} D &= \frac{1}{r_0^2} \cdot \frac{k_B T}{C} \cdot \frac{\omega_0}{Q_{loaded}} \\ &= NCR \cdot \frac{\omega_0}{Q_{loaded}} \end{aligned} \tag{6.89}$$

[5]The start-up constraint is normally imposed by specifying the minimum small-signal loop gain between 2 and 3. Hence the design at the verge of the start-up constraint still has a sufficient margin on the loop gain.

where Q_{loaded} is the loaded tank quality factor given by (6.63), which is rewritten in the following for the sake of convenience:

$$Q_{loaded} \equiv \omega_0 C \left[\frac{R_1}{\Gamma^2_{eff,rms,1}} || \cdots || \frac{R_N}{\Gamma^2_{eff,rms,N}} \right] \tag{6.90}$$

Here, the effective resistance, R_n, (for $n = 1, 2, 3, ..., N$) is given by

$$\frac{\overline{i_n^2}}{\Delta f} = \frac{4k_B T}{R_n} \tag{6.91}$$

as discussed earlier in Section 6.5 where i_n is the n-th current noise source. For instance, for the MOS transistor, $R_n = (\gamma g_{d0})^{-1}$ [47]. As will be seen later with an example in the next section, the loaded tank quality factor, Q_{loaded}, is normally dominated by the active devices. In the active devices, R_n is typically the function of the bias currents [46], and hence Q_{loaded} in (6.90) can be reexpressed as

$$Q_{loaded} \propto \omega_0 C \times F(I_{bias}) \tag{6.92}$$

where $F(I_{bias})$ is a certain function of the bias current[6]. Combining (6.88) and (6.92) in (6.89), we obtain

$$D \propto \begin{cases} L^2/R_L^2 \times [I_{bias}^2 F(I_{bias})]^{-1} & (L\text{-limited}) \\ L^2 \times [F(I_{bias})]^{-1} & (V\text{-limited}) \end{cases} \tag{6.93}$$

Now we will discuss the dependence of the phase diffusion constant, D, upon the inductance, L, for a fixed bias current, I_{bias}. The dependence upon the bias current will be discussed in the next section with a specific example with which $F(I_{bias})$ is explicitly known. For a given bias current, diffusion constant in (6.93) increases with an increasing L in the voltage-limited regime, which corresponds to *waste of inductance.*

In the inductance-limited regime, $D \propto L^2/R_L^2$ has both sensitivity element ($L \sim 1/C$) and friction element (R_L^{-2}) and the behavior of D is determined by the delicate balance between these two elements. For typical on-chip spiral inductors, the minimum effective parallel conductance $g_L \equiv (R_L)^{-1}$ for a given inductance L decreases with an increasing inductance when the diameter of the inductor is constrained with an upper-bound [110]. An example of such dependence is shown in Fig. 6.23 [110]. Using this data of Fig. 6.23, it can be seen that the factor L^2/R_L^2 in (6.93) increases with an increasing inductance as shown in Fig. 6.24. Consequently, for a given I_{bias}, phase noise increases with the inductance in the inductance-limited regime and *a smaller inductance results in a better phase noise.* However, the inductance L cannot be indefinitely reduced since it will eventually reduce the voltage swing and the small-signal loop gain below the specification. The optimum

[6]For instance, in case of the short channel MOS transistor, $R_n = (\gamma g_{d0})^{-1} \propto I_{bias}^{-1}$ [47] and hence, $F(I_{bias}) = I_{bias}^{-1}$.

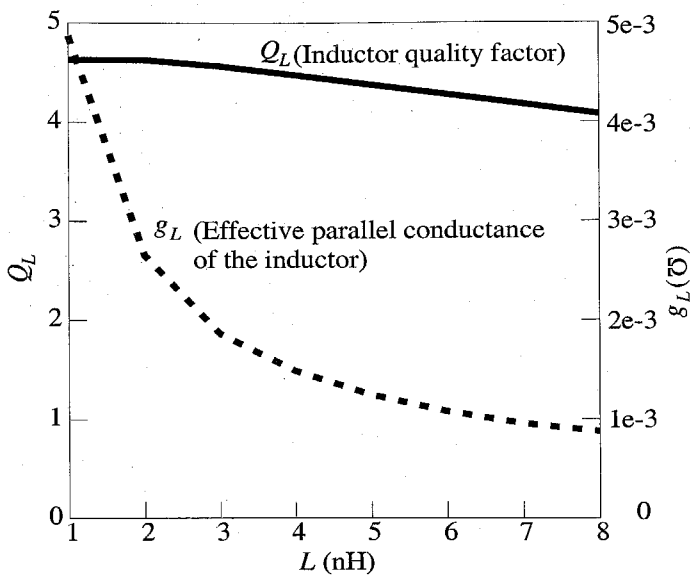

Figure 6.23: Simulated maximum inductor quality factor Q_L and minimum effective parallel conductance g_L versus the inductance L.

inductance is then the one that places the oscillator at the verge of either the voltage swing or the start-up constraint. Hence, the design strategy for the LC oscillator utilizing the on-chip spiral inductors is to find *the minimum inductance* that satisfies both the tank amplitude and start-up constraints. This design strategy will be executed using a practical graphical optimization method in the next section.

6.8 Design Example

In the previous section, we considered underlying physics of LC oscillators, concluding that *inductance selection process* plays a central role in oscillator noise optimization. An investigation of phase noise properties led to a design strategy based on an inductance selection scheme, providing a basis for a detailed optimization methodology presented later in this work. This optimization process entails an intuitive graphical method to visualize the design constraints such as tank amplitude, frequency tuning range and start-up condition, allowing minimization of phase noise while satisfying all design constraints.

In Subsection 6.8.1, a specific oscillator topology is chosen as a design example and design constraints are imposed on the oscillator. The inherent properties of phase noise lead to a design strategy. Subsection 6.8.2 explains the details of our graphical optimization process. Elaborate simulation results of the optimized VCO accurately predicting phase noise are shown in Subsection 6.8.3. Subsection 6.8.4 presents the experimental results and compares the performance of our VCO

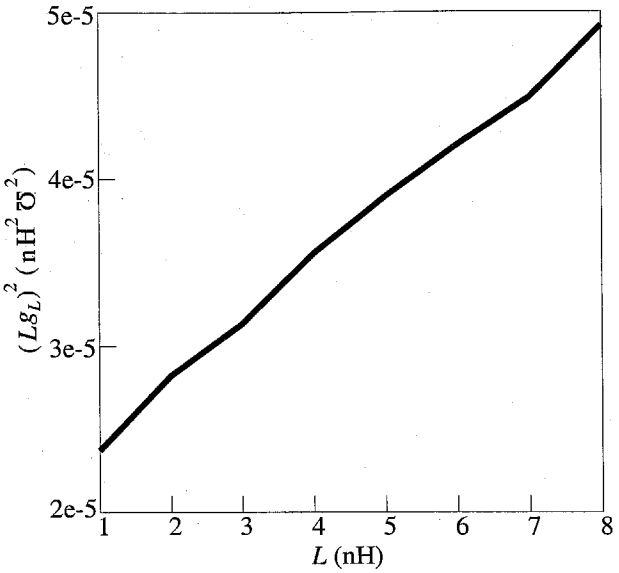

Figure 6.24: $L^2 g_L^2$ versus the inductance L.

to that of other reported LC oscillators to prove the adequacy of our design methodology.

6.8.1 LC VCO Topology, Design Constraints and Phase Noise

In this section, we demonstrate the design strategy through the oscillator topology of Fig. 6.25. Design constraints are specified and a design strategy specific to the circuit is devised for phase noise optimization.

Design Topology

The cross-coupled LC oscillator of Fig. 6.25 is selected as a vehicle to demonstrate our optimization process. Full exploitation of differential operation lowers undesirable common-mode effects such as extrinsic substrate and supply noise amplification and up-conversion. The oscillation amplitude of this structure is approximately a factor of two larger than that of the NMOS-only structure due to the PMOS pair [104], [112], [86]. The rise and fall time symmetry is also incorporated to further reduce the *1/f* noise upconversion [63]. These properties result in a better phase noise performance for a given tail current.

There are twelve initial design variables associated with this specific oscillator: MOS transistors dimensions (W_n, W_p, L_n, and L_p), geometric parameters of on-chip spiral inductors (metal width b, metal spacing s, number of turns n, and diameter d), maximum and minimum values of the varactors ($C_{v,max}$ and $C_{v,min}$), load capacitance (C_{load}) and tail bias current in the oscillator core (I_{bias}). These design variables are listed in Table 1. Later, we will reduce the number of independent

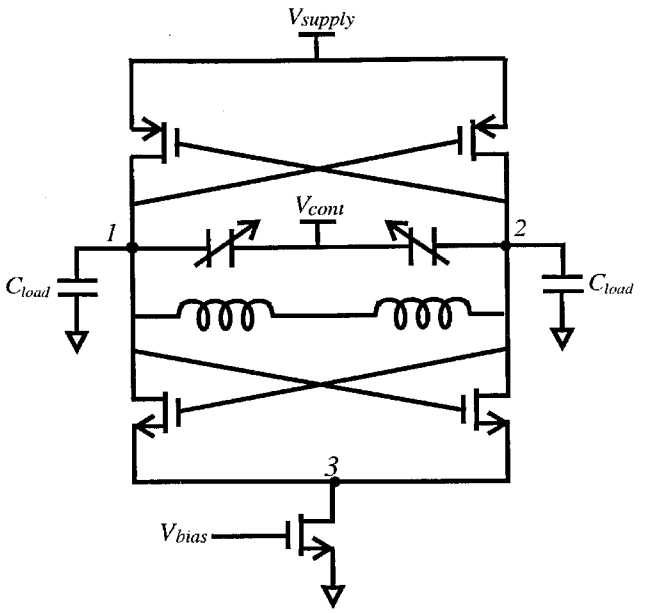

Figure 6.25: VCO core schematic.

design variables to six through proper design considerations.

Components	Initial Design variables
Transistors	W_n, W_p, L_n, L_p
Spiral inductors	b, s, n, d
Varactors	$C_{v,max}$, $C_{v,min}$
Load capacitors	C_{load}
Bias current	I_{bias}

Table 1 : Twelve initial design variables

The equivalent circuit model of the oscillator is shown in Fig. 6.26 [111], where the broken line in the middle represents either the common mode or ground. The symmetric spiral inductor model of Fig. 6.27 [113] with identical RC loading on both terminals is used as a part of the tank model. Varactors for frequency tuning are made out of the gate channel capacitor of standard PMOS transistors in inversion mode. They are modeled with a capacitor C_v in series with a resistor R_v as in Fig. 6.28, which is used as a part of the tank model.

In Fig. 6.26, C_{NMOS} and C_{PMOS} are the total parasitic capacitances of the NMOS and PMOS transistors, respectively[7], and g_m and g_o are small-signal transconductance and output conductance of the transistors, respectively. Although the values of g_m and g_o vary with the change of the operating points of transistors in the course of oscillation, we will use the values of g_m and g_o when

[7] $C_{\text{NMOS}} = C_{gs,n} + C_{db,n} + 4C_{gd,n}$, $C_{\text{PMOS}} = C_{gs,p} + C_{db,p} + 4C_{gd,p}$.

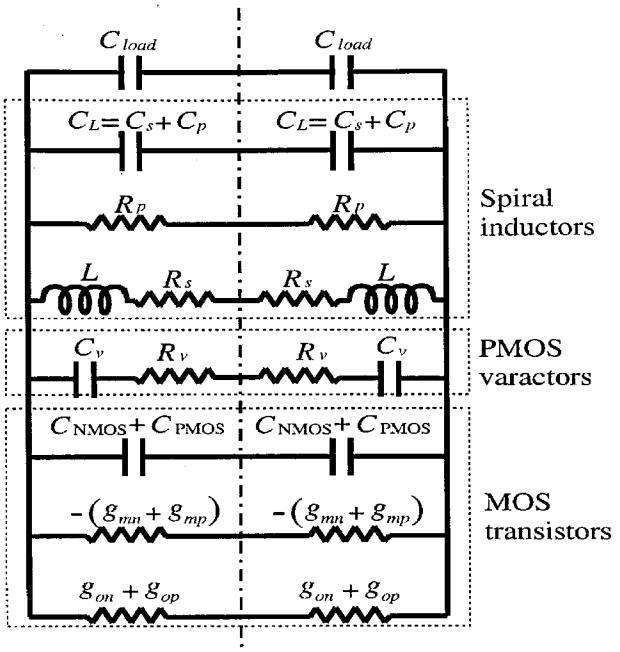

Figure 6.26: Equivalent oscillator model.

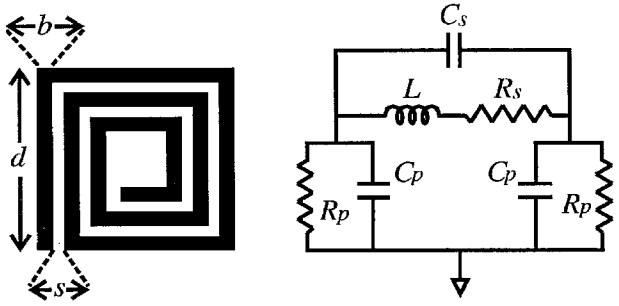

Figure 6.27: Symmetric spiral inductor model.

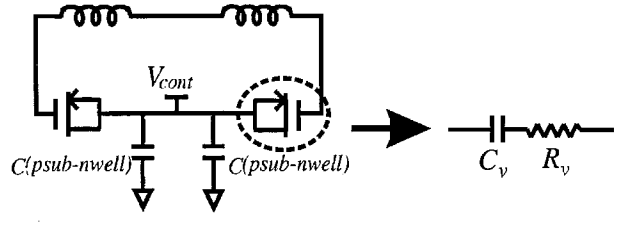

Figure 6.28: *LC* tank and MOSCAP varactor.

the voltage across the LC tank is zero. This approximation facilitates the analytical expression of design constraints. We will justify that the approximation does not mislead the design shortly. All the electrical parameters in the equivalent circuit model can be expressed in terms of design variables, by utilizing existing formulae for transistor parameters and on-chip resonator parameters [110], [111].

The frequently appearing parameters in our optimization process are the tank loss, g_{tank}, effective negative conductance $-g_{active}$, tank inductance, L_{tank}, and tank capacitance, C_{tank}, given by

$$2g_{tank} = g_{on} + g_{op} + g_v + g_L, \tag{6.94}$$

$$2g_{active} = g_{mn} + g_{mp}, \tag{6.95}$$

$$L_{tank} = 2L, \tag{6.96}$$

$$2C_{tank} = C_{\text{PMOS}} + C_{\text{NMOS}} + C_L + C_v + C_{load}, \tag{6.97}$$

respectively, where g_L and g_v are the effective parallel conductance of the inductors and varactors, respectively[8]. As g_{tank} and C_{tank} assume certain range of values as the varactor capacitance varies, their maximum and minimum values will be denoted by subscripts *max* and *min*.

Design Constraints

Design constraints are imposed on power dissipation, tank amplitude, frequency tuning range, start-up condition, and diameter of spiral inductors.

First, the maximum power constraint is imposed in the form of the maximum bias current I_{max} drawn from a given supply voltage V_{supply}, *i.e.*,

$$I_{bias} \leq I_{max} \tag{6.98}$$

Second, the tank amplitude is required to be larger than a certain value, $V_{tank,min}$, to provide a large enough voltage swing for the next stage:

$$r_0 = \frac{I_{bias}}{g_{tank,max}} \geq V_{tank,min} \tag{6.99}$$

The subscript *max* in $g_{tank,max}$ signifies the worst case scenario. Since g_L is the dominant term in (6.94), the approximation for g_o mentioned earlier does not lead to a significant error.

Third, the tuning range of the oscillation frequency is required to be in excess of a certain

[8] $g_L = 1/R_p + R_s/(L\omega)^2$ and $g_v = (C_v\omega)/Q_v$.

minimum percentage of the center frequency, ω, *i.e.*,

$$L_{tank}C_{tank,min} \leq \frac{1}{\omega_{max}^2} \tag{6.100}$$

$$L_{tank}C_{tank,max} \geq \frac{1}{\omega_{min}^2} \tag{6.101}$$

where $(\omega_{max} - \omega_{min})/\omega =$ (minimum fractional tuning range) and $(\omega_{max} + \omega_{min})/2 = \omega$.

Fourth, the start-up condition with a small-signal loop gain of at least α_{min} can be expressed as

$$g_{active} \geq \alpha_{min} g_{tank,max} \tag{6.102}$$

where the worst-case condition is imposed by $g_{tank,max}$. To overcome the possible error that the approximation for g_m mentioned previously might cause, we can select a conservative minimum small-signal loop gain α_{min} (*e.g.*, 3).

Finally, we specify a maximum diameter for the spiral inductor as d_{max}, *i.e.*,

$$d \leq d_{max} \tag{6.103}$$

to limit the die area.

Phase Noise in the Cross-Coupled Topology

In the $1/f^2$ region, the phase noise is given by [63]

$$\mathcal{L}\{f_{off}\} = \frac{1}{8\pi^2 f_{off}^2} \cdot \frac{1}{q_{max}^2} \cdot \sum_n \left(\frac{\overline{i_n^2}}{\Delta f} \cdot \Gamma_{rms,n}^2\right) \tag{6.104}$$

where f_{off} is the offset frequency from the carrier and q_{max} is the total charge swing of the tank. The *impulse sensitivity function* (ISF), Γ, represents the time-varying sensitivity of oscillator's phase to perturbations [63]. Each $\Gamma_{rms,n}$ in (6.104) is the *rms* value of the ISF for each noise source and is $1/\sqrt{2}$ for an ideal sinusoidal waveform. It can be evaluated more accurately from simulations as shown in Sec. 6.8.3.

The $\overline{i_n^2}/\Delta f$ terms in the sum of (6.104) represent the equivalent differential noise power spectral density due to drain current noise, inductor noise and varactor noise and they are given by [104], [47], [114]

$$\frac{\overline{i_{M,d}^2}}{\Delta f} = 2kT\gamma(g_{d0,n} + g_{d0,p}) \tag{6.105}$$

$$\frac{\overline{i_{ind}^2}}{\Delta f} = 2kTg_L \tag{6.106}$$

$$\frac{\overline{i_{var}^2}}{\Delta f} = 2kTg_{v,max} \tag{6.107}$$

where $\gamma \sim 2/3$ and $\gamma \sim 2.5$ for long- and short-channel transistors, respectively. g_{d0} is the channel conductance at zero V_{DS} and is equal to g_m for long-channel transistors while it is given by $2I_{drain}/(L_{channel}E_{sat})$[9] for short-channel transistors [114]. $g_{v,max}$ in the varactor noise power spectral density is used for the worst-case noise.

Dominance of Drain Current Noise

In this subsection, we demonstrate the dominance of drain current noise for the design topology of Fig. 6.25, which will be used to simplify (6.104).

According to (6.94), (6.106) and (6.107), the equivalent current noise density due to the varactors and the inductors is less than $4kTg_{tank,max}$, *i.e.*,

$$\frac{\overline{i_{ind}^2}}{\Delta f} + \frac{\overline{i_{var}^2}}{\Delta f} < 4kTg_{tank,max} \tag{6.108}$$

While $g_m = g_{d0}$ for long-channel transistors, $g_m < g_{d0}$ for short-channel transistors by definition of the short-channel regime, *i.e.*,

$$\frac{g_m}{g_{d0}} = \frac{L_{channel}E_{sat}}{2(V_{GS} - V_{TH})} < 1 \tag{6.109}$$

Therefore, from (6.95) and (6.105), we obtain

$$\frac{\overline{i_{M,d}^2}}{\Delta f} \geq 4kT\gamma g_{active} \tag{6.110}$$

where the equality and the inequality are valid for the long- and short-channel transistors, respectively.

Now the ratio of the equivalent current noise density due to the tank components to that of the drain current can be upper-bounded using (6.108) and (6.110), *i.e.*,

$$\frac{\overline{i_{ind}^2}/\Delta f + \overline{i_{var}^2}/\Delta f}{\overline{i_{M,d}^2}/\Delta f} < \frac{4kTg_{tank,max}}{4kT\gamma g_{active}} \leq \frac{1}{\gamma\alpha_{min}} \tag{6.111}$$

where we used the start-up condition (6.102) to obtain the last inequality. The inequality of (6.111) predicts that with $\alpha_{min} = 3$ the drain current noise contributes more than 88% of the circuit noise for short-channel transistors. This prediction agrees well with the simulation result shown later.

Now by taking only the dominant drain current noise term into account in (6.104), we can obtain

[9] E_{sat} is the electric field at which the carrier velocity reaches half its saturation velocity.

an insightful approximation for phase noise. Using (6.104) and (6.105) while replacing q_{max} with $r_0/(L_{tank}\omega^2)$, we obtain

$$\mathcal{L}\{f_{off}\} \propto \frac{L^2 I_{bias}}{r_0^2} \tag{6.112}$$

where $g_{d0} = 2I_{drain}/(L_{channel}E_{sat})$ was used for short-channel transistors[10] and $\Gamma_{rms}^2 = 1/2$ was used for a pure sinusoidal waveform. Equation (6.112) can be easily interpreted by noting that $r_0 = I_{bias}/g_{tank} \approx I_{bias}/g_L$ in the inductance-limited regime and $r_0 = V_{limit} = V_{supply}$ in the voltage-limited regime, *i.e.*,

$$\mathcal{L}\{f_{off}\} \propto \begin{cases} L^2 g_L^2/I_{bias} & (L\text{-limited}) \\ L^2 I_{bias} & (V\text{-limited}) \end{cases} \tag{6.113}$$

This equation is in perfect agreement with (6.93), which led to a convenient design strategy that the inductance should be minimized (while satisfying the design constraints) for a given bias current in the previous section.

Now, let us see how the phase noise depends upon the bias current. Equation (6.113) indicates that for a given inductance L, phase noise increases with the bias current in the voltage-limited regime, inducing *waste of power*. Note that (6.113) ignores the cyclostationary effects that can change the dependence of the phase noise on the bias current in the voltage-limited regime. A more rigorous treatment taking the cyclostationary noise into account shows that phase noise reaches a plateau with an increase of the bias current in the voltage-limited regime [104]. Even with this consideration, the current that places the design in the voltage-limited regime causes waste of power as unnecessary power dissipation occurs without a significant improvement in phase noise.

Now we demonstrate the power-noise trade-off in the design of LC oscillators, assuming that the inductance reduction is limited by the tank amplitude constraint (6.99). One can obtain the optimum inductance for a given I_{bias} by calculating the maximum allowable g_L using $I_{bias}/g_{tank} \approx I_{bias}/g_L = V_{tank,min}$. This maximum allowable g_L will correspond to the minimum (and hence optimum) allowable L in Fig. 6.23. The optimum $L^2 g_L^2/I_{bias}$ given in (6.113) is then plotted for different values of I_{bias} in Fig. 6.29. As can be seen from Fig. 6.29, a larger bias current results in a better optimum phase noise, concluding that I_{bias} should always be set to its maximum value allowed by (6.98). Hence, this design constraint is tight.

The design strategy for the oscillator in Fig. 6.25 can be summarized in the following way: Find *the minimum inductance* that satisfies both the tank amplitude and start-up constraints for *the maximum bias current* allowed by the design specifications. This design strategy will be executed using a practical graphical optimization method in the following section.

[10] $I_{bias} = 2I_{drain}$

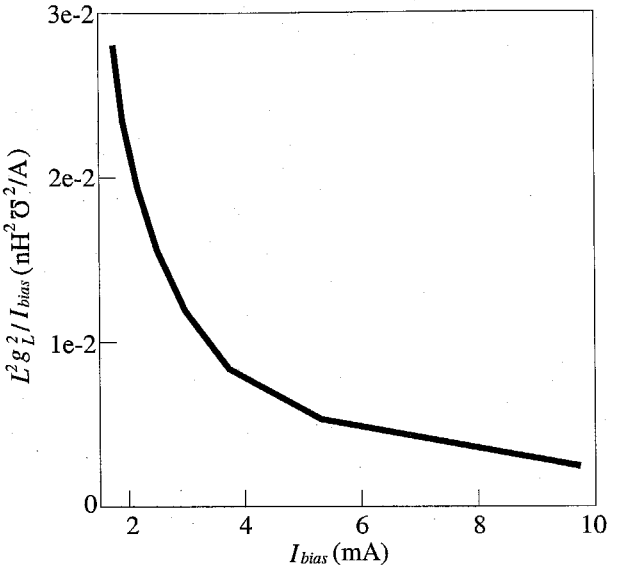

Figure 6.29: $L^2g_L^2/I_{bias}$ versus the bias current I_{bias}.

6.8.2 *LC* VCO optimization via graphical methods

As mentioned earlier, phase noise of the *LC* oscillator in Fig. 6.25 can be optimized by reducing the inductance as far as both the tank amplitude and start-up constraints allow. While it may appear trivial, performing such inductance reduction is challenging in practice, as the L-reduction should be executed while satisfying all the design constraints. This challenge can be overcome by visualizing the design constraints graphically.

It is noteworthy that the following optimization will result in a *near optimum* design, as time varying effects, such as cyclostationarity, are ignored and the ISF is assumed to have an rms value of $1/\sqrt{2}$. A final quick fine-tuning simulation has to be performed to obtain the most accurate predictions, as shown in the next section.

Now we demonstrate the optimization process, starting with the reduction of the number of independent design variables through appropriate design considerations, in the context of a numerical example.

Independent Design Variables and Numerical Design Constraints

In this subsection, we reduce the number of design variables from the original twelve to six [115]. First, as shown in the previous section, the power consumption constraint (6.98) is tight and I_{bias} is set to I_{max}. Second, in the cross-coupled MOS transistors, both channel length L_n and L_p are set to the minimum allowed by the process technology to reduce parasitic capacitance and

achieve the highest transconductance. Also, a symmetric active circuit with $g_{mn} = g_{mp}$[11] is used to improve the $1/f^3$ corner of phase noise, which establishes a relation between W_p and W_n. Therefore, MOS transistors introduce only one independent design variable, W_n. Third, MOSCAP varactors introduce only one design variable $C_{v,max}$ since in a typical varactor, the ratio $C_{v,max}/C_{v,min}$ is primarily determined by underlying physics of the capacitor and remains constant for a scalable layout. Fourth, the size of the output driver transistors can be pre-selected so that they can drive a 50 Ω load with a specified output power with the worst-case minimum tank amplitude of $V_{tank,min}$. This results in a specific value for C_{load}, excluding it from the set of design variables. Table 2 shows the reduced set of independent design variables, together with their abbreviated notation that will be used from now on.

Components	Design variables	Notation
Transistors	W_n	w
Spiral inductors	b, s, n, d	b, s, n, d
Varactors	$C_{v,max}$	c

Table 2 : Six independent design variables

To demonstrate a typical design problem, specific numerical design constraints are imposed in accordance with Subsection 6.8.1 as shown in Table. 3.

Eq.	Specifications	Value
N/A	V_{supply}	2.5V
(6.98)	I_{max}	4mA
(6.99)	$V_{tank,min}$	2V
(6.100),(6.101)	f_{center}	2.4GHz
(6.100),(6.101)	minimum tuning range	15%
(6.102)	α_{min}	3
(6.103)	d_{max}	200μm

Table 3 : Example of design constraints

Identification of Feasible Design Regions

In this subsection, L is fixed to show how feasible design points in the cw-plane can be identified. The numerical value of the selected inductance in this subsection is $2.7nH$ where the inductor geometric parameters, b, s, n and d, are chosen such that g_L becomes minimum for this value of L.

The design constraints given by (6.99) - (6.102) are visualized in Fig. 6.30 in the cw-plane where w is in μm and c is in pF. The tank amplitude line is the loci of the cw points resulting in a tank

[11]This is an approximate criterion. More accurate criteria for minimization of $1/f$ noise can be found in [86].

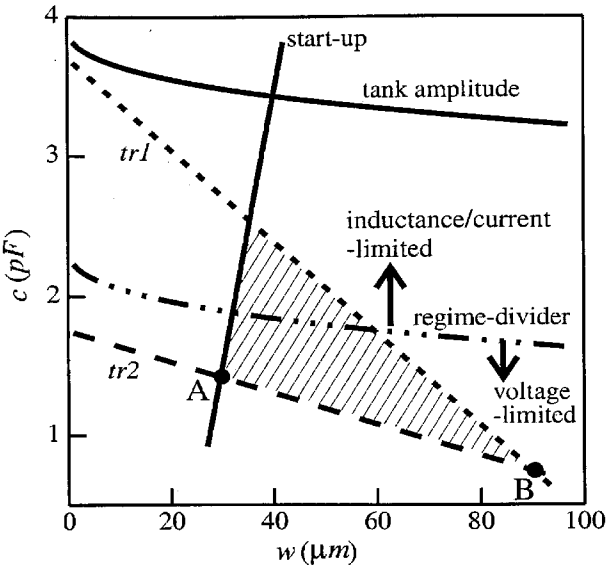

Figure 6.30: Design constraints for $I_{bias} = 4$ mA.

amplitude of $V_{tank,min} = 2V$, using (6.99). Points below this tank amplitude line correspond to a r_0 larger than 2V. The broken line with one dash and three consecutive dots represents the *regime-divider line*, below which the oscillation occurs in the voltage-limited regime with the tank amplitude of $V_{limit} = V_{supply} = 2.5$V. The *tr1* and *tr2* lines are obtained from (6.100) and (6.101), respectively. A tuning range of at least 15% with a center frequency of 2.4GHz is achieved if a design point lies below the *tr1* line and above the *tr2* line. The start-up line is obtained from (6.102). The small-signal loop gain is over $\alpha_{min} = 3$ on the right-hand side of the start-up line to guarantee start-up. The shaded region in Fig. 6.30 satisfies all the constraints in (6.99) to (6.102) and therefore represents a set of feasible design points.

Further intuition can be obtained from this graphical representation. For instance, the effect of the start-up condition on the size of the region of plausible design can be seen in Fig. 6.31. It shows the effect of the loop-gain constraint, where increasing the minimum small-signal loop gain, α_{min}, shrinks the region of feasibility. Intuitively, a higher small-signal loop gain requires larger transistor dimensions, and therefore the resultant increase in the parasitic capacitances makes it more difficult to obtain the desired tuning range.

The dominance of drain current noise lowers the dependence of phase noise on transistor width, w, and the maximum capacitance of varactors, c. Therefore, the phase noise difference across the feasible design area in the cw-plane is expected be small. For example, in Fig. 6.30, phase noise difference between points **A** and **B** is no more than 0.5 dB where the phase noise was calculated from (6.104). This fact is well reflected in phase noise approximation (6.113), which suggests a strong

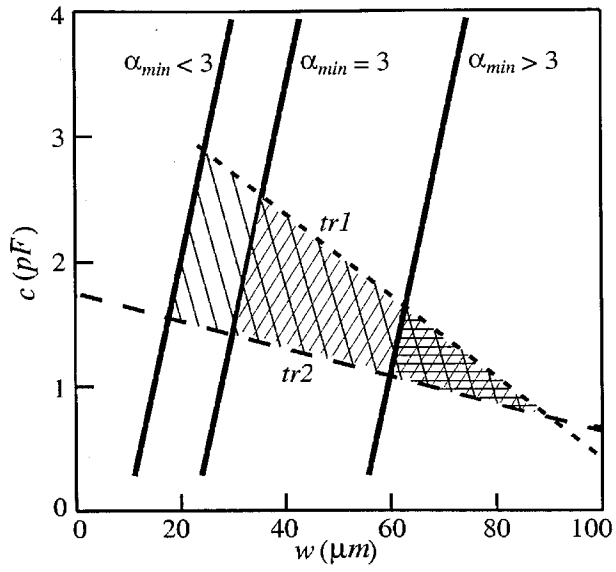

Figure 6.31: Effect of changes in the minimum small-signal loop gain.

dependence of phase noise on the choice of inductor rather than c and w.

Inductance Selection

We now execute the design strategy obtained in Sec. 6.8.1, exploiting the graphical representation of the design constraints. As $g_{tank} \approx g_L$ increases with a decreasing L as shown in Fig. 6.23, the L-reduction will translate the tank amplitude line downward and the start-up line to the right, shrinking the feasible design area in the cw-plane. For g_L in excess of a certain critical value, either the minimum tank amplitude constraint or the start-up constraint will be violated as can be seen from (6.94), (6.99) and (6.102). The inductance corresponding to this critical g_L is the optimum inductance, L_{opt}. Tuning range constraints are of no concern with the L-reduction process as decreasing L increases the capacitance budget, relaxing the tuning-range constraints. With $L = L_{opt}$, there exists only a single feasible design point in the cw-plane, which lies on either the tank amplitude line or the start-up line.

Different scenarios can be envisioned depending on the order the constraints are encountered with the reduction of L, as shown in Fig. 6.32. If the tank amplitude limit is reached first, the single feasible design point lies on the tank amplitude line at $L = L_{opt}$, as shown in Fig. 6.32(a). This unique design point **A** in the cw-plane represents the optimum c and w.

On the other hand, when the start-up constraint becomes active first, the region of feasibility will shrink to a single point **B** located on the start-up line, as shown in Fig. 6.32(b) and (c). Two different cases can be identified here. If point **B** lies in the inductance-limited regime (between the

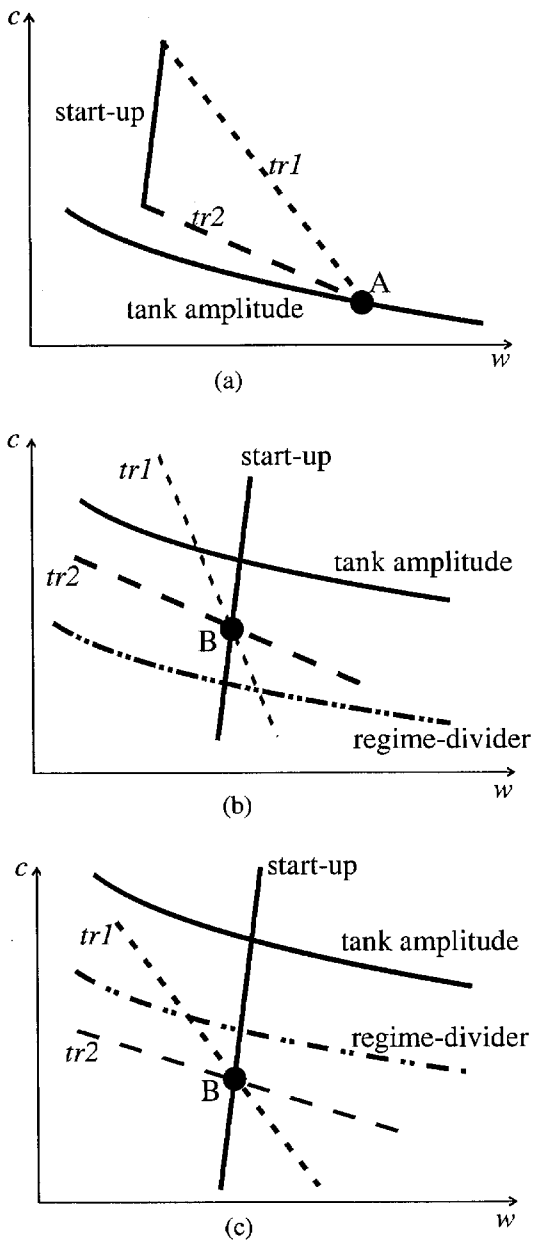

Figure 6.32: Design constraints with $L = L_{opt}$. (a) L-reduction limited by the tank amplitude constraint (b) L-reduction limited by the start-up constraint without waste of power (c) L-reduction limited by the start-up constraint with waste of power.

tank amplitude and regime-divider lines) as shown in Fig. 6.32(b), point **B** will correspond to the optimum design and no further action is necessary. However, if **B** resides in the voltage-limited regime (below the regime-divider line), as depicted in Fig. 6.32(c), the design suffers from waste of power. In this case, the bias current should be reduced to make the regime-divider line translate downward and pass through point **B**[12].

Summary of the Optimization Process

The design optimization process can be summarized as follows. Set the bias current to I_{max}, and pick an initial guess for the inductance value. Find the inductor with this inductance that minimizes g_L. This can be done using the method proposed in [110] or using simulation tools such as ASITIC [116]. Plot the design constraints in the cw-plane using the selected inductor. If there are more than one feasible design points in the cw-plane, decrease the inductance and repeat until the feasible design area shrinks to a single point, as in Fig. 6.32. The single design point in the cw-plane represents the optimum c and w and the corresponding inductor with $L = L_{opt}$ is the optimum inductor. If the single design point lies in the voltage-limited regime, the bias current should be reduced from I_{max} until the regime-divider line passes through the single feasible design point to avoid waste of power.

Robust Design

The graphical visualization of design constraints can help us cope with possible process variations, leading to a robust design. In the presence of process variations, the constraint lines turn into bands as shown hypothetically in Fig. 6.33. The broken and solid lines represent design constraints in the slow and fast process corner, respectively. The robust design points are selected inside the inner triangle, sides of which consist of broken lines. The shaded area in the figure represents unreliable design in the presence of process variations. Accordingly, the optimization process should be modified to turn the region of reliable design to a single point, instead.

6.8.3 Simulation

Validity of the approximations made in the previous sections can be verified using simulations. In this section, an accurate phase-noise simulation is performed [115] on the VCO designed using our optimization process. The more accurate nonsymmetric equivalent circuit for spiral inductors used in simulations is depicted in Fig. 6.34. This nonsymmetric model was developed using *ASITIC* to address the physical asymmetry of the spiral structure [116].

Phase noise simulation is performed at a center frequency of 2.22 GHz with a tail current of

[12]The start-up and tuning range lines show little dependence on the bias current. It is obvious that the tuning range is not affected by the bias current. The start-up constraint is almost independent of the bias current as the transconductance of short-channel transistors shows little dependence on the bias current.

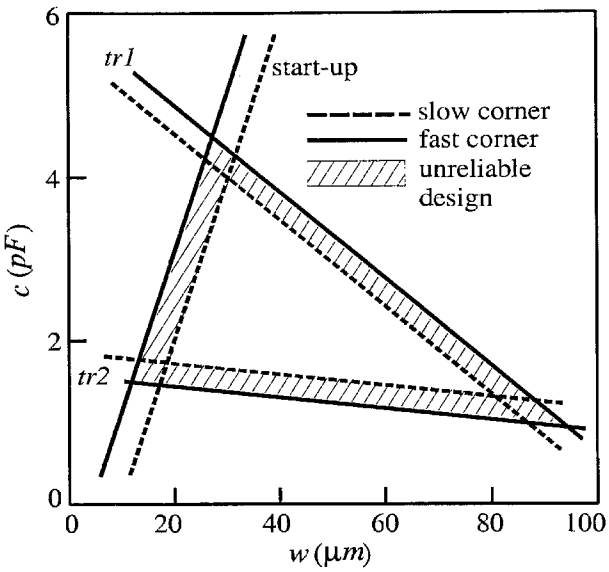

Figure 6.33: Process variations and resultant constraint change.

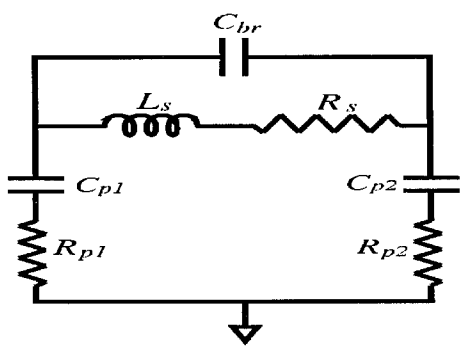

Figure 6.34: Nonsymmetric spiral inductor model.

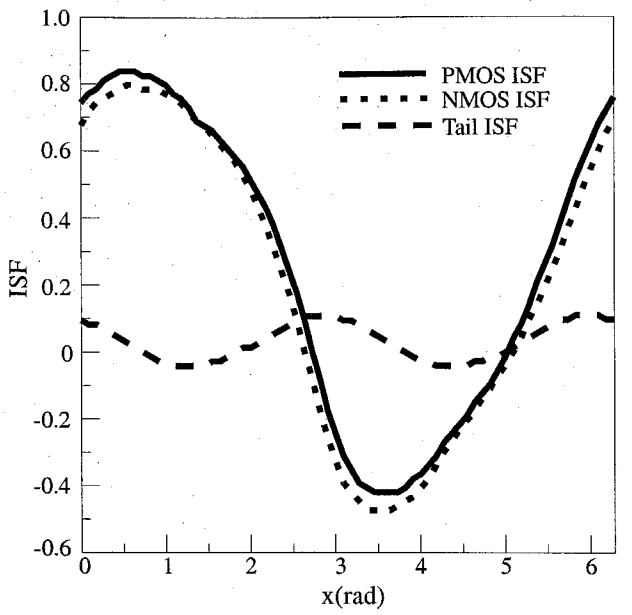

Figure 6.35: Impulse sensitivity function (ISF).

4mA. The *impulse sensitivity functions* (ISF) of various noise sources are obtained by performing the charge injection simulation [63] and are depicted in Fig. 6.35 for the PMOS, NMOS and tail transistors. The cyclostationary effect of the drain current noise due to the periodic operating point change can be taken into account by the *noise modulating function* (NMF), which is proportional to $\sqrt{g_{d0}}$ [63]. The simulated NMF for PMOS and NMOS transistors is shown in Fig. 6.36. The effective ISF, which is the product of the original ISF and the NMF for the drain current noise, is depicted in Fig. 6.37.

The total simulated phase noise is -120 dBc/Hz at 600 kHz offset from a 2.22 GHz carrier. The circuit noise contributions from each noise source are shown in Table 4. Note that most of the circuit noise is contributed by the drain current noise of the cross-coupled transistors, as demonstrated earlier. The approximate equation (6.113) predicts a phase noise of -121 dBc/Hz at 600 kHz offset. This is only 1 dB different from the simulation results, confirming the validity of the assumption leading to (6.113). The $1/f$ noise reduction factors are 0.18 and 0.25 for NMOS and PMOS transistors, respectively [63].

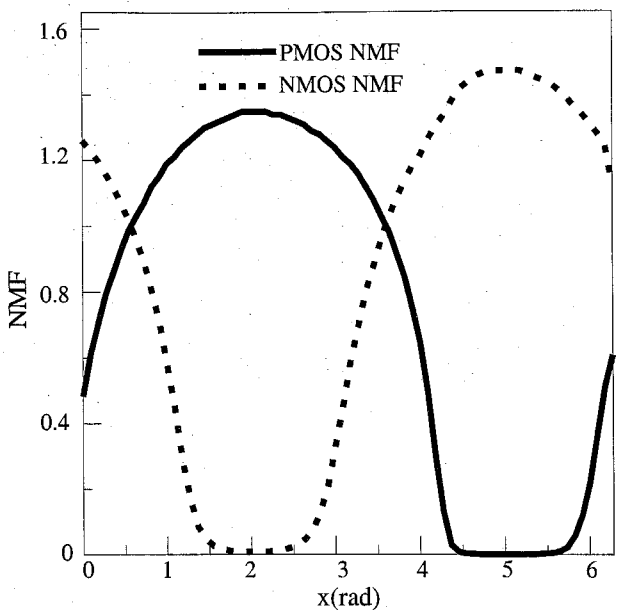

Figure 6.36: Noise modulating function (NMF).

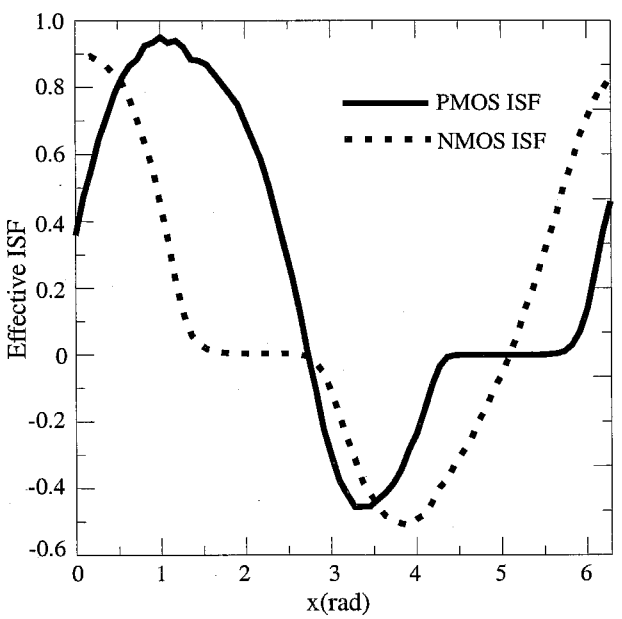

Figure 6.37: Effective ISF.

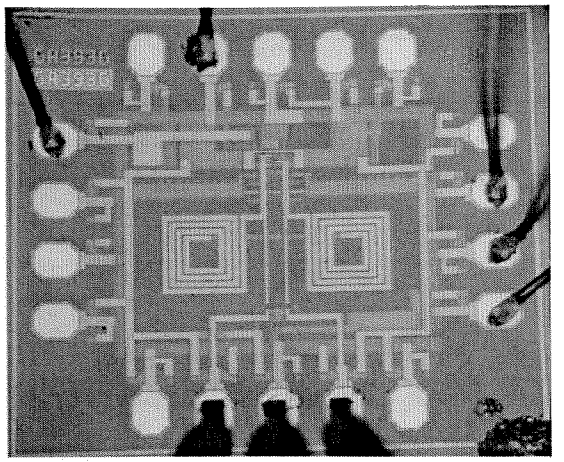

Figure 6.38: Chip photograph.

Noise source	PSD (A^2/Hz)	Contribution
Drain current	6.90×10^{-23}	86 %
Gate	1.20×10^{-24}	1.5%
Inductor	4.49×10^{-24}	5.6 %
Varactor	1.77×10^{-24}	2.2 %
Tail current	3.73×10^{-24}	4.7%

Table 4 : Simulated result of noise contributions from each noise source

6.8.4 Experimental Results

Table 5 summarizes performance of the VCO, which was implemented in a three-metal, $0.35\mu m$ BiCMOS technology, only using MOS transistors. Fig. 6.38 shows the VCO chip photograph. A tuning range of 26% is achieved, as shown in Fig. 6.39. Phase noise is measured using an HP8563 spectrum analyzer with phase noise measurement utility. The measured phase noise at 2.2 GHz is about 3 dB higher than the simulated phase noise. This 3 dB difference can be attributed to the uncertain channel noise factor, γ, degradation of tank amplitude caused by the parasitic resistors in metal layers and high sensitivity of the oscillation frequency to extrinsic supply and control line noise due to the high VCO gain at this frequency.

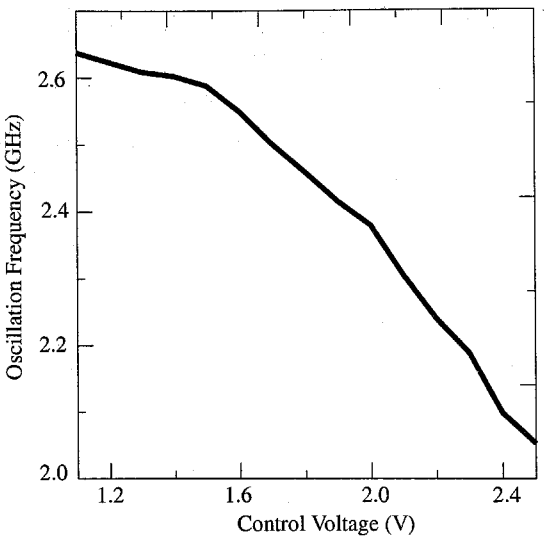

Figure 6.39: Frequency tuning.

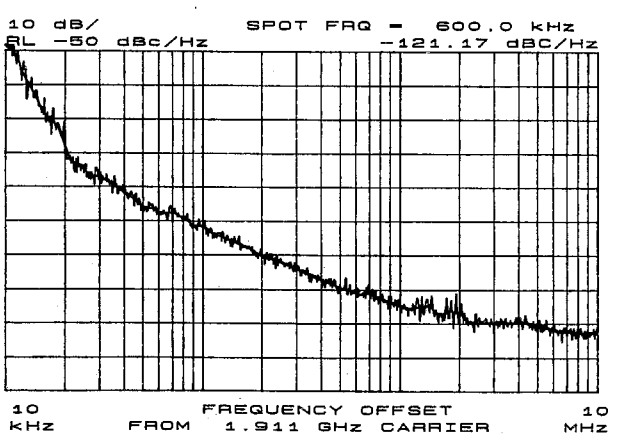

Figure 6.40: Measured phase noise versus f_{off} at 1.91GHz.

Supply voltage	2.5V
Current (core)	4mA
Center frequency	2.33GHz
Tuning range	26 %
Output power	0dBm
Phase noise ($f_c = 1.91GHz$, @$600kHz$)	-121dBc/Hz
Phase noise ($f_c = 2.03GHz$, @$600kHz$)	-117dBc/Hz
Phase noise ($f_c = 2.63GHz$, @$600kHz$)	-115dBc/Hz

Table 5 : VCO performance summary

To measure the phase noise more accurately, we increased the control voltage up to 3.5V which further reduces the oscillation frequency down to 1.91GHz where the VCO gain is very low. Fig. 6.40 shows a plot of phase noise versus offset frequency from the 1.91GHz carrier. The phase noise measurement at 600kHz offset from the 1.91GHz carrier yields -121dBc/Hz.

To compare the performance of our oscillator to recently reported results [87] - [109], we define two figures of merit. First, *power-frequency-normalized (PFN)* figure of merit

$$PFN = 10\log[\frac{kT}{P_{sup}} \cdot (\frac{f_0}{f_{off}})^2] - \mathcal{L}\{f_{off}\} \tag{6.114}$$

was devised noting that phase noise of an oscillator measured at an offset f_{off} from a carrier at f_0 is proportional to f_0^2 and inversely proportional to f_{off}^2 [77] as well as the power dissipated in the resistive part of the tank. As the power dissipated in the resistive part of the tank cannot be easily calculated from the VCO specification, phase noise is normalized to kT/P_{sup} in (6.114), where P_{sup} is the total dc power dissipated in the VCO. PFN is a unitless figure of merit expressed in dB. A larger PFN corresponds to a better oscillator.

To take tuning range into account in the comparison of different oscillators, a second figure of merit called, *power-frequency-tuning-normalized (PFTN)*

$$PFTN = 10\log[\frac{kT}{P_{sup}} \cdot (\frac{f_{tune}}{f_{off}})^2] - \mathcal{L}\{f_{off}\} \tag{6.115}$$

was devised where $f_{tune} = f_{max} - f_{min}$. Note that $PFTN$ is a normalization of PFN to the squared tuning range, $(f_{tune}/f_0)^2$. Again a larger $PFTN$ corresponds to a better oscillator.

Using these two figures of merit, the designed oscillator is compared to those reported in [87] - [109] in Fig. 6.41 and 6.42. The reported oscillator in this paper has the second largest PFN and the largest $PFTN$ among the oscillators with on-chip inductors using standard metal layers.

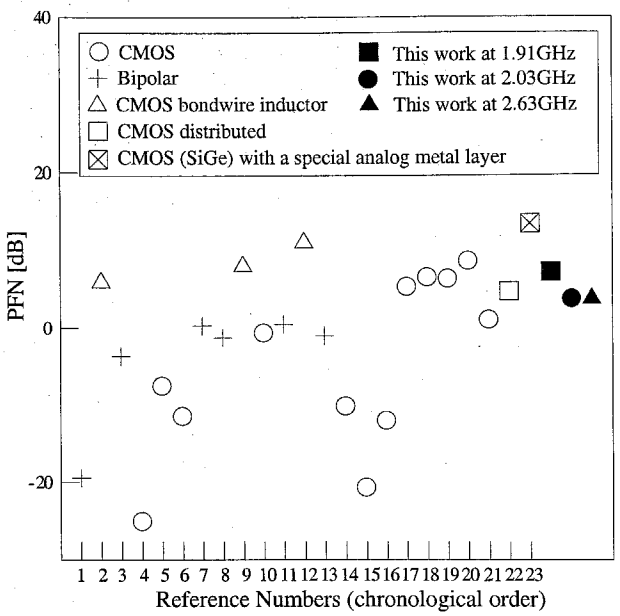

Figure 6.41: PFN for various oscillators.

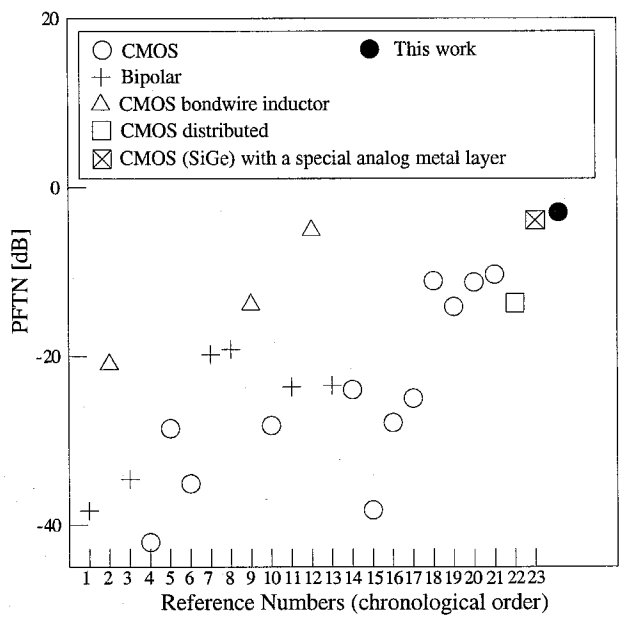

Figure 6.42: PFTN for various oscillators.

Chapter 7 Conclusion

This thesis presented a general study of noise in electrical circuits and developed a new physical theory of noise in mixers and oscillators. The scientific importance of our results includes several new observations of thermal fluctuations in nonlinear time-varying circuits and original physical insight into the noise processes. Technologically, our investigation has considerable engineering significance as a demonstration of how we can develop practical novel circuit designs starting from fundamental physical considerations. The power of our approach was demonstrated by applying our theory to three practical topics which remain active fields of research: (1) fluctuations in nonlinear electrical circuits, (2) noise in mixers, and (3) noise in oscillators.

In Chapter 4, we rigorously investigated thermal fluctuations in nonlinear electrical circuits, providing profound insights into and tangible understandings of nonlinear fluctuation phenomena. Particularly, our study of fluctuations in nonlinear resistors was an important sector of this investigation, verifying the physical soundness of the contemporary noise models for certain active devices. This investigation was facilitated through a close examination of the energetics in nonlinear electrical systems.

Chapter 5 studies noise in mixers, and presents two new observations: noise figure degradation due to cyclostationary noise and conversion gain enhancement, both dependent on the size of energy storing elements. These novel behaviors were experimentally verified with a direct measurement of integrated switching mixers. The results provided new insights into cyclostationary noise processes in mixers and optimum design.

Chapter 6 presents our study on noise in oscillators. The fundamental physical investigation of noise in oscillators results in a new oscillator noise theory, bringing a transparent insight into oscillator phase noise. Novel concepts of virtual damping and linewidth compression put resonators and oscillators in a unified framework, leading to a general oscillator design otpimization strategy. Demonstration of a direct correspondence between oscillator phase noise and Einstein relation reveals the underlying physics of phase noise. The theory was verified with experiments using various oscillator prototypes. Additionally, as a useful engineering method, we have developed an intuitive graphical optimization method for oscillator design.

Overall, this thesis is a comprehensive physical theory of noise in electronics. Many of the results are easily applied and should become part of the working knowledge of RF and microwave engineers.

Chapter 8 Appendices

8.1 Appendix 1

Since the weak nonlinearity regime is characterized by the condition $\omega_0 \gg \omega_\tau$ and hence there are two major time-constants inherent in the oscillator (ω_0^{-1} and γ^{-1}), we define a new parameter $\lambda \equiv \gamma/\omega_0 = Q^{-1} \ll 1$ and introduce two independent time variables τ_0 and τ_1:

$$\begin{aligned} \tau_0 &= t \\ \tau_1 &= \lambda t \end{aligned} \tag{8.1}$$

Having $v = v_0 + \lambda v_1 + \cdots$ on one hand and (8.1) on the other, we can obtain the following equations from (6.3):

$$\frac{\partial^2 v_0}{\partial \tau_0^2} + \omega_0^2 v_0 = 0 \qquad [O(\lambda^0) \text{ terms}] \tag{8.2}$$

$$\frac{\partial^2 v_1}{\partial \tau_0^2} + \omega_0^2 v_1 = -2\frac{\partial^2 v_0}{\partial \tau_1 \partial \tau_0} - \omega_0 f(v_0)\frac{\partial v_0}{\partial \tau_0} \qquad [O(\lambda^1) \text{ terms}] \tag{8.3}$$

where our approximations are consistent up to the first order of λ and $f(v) \approx f(v_0) + \lambda v_1 f'(v_0)$ was used. The solution of (8.2) is

$$v_0(\tau_0, \tau_1) = r(\tau_1)\cos(\omega_0 \tau_0 - \theta(\tau_1)) \tag{8.4}$$

This $O(\lambda^0)$-order solution corresponds to the near-sinusoid approximation while the detailed information on r and θ is to be obtained from the $O(\lambda^1)$-order equation. By plugging (8.4) into (8.3), we obtain

$$\frac{\partial^2 v_1}{\partial \tau_0^2} + \omega_0^2 v_1 = (\omega_0^2 r f(v_0) + 2\omega_0 \frac{dr}{d\tau_1})\sin(\omega_0 \tau_0 + \theta) + 2\omega_0 r \frac{d\theta}{d\tau_1}\cos(\omega_0 \tau_0 + \theta) \tag{8.5}$$

which becomes, for the Van der Pol oscillator,

$$\frac{\partial^2 v_1}{\partial \tau_0^2} + \omega_0^2 v_1 = (2\omega_0 \frac{dr}{d\tau_1} - k\omega_0^2 r - \frac{1}{4}a\omega_0^2 r^3)\sin(\omega_0 \tau_0 + \theta) + 2\omega_0 r \frac{d\theta}{d\tau_1}\cos(\omega_0 \tau_0 - \theta) \tag{8.6}$$

$$+ \text{ third-order harmonics} \tag{8.7}$$

To exclude the nonrealistic case in which $v_1(t)$ becomes unstable, we set the coefficients of the cosine and sine of the first and second term to zero, leading to

$$\frac{dr}{d\tau_1} = \frac{a\omega_0 r}{8}(\frac{4k}{a} - r^2) \tag{8.8}$$

$$\frac{d\theta}{d\tau_1} = 0 \tag{8.9}$$

8.2 Appendix 2

If a probability distribution function for $\phi(t)$ is Gaussian at a given time t, we can obtain an explicit expression for averages such as $\langle \cos\phi \rangle$, $\langle \cos\phi(t_1)\cos\phi(t_2) \rangle$, etc., by appealing to the fact that the Gaussian distribution has zero $n-th$ order cumulants for $n \geq 3$, *i.e.*, $\langle e^{j\phi} \rangle = e^{-\langle \phi^2 \rangle/2}$ and $\langle e^{j(\phi(t_1)+\phi(t_2))} \rangle = e^{-(1/2)(\langle \phi^2(t_1)\rangle + \langle \phi^2(t_2)\rangle - 2\langle \phi(t_1)\phi(t_2)\rangle)} + e^{-(1/2)(\langle \phi^2(t_1)\rangle + \langle \phi^2(t_2)\rangle + 2\langle \phi(t_1)\phi(t_2)\rangle)}$. From these, the following Table 3 is constructed which is essential in evaluating the statistical properties of the signal $v(t) = \cos(\omega_0 t + \phi(t))$:

Ensemble average	Analytical expressions in terms of $\langle \phi^2(t) \rangle$ and $\langle \phi(t_1)\phi(t_2) \rangle$
$\langle \cos\phi(t) \rangle$	$e^{-\langle \phi^2(t)\rangle/2}$
$\langle \sin\phi(t) \rangle$	0
$\langle \sin\phi(t_1)\sin\phi(t_2) \rangle$	$[e^{-(1/2)(\langle \phi^2(t_1)\rangle + \langle \phi^2(t_2)\rangle - 2\langle \phi(t_1)\phi(t_2)\rangle)} - e^{-(1/2)(\langle \phi^2(t_1)\rangle + \langle \phi^2(t_2)\rangle + 2\langle \phi(t_1)\phi(t_2)\rangle)}]/2$
$\langle \cos\phi(t_1)\cos\phi(t_2) \rangle$	$[e^{-(1/2)(\langle \phi^2(t_1)\rangle + \langle \phi^2(t_2)\rangle - 2\langle \phi(t_1)\phi(t_2)\rangle)} - e^{-(1/2)(\langle \phi^2(t_1)\rangle + \langle \phi^2(t_2)\rangle + 2\langle \phi(t_1)\phi(t_2)\rangle)}]/2$
$\langle \sin\phi(t_1)\cos\phi(t_2) \rangle$	0
$\langle \cos\phi(t_1)\sin\phi(t_2) \rangle$	0

Table 3: Ensemble averages of various triangular functions whose arguments are diffusion processes.

Bibliography

[1] H. Nyquist, *Phys. Rev.*, **32**, 110, 1928.

[2] A. Abramovici *et al.*, "LIGO: the laser interferometer gravitational-wave observatory," *Science*, **256**, 325-333, 1992.

[3] P. Saulson, *Fundamentals of Interferometric Gravitational Wave Detectors*, World Scientific, 1994.

[4] C. E. Shannon and W. Weaver, *The Mathematical Theory of Communication*, University of Illinois Press, 1949.

[5] J. B. Hagen, *Radio-Frequency Electronics : Circuits and Applications*, Cambridge University Press, 1996.

[6] K. Clarke and D. Hess, *Communication Circuits : Analysis and Design*, Krieger Publishing Co., 1971.

[7] T. H. Lee, *The Design of CMOS Radio-Frequency Integrated Circuits*, Cambridge University Press, 1998.

[8] B. Razavi, *RF Microelectronics*, Prentice-Hall,Inc. 1998

[9] P. Horowitz and W. Hill, *The Art of Electronics*, Cambridge University Press, 1980.

[10] J. D. Kraus, *Radio Astronomy*, Cygnus-Quasar Books, 1986.

[11] R. Hartley, "Modulation system," U.S. Patent 1,666,206, April 1928.

[12] D. K. Weaver, "A third method of generation and detection of single-sideband signals," *Proceedings in IRE*, vol. 44, pp. 1703-1705, December 1956.

[13] H. T. Friis, "Noise figure of radio receivers," *Proceedings in IRE*, vol. 32, pp. 419-422, July 1944.

[14] M. Strutt *et. al.*, "Suppression of spontaneous fluctuations in amplifiers and receivers for electrical communication and for measurement devices," *Physics*, June 1942.

[15] H. Fukui, *Low-noise microwave transistors and amplifiers*, IEEE Press, 1981.

[16] R. Meyer *et. al.*, "A 1-GHz BiCMOS RF front-end IC," *IEEE Journal of Solid-State Circuits*, Mar. 1994.

[17] D. Shaeffer *et. al.*, "A 1.5-V 1.5-GHz CMOS low noise amplifier," *IEEE Journal of Solid-State Circuits*, May 1997.

[18] N. Wax, *Selected Papers on Noise and Stochastic Processes*, Dover Publication, 1954.

[19] N. G. Van Kampen, *Stochastic Processes in Physics and Chemistry*, North-Holland Personal Library, 1992.

[20] S. R. de Groot and P. Mazur, *Nonequilibrium Thermodynamics*, North-Holland, Amsterdam 1962.

[21] W. Feller, *An Introduction to Probability Theory and its Applications, Vol. I & II*, Wiley, New York, 1957 and 1966.

[22] A. T. Bharucha-Reid, *Elements of the Theory of Markov Processes and their Applications*, McGraw-Hill, New York, 1960.

[23] D. R. Cox and H. D. Miller, *The Theory of Stochastic Processes*, Chapman and Hall, London, 1972.

[24] C. W. Gardiner, *Handbook of Stochastic Methods for Physics, Chemistry and the Natural Sciences*, Springer-Verlag, second Edition, 1985.

[25] H. Risken, *The Fokker-Planck Equation*, Springer-Verlag, second Edition, 1989.

[26] A. Einstein, *Annalen der Physik* (Leipzig), **17**, 549, 1905.

[27] A. Einstein, *Investigation on the Theory of the Brownian Motion*, Dover Publication, 1956.

[28] M. von Smoluchowski, *Annalen der Physik* (Leipzig), **21**, 756, 1906.

[29] P. Langevin, Comptes Rendus Acad. Sci. (Paris) **146**, 530, 1908.

[30] A. D. Fokker, *Annalen der Physik* (Leipzig), **43**, 810, 1914.

[31] M. Planck, *Sitzungsber. Preuss. Akad. Wissens.* p. 324. 1917.

[32] F. Reif, *Fundamentals of Statistical and Thermal Physics*, McGraw-Hill, 1985.

[33] A. Leon-Garcia, *Probability and Random Processes for Electrical Engineering*, Addison-Wesley, 1994.

[34] H. B. Callen and T. A. Welton, *Phys. Rev.*, **83**, 34, 1951.

[35] H. B. Callen and R. F. Greene, *Phys. Rev.*, **86**, 702, 1952.

[36] H. B. Callen and R. F. Greene, *Phys. Rev.*, **88**, 1387, 1952.

[37] J. L. Jackson, *Phys. Rev.*, **87**, 471, 1952.

[38] W. Bernard and H. B. Callen, *Rev. Mod. Phys.*, **31** 1017, 1959.

[39] J. B. Johnson, *Phys. Rev.*, **32**, 97, 1928.

[40] R. L. Stratonovich, *Nonlinear Nonequilibrium Thermodynamics I*, Springer-Verlag, 1992.

[41] G. E. Uhlenbeck, L. S. Ornstein, *Phys. Rev.*, **36**, 823, 1930.

[42] J. L. Doob, *Annals of Math.*, **43**, 351, 1942.

[43] K. Ito, *Proc. Imp. Acad.* Tokyo, **20**, 519, 1944.

[44] K. Ito, *Mem. Amer. Mathem. Soc.* **4**, 51, 1951.

[45] R. L. Stratonovich, *SIAM J. Control*, **4**, 362, 1966.

[46] P. Gray and R. Meyer, *Analysis and Design of Analog Integrated Circuits*, third edition, John Wiley & Sons, Inc., 1993.

[47] A. van der Ziel, "Thermal noise in field effect transistors," *Proc. IEEE*, pp. 1801-12. August 1962.

[48] A. A. Abidi, "High-frequency noise measurements on FET's with small dimensions," *IEEE Transactions on Electron Devices*, vol. ED-33, no. 11, November 1986.

[49] J. L. Wyatt, Jr. and G. J. Coram, "Nonlinear device noise models: Satisfying the thermodynamic requirements," *IEEE Transactions on Electron Devices*, vol. 46, no. 1, January 1999.

[50] B. Razavi, *Design of Analog CMOS Integrated Circuits*, McGraw-Hill, Boston, 2000.

[51] L. D. Landau and E. M. Lifshitz, *Statistical Physics*, pergamon, New York, 1980.

[52] D. Ham and A. Hajimiri, "Complete noise analysis for CMOS switching mixers via stochastic differential equations," *IEEE Custom Integrated Circuit Conference*, Orlando, Florida, May, 2000.

[53] D. Ham and A. Hajimiri, "Switching mixers - theory and measurement," submitted to *IEEE Journal of Solid-State Circuits.*

[54] M. Okumura, H. Tanimoto, T. Itakura and T. Sugawara, "Numerical noise analysis for nonlinear circuits with a periodic large signal excitation including cyclostationary noise source," *IEEE Transactions on Circuits and Systems- I. Fundamental Theory and Applications*, vol. 40, no. 9, September 1993.

[55] C. D. Hull and R. G. Meyer, "A systematic approach to the analysis of noise in mixers," *IEEE Trans. Circ. and Syst.-1:Fund. Theory and Applications*, vol. 40, no. 12, December 1993.

[56] A. Demir, W. Y. Liu, and A. L. Sangiovanni-Vincentelli, "Time-domain non-Monte Carlo noise simulation for nonlinear dynamic circuits with arbitrary excitations," *IEEE Transactions on Computer-Aided Design of Integrated Circuits and Systems*, vol. 15, no. 5, May 1996.

[57] J. Roychowdhury, D. Long and P. Feldman, "Cyclostationary noise analysis of large RF circuits with multitone excitations," *IEEE Journal of Solid-State Circuits*, vol. 33, no. 3, March 1998

[58] M. T. Terrovitis and R. G. Meyer, "Noise in current-commutating CMOS mixers," *IEEE J. Solid-State Circ.* vol.34, no. 6, June 1999.

[59] W. Yue and B. H. Leung, "Noise analysis for sampling mixers using stochastic differential equations," *IEEE Trans. Circ. and Syst.-2:Analog and Digital Signal Proc.*, vol. 46, no. 6, June 1999.

[60] H. Darabi and A. Abidi, "Noise in RF-CMOS mixers: a simple physical model," *IEEE J. Solid-State Circ.*, vol. 35, no. 1, Jan. 2000.

[61] W. A. Gardner, *Cyclostationarity in Communications and Signal Processing*: Piscataway, NJ:IEEE Press, 1993.

[62] J. Phillips and K. Kundert, "Noise in mixers, oscillators, samplers, and logic: an introduction to cyclostationary noise," *IEEE CICC 2000.*

[63] A. Hajimiri and T. H. Lee, "A general theory of phase noise in electrical oscillators," *IEEE Solid-State Circuits,* vol. 33, pp. 179-194, Feb. 1998.

[64] A. Van Der Ziel, *Noise in Solid-State Devices and Circuits*, John Wiley & Sons, 1986.

[65] L. W. Couch, *Digital and Analog Communication Systems,* 4th ed., New York: Macmillan, 1993.

[66] D. Ham "Switching mixers," *technical report,* California Institute of Technology, November, 2001.

[67] J. Crols and M. Steyaert, "A 1.5 GHz Highly Linear CMOS Downconversion Mixer," *IEEE Journal of Solid-State Circuits,* vol. 30, no. 7, July 1995.

[68] A. N. Karanicolas, "A 2.7-V 900-MHz CMOS LNA and Mixer," *IEEE Journal of Solid-State Circuits,* vol. 31, no. 12, pp. 1939-1944, Dec. 1996.

[69] A. R. Shahani, D. K. Shaeffer, and T. H. Lee, "A 12-mW wide dynamic range CMOS front-end for a portable GPS receiver," *IEEE J. Solid-State Circ.*, vol. 32, no. 12, Dec. 1997.

[70] B. Razavi, *Design of Analog CMOS Integrated Circuits*, McGraw-Hill, 1999.

[71] P. Ritger and N. Rose, *Differential Equations with Applications*, McGraw-Hill, 1968.

[72] D. Ham and A. Hajimiri, "Virtual damping in oscillators," *IEEE Custom Integrated Circuits Conference*, Orlando, Florida, May 2002.

[73] D. Ham and A. Hajimiri, "Concepts and methods in optimization of integrated *LC* VCO," *IEEE Journal of Solid-State Circuits*, vol. 36, no. 6, pp. 896-909, June 2001.

[74] M. Lax, "Classical noise. V. noise in self-sustained oscillators," *Phys. Rev.*, vol. CAS-160, pp. 290-307, 1967.

[75] F. K. Kartner, "Analysis of white and $f^{-\alpha}$ noise in oscillators," *Int. J. Circuit Theory Appl.*, vol. 18, pp. 485-519, 1990.

[76] A. Demir, A. Mehrotra, and J. Roychowdhury, "Phase noise in oscillators: a unifying theory and numerical methods for characterization," *IEEE Trans. on Circuits and Systems-I: Fundamental theory and appl.*, vol. 47, no. 5, May 2000.

[77] D. B. Leeson, "A simple model of feedback oscillator noise spectrum," *Proc. IEEE*, vol. 54, pp. 329-330, Feb. 1966.

[78] B. Van der Pol and J. Van der Mark, *Nature*, **120**, 363, 1927.

[79] B. Van der Pol, "The nonlinear theory of electrical oscillators," *Proc. IRE*, vol. 22, pp. 1051 - 1086, Sep. 1934.

[80] A. A. Andronov, A. A. Vitt, and S. E. Khaikin, *Theory of Oscillators*, Oxford, New York, Pergamon Press, 1966.

[81] S. Strogatz, *Nonlinear Dynamics and Chaos: with Applications in Physics, Biology, Chemistry, and Engineering*, Addison-Wesely, 1994.

[82] D. Ham and A. Hajimiri, "Concepts and methods in optimization of integrated *LC* VCOs," *IEEE Solid-State Circuits*, vol. 36, pp. 896-909, June, 2001.

[83] P. Grivet and A. Blaquiere, "Nonlinear effects of noise in electronic clocks," *Proceedings of the IEEE*, pp. 1606-1614, vol. 51, no. 11, November 1963.

[84] J. A. McNeill, "Jitter in ring oscillators," Ph.D. dissertation, Boston Univ., 1994.

[85] A. Hajimiri, S. Limotyrakis and T. H. Lee, "Jitter and phase noise of ring oscillators," *IEEE Solid-State Circuits*, vol. 34, pp. 790-804, June 1999.

[86] A. Hajimiri and T. H. Lee, *The Design of Low Noise Oscillators*, Kluwer Academic Publishers, 1999.

[87] N. M. Nguyen and R. G. Meyer, "A 1.8-GHz monolithic *LC* voltage controlled oscillator," *IEEE Journal of Solid-State Circuits*, vol. 27, no. 3, pp. 444-450, March 1992.

[88] J. Craninckx and M. Steyaert, "A 1.8-GHz CMOS low-phase-noise voltage-controlled oscillator with prescaler," *IEEE Journal of Solid-State Circuits*, vol. 30, no. 12, pp. 1474-1482, December 1995.

[89] A. Ali and J. L. Tham, "A 900MHz frequency synthesizer with integrated *LC* voltage-controlled oscillator," *ISSCC Digest of Technical Papers*, pp. 390-391, February 1996.

[90] A. Rofougaran, J. Rael, M. Rofougaran and A. Abidi, "A 900MHz CMOS LC-Oscillator with quadrature outputs," *ISSCC Digest of Technical Papers*, pp. 392-393, February 1996.

[91] M. Soyuer, K. A. Jenkins, J. N. Burghartz and M. D. Hulvey, "A 3-V 4-GHz nMOS voltage-controlled oscillator with integrated resonator," *IEEE Journal of Solid-State Circuits*, vol. 31, no. 12, pp. 2042-2045, December 1996.

[92] B. Razavi, "A 1.8GHz CMOS voltage-controlled oscillator," *ISSCC Digest of Technical Papers*, pp. 388-389, February 1997.

[93] L. Dauphinee, M. Copeland and P. Schvan, "A balanced 1.5GHz voltage controlled oscillator with an integrated *LC* resonator," *ISSCC Digest of Technical Papers*, pp. 390-391, February 1997.

[94] B. Jansen, K. Negus and D. Lee, "Silicon bipolar VCO family for 1.1 to 2.2GHz with fully integrated tank and tuning circuits," *ISSCC Digest of Technical Papers*, pp. 392-393, February 1997.

[95] T. Ahrens, A. Hajimiri and T. H. Lee, "A 1.6-GHz 0.5-mW CMOS *LC* low phase noise VCO using bondwire inductance," *First International workshop on Design of Mixed-Mode Integrated Circuits and Applications*, pp. 69-71, July 1997.

[96] P. Kinget, "A fully integrated 2.7 V 0.35 μm CMOS VCO for 5GHz wireless applications," *ISSCC Digest of Technical Papers*, pp. 226-227, February 1998.

[97] T. Wakimoto and S. Konaka, "A 1.9-GHz Si bipolar quadrature VCO with fully integrated *LC* tank," *VLSI Symp. Digest of Technical Papers*, pp. 30-31, June 1998.

[98] T. Ahrens and T. H. Lee, "A 1.4-GHz 3-mW CMOS *LC* low phase noise VCO using tapped bond wire inductance," *International Symposium on Low Power Electronics and Design*, August 1998.

[99] M. Zannoth, B. Kolb, J. Fenk and R. Weigel, "A fully integrated VCO at 2 GHz," *IEEE Journal of Solid-State Circuits*, vol. 33, no. 12, pp. 1987-1991, December 1998.

[100] J. Craninckx and M. Steyaert, "A fully integrated CMOS DCS-1800 frequency synthesizer," *IEEE Journal of Solid-State Circuits*, vol. 33, no. 12, pp. 2054-2065, December 1998.

[101] C. Lam and B. Razavi, "A 2.6 GHz/5.2 GHz CMOS voltage-controlled oscillator," *ISSCC Digest of Technical Papers*, pp. 402-403, February 1999.

[102] T. Liu, "A 6.5 GHz monolithic CMOS voltage-controlled oscillator," *ISSCC Digest of Technical Papers*, pp. 404-405, February 1999.

[103] H. Wang, "A 9.8 GHz back-gate tuned VCO in 0.35 μm CMOS," *ISSCC Digest of Technical Papers*, pp. 406-407, February 1999.

[104] A. Hajimiri and T. H. Lee, "Design issues in CMOS differential *LC* oscillators," *IEEE Journal of Solid-State Circuits*, vol. 34, no. 5, pp. 717-724, May 1999.

[105] C. Hung and K. O. Kenneth, "A packaged 1.1-GHz CMOS VCO with phase noise of -126dBc/Hz at a 600-kHz offset," *IEEE Journal of Solid-State Circuits*, vol. 35, pp. 100-103, January 2000.

[106] J. Kim and B. Kim, "A low-phase-noise CMOS *LC* oscillator with a ring structure," *ISSCC Digest of Technical Papers*, pp. 430-431, February 2000.

[107] F. Svelto, S. Deantoni and R. Castello, "A 1.3 GHz low-phase noise fully tunable CMOS *LC* VCO," *IEEE Journal of Solid-State Circuits*, vol. 35, no. 3, pp. 356-361, March 2000.

[108] H. Wu and A. Hajimiri, "A 10 GHz CMOS distributed voltage controlled oscillator," *IEEE 2000 CICC*, pp. 581-584, May 2000.

[109] H. Ainspan and J. O. Plouchart, "A comparison of MOS varactors in fully integrated CMOS *LC* VCO's at 5 and 7 GHz," *ESSCIRC*, September 2000.

[110] M. Hershenson, S. S. Mohan, S. P. Boyd and T. H. Lee, "Optimization of inductor circuits via geometric programming," *Proc. Design Automation Conf.*, session 54.3, pp. 994-998, June 1999.

[111] M. Hershenson, A. Hajimiri, S. S. Mohan, S. P. Boyd and T. H. Lee, "Design and optimization of *LC* oscillators," *Proc. IEEE/ACM Int. Conf. Computer Aided Design*, San Jose, CA, November 1999.

[112] H. Wang ; A. Hajimiri and T. H. Lee, "Correspondence: comments on "Design issues in CMOS differential *LC* oscillators"" *IEEE Journal of Solid-State Circuits*, vol. 35, no. 2, pp. 286-287, February 2000.

[113] C. P. Yue, C. Ryu, J. Lau, T. H. Lee and S. S. Wong, "A physical model for planar spiral inductors on silicon," *Int. Electron Devices Meeting*, pp. 155-158, December 1996.

[114] Y. P. Tsivids, *Operation and Modeling of the MOS Transistor*, McGraw-Hill, 1987.

[115] D. Ham and A. Hajimiri, "Design and optimization of a low noise 2.4GHz CMOS VCO with integrated *LC* Tank and MOSCAP tuning," *IEEE International Symposium on Circuits and systems*, Geneva, Switzerland, May 2000.

[116] A. M. Niknejad and R. G. Meyer, "Analysis, design, and optimization of spiral inductors and transformers for Si RF IC's," *IEEE Journal of Solid-State Circuits*, vol. 33, no. 10, pp. 1470-1481, October 1998.